Self-Heating in Spray Dried Detergents

Lewis Maxfield

Submitted in accordance with the requirements for the degree of

Doctor of Philosophy

The University of Leeds

School of Chemical and Process Engineering

July 2018

The candidate confirms that the work submitted is his/her/their own and that appropriate credit has been given where reference has been made to the work of others.

Acknowledgements

Firstly, I would like to take this opportunity to say thanks to my supervisor, Prof Andrew Bayly, for giving me this opportunity and for his assistance throughout the past four years. Without his help I would not have been able to accomplish what I have done. I would also like to take this opportunity to thanks to my second supervisor, Dr Ali Hassanpour. Although we did not involve him as much as we could have done, I would like to thank him for being available when needed and for welcoming me into his research group.

I would like to show my appreciation to all the members of both Prof Andrew Bayly's and Dr Ali Hassanpour's research groups, past and present, for their helpful inputs throughout the years, and for making this experience much more enjoyable.

I would not have gotten very far without the help of a number of people at the P&G Innovation Centre in Newcastle upon Tyne. I would like to express my gratitude in particular to my industrial supervisor, Dr Luis Martin de Juan, who was always available to help and was ever welcoming when I travelled up to Newcastle to work. Your regular input into my work provided me with much of the inspiration for the ideas pursued in this research. Although only involved in the first couple of years, I would like to thank Simon Greener for his help and input. I would also like to Bill Caufield, Lauren Oakley, and Tara Aziz for all their help with the experimental work I conducted in Newcastle.

I'd like to show my appreciation to the Engineering and Physical Sciences Research Council (EPSRC), Procter and Gamble (P&G), and Process Systems Enterprises (PSE) who funded this research.

Finally I would like to acknowledge and thank my family and friends, especially my father, Peter, and my mother, Mandy, for their love and support throughout the years.

Abstract

During the spray drying of detergent formulations, powder commonly accumulates on the inner walls of the spray drying tower. Under certain conditions, when these accumulations are large enough, self-heating can occur, whereby exothermic reactions within the accumulations cause an increase in the powder temperature within these layers. This can lead to unwanted charring and in severe cases to thermal runaway.

This study aims to evaluate the methods for characterising the self-heating behaviour of these detergent powders. Firstly, two basket heating methods, namely the steady-state approach and cross-point temperature (CPT) method, were used to estimate the zero-order kinetics of the self-heating reaction of a typical detergent formulation. The resulting kinetics of these methods were not in agreement, with this being attributed to the CPT method's sensitivity to errors.

The kinetics estimated from these methods were used in a developed 2D-axismmetric transient model of heat and mass transfer within an oven heated basket of detergent powder. This was used to make temperature-time profile and critical ambient temperature (temperature above which thermal runaway occurs) predictions, and to simulate aspects of the basket heating experiments.

A novel approach was developed using a combination of the basket experiments and the numerical model. This "parameter estimation approach" uses maximum likelihood estimations to estimate the required parameters. The model was fitted to experimentally measured temperature data, allowing the values of the powder thermal conductivity, specific heat capacity, and self-heating reaction kinetics could be estimated. Determining the specific heat capacity prior to fitting greatly improved the results. This approach was found to be considerably faster than the existing oven based methods (5 times faster than steady-state approach), determine more parameters, and improve greatly on the error of the estimated parameters (over 20 times more accurate than CPT method).

An approach was presented showing how the findings of this research are applied in predicting self-heating in spray dryers for different tower temperatures, heat transfer coefficients, and build-up thicknesses.

Table of Contents

List of Tables

List of Figures

Nomenclature

Latin Characters

A	Pre-Exponential Factor	s^{-1}
A_p	Particle Surface Area	m^2
Bi	Biot Number	-
c_{rc}	Concentration of Reactive Component	kg m^{-3}
C_p	Specific Heat Capacity	J kg^{-1} K^{-1}
D_{vap}	Vapour Diffusion Coefficient	m^2 s^{-1}
E	Activation Energy	J mol^{-1}
ΔE_v	REA Activation Energy Correction Factor	J mol^{-1}
h	Heat Transfer Coefficient	W m^{-2} K^{-1}
h_m	Mass Transfer Coefficient	m s^{-1}
$h_{m,in}$	Internal Mass Transfer Coefficient	m s^{-1}
H_v	Heat of Drying	J kg^{-1}
j	Shape Factor	-
k	Thermal Conductivity	W m^{-1} K^{-1}
L	Characteristic Length	m
n	Reaction Order	-
n_p	Number of Particles per Unit Volume	m^{-3}
Nu	Nusselt Number	-
p	Partial Pressure	Pa
Pr	Prandtl Number	-
Q	Heat of Reaction	J kg^{-1}
R	Universal Gas Constant	J mol^{-1} K^{-1}
r	Radius	m
Re	Reynolds Number	-
RH_s	Surface Relative Humidity	-
t	Time	s
T	Temperature	K
T_{CPT}	Cross-Point Temperature	K
u	Air Velocity	m s^{-1}
X	Moisture Content on a Dry Basis	kg kg^{-1}
Y	Vapour Concentration	kg m^{-3}

$Y_{s,in}$	Internal Surface Vapour Concentration	kg m^{-3}
Y_{sat}	Saturated Vapour Concentration	kg m^{-3}

Greek Characters

α	Reaction Conversion	-
β	Heating Rate	K s^{-1}
δ	F-K Parameter	-
ϵ	Emissivity	-
ε	Porosity/ Void Fraction	-
θ	Dimensionless Temperature Difference	-
μ	Dynamic Viscosity	N m^2 s^{-1}
ν	Stoichiometric Coefficient	-
ξ	Dimensionless Length	-
ρ	Density/ Concentration	kg m^{-3}
ρ_{sd}	Solid Density	kg m^{-3}
σ	Stefan Boltzmann Constant	W m^{-2} K^{-4}
τ	Dimensionless Time	-
φ	Dimensionless Exponent	-
ω	Variance	-

Subscripts

cr	Critical
0	Initial
∞	Ambient

1. Introduction

1.1. Self-Heating in Spray Dried Detergents

The focus of this thesis is on the problem of self-heating that is observed to occur in the spray drying of laundry detergent powders. Laundry detergents are used across the globe to help with the cleaning of clothing and other fabrics. Detergents come in an array of forms, but detergent powders are still commonly used, particularly in developing countries where the majority of consumers still hand wash their laundry.

Detergent powders are typically manufactured in two ways: agglomeration and spray drying. Agglomeration consists of mixing smaller particles with a liquid binder in order to produce larger granules. Spray drying on the other hand is a process by which a slurry of ingredients is atomised into small droplets, which when introduced into hot air are dried and form a powder product.

In the spray drying of these detergent powders, it is common for layers of the newly formed powder product to deposit on the inner walls of the spray drying tower (Francia, et al., 2015) (Hassall, 2011). This is not a problem exclusive to detergent powders and has also been shown to occur in the spray drying of milk powders (Beever, 1985) (Chen, et al., 1993). At the high temperatures at which these towers operate these powder deposits have the propensity to “self-heat”. Self-heating is the process by which some materials can increase in temperature without the application of an external energy source. Exothermic reactions within the material causes an increase in temperature. The stability of these systems is a balance between the internal heat generation and heat loss from the boundaries. If the rate of heat generation is lower than the rate of heat loss from the boundaries, these systems will reach a steady elevated temperature and remain stable. However, if the rate of heat generation exceeds the rate of heat loss from the boundaries, then thermal runaway will occur, whereby a runaway reaction causes a substantial rise in temperature. Many materials exhibit self-heating behaviour including milk powder (Chong, et al., 1996), coal (Sujanti, et al., 1999), and biomass (Caballos, et al., 2015). Self-heating is not only a problem in spray drying, but is also a problem in the storage and transport of these materials.

Consumers have come to expect certain requirements from their laundry detergent. The obvious requirements are that the detergent performs well in cleaning their laundry, while also protecting it from damage. In addition to this, the consumer expects the detergent itself to look and smell clean and appealing. The problem with self-heating is not only the heat generated in the process, but the effect is has on the product. Significant self-heating in the powder deposits on the inner spray dryer walls can cause the powder to char. This produces charred, or burnt, particles which are at risk of falling from the walls and getting collected along with the finished product. Over 20% of the finished product comes from the wall (Francia, et al., 2015) highlighting why self-heating in these build-ups is an issue. This compromises the quality of the finished product, and leaves the consumer with a product that does not meet their requirements of looking clean and appealing.

Limiting the threat of self-heating and charring requires an understanding of the mathematics behind these reactions. The fundamentals of self-heating can be traced back to Frank-Kamenetskii and his Theory of Thermal Explosions (Frank-Kamenetskii, 1969). Frank-Kamenetskii explored the mathematics governing self-heating in an idealised system with a zero-order reaction self-heating reaction. In doing so he derived a dimensionless parameter, δ, often referred to as the Frank-Kamenetskii parameter. This parameter is a ratio of the heat generated to the heat dissipated and encompasses all the quantities required to describe the problems associated with self-heating, inflammation, and ignition. This parameter is a function of the geometry of the problem, the reaction kinetics, and the boundary conditions, such that if these are known, then predictions of self-heating and thermal runaway can easily be made. Much of the subsequent research was based around this important parameter.

Different approaches have previously been applied to address the problem of self-heating. Experimental methods have been applied to measure the self-heating reaction kinetics of similar materials. The long established method is the steady-state method based on Frank-Kamenetskii's theory of thermal explosions (Frank-Kamenetskii, 1969). This is a basket heating method which was originally used to estimate self-heating kinetics for activated carbons (Bowes & Cameron, 1971). More recent work makes use of the cross-point temperature method, first proposed by Chong *et al.* (1996), and originally used to estimate the self-heating kinetics of skimmed and whole milk powders.

These two methods are based around oven heated baskets, and have been effectively used to make predictions of self-heating and thermal runaway in a range of materials.

1.2. Objective of Thesis

The overall objective of this thesis is to understand, and address the problem of self-heating in spray drying and spray dryer wall build-up. In doing this, the research seeks to determine the best means of measuring the self-heating reaction kinetics of a typical detergent powder, and seeks to apply these kinetics in order to predict self-heating and charring in oven heated powder baskets and spray dryer wall deposits. This is broken down further into the following objectives:

1. Review the literature that addresses the fundamentals of self-heating and thermal runaway.
2. Evaluate the self-heating behaviour that occurs in detergent powders and the detrimental effects of this under different heating conditions.
3. Apply a range of experimental techniques to measure the self-heating reaction kinetics of a typical detergent powder and determine the best methods for measuring these self-heating reaction kinetics.
4. Develop numerical models capable of predicting self-heating and thermal runaway in oven heated baskets of powder and spray dryer wall build-up.
5. Advance the overall research in this area such that the knowledge gained and methods develop in this investigation can be applied by industry to address the problem of self-heating in the spray drying of detergent powders.

1.3. Structure of Thesis

This thesis aims to meet these objectives by using a combination of experimental methods and numerical models to explore the self-heating behaviour of detergent powders. The breakdown of the thesis chapters is outlined below.

Chapter 2 - Literature Review

This chapter of this thesis consists of a review of the literature relevant to the problem of self-heating in spray dried detergents. This chapter is broken down into five sections. The first section addresses the literature about self-heating and charring in the process of spray drying. This covers both the spray drying of detergent and the related area of the spray drying of milk powders, which exhibits similar self-heating. The second section address the mathematical fundamentals of self-heating and thermal runaway, and the analytical solutions that spawned from this. These analytical solutions are for the critical parameter δ_{cr} for different geometries. The third section is a brief section reviewing a numerical, rather than analytical, approach for determining the critical parameter δ_{cr}. The fourth section details the experimental methods commonly used in characterising self-heating materials. The primary focus is on a number of oven heated basket methods, while DSC and TGA based methods are also explored. The final section reviews the numerical models frequently used to model and predict self-heating and thermal runaway. These model are used to make predictions in material stockpiles and to explore experimental phenomena in the oven heated basket methods.

Chapter 3 - Evaluation of Self-Heating in Detergent Powders

This chapter details the initial experimental evaluation of the self-heating behaviour observed in a typical detergent powder. Baskets of detergent powder were heated in an oven and the self-heating evaluated by looking at the measured temperature-time profiles at the basket centre and charring that occurs. Initial cross-point temperature method experiments were also performed. Differential Scanning Calorimetry (DSC) and Thermogravimetric Analysis (TGA) were also used to evaluate the self-heating behaviour.

Chapter 4 - Numerical Model of Self-Heating Detergent Powder Systems

This chapter details the numerical model used in this investigation. It details the variants of the model used depending on whether drying and/or reactant consumption is being modelled. This model was code validated against analytical solutions. The validity of a

shape factor approximation, used in some of the literature, for approximating 2D and 3D geometries with 1D equations was tested.

Chapter 5 - Assessment of Methods for Characterising Detergent Formulations

This chapter covers a more comprehensive assessment of the self-heating behaviour, and explores means of characterising the reaction kinetics of the detergent powder. Firstly, the reaction kinetics are measured using the steady-state method. In doing this, the critical parameter δ_{cr} was solved for numerically as a function of the boundary conditions and the reaction activation energy. The cross-point temperature method was then used, the results discussed, and model simulation of this method explored in order to address a number of arising issues. A method known as the DTG method was then used to fit n^{th} order kinetics to thermogravimetric data. The measured kinetics of all these methods were compared using the numerical model outlined in Chapter 4. The influence of different model parameters and the use of zero and n^{th} order reaction models were explored.

Chapter 6 - Novel Parameter Estimation Approach for Characterising Self-Heating Powders

This chapter outlines a novel parameter estimation approach for characterising the self-heating behaviour of these detergent powders. This approach determines the specific heat capacity, thermal conductivity, and self-heating reaction kinetics of the powder though parameter estimation. The development, approximations, and procedure of this approach are all detailed. Also detailed are the DSC based methods used to determine the specific heat capacity and reaction activation energy prior to fitting. This approach is applied to a single formulation of detergent. The results of this approach for different fitting scenarios are discussed, and the results of this method compared with the oven heated basket methods. The advantages of this approach over the existing methods are also discussed.

Chapter 7 - Parameter Estimation Approach Workflow and Application to Other Detergent Formulations

A recommended workflow for applying this approach to new formulations is detailed. The parameter estimation approach is then applied to three additional detergent powder formulations to help in validating this approach as an alternative to the existing characterisation methods.

Chapter 8 - Modelling of Self-Heating in Spray Drying Towers

This chapter briefly demonstrates how the experimental methods and developed models are to be applied to predict self-heating in spray dryer wall deposits of detergent powders. A 1D adaption of the model used in this investigation is applied to spray dryer wall build-up, and the influence of the ambient temperature, heat transfer coefficient, and build-up thickness explored.

Chapter 9 - Conclusions and Recommended Future Work

Chapter 9 draws conclusions from this research and recommends future work that could follow on from this.

2. Literature Review

2.1. Introduction

The problem of self-heating is not exclusive to the spray dryer wall build-ups, and not exclusive to detergent powders. In order to have a greater understanding as to the state of the current research, it is necessary to look beyond detergent powders and spray dryer build-ups, and to look at other related areas. In doing so, this literature review will cover self-heating in many different materials and scenarios, and means of characterising this behaviour and predicting it. It will also address the fundamentals of self-heating by looking at the analytical origins of Frank-Kamenetskii's Theory of Thermal Explosions (Frank-Kamenetskii, 1969), and the more recent developments in numerical analysis and modelling of self-heating systems.

This literature review explores these problems in four major sections:

- *Self-Heating in Spray Drying Operations*. This section looks at some of the published research which explores self-heating as an issue in the spray-drying process, with much of the work centring on the spray drying of milk-powders. Also discussed are the deposition and re-entrainment rates of detergent powders in a counter current spray dryer.
- *Analytical Solutions to the Problem of Self-Heating.* The mathematical fundamentals of self-heating are discussed here, including Frank-Kamenetskii's Theory of Thermal Explosions (Frank-Kamenetskii, 1969) which provided the basis from which much of the future work on predictions of self-heating and thermal runaway was developed. Also discussed are analytical solutions to a number of simple cases, such as slabs and cylinders with differing boundary conditions.
- *Experimental Methods for the Characterisation of Self-Heating.* This sections explores different methods used to measure the self-heating reaction kinetics of a range of materials. A number of methods are explored including some based around oven heated baskets of powder, DSC and TGA based isoconversional techniques, and a method where kinetics are fit to measured thermal degradation profiles.

- *Numerical Modelling of Self-Heating Powder Systems.* Finally, the use of numerical models in predicting self-heating are discussed. Numerical models of self-heating in powder baskets and stockpiles are explored. These models are not only used to predict self-heating and thermal runaway in the storage of these materials, but they have also been used to simulate the basket heating experiments such that issues and phenomena of these methods can be explored.

The literature reviewed here will help to determine the best approach that can be used to address the problem of self-heating in detergent powders. The analytical solutions help to provide an understanding of the fundamentals of the self-heating, and the basis on which some of the experimental methods are based. Understanding the available methods, and the associated advantages and disadvantages of each will help in making informed decisions with regards which methods to use. Finally the measured kinetics can be used to develop a numerical model of a self-heating powder basket. This model can be used to explore the methods further, and having validated it, it can be adapted to model self-heating in spray dryer deposits, allowing predictions to be made in the spray drying tower.

2.2. Self-Heating in Spray Drying Operations

Self-heating and spontaneous combustion is a phenomena long observed in spray drying, and this problem is not exclusive to spray dried detergent powders. Beever (1985) and Beever and Crowhurst (1989) noted that although the spray drying of milk powders is not considered to be a particularly hazardous operation, charring and minor fires are seen to occur regularly, whilst occasionally more severe dust exposition are seen to occur. He noted that thirty five major accidents occurred in the French dairy industry between the years of 1967 and 1982, and that fourteen of these accidents involved fire and explosion. Dust explosions are known to occur when fine particulate material is dispersed in air in the presence of an ignition source. It was noted in certain regions of the spray drying tower, all the conditions required for a dust explosion exist during normal operation, other than the existence of an ignition source.

Beever noted that self-ignition is believed to be the ignition source for most fires in milk powders, arising from oxidation of powder build-ups which are exposed to high

temperatures in the spray dryer. These reactions are known to all be exothermic with heat generation increasing substantially with temperature. In the case of milk powders, heat generation at an ambient temperature of 100°C will be 1,000 times greater than at 20°C, and more than 100,000 time greater at 200°C, with self-heating in milk powder deposits increasing their temperatures to in excess of 700°C. These heated deposits serve as an ignition source for dust explosions in the spray dryer.

In the spray drying of milk, as in the spray drying of detergent powders, the size of the deposits are key to the extent to which they will self-heat. For small deposits, all the heat generated by the reaction can be dissipated such that there is no risk of explosion, although it has been observed that discolouration of the milk powder may occur. Similar behaviour is observed when slight self-heating is observed in detergent powders. As the deposits increase in size, the heat generation increases with little increase in heat dissipation. In such cases, if heat generation exceeds heat dissipation, thermal ignition occurs, and dust explosions now become a potential hazard. He noted that because this heat generation is so strongly dependent on temperature, then the critical thickness for self-ignition is also strongly dependent on temperature.

Typically deposits and temperatures as documented by Beever in a co-current spray dryer can be seen in Figure 2-1. It can be seen that the largest deposits are found in the corners where the cone begins to slope, and in the top corners, where the turbulence induced by the rotary atomiser creates eddies which throws the powder up to these corners. Deposits can also form layers on the wall, and even build-up in the exhaust and fines return pipes.

In regions where temperatures are about 200°C, the time to ignition is approximately an hour, whereas at 100°C this increases to a few hours. This is assuming an instantaneous build-up, whereas in practice these layers will oxidise as they are formed and present less of a hazard. It has been suggested that the region considered to be of greatest risk to self-ignition is at the outlet of the spray dryer, which would typically be at about 80°C. At this temperature a thickness of 20-40cm would be required, taking many hours to self-ignite, although it is hard to imagine that such deposits would go unnoticed. Nonetheless, it is also stated that this analysis is worth noting for the storage of these milk powders. Even at the lower temperatures at which the powder leaves the production cycle, there may be a risk of self-ignition if large quantities are stored.

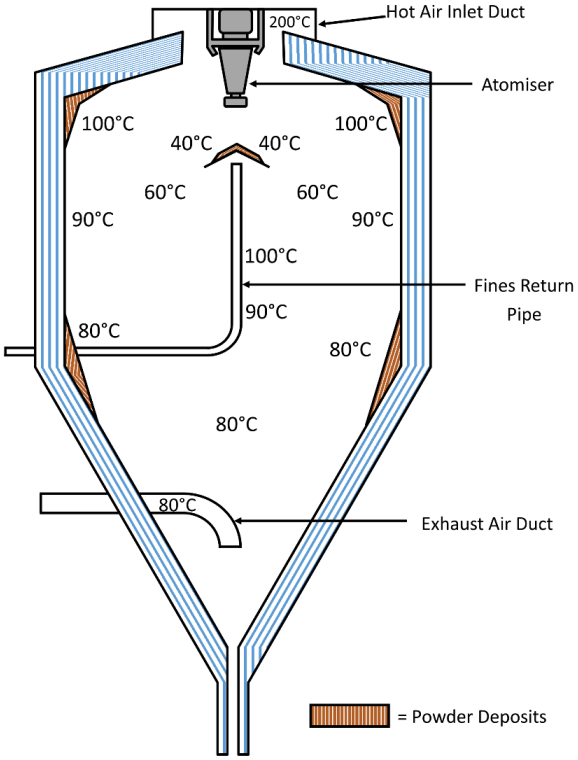

Figure 2-1: Co-current spray dryer for milk products showing typical temperature distribution and regions of powder deposits, as detailed by Beever (1985).

Beever also outlines approaches to avoid ignition of dust explosions in spray drying. Correct maintenance of equipment prevents sources of ignition such as sparks and adverse heating as a result of mechanical failure, but the risk of self-ignition in powder deposits is not so easily addressed. Often it is not possible to operate these spray dryers without the build-up of powder, and in some cases mechanical means of preventing build-up have been applied. Devices such as knocking hammers, vibrators or scrapers have been used, but should any of these devices develop a fault, then build-up could occur which isn't being actively monitored. Typically, regular cleaning of the spray dryers is used to prevent self-ignition by cleaning at such intervals that deposits do not have sufficient time to reach critical thickness.

Even for dryers that are regularly cleaned, or which typically stay clean, it is possible for deposits to unexpectedly form. The start-up procedure of the spray dryer is the most important factor in this. If the dryer is not given sufficient time to heat up, then damp patches can form on the dryer walls, to which powder is more likely to deposit. Once such depositions are made, they provide a layer to which powder can more easily deposit. For this reason, regular visual inspections need to be carried out, and sufficient

care taken in cleaning and dryer start-up. Beever notes that charred lumps, caused by the self-heating of deposits, may fall from the walls and be collected in the finished product. Watching for these lumps is important as not only do they compromise the finished product, but they also give an indication that the tower needs to be cleaned. These problems are not limited to milk powders and are readily observed in detergent powders. The issue of charred product being found in the finished product is the primary motivation of this research, whereas the problem of self-ignition and thermal runaway not as important, although it is still a concern that is being addressed.

Chen *et al.* (1993) also looked at the issue of milk powder depositions in industrial spray dryers. They note that the milk powder deposits that form on the internal walls of these dryers need to be regularly cleaned for a number of reasons. These build-ups are a fire safety hazard due to the risk of self-ignition and are a risk to product quality because these deposits can fall off into the product, but in milk powder dryers they also pose a hygiene risk. Chen *et al.* noted that in co-current spray dryers, deposits are seen to occur in three regions

1. Deposits form on the side walls of the dryer due to direct impact of wet particles with high velocities
2. Deposits form on the lower cone of the dryer, either by direct impact of wet particles, or by dry particles swirling downwards and striking the sloping walls of the cone.
3. Deposits form on the ceiling of the dryer, either by dispersion from the atomiser, or by entrainment of particles in the turbulent air caused by the sudden expansion of air entering the dryer.

The deposits that form on the ceiling are of particular risk. Because of the high inlet temperature, with the inlet at the ceiling of these co-current dryers, these deposits are at risk of self-ignition should they become sufficiently large. Similarly, in counter-current spray dryers, although the inlets are in the lower portion of the tower, build-up around these inlets is of particular risk. The probability of powder deposition in milk powders is highly dependent on formulation, with fat and lactose content and how their physical properties change with temperature believed to be the most important factors.

Chen *et al.* also noted this issue of “browning” or “scorching” of milk powder particles which can impact on the quality of the final product. In milk powder there are strict

limitations on the permitted amount of scorched particles in the final product, such that limiting this problem is of high importance in this industry, just as it is in detergent powders.

Milk powders are typically dried using co-current spray dryers, whereas detergent powders tend to be dried using counter-current swirl spray dryers (Francia, et al., 2015), the difference being that the air hot inlet of a counter-current dryer is towards the bottom with the outlet at the top. Francia *et al.* (2015) looked to understand the role that wall depositions and particle re-entrainment plays in these counter-current spray dryers when drying detergent powders. These dryers operate differently to co-current in that the counter-current design creates a strong turbulent swirling flow which increases the particle residence time and helps to increase process efficiency. This counter flow also increases particle concentration, such that more particle-particle contacts and agglomeration occurs. The swirl aspect of the dryer creates a size preferential concentration of particle close to the dryer internal walls. This concentration close to the walls leads to more impacts and a much higher rate of deposition.

In drying these detergent powders, deposition and re-entrainment contribute to three main issues: (1) product degradation and the safety and quality concerns associated with self-heating, (2) a decrease in product yield and process efficiency, and (3) increased costs due to cleaning and maintenance. Despite this, these swirl counter-current towers are known to operate for longer without cleaning than their co-current counterparts, as it is thought that the rate of deposition is balanced, or supressed by the re-entrainment of wall deposited particles. In exploring the role of these depositions, Francia *et al*. developed a new experimental approach to study deposition rates. Deposits were made traceable by injecting a dye into the slurry feed. Firstly a non-dyed batch is run to allow a build-up to form on the walls. The dye is then injected into the slurry feed such that the next batch is visibly pink in colour. This batch is run for some time and the pink powder is seen to deposit on the walls. The dye injector is then turned off and normal, white powder is produced. A section of the internal wall is periodical monitored throughout this entire process to determine deposition rates. The powder was also monitored as it exited to tower which allowed the re-entrainment of the pink particles to be monitored. It was found that clusters of particle form and break at the walls, such

that an active layer of deposits is formed, with a degree of constant surface refreshment. The impact on this investigation is that constant refreshment of the powder layer will have significant effects on the self-heating in these layers, although it will also be difficult to account for using models. Francia *et al.* also remarked that particles falling from the walls account for more than 20% of the final product, and the majority of the large granules. Having such a high proportion of the powder come from the walls increases the risk of charred powder, charred due to self-heating in layers on the walls, finding its way into the finished product, greatly reducing the product quality.

Other work has addressed the problem of self-heating in different ways. Chong and Chen (1999), and Chen (2001) used a similar approach to model heat and mass transfer in oven heated baskets of milk powder using a pseudo-1D finite difference model. This model was used to simulate the basket-heating methods but it was noted by the authors that these milk powders deposit in layers in the spray dryer and that this model could be extended to model these layer scenarios. Liang and Tanaka (1987) also modelled spontaneous ignition in dust deposits, but using a generalised model not specific to any material. They used a 1D model of heat transfer in a dust layer, looking at different scenarios that may arise. These articles show how the problem of self-heating is being addressed for more than just powder storage problems. These models will be explored in more detail in subsequent sections.

2.3. Analytical Solutions to Self-Heating Problems

2.3.1. The Theory of Thermal Explosions

Self-heating systems are complex in that they are transient systems involving the evolution of reactants, products and temperatures. The Theory of Thermal Explosions was first proposed by Semenov (1928) and this work simplified these concepts to understand the evolution of heat generation in reactant containing vessels and the critical conditions that would lead to thermal explosions. Semenov primarily worked with gaseous systems and remarked that under certain conditions for temperature, pressure, and heat dissipation from the system, it could be seen that the heat generated by the reactions occurring could not fully escape through the walls of the system, and this would lead to an increases in the temperature of the gas. This increase in

temperature would cause an acceleration of the reaction, and a further increase in heat generation. This process is what leads to these thermal explosions. Knowing the kinetics laws that govern this heat generation, the mechanisms of heat transfer, the initial conditions, and the boundary conditions, this theory of thermal explosions allows the critical conditions of these systems to be determined.

Frank-Kamenetskii, a former student of Semenov, further developed this theory of thermal explosions, working initially on gaseous systems, but also later applying this theory to condensed, self-heating materials. In approaching this issue Frank-Kamenetskii (1969) focused on the use of dimensionless parameters for simplified systems. In choosing the correct dimensionless variables, he noted that it would be possible to interpret the physical laws that govern inflammation and ignition, and determined the critical conditions that lead to thermal ignition.

Firstly he defined the basic equation of combustion theory, which measures the transient evolution of temperature in a self-heating system. He noted that the reaction rate in these systems is non-linearly dependent on temperature. This non-linearity is important because without it critical conditions would not exist, and combustion could not occur. Essentially it is an energy balance defined by the following quasilinear equation:

For $0 \leq x \leq r$ and $t \geq 0$,

$$\rho C_p \frac{\partial T}{\partial t} = \nabla\left(k\nabla T - \rho C_p v T\right) + \rho Q A e^{-\frac{E}{RT}} \qquad (2\text{-}1)$$

Where T is the temperature, ρ is the density of the material, C_p is the specific heat capacity, k is the thermal conductivity, Q the heat of reaction, A the Arrhenius pre-exponential factor, E the activation energy of the reaction, and R the universal gas constant. v is the flow velocity which stems from this theory's application to gaseous systems. In condensed medium, such as the powder layers of interest to this investigation, the medium is assumed stationary. The temperature dependence of the thermal conductivity, k, is also neglected, and this equation reduces to:

For $0 \leq x \leq r$ and $t \geq 0$,

$$\rho C_p \frac{\partial T}{\partial t} = k\nabla^2 T + \rho Q A e^{-\frac{E}{RT}} \qquad (2\text{-}2)$$

This equation forms the basis of Frank-Kamenetskii's Stationary Theory of Thermal Explosion. It captures the change in energy of the system as a function of time, due to conduction of heat into/out of the system, and addition/loss of heat from the system because of exothermic/endothermic reactions described using an Arrhenius expression. This steady-state form is given as:

For $0 \leq x \leq r$,

$$k\nabla^2 T = -\rho Q A e^{-\frac{E}{RT}} \tag{2-3}$$

The goal of this theory is to reduce the basic equation down to a dimensionless equation such that the critical conditions of the system can be determined. These critical conditions are defined to be those at which the steady-state distribution of temperature becomes impossible. Because of this, the method for transforming this equation into one containing only dimensionless variables is of vital importance. There are two means of doing this, one stems from the exact form of the Arrhenius expression, and the other uses an approximation known as the method of expanding the exponent. For both approaches the following dimensionless parameters, the dimensionless coordinate, ξ, and the dimensionless temperature, θ, are defined:

$$\xi = \frac{x}{r} \tag{2-4}$$

$$\theta = \frac{E}{RT_*^2}\Delta T = \frac{E}{RT_*^2}(T - T_*) \tag{2-5}$$

Where x is the usual spatial coordinates, r is some characteristic length, and T_* is a temperature near to which the reaction takes place. According to the basic empirical law of chemical kinetics, as described by the Arrhenius expression, the rate of chemical reaction never reduces to zero, as can be seen. Instead it decreases exponentially with temperature, and must react after a sufficiently long period of time. If the reaction is not neglected at the initial temperature, then the initial state cannot be regarded as stationary. If the exponential term reduces to zero at the initial temperature (i.e. the reaction rate reduces to zero), then the system can be assumed stationary, but unstable, since any small change in conditions can impart a change in reaction rate.

The method of expanding the exponent uses the following expansion of the Arrhenius exponent which still retains the exponential nature of the term:

$$\frac{E}{RT} = \frac{E}{R(T_* + \Delta T)} = \frac{E}{RT_*}\frac{1}{1 + \frac{\Delta T}{T_*}} \tag{2-6}$$

The final term can be approximated by the Taylor series expansion of $\frac{1}{1+x}$:

$$\frac{1}{1 + \frac{\Delta T}{T_*}} \approx 1 - \frac{\Delta T}{T_*} + \left(\frac{\Delta T}{T_*}\right)^2 - \left(\frac{\Delta T}{T_*}\right)^3 + \cdots \tag{2-7}$$

In the problem of spontaneous inflammation the temperature T_* is taken to be the ambient temperature T_∞. ΔT is the difference between the temperature T_* and the temperature at a point of interest, such that $\Delta T \ll T_*$. This means that the first two terms of the above expansion are a sufficient approximation of this term, and the exponent can be expressed as:

$$\frac{E}{RT} \approx \frac{E}{RT_*} - \frac{E\Delta T}{RT_*^2} \tag{2-8}$$

And the Arrhenius term approximated by:

$$e^{-\frac{E}{RT}} \approx e^{-\frac{E}{RT_*}} \cdot e^{\theta} \tag{2-9}$$

Using this approximation, as well as the previously defined dimensionless coordinate and temperature, the steady-state energy balance in equation (A-1) can be reduced to:

$$\nabla_\xi^2 \theta = -\frac{E}{RT_*^2}\frac{\rho Q A}{k} r^2 e^{-\frac{E}{RT_*}} \cdot e^{\theta} \tag{2-10}$$

From this equation, the following dimensionless parameter can be defined:

$$\delta = \frac{E}{RT_*^2}\frac{\rho Q A r^2}{k} e^{-\frac{E}{RT_*}} \tag{2-11}$$

This term encompasses all the quantities essential in discussing the problems associated with inflammation and ignition. It is a ratio of the heat generated due to the reaction to the heat dissipation from the system, via the conduction and the heat loss across the boundary. Soon it will be shown how this parameter can be used to predict thermal runaway in these self-heating systems. In future work following the publication of this by Frank-Kamenetskii, this dimensionless parameter is often referred to as the Frank-Kamenetskii parameter. Using this term equation (2-10) is reduced to its dimensionless form:

For $0 \leq \xi \leq 1$,

$$\nabla_{\xi}^{2}\theta = -\delta e^{\theta} \tag{2-12}$$

The other method of reducing equation (2-10) to its dimensionless form involves the exact form of the Arrhenius exponent rather that the approximation used here. Using the dimensionless temperature difference term in equation (2-8), the exponent can be expressed in the following, exact form:

$$e^{-\frac{E}{RT}} = e^{-\frac{E}{RT_*}} \cdot e^{\frac{\theta}{1+\frac{\theta}{\varphi}}} \tag{2-13}$$

Where φ is defined as:

$$\varphi = \frac{E}{RT_*} \tag{2-14}$$

This derivation in detail can be seen in Appendix A. Using this, equation (A-1) in exact dimensionless form is expressed as:

For $0 \leq \xi \leq 1$,

$$\nabla_{\xi}^{2}\theta = -\delta e^{\frac{\theta}{1+\frac{\theta}{\varphi}}} \tag{2-15}$$

It can be seen that for high activation energies the value of φ approaches infinity, and equation (2-15) reduces to equation (2-12). This is in agreement with the assumption made in the method of the exponent that $\Delta T \ll T_*$, where T_* is taken as the ambient temperature. This equation will be used later in the numerically solving for the critical parameter δ_{cr}.

The importance of these equations was evident to Frank-Kamenetskii. He noted that the stationary temperature distribution must have a solution of the form:

$$\theta = f(\xi, \delta) \tag{2-16}$$

He also noted that the critical condition for inflammation or ignition is the condition for which this stationary temperature distribution ceases to exist. For the simplest case, the boundary condition is expressed by $\theta = 0$ at the surface, and the critical condition reduces to:

$$\delta = constant = \delta_{cr} \tag{2-17}$$

This is because the parameter δ is the only parameter in either the equation or the boundary conditions at this point. By substituting the system values into equation (2-11), one obtains the value of δ for that system. A critical value of δ can be defined, δ_{cr}, based on the system geometry, boundary conditions, and reaction kinetics. This will be explored in detail in the next few sections. If the value of δ is below δ_{cr} then a steady-state temperature distribution exists, otherwise thermal runaway will occur. This has many uses in understanding the problem of self-heating in a range of systems. The next issue was to determine this critical value δ_{cr} for the system in question.

2.3.2. Solutions for the Critical Condition δ_{cr} for Infinite Slabs

Semenov's approach to such inflammation problems considered a vessel in which it is assumed that the temperature is uniform at all points. This "homogenous inflammation" does not agree with the fact that inflammation is known to begin at a single point, and propagate from there. Such systems with this temperature uniformity only exist where high levels of convection occur, typically with stirring. Frank-Kamenetskii considered a vessel filled with a reacting gas in which heat transfer occurs purely by conduction. This system is of interest because this condition also describes how heat transfer occurs in powder systems. A temperature gradient exists in this system with the highest temperature being at the centre of the vessel, where it is thought inflammation ought to start. This allows the critical condition for inflammation to be determined by the temperature distribution, with inflammation occurring when this temperature distribution ceases to exist.

Firstly three assumptions must be made in order to develop a solution;

1. The pre-explosion temperature rise is considered small in comparison to the absolute temperature of the vessel walls. i.e. $\Delta T/T \ll 1$. This is equivalent to $RT \ll E$ and is the foundation of the method of expanding the exponent.
2. The reaction rate is assumed to depend only on temperature in accordance with the Arrhenius expression $\exp\left(-\frac{E}{RT}\right)$, such that the depletion of fuel, any temperature dependence of pre-exponential factor, and any change in density is neglected.

3. The thermal conductivity of the system boundary walls is regarded as infinitely large. This corresponds to an infinite Biot number, given by hL/k, where h is the external heat transfer coefficient, k the thermal conductivity, and L some characteristic length.

Frank-Kamenetskii solved this for an infinite vessel with plane-parallel walls, equivalent to an infinite slab of powdered material. For this geometry, where r is the vessel half-width, equation (A-1) can be expressed as:

For $-r \leq x \leq r$,

$$k\frac{d^2T}{dx^2} = -\rho Q A e^{-\frac{E}{RT}} \tag{2-18}$$

In dimensionless form this expressed as:

For $0 \leq \xi \leq 1$,

$$\frac{d^2\theta}{d\xi^2} = -\delta e^{\theta} \tag{2-19}$$

The solution to this equation, found by integration by substitution is:

$$e^{\theta} = \frac{a}{\cosh^2\left(b \pm \sqrt{\frac{a\delta}{2}} \cdot \xi\right)} \tag{2-20}$$

This solution contains two arbitrary constant a and b. Because of the symmetry of the system:

$$\frac{d\theta}{d\xi}_{\xi=0} = 0 \tag{2-21}$$

From this it can be seen that $\theta(\xi) = \theta(-\xi)$, from which it can be deduced that the constant b must be equal to zero. The constant a is determined using the boundary conditions at the wall of the vessel, $\theta = 0$ at $\xi = 1$. This gives the transcendental equation for a:

$$a = \cosh^2\sqrt{\frac{a\delta}{2}} \tag{2-22}$$

A transcendental equation is a non-algebraic equation where the equation is a function of the variable that is being solved for. Often such equations do not have closed form

solutions. A stationary temperature distribution exists only for values of δ at which equation (2-22) has a solution. If a solution exists then the corresponding values of a and δ can be used in (2-20) to obtain this distribution. An explosion must occur for values of δ for which no solution exists. The largest value of δ for which (2-22) a solution exists is considered to be δ_{cr} and is the critical condition for inflammation.

By defining the following:

$$a = \cosh^2 \sigma \tag{2-23}$$

It is possible to redefine the transcendental equation (2-22) as:

$$\frac{\cosh \sigma}{\sigma} = \left(\frac{\delta}{2}\right)^{-\frac{1}{2}} \tag{2-24}$$

From this it is possible to see that the critical condition for inflammation occurs for the minimum value of $\frac{\cosh \sigma}{\sigma}$, which occurs for $\sigma_{cr} = 1.2$, which when substituted back gives:

$$\delta_{cr} = 0.88 \tag{2-25}$$

This result can also be seen from the plot of the solution to the transcendental equation (2-22) in Figure 2-2 where the extreme value on the right is the critical conditions for inflammation.

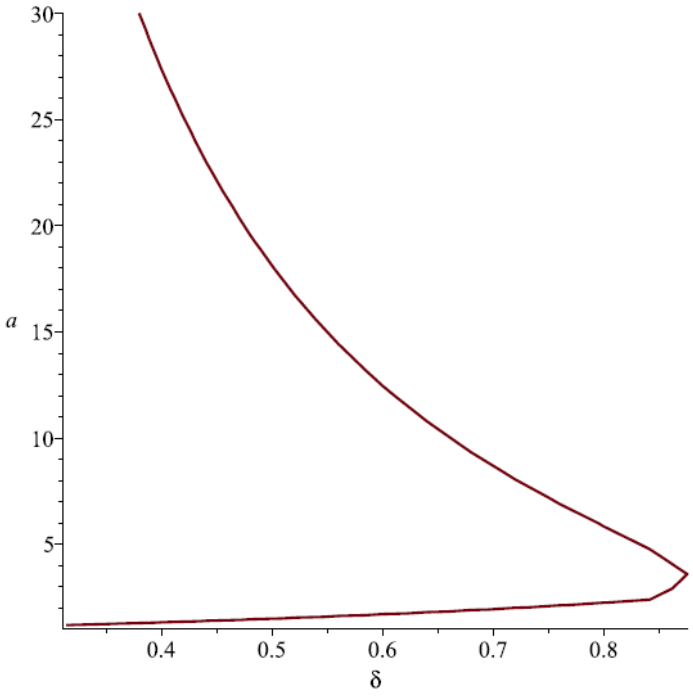

Figure 2-2: Solution of the transcendental equation (2-22) illustrating the critical condition $\delta_{cr} = 0.88$.

It can be seen that no solution exists for a value of δ greater than 0.88. This occurs for a value of a_{cr} of 3.28, which corresponds to a value for σ_{cr} of 1.2. If the system has a δ value equal to δ_{cr} then after an infinite amount of time the system will combust.

Although this was original developed for gaseous systems, it is clear that the assumption of heat transfer purely by conduction allows this solution to be applied to the problem of self-heating in condensed powder geometries. However, this solution still only holds true for the assumption that $\theta = 0$ at the vessel surface, corresponding to an infinite Biot number. Thomas (1957) extended this approach to determining the critical condition for self-heating materials that are subjected to surface cooling. In doing so the same approach is used as by Frank-Kamenetskii and the solution to the energy balance equation is equivalent to equation (2-20). Taking the logarithmic form of this equation gives:

$$\theta = \ln a - 2\ln\cosh\left(b \pm \xi\sqrt{\frac{a\delta}{2}}\right) \tag{2-26}$$

In this case though, the reacting substance is a self-heating infinite slab of material subjected to boundary cooling. This system is illustrated in Figure 2-3.

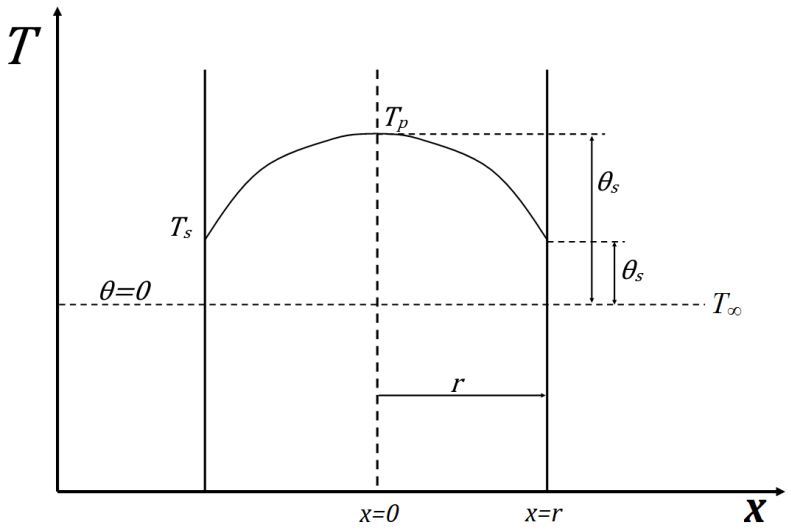

Figure 2-3: Temperature profile across a symmetrically cooled self-heating slab, with ambient temperature T_∞, surface temperature T_s, peak temperature T_p, characteristic dimension r, and overall width $2r$.

The maximum temperature occurs at the basket centre and the boundary condition is given by:

At $\xi = 0$

$$\frac{d\theta}{d\xi} = 0 \tag{2-27}$$

At the slab surface, the external convective heat transfer from the surface is equal to the conductive heat transfer to the surface:

At $\xi = 1$,

$$Bi\ \theta + \frac{d\theta}{d\xi} = 0 \tag{2-28}$$

Here the Biot number, Bi, is the ratio of heat transfer resistance inside of a body to the heat transfer resistance at the surface of a body, given by hr/k. The first of these boundary conditions is satisfied if the constant of integration, b, is equal to zero. The second is satisfied as long as the following holds true:

$$\ln \delta = \frac{2\sigma^2}{\cosh^2 \sigma} - \frac{2\sigma \tanh \sigma}{Bi} \tag{2-29}$$

For this case, the critical value σ_{cr} is found in terms of the Biot Number, Bi, when the value of δ is maximised. This is done by differentiating (2-29) which gives:

$$Bi = \frac{\sigma_{cr}\ \sinh \sigma_{cr}\ \cosh \sigma_{cr} + \sigma_{cr}^2}{(1 - \sigma_{cr}\ \tanh \sigma_{cr})\ \cosh^2 \sigma_{cr}} \tag{2-30}$$

The solution to (2-30) is plotted in Figure 2-4 and shows that as the Biot number approaches infinity, the value of σ_{cr} approaches 1.2, corresponding to the value of δ_{cr} calculated by Frank-Kamenetskii (1969) of 0.88.

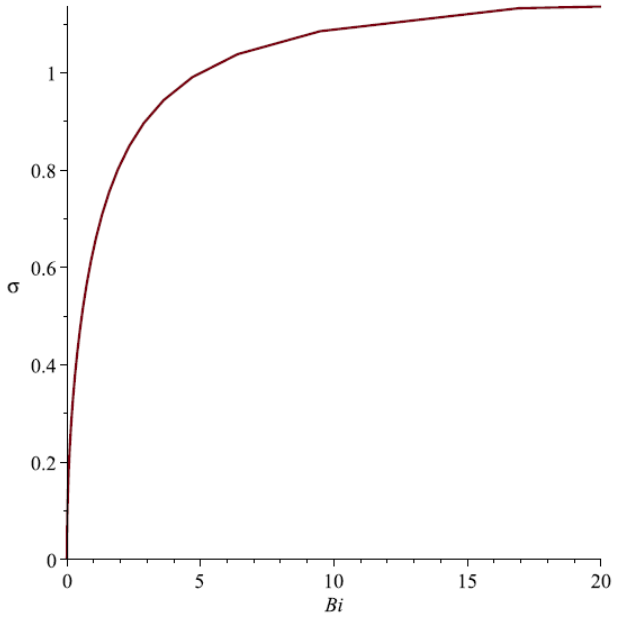

Figure 2-4: δ as a function of Biot number for an infinite slab with boundary cooling.

2.3.3. Extension of Solutions to Other Geometries

Thomas (1957) also solved for the critical conditions for an infinite cylinder and a sphere subjected to boundary cooling, as was done for an infinite slab. For geometries where the conduction is only dependent on one spatial coordinate, the Laplacian operator can be made dimensionless, resulting in the following equation:

For $0 \leq xi \leq 1$,

$$\frac{d^2\theta}{dz^2} + \frac{\kappa}{\xi}\frac{d\theta}{d\xi} = -\delta e^{\theta} \tag{2-31}$$

Where $\kappa = 0$ for an infinite slab, $\kappa = 1$ for an infinite cylinder, and $\kappa = 2$ for a sphere. Chambré (1952) solved for these systems using the infinite Biot number assumption of Frank-Kamenetskii. Thomas (1957) continued this work to solve for these geometries with boundary cooling. He showed that the dimensionless temperature difference for a cylinder can be expressed as:

$$\theta = \ln\left(\frac{2F^2 B\xi^{F-2}}{\delta(1 + B\xi^F)^2}\right) \tag{2-32}$$

Where B is a constant of integration and:

$$F^2 = E + 4 \tag{2-33}$$

For the case of a hollow cylinder E is non-zero, and this case is defined by the above equation. For a solid cylinder E is equal to zero, such that $F = 2$ and the equation reduces to:

$$\theta = \ln\left(\frac{8B}{\delta(1 + B\xi^2)^2}\right) \tag{2-34}$$

Applying this equation to the surface boundary condition, and applying the conditions such that δ is maximised gives the following equation for the critical value of the constant of integration, B_{cr}, with respect to the Biot number:

$$Bi = \frac{4B_{cr}}{1 - B_{cr}^2} \tag{2-35}$$

This can be plotted similar to Figure 2-4, to show that the critical condition δ_{cr} for a solid cylinder as Bi approaches infinity is 2.0. For a sphere, it was shown that as Bi approaches infinity the critical condition δ_{cr} approaches 3.32, as can be calculated from:

$$Bi = \frac{\eta_s^2 e^{-\eta_s} - \eta_s \left(\frac{d\psi}{d\eta}\right)_s}{1 - \eta_s \left(\frac{d\psi}{d\eta}\right)_s} \tag{2-36}$$

Where the subscript s denotes at the surface (i.e. $\xi = 1$) and

$$\psi = \theta_0 - \theta \tag{2-37}$$

$$\eta = \xi\left(\delta e^{\theta_\infty}\right)^{\frac{1}{2}} \tag{2-38}$$

Other analytical solutions have been developed that look to determine the critical parameter δ_{cr} under different conditions. One such solution is that of Thomas and Bowes (1961) who solved for δ_{cr} for the case of a self-heating infinite slab with unsymmetrical boundary conditions, such that one surface is at a constant high temperature. Another case is that of Bowes and Thomas (1966) who investigated the ignition and extinction phenomena which accompany oxygen-dependent self-heating reactions in porous bodies. These solutions are rather complex, and will not be discussed any further, but they are worthy of mentioning.

Nelson and Chen (2007) summarised the values of δ_{cr} and the maximum dimensionless temperature rise, θ_{max}, for common geometries under the following two assumptions:

- The activation term is sufficiently high, such that $E \gg RT$, an approximation made in the method of expanding the exponent.
- The Biot number is sufficiently high that the surface of the body can be assumed equal to the surrounding temperature.

These values are shown in Table 2-1. The following section will explore how δ_{cr} can be determined when the first of these assumptions is not being applied.

Table 2-1: δ_{cr} and θ_{max} values for common geometries as summarised by Nelson and Chen (2007) with the assumption that $E \gg RT$ and $Bi = \infty$ applied.

Geometry	$\boldsymbol{\delta_{cr}}$	$\boldsymbol{\theta_{max}}$
Infinite Slab	0.878	1.119
Infinite Cylinder	2	1.386
Equi-Cylinder	2.844	1.778
Cube	2.569	1.888

2.3.4. Numerical Solutions for the Frank-Kamenetskii Critical Criterion δ_{cr}

The literature covered to date shows the difficulty in analytically calculating the Frank-Kamenetskii critical criterion δ_{cr}, and how it can only be calculated for very specific conditions, such as for an infinite Biot number or where $\Delta T/T \ll 1$. Parks (1961) sought to evaluate this critical criterion for a broader range of circumstances numerically using an IBM 704 data processing machine and using analogic method using a Pace analogue computer. In doing so, the energy balance in equation (2-2) was reduced to its steady-state dimensionless form, using the exact form of the exponent in equation (2-13), to give:

For $0 \leq \xi \leq 1$,

$$\nabla_{\xi}^{2}\theta = -\delta e^{\frac{\theta}{1+\frac{\theta}{\varphi}}} \tag{2-39}$$

The analogue computer was used to explore the solutions of the steady-state energy balance in spherical coordinates and is of little interest due to its dated approach. The digital computer was used to numerical solve the steady-state equation (2-39). Parks

modified the Laplacian term and the boundary conditions to model a sphere, an infinitely long cylinder, an infinite slab of finite thickness, a cube, and an equi-cylinder (a cylinder of equal height and diameter). The equations were reduced to difference equations with spatial increments in ξ of 0.1.

The analytical solution assumes that $\Delta T/T \ll 1$, which means $RT \ll E$ and the exponential reduces to e^{θ}. Parks sought to evaluate the critical criterion for finite values of φ $(= E/RT)$, allowing this critical criterion to be applied to a greater range of situations. To do this, a value of φ was selected and a double iterative procedure was used. The devised program would select a value of β from a range in increments of k, with $\varphi\beta = \delta$. For each selected value of β_k, the computer would numerically solve for the steady-state solution that meets the boundary conditions. If a solution existed then the computer would increase the value of β_k to β_{k+1}. This would be repeated until no steady-state solution could be found. At this point, where no solution could be found, the critical criterion could be defined as:

$$\varphi\beta_k < \delta_{cr} < \varphi\beta_{k+1} \tag{2-40}$$

Using this approach. Parks produced the results shown in Table 2-2. The computational limitations of the time meant that iteration in φ of 10 were used for the cube and regular right circular cylinder. As the value of α increases, these results can be seen to approach the values solved for analytically as documented previously.

Parks' calculated values of δ_{cr} for the cube and regular right circular cylinder are seen to make abrupt changes between some values of α, implying that the precision of these results can be improved on massively using modern computation techniques. Additionally, although these values were calculated for a range of values for φ, this approach still applies the infinite Biot number assumption to the boundary conditions, as used by Frank-Kamenetskii. This leaves scope to improve on this work by solving for a greater, and finer range of α values, as well as for a wide range of Biot numbers.

Table 2-2: Numerical solutions for δ_{cr}, as calculated by Parks (1961) for a sphere, infinitely long cylinder, infinite slab of finite thickness, cube, and regular right circular cylinder.

	Sphere	**Infinitely Long Cylinder**	**Infinite Slab of Finite Thickness**	**Cube**	**Regular Right Circular Cylinder**
φ	δ_{cr}	δ_{cr}	δ_{cr}	δ_{cr}	δ_{cr}
20	3.51	2.11	0.927	2.68	2.93
25	3.47	2.08	0.915		
30	3.44	2.07	0.911	2.63	2.88
35	3.42	2.06	0.905		
40	3.41	2.05	0.904	2.58	2.83
45	3.40	2.04	0.894		
50	3.38	2.04	0.892	2.58	2.83
55	3.38	2.03	0.892		
60	3.38	2.03	0.891	2.58	2.83
65	3.37	2.03	0.886		
70	3.36	2.02	0.884	2.58	2.83
75	3.36	2.02	0.882		
80	3.35	2.01	0.881	2.58	2.83
85	3.35	2.01	0.880		
90	3.35	2.01	0.880	2.53	2.78
95	3.34	2.01	0.880		
100	3.34	2.01	0.880	2.53	2.78

2.4. Experimental Methods for the Characterisation of Self-Heating

The characterisation of detergent powders and spray drying tower wall make-up as explored by this project focuses largely around determining the nature and kinetics of the self-heating reaction occurring within the powder. Methods for doing this include basket heating methods of determining zero-order kinetics. These methods are the steady-state, cross-point temperature, and heat release methods. Other methods include micro-gram scale techniques that use thermogravimetric analysis (TGA) and differential scanning calorimetry (DSC). These methods are the Ozawa-Flynn-Wall method, Friedman method, and the DTG curve fitting approach.

These methods have been applied to the study of many materials including coal, activated carbons, and milk powders. Little work has been done on the reaction kinetics of detergent powders and as such the nature of the reaction and the best methods to use are largely unknown. This section will review these methods, their applications, and the advantages of each in order to make a better informed decision as to which methods to use in characterising these detergent powders.

2.4.1. The Steady-State/ Frank-Kamenetskii Basket Heating Method

2.4.1.1. Basis of the Steady-State Method

The steady-state method, often referred to as the Frank-Kamenetskii method, is so called because it is based on the theory of thermal explosions developed by Frank-Kamenetskii (1969). This method is largely dependent on the dimensionless parameter derived for predicting criticality, δ, which is often referred to as the Frank-Kamenetskii parameter. The steady-state method has been used extensively to characterise the self-heating behaviour of many materials such as charcoal (Bowes & Cameron, 1971) (Cameron & MacDowall, 1972), bagasse (Gray, et al., 1984), milk powder (Duane & Synnot, 1992), and in particular coal (Jones & Raj, 1989) (Jones & Vais, 1991). This approach is widely documented and has been also standardised as EN 15188:2007 entitled “Determination of the spontaneous ignition behaviour of dust accumulations” (British Standards Institution, 2007). This method is a basket heating method in which mesh baskets of different shapes and sizes, full of the self-heating powdered material, are heated in an oven under highly convective conditions. The critical ambient temperature for different materials, and for differently shaped and sized baskets are determined. From this, the self-heating reaction kinetics can be measured.

The steady-state method is based on the steady-state form of the energy conservation equation of a self-heating system, given by equation (2-3). In this method, the dimensionless form of this equation is used, along with the approximation from the method of expanding the exponent. This is given by equation (2-12). The dimensionless parameter δ is key to this method, and is defined as:

$$\delta = \frac{E}{RT_\infty^2}\frac{\rho Q A L^2}{k} e^{-\frac{E}{RT_\infty}} \tag{2-41}$$

From the formula for δ it can be seen that this parameter is dependent on:

- The reaction parameters such as activation energy, E, pre-exponential factor, A, and heat of reaction, Q.
- The material properties such as conductivity, k.
- The ambient temperature, T_∞.
- And the characteristic length of the geometry (i.e. slab thickness, basket radius, etc.), L.

This model is limited in that it is subjected to the following assumptions:

- The material is assumed to be homogeneous and isotropic with regards to chemical and thermal properties. The structure of the particles is not considered, and instead the system is considered in bulk.
- The heat generation term is for one exothermic reaction, or several reactions occurring simultaneously but considered to be one reaction.
- Heat transfer through the powder material is by conduction alone. Connectivity between the individual powder particles is not considered.

This dimensionless Frank-Kamenetskii parameter is used in predicting the criticality of a system. If the δ value of the system in question, based on the physical parameters of that system, exceeds the critical value δ_{cr}, then the system is predicted to thermally runaway (i.e. the heat generation rate will exceed the rate of heat dissipation from the system). Much of the literature that uses this method applies the following two assumptions which were also used by Frank-Kamenetskii in determining analytical solutions for the parameter δ_{cr}:

- The activation term is sufficiently high, such that $E \gg RT$, an approximation made in the method of expanding the exponent.
- The Biot number is sufficiently high that the surface of the body can be assumed equal to the surrounding temperature.

Using these assumptions, the value of δ_{cr} is assumed constant, solely dependent on the system geometry. It has already been shown in previous sections that δ_{cr} is in fact also

dependent on the activation energy and the boundary conditions of the system, and in order to use an accurate value for δ_{cr}, these two assumptions cannot be applied. In carrying out this method, a number of baskets filled with self-heating materials are heated in a forced convection oven such that their critical ambient temperatures can be determined. Knowing the critical ambient temperatures and the critical criteria δ_{cr} for a number of different baskets allows the data to be plotted according to the following manipulation of equation (2-41):

$$\ln\left(\frac{\delta_{cr}T_{\infty,cr}^2}{L^2}\right) = -\frac{E}{RT_{\infty,cr}} + \ln\left(\frac{\rho Q A}{k}\frac{E}{R}\right) \qquad (2\text{-}42)$$

From this it can be seen that by plotting the reciprocal of the critical ambient temperature, $1/T_{\infty,cr}$, against $\ln\left(\frac{\delta_{cr}T_{\infty,cr}^2}{L^2}\right)$ allows the activation energy, E, to be determined from the slope, and the product of the pre-exponential factor, A, and the heat of reaction, Q, to be determined from the intercept of the line fitted to these points.

In performing these experiments, EN 15188:2007 (British Standards Institution, 2007) dictates that at least three mesh baskets of different volumes are to be used. It also suggest that a higher level of certainty can be achieved from using four different baskets. It recommends that the smallest volume should be of the order of 10 cm^3, and the largest should be at least 1000 cm^3, although if sample material is limited then smaller baskets can be used. It also recommends that the baskets as a series should increase in volume by at least a factor of 2. Each basket is heated in an oven with a temperature controller than can maintain the temperature within a range of ±1% of the oven temperature. Tests are run to determine the critical ambient temperature using a "closing in" approach. Mathematically speaking, the critical ambient temperature is the temperature at which a solution to the temperature distribution fails to exist. Practically speaking, baskets are heated at different oven temperature to the highest oven temperature at which no ignition occurs, and the lowest temperature at which ignition does occur, with the critical ambient temperature taken as the mean of these two values.

Having these data it is then possible to determine the critical ambient temperature for any geometry by substituting for the newly calculated reaction kinetics, and

characteristics of the geometry for which the critical ambient temperature is being sought (i.e. δ_{cr} for the geometry type, and characteristic dimension L), into equation (2-41).

2.4.1.2. Applications of the Steady-State Method in Literature

Bowes and Cameron (1971) were one of the early adopters of the steady-state method and they used it to examine the self-heating behaviour of activated carbons. They had observed that self-heating was an issue in the transport of activated carbon, with six fires breaking out in shipments of activated carbon on board ships between May 1962 and May 1963. This self-heating is known to be due to the oxidation of the carbon, but this oxidation is a slow process and can continue for weeks or even months, with these fires being discovered 3 to 4 weeks after stowing.

Bowes and Cameron applied the Theory of Thermal Explosions and the steady-state method to address this issue. They used phosphoric acid-activated vegetable charcoal and cubic wire mesh baskets ranging in size from 25.4 mm to 610 mm, which is particularly large and took 68 hours to ignite. A chromel/ alumel thermocouple was placed at the centre of the basket and the basket heated to determine the minimum ambient temperature to within ±5°C or better. This is not a particularly accurate range but it was chosen such that a larger range of sizes could be covered in a relatively short period of time. The results of these experiments were plotted in accordance with equation (2-42). They realised that the value of δ_{cr} for cubic baskets in Table 2-1 was not sufficient for this analysis. Instead they used the δ_{cr} values numerically calculated by Parks (1961), using values from the range of $30 \leq \frac{E}{RT_{\infty}} \leq 80$. They found that using this method to measure small-scale self-ignition allowed them to make realistic estimates for the critical ambient temperatures of considerably larger quantities, although the times to ignition were found to be overestimated by a factor of 5. In addition to the long-term self-heating reaction which causes the majority of the observed temperature rise, there are also short-term temperature rises caused by processes such as the attainment of moisture equilibrium. It was also found that the use of polyethylene bags for storing this material can limit the fires observed in transport.

Cameron and MacDowall (1972) was another early adopter of this method, and again look at the problems seen in shipping activated carbons. These carbons were packed

into cubic baskets ranging in sizes from 51 mm to 305 mm and heated in accordance with the steady-state method, using a constant value for δ_{cr} of 2.6, based on the numerical values calculated by Parks (1961). They also looked at activated carbons made using different processes as it had been suggested that the two common methods of making activated carbons result in carbons with different oxygen contents which may react differently.

The first method is the chemically activated process where carbons are produced by mixing a chemical with a carbonaceous materials, generally wood. This process is done at what is considered a relatively low temperature of 400 to 500°C. The second method is the steam activated process, typically done using starting materials of peat, coal, lignite, and wood. Firstly the materials are carbonised but the pores produced are too small to be useful as an absorbent. The carbon is reacted with steam at between 900 and 1000°C to enlarge the pores. This high temperature is what leads to a different chemical structure, which is reflected in the chemical analysis of the carbons used in this investigation. All steam activated carbons were found to have oxygen contents of less than 2%, whereas the chemically activated carbons have much greater oxygen contents.

It was found that the critical ambient temperatures of these carbons increases for a decrease in the oxygen content, and for an increase in carbon content, as shown in Figure 2-5. The difference in self-heating behaviour of powdered materials with chemical composition is important for most materials, but in particular detergent powders which have many different formulations. In this case oxygen content is the biggest contributor, but in detergents a different oxidizer content may be important.

Gray *et al.* (1984) used the steady-state method to examine the problem of self-heating in bagasse stock-piles. Bagasse is residue from the processing of sugar cane. The bagasse exits the mill at a very high water content and at temperatures between 50 and 70°C where it is immediately stock-piled. In these stockpiles there is a risk of spontaneous ignition because of the self-heating this material is known to undergo. Bagasse consists of cellulose, hemi-cellulose and lignin. This material is quite fibrous and in order to eliminate variations in density and surface area, it was sieved using a 3mm mesh. The method was applied as before, but in this case the critical ambient temperature was found to within ±0.25°C, which is a much greater precision than the previous examples.

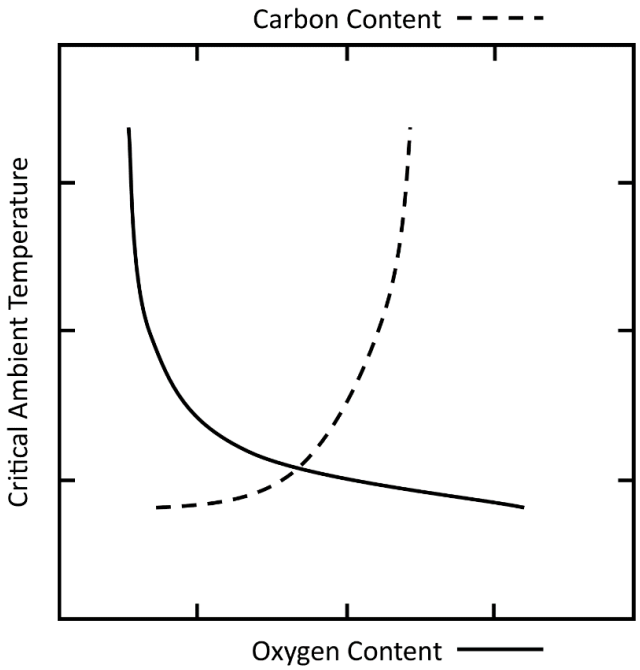

Figure 2-5: Qualitative relationship between critical ambient temperature and the oxygen and carbon contents for charcoal, as measured by Cameron and MacDowall (1972).

In heating theses samples Gray *et al.* noted that each sample exhibit a quasi-stationary central temperature during the experiment. This behaviour is due to evaporation of water from the sample. This behaviour would be expected of any material that is not entirely dry before commencing the experiment, including detergent powder which may contain residual moisture. During this period the temperature attained was found to be dependent on the packing density, while the duration is dependent on the amount of water present. Despite this, it was seen that self-heating is unaffected by the amount of drying required, which is useful information when it comes to exploring the self-heating of detergent powders.

Interestingly, Gray *et al*. used a different approach to determine the value for δ_{cr} in this case. The previous cases, and many other cases, refer to the work of Parks (1961) and the numerically solved values he obtained for δ_{cr} as a function of the activation energy, E. In this case, the approach of Boddington *et al.* (1971) was used. Here, the harmonic root-mean square radius R_0 is used as an approximation for the Frank-Kamenetskii radius. This can then be used along with the Semenov radius R_s, where $R_s = 3V/S$. V is the geometry volume and S the surface area, and this is used to define a shape factor j:

$$j = 3\left(\frac{R_0^2}{R_s^2}\right) - 1 \tag{2-43}$$

From this, the critical value δ_{cr} for an arbitray shape can be determined using:

$$\delta_{cr}(R_0) = 3\left(\frac{2j+6}{j+7}\right) \tag{2-44}$$

The values determined by Boddington *et al.* are shown in Table 2-3. The problem with this approach is that the δ_{cr} values calculated using this approach are different from those determined analytically by Frank-Kamenetskii (1969) and Chambré (1952), and from those calculated numerically by Parks (1961). In some case they vary largely, as can be seen in Table 2-4. This shows that care must be taken when choosing the value of δ_{cr} to use, especially when taking these values from literature.

Table 2-3: δ_{cr} as used by Gray *et al.* (1984), calculated from the shape factor approach of Boddington *et al*. (1971).

Shape	R_0	R_s	j	δ_{cr}
Infinite Slab, thickness = 2a	1.732a	3a	0	2.571
Infinite Cylinder, radius = a	1.225a	1.5a	1	3
Equi-Cylinder, radius = a	1.115a	1a	2.728	3.531
Cube, side = 2a	1.194a	1a	3.280	3.663

Table 2-4: Comparison between analytically solved for δ_{cr} values and those calculated using the method of Boddington *et al* (1971).

Geometry	δ_{cr} - Analytical	δ_{cr} – Boddington et al.
Infinite Slab	0.878	2.571
Infinite Cylinder	2	3
Equi-Cylinder	2.844	3.531
Cube	2.569	3.663

In this work Gray *et al.* (1984) had difficulty in matching predictions of self-ignition to experimental results, noting that they only matched over a limited range of sizes. This

maybe because of the incorrect values of δ_{cr} used which would impact on the scaling of predictions. They also noted that a measured temperature difference of 4.5°C between the surface and ambient temperature implies that the infinite Biot number assumption may not hold in these experiments. A finite value for the Biot number would also impact on the value of δ_{cr} that should be used in these experiments, further increasing the errors in scaling predictions.

Jones and Raj (1989) and Jones and Vais (1991) looked at self-heating in coals. Jones and Raj explored the self-heating of solar-dried coal slurry in particular but did little to add to the knowledge in the area, other than determining that lime-treated samples had a larger activation energy, attributed to a lower oxygen penetration of the micropores due to the calcium treatment. Jones and Vais examined self-heating in four different low-rank coals. In doing so it is worth noting that they used a value for δ_{cr} for a cubic basket of 3.663, which is the same as that used by Gray *et al.* (1984). This was the value calculated by Boddington *et al.* (1971) that was shown to disagree with the analytical and numerical solutions for δ_{cr}. This shows that there are two sets of δ_{cr} values being used in the literature, and it is important to choose the correct set of values.

Jones and Wake (1990) briefly explored the measured activation energies of a number of different solid materials. These include carbonaceous materials, solar dried coal slurry, protein-containing materials, and cellulosic materials. They used the δ_{cr} value of 2.569 as calculated by Parks (1961). They noted that this value is dependent on the Biot number of the system, with this value suitable for very large Biot numbers. Despite this, they concluded that this condition is met for baskets heated in air ovens, but without measuring the heat transfer coefficient of the system it is difficult to verify this.

Duane and Synnott (1992) used the steady-state method to explore self-heating in spray-dried milk powders. Being a spray-dried powder, the self-heating of milk powder has more in common with detergent powders than the previous cases of coal and other carbonaceous materials. They used cubes ranging in size from 25mm to 102mm in side length. This work also realised that the value of δ_{cr} is dependent on the Biot number. To correct for this the heat transfer coefficient, h, was measured using the lumped capacity method. Aluminium cubes were heated in the same oven used for the steady-state method experiments and the heat-up curves analysed to determine h from:

$$\frac{T - T_\infty}{T_0 - T_\infty} = e^{-\frac{hA}{C_p m}t} \quad (2\text{-}45)$$

Here, T is the temperature at time t, T_∞ is the ambient temperature, T_0 is the initial temperature at time $t = 0$, A is the surface area of the aluminium cube, and m is the mass. Knowing the heat transfer coefficient and the thermal conductivity, Duane and Synnott were able to calculate the Biot number. Based on this value, and using the work of Thomas (1960), the values of δ_{cr} ranged from 1.3664 to 2.0386, corresponding to Biot numbers between 2.625 to 8.450. This shows that the variation in δ_{cr} due to finite Biot numbers is an important factor that must be considered to accurately measure the correct self-heating reaction kinetics.

There can be large variations in the contents of different formulations of milk powder, and it is widely accepted that the presence of unsaturated products in milk powders increase the susceptibility of these powders to self-heating. Duane and Synnott showed that high levels of unsaturated products lowers the critical ambient temperature of these powders, which has implications in the manufacturing of powders with increased amounts of unsaturated fats. Interestingly, they were able to establish a relation for the critical ambient temperature relative to the fat and protein content of the powder:

$$T_{crit} = 282.6 - 1.35664(\%\, protein) - 2.3133(\%\, fat) \quad (2\text{-}46)$$

Such an analysis could be applied to determine critical ambient temperatures of detergent powders relative to the percentage content of particular ingredients.

Another piece of work which accounts for finite Biot numbers is that of Gray and Halliburton (2000), which explores the thermal decomposition of hydrated calcium hypochlorite. Because of a relatively high value of thermal conductivity, they realised that the Biot number was not sufficiently large for the infinite Biot number approximation often used. They used the measured Biot number to correct the value of δ_{cr} for each sample size used. The corrected δ_{cr} values are all significantly smaller than those for the infinite Biot number approximation and affect the results. The results were processed using both sets of δ_{cr} values, corrected and non-corrected, and it was found that the correct values considerably reduced the deviations in the steady-state method results in comparison. They also noted that corrections for finite Biot numbers are larger for smaller sample sizes, which is important to take note of when choosing baskets sizes

for these experiments. The other interesting element of this work is that the steady-state method plot of hydrated calcium hypochlorite exhibited a bi-linear profile, showing that two reactions occur in this material. There is a high temperature reaction and a low temperature reaction, which can only be seen using a wide range of basket sizes in the experiments.

The steady-state technique is widely used and a very capable method for measuring the self-heating reaction kinetics of these systems. It is a well-established method with plenty of available literature with regards technique and results for different materials, including coal, sawdust, and milk powder. Applying the theory of thermal explosions of Frank-Kamenetskii and in particular the Frank-Kamenetskii parameter, δ, it is easy to evaluate the criticality of different geometries and materials, and at different ambient temperatures. Using the correct value of δ_{cr} is important as this will impact on the results. Often the assumptions that the activation energy is sufficiently large and the Biot number infinite are used, such that the analytically calculated values of δ_{cr} for these ideal cases can be used. Many of the covered works address the approximation applied for high activation energies, and correct the value using the numerically calculated values of Parks (1961). More recent work also accounts for finite Biot numbers and correct the value of δ_{cr} accordingly, again improving results.

Despite this it can also be seen that there are a number of disadvantages to this method. Not every test that is run yields a usable data point. A number of runs need to be completed using the "closing in" approach to determine the critical ambient temperature for a specific geometry. This is time consuming and inefficient, given that each test can take a number of hours to complete. For particularly large baskets used these tests can take upwards of days to lead to self-ignition. Because a number of noticeably different sized baskets must be used, oven size may also be an issue, as sufficient space to allow for convection at the basket boundaries is required.

2.4.2. The Transient/ Cross-Point Temperature Method

In modelling the transient energy conservation equation for a self-heating slab, Chen and Chong (1995) noticed the existence of what has come to be referred to as the

"crossing-point" or "cross-point" temperature. This transient energy conservation equation for a slab is written as:

For $0 \leq x \leq r$ and $t \geq 0$,

$$\rho C_p \frac{\partial T}{\partial t} = k \frac{\partial^2 T}{\partial x^2} + \rho Q A e^{-\frac{E}{RT}} \tag{2-47}$$

If it is assumed that the activation energy is sufficiently large, then in dimensionless form this equation reduces to:

For $0 \leq \xi \leq 1$ and $\tau \geq 0$,

$$\frac{\partial \theta}{\partial \tau} = \frac{\partial^2 \theta}{\partial \xi^2} + \delta e^{\theta} \tag{2-48}$$

In this case, the dimensionless time, τ, is defined as:

$$\tau = \frac{t}{r^2} \frac{k}{\rho C_p} \tag{2-49}$$

Using these model equations, Chen and Chong simulated these self-heating slabs, with particular interest paid to the temperature-distance profiles produced at different times. The sample initially heat-up from the peripheries inwards. The heat conduction term in this model increases from zero initially, before decreasing monotonically. In doing so it goes from a positive to a negative value, and therefore there must be some point at which this term becomes zero. The temperature at the slab centre at this point in time is what Chen and Chong defined as the crossing-point temperature. This phenomena can be seen in the qualitative plot of the temperature-distance profiles in Figure 2-6 adapted from Chen and Chong (1995), which shows how at some point this profile must become flat, at which point conduction at the centre becomes zero. At this point, with the conduction term equal to zero, equation (2-47) at $x = 0$ reduces to:

$$\left.\frac{\partial T}{\partial t}\right|_{T=T_{CPT}} = \frac{QA}{C_p} e^{-\frac{E}{RT_{CPT}}} \tag{2-50}$$

They hypothesised that should you be able to experimentally determine the crossing-point temperature, T_{CPT}, and record the temperature-time profile, which would be used to determine the value of $\partial T/\partial t$ at the crossing-point temperature, then this could used to measure the self-heating kinetics. This would be done by plotting $\ln\left(\frac{dT}{dt}\right)$ at the crossing-point and $1/T_{CPT}$.

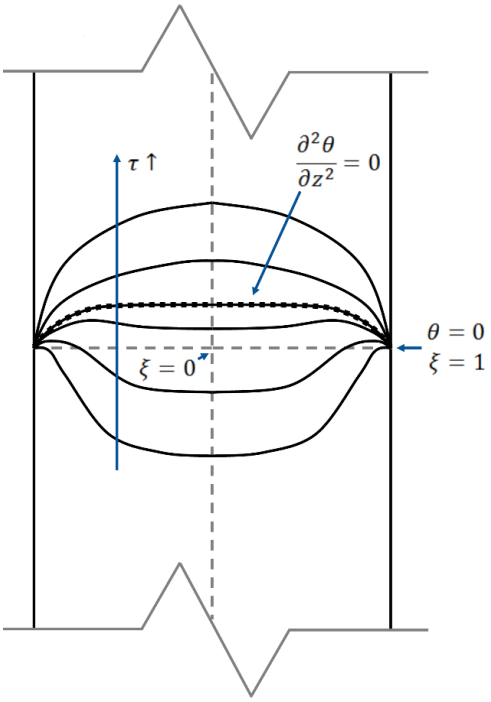

Figure 2-6: Qualitative plot of temperature-distance profiles in a self-heating slab. It can be seen that at some point the profile becomes flat and the conduction at the centre reduces to zero. This is the crossing-point.

Chong *et al.* (1996) applied this concept as a novel procedure for determining exothermic reactivates of skimmed and whole milk powders. As discusses previously, this method is based on equation (2-50), and in logarithmic form this is expressed as:

$$\ln\left(\frac{dT}{dt}\right)_{T=T_{CPT}} = -\frac{E}{RT_{CPT}} + \ln\frac{QA}{C_p} \qquad (2\text{-}51)$$

Baskets of powder are oven heated at different ambient temperature with two thermocouples placed within the powder. One of these thermocouples is at the basket centre and one is offset by a small difference along the basket radius in the same cross-sectional plane. A typical experimental setup for this method is shown in Figure 2-7. Temperatures are measured by these thermocouples and when these temperatures are equal conduction in that region is assumed to be equal to zero. This is the crossing-point temperature and a typical temperature-time profile showing how this occurs is shown in Figure 2-8.

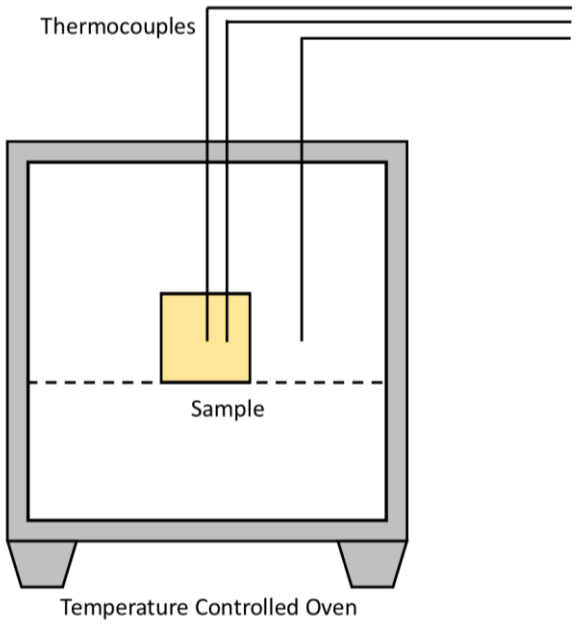

Figure 2-7: Typical apparatus set-up for cross-point temperature method, illustrating the placement of the thermocouples at the centre of the geometry and offset from this on the same plane.

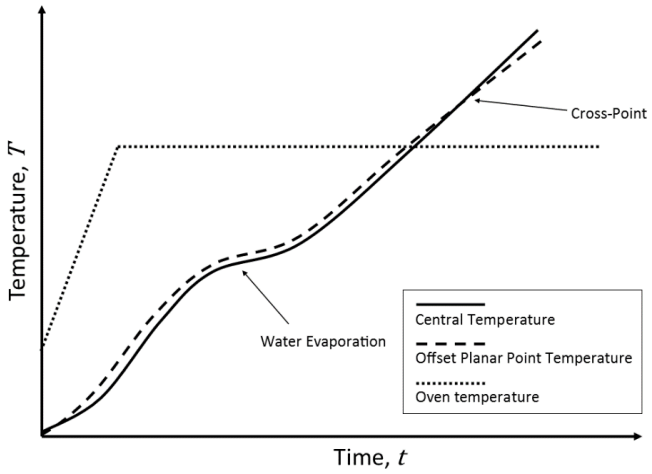

Figure 2-8: Typical plot of temperature as a function of time for the cross-point temperature method illustrating the existence of the cross-point.

Plotting $\ln(dT/dt)$ at the crossing-point temperature against the reciprocal of the crossing-point temperature $1/T_{CPT}$, will make a line with a slope of $-E/R$ and an intercept of $\ln(QA/C_p)$. From this it is simple to extract values for the activation energy, E, and the product of the heat of reaction and the pre-exponential factor, QA, so long as the specific heat capacity, C_p, of the material is accurately known.

Chong *et al.* states that this method has been proven to be independent of the boundary conditions, unlike the steady-state method which requires a "well agitated" oven to

ensure that the Biot number is sufficiently large. It is incorrect to say that the steady-state method requires an infinite Biot number, but this is commonly stated in literature. In fact a "well agitated" oven is only required when the analytical solutions for δ_{cr}, calculated under the assumption of an infinite Biot number, discussed previously are used. The value of δ_{cr} can be solved for finite Biot numbers and these corrected values have been used in the steady-state method previously (Duane & Synnot, 1992) (Gray & Halliburton, 2000).

Chen and Chong (1995) noted that if this phenomena is to be used as a means of measuring the reaction kinetics, then it must be shown that the crossing-point temperature is constant for the same exothermicity, activation energy, thermal properties, slab-thickness, and boundary temperatures, regardless of the initial uniform temperature. To do this, they built a simple 1D model using the energy conservation equation in (2-47), and solved it using time increments of 1s and an x-axis discretised into 40 sections. They validated this model by predicting the critical ambient temperatures of different slabs and comparing these to those predicted using steady-state theory, which they did to within ±0.5°C.

Using this model they sought to verify the uniqueness of the cross-point temperature. Simulations were performed for slabs of half-widths from 20mm to 50mm, for boundary temperature between 90 and 140°C, and for initial temperatures from 5 to 120°C. Comparing the results of simulations where only the initial temperature varied showed that the crossing-point temperature is indeed unique, and in this case a discrepancy of ±0.01°C was seen across all simulations, which is smaller than the experimental error. The only exceptions were for the cases where the boundary temperature was high enough to lead to peripheral ignition or the initial temperature was in excess of the slab critical ambient temperature. This means that this unique crossing-point temperature can be used as a physico-chemical property that can be used to determine if a system will lead to self-ignition.

The concept of the crossing-point temperature and its uniqueness was also validated experimentally. This was done by performing basket tests using dried sawdust. A cylindrical stainless steel mesh basket of height and diameter 6cm was used. This basket was packed with sawdust to the same density for each experiment and heated from different initial temperatures with a constant oven temperature of 200°C. These initial

temperatures were 1°C, achieved using an ice-making machine, 24°C, 25°C, and 38°C. Three thermocouples were placed into the sawdust sample. The first thermocouple was placed at the geometric centre of the basket, the second was offset by 7mm from this, and the third 7mm from the second, on the same cross-sectional plane both horizontally and vertically. Using this setup the crossing-point temperature was determine in three ways:

1. The crossing-point between the first thermocouple, T_1, and second thermocouple, T_2.
2. The crossing-point between the first thermocouple, T_1, and third thermocouple, T_3.
3. A second order difference approximation for the temperature derivative:

$$\frac{\partial^2 T}{\partial x^2} \approx \frac{T_3 - 2T_2 + T_1}{(\Delta x)^2} \tag{2-52}$$

Where Δx is the spacing between the thermocouples, i.e. 7mm. The issue using the third method is that this finite difference approximation measures the crossing-point temperature at the position of the second thermocouple, T_2, while dT/dt is measured at the central thermocouple, T_1.

The crossing-points as measured using the three methods are shown in Table 2-5. The error across all the experiment for each method are ±0.6°C, ±0.7°C, and ±3.3°C respectively. The error in method 3 is considerably larger. This error is a combination of the errors in thermocouple measurement (±0.2°C) and the error in thermocouple placement (±1mm) across the three thermocouples. It may also be because the temperature derivative is measured at the wrong point as explained above. The difference in temperatures across the three thermocouples at the crossing-point is within ±0.5°C, which makes the error in the measurement error of ±0.2°C significant. Despite this, these errors are within acceptable limits and suggest that the crossing-point temperature is independent of the initial temperature.

Table 2-5: The crossing-point temperatures measured by Chen and Chong (1995) for the three different methods.

	T_{CPT} (°C)		
T_0 (°C)	**Method 1**	**Method 2**	**Method 3**
1	214.5	214.8	216.0
24	214.8	214.1	211.1
25	215.7	213.5	212.8
38	214.8	216.0	218.3

In their investigation, Chong *et al.* (1996) tested skimmed and whole milk powder samples using a forced convection oven. A number of insulation bricks were placed on the floor of the oven, increasing the thermal capacity of the oven and hence decreasing the time taken for the temperature to stabilise. The temperature distribution in the region where the sample was to be placed was measured, with little variation (±1.5°C) found over the area. The samples were packed into cubic (5cm and 6cm side lengths) and cylindrical baskets (height x diameter of 6 x 6cm and 12 x 4cm) at constant density. Two type K thermocouples placed within the sample at spacings ranging from 0.4cm to 0.8cm, depending on the basket used. To confirm the placement of the thermocouples, each sample was cut in half following the experiment. The experiment was repeated if any of the thermocouples were out of position. Tests were run at temperatures between 130 and 170°C depending on the milk sample and basket used.

Being able to cut through the sample to verify thermocouple position implies that at these temperatures the milk powder exhibits significant self-heating and form a burnt solid mass, even in the peripheral regions. This is confirmed in how Chong *et al.* refers to the “dark brown colour” of the powder, which increased in intensity as the temperature increased. These temperature put the experiments at risk of contradicting the observation made using the simulations by Chen and Chong (1995) in which it was shown that the boundary temperature must not lead to peripheral ignition. This degree of self-heating may also damage the thermocouples and limit the number of runs they can be used for.

In terms of results, they found that the plot of results for whole milk powder has two slope regions. This was attributed to Maillard reactions in the lower temperature range and fat oxidation in the high temperature range. This was confirmed by the skimmed milk powder, which only exhibited the Maillard reactions because the fat content of this powder was only 0.8%. The results were found to compare reasonably well with those of others found in literature. They also confirmed that pre-heating has little effect on the results, and that the effects of size and shape of the baskets are negligible.

With such small distances between thermocouples, accuracy is always going to be an issue. The accuracy of thermocouple measurements was found to be ±0.2°C. This lead to an error in the measurement of the crossing-point temperature of ±1% and error in measuring $\ln(dT/dt)$ of ±10%. This culminates in an error in the measured activation energy of ±1 kJ mol^{-1}, a similar error to the steady-state method. They also found these results to be reproducible and suitable as a replacement for the steady-state method which can considerably reduce the time required to measure the self-heating kinetics.

In comparing this approach to the steady-state method, Chen and Chong (1998) noted the following advantageous:

- Only one basket size is required, which means oven size is not restricted.
- An infinite Biot number is not required, although this point has already been refuted above.
- Only one experiment is required to determine each point on the kinetic plot.
- This method can determine temperature dependence of the kinetic parameters (because E and QA are measured at the reaction temperature).
- This method can also be used to explore a process without gaseous reactions.

In publishing these data, a number of issues arose from other researchers with regards the cross-point temperature method. Chen and Chong addressed these issues. Firstly they stated that in discussing the method with other researchers, a question that was frequently posed was whether or not two temperatures is enough to determine that the heat conduction term was equal to zero. To show this, Chen and Chong firstly approximated the second derivative using a finite (central) difference approximation:

$$\frac{\partial^2 T}{\partial x^2} \approx \frac{T_{i+1} - 2T_i + T_{i-1}}{(\Delta x)^2} \tag{2-53}$$

T_i is the temperature at the centre, and because of the symmetrical boundary condition T_{i+1} and T_{i-1} are equally spaced either side of the centre and must be equal such that:

$$\frac{\partial^2 T}{\partial x^2} \approx \frac{2T_{i+1} - 2T_i}{(\Delta x)^2} \tag{2-54}$$

From this it can be seen that if the temperature at the centre T_i and at the offset point T_{i+1} at a distance Δx away are equal, then the second derivative, and thus the conduction term, reduces to zero. However, because only two thermocouples are used, it is important that they are accurately placed, especially the central one. Chong *et al.* (1996) sliced the down the middle after the experiment to confirm the thermocouple position, but this may not always be possible.

The second problem is the extension of this slab justification for two temperatures to other symmetrical geometries. The full form of the heat balance equation for symmetrical geometries is given as:

$$\rho C_p \frac{\partial T}{\partial t} = k\left(\frac{\partial^2 T}{\partial x^2} + \frac{j}{x}\frac{\partial T}{\partial x}\right) + \rho Q A e^{-\frac{E}{RT}} \tag{2-55}$$

Where $j = 0$ for an infinite slab, $j = 1$ for an infinite cylinder, $j = 2$ for a sphere, $j = 2.728$ for a short cylinder, and $j = 3.28$ for a cube. At the centre it can be shown using l'Hôpital's rule that as $x \to 0$;

$$\frac{\partial^2 T}{\partial x^2} + \frac{j}{x}\frac{\partial T}{\partial x} \approx (j+1)\frac{\partial^2 T}{\partial x^2} \tag{2-56}$$

Such that the same finite difference approach can be applied and two temperatures is sufficient to determine the cross-point temperature.

The specific heat capacity cannot always be assumed constant, as has been done up to this point, and is often a function of temperature over the range being used. If it is being treated as temperature dependent then the following form of equation (2-51) is to be used:

$$\ln\left(\frac{dT}{dt}\right)\Big|_{T=T_{CPT}} + \ln C_p(T_{CPT}) = \ln(QA) - \frac{E}{RT_{CPT}} \tag{2-57}$$

If the relationship for specific heat capacity, C_p, as a function of cross-point temperature, T_{CPT}, is known then $\ln\left(\frac{dT}{dt}\right)\Big|_{T=T_{CPT}} + \ln C_p(T_{CPT})$ can be plotted against $1/T_{CPT}$ to obtain E and QA in a similar manner as before.

Sujanti *et al.* (1999) used this new method, now being referred to as the cross-point temperature method or the transient method, and the more established steady-state method to characterise the low-temperature oxidation of coal. Seven cylindrical baskets were used for the steady-state method but a constant value for δ_{cr} was used for each basket. This means that the dependency of δ_{cr} on both the activation energy and the Biot numbers were not accounted for, and will have implications when comparing the results of the methods.

For the cross-point temperature method experiment, they used three thermocouples similar to Chen and Chong (1995), with T_1 at the centre, T_2 offset from this, and T_3 offset from this. One cross-point is determined using these thermcouples using the following expression:

$$\frac{T_3 - 2T_2 + T_1}{(\Delta r)^2} + \frac{T_3 - T_1}{2\Delta r} \approx 0 \qquad (2\text{-}58)$$

The problem here is the same as that of Chen and Chong (1995), in that this term determines the cross-point at T_2 while dT/dt is measured at T_1, which is inconsistent with the equations.

Despite these issues, Sujanti *et al.* appeared to have good results, with a good linear fit achieved for both methods, with the effects of these issues not obvious without further analysis. Variations were seen in both E and A, but in general a higher value of E corresponds to a higher value of A, which indicates similar reactivates. To compare these results, they predicted critical ambient temperatures using the results of the cross-point temperature method for each basket, and for the steady-state methods. The predicted critical thicknesses compare well across the results of all the experiments. Again this shows that this method is a suitable alternative to the steady-state method.

2.4.3. Heat Release Method

The heat release (HR) method is a method that was proposed at around the same time as the cross-point temperature method by Jones *et al.* (1996). They stated that no matter whether the experiment is run at a sub-critical or super-critical ambient temperature, when the sample it at or very close to the ambient temperature there must be no heat transfer between the ambient and the sample. At this point the sample temperature is assumed to be spatially uniform, although in reality it is thought that this is not the case, such that the following is true:

$$\left.\frac{\partial T}{\partial t}\right|_{T=T_\infty} = \frac{QA}{C_p} e^{-\frac{E}{RT_\infty}} \tag{2-59}$$

This is very similar to the cross-point temperature assumption, except this occurs when the sample is equal to the ambient temperature, rather than at the cross-point temperature. In a similar way to the cross-point temperature method, the logarithmic form is expressed as:

$$\ln\left(\frac{dT}{dt}\right)_{T=T_\infty} = -\frac{E}{RT_\infty} + \ln\frac{QA}{C_p} \tag{2-60}$$

Plotting $\ln dT/dt$ when $T = T_\infty$ against $1/T_\infty$ as before allows the reaction kinetics to be determined. Jones *et al.* noted that it has been postulated that the existence of peripheral self-heating means the assumption that the sample is spatially uniform may be wrong, for which they suggested a modification to the analysis. Nonetheless, they suggested that this method is capable of characterising self-heating materials effectively. In a second paper Jones *et al.* (1996) used this method to characterise two different Scottish bituminous coals. They successfully used this method to relatively characterise them, i.e. being able to determine which is more likely to self-heat, but without comparing to the steady-state method, it is not known how reliable this method is.

Chen (1999) sought to compare the validity of the heat release and cross-point temperature methods, and the extent to which the cross-point temperature departs from that of the oven. They noted that Nugroho *et al.* (1998) compared a number of methods in their assessment of Indonesian coals and showed that the cross-point temperature method and the steady-state method gave practically the same results.

Sujanti *et al.* (1999) also showed this. Nugroho *et al.* also noted in comparing these experimental techniques that it is difficult to assess the validity of the heat release method as it ignores the fundamental principle of the cross-over temperature effect.

Chen noted that in some cases the cross-point temperature method and the heat release method can yield similar results, although in some cases the results can be significantly different. In directly comparing the cross-point temperature, T_{CPT}, to the oven temperature, T_{∞}, he observed that they are relatively close for low temperatures, which for testing sawdust was approximately 180°C, and for milk powder approximately 130°C. As the oven temperature increased, so did the departure of the cross-point temperature from it, with temperature differences up to 10°C observed in sawdust and 30°C observed in milk powders.

Plotting the HR and CPT plots together shows, the HR method produces a line of similar slope, but a significantly higher y-axis intercept, corresponding to $\ln(QA/C_p)$. The slopes for the wood sawdust tests strongly agree, whilst there is more of a difference between the slopes of the milk powder plots. The departure of the cross-point temperature from that of the oven is attributed to the how the reaction initially begins in the regions away from the centre of the material, with the centre temperature initially at a temperature much less than that of the oven. This is deduced from the comparison of the cross-point temperature and oven temperature. As the cross-point temperature increases, which occurs for increasing basket sizes, the departure also increases. For larger baskets, heating in the regions away from the centre and closer to the edges occurs to a greater extent before the reaction at the centre begins to speed up, thus increasing the cross-point temperature.

It is difficult to know beforehand whether the heat release method will be suitable for the material used. For particulate materials in particular, Chen recommend the cross-point temperature method, although there may be an element of bias here. This analysis also illustrates the importance of accurate placement of the thermocouples in the CPT method. A suitable distance between the two (or three) thermocouples is important, as too great a distance is analogous to the HR method, whereby the extent of periphery self-heating can affect the results.

Malow and Krause (2004) sought to compare the steady-state, cross-point temperature (CPT), and heat release (HR) methods for a number of thermally unstable materials. These methods are referred to as the self-heating experiments and are run at constant ambient temperatures. Two different methods that utilise differential scanning calorimetry (DSC) are also used. These methods are the Ozawa-Flynn-Wall method and the Kissinger-Akahira-Sunose method and will be discussed in more detail in later sections. These methods are known as the temperature programmed experiments as they are run at a programmed constant heating rate. The materials tested were a German lignite coal dust, a cork dust, a riboflavin (vitamin B2), and a detergent powder. This paper is of particular interest because it is one of few, if not the only, paper that seeks to characterise self-heating in a detergent powder, even though no details of the formulation are shared.

The results of these methods are compared. For the lignite coal dust, cork dust, and the riboflavin, it was found that the results of the steady-state method and CPT method agree very well, but the HR method give slightly higher activation energy values. For the detergent powder, the steady-state and CPT methods again agree well, but the HR method gives much higher activation energy values. This confirms that the HR method is not suitable for use with detergent powders, which can be explored later. It can be seen for all samples that the cross-point temperature is much higher than the ambient temperature, particularly in the case of the detergent powder. It can also be seen that the higher the ambient temperature, the higher the difference between the cross-point temperature and the ambient temperature. This is in agreement with the observations of Chen (1999) and it is thought that this is what leads to differences in these methods. The uncertainty in these measurements are attributed to a 2°C error in thermocouple readings, and an uncertainty in dT/dt of approximately 5%.

2.4.4. DSC and TGA Methods for determining n^{th} Order Reaction Kinetics

Two differential scanning calorimetry (DSC) based, isoconversional methods are commonly used in measuring the kinetics of self-heating reactions, the Ozawa-Flynn-Wall approach, proposed independently by Ozawa (1965) and Flynn and Wall (1966), and the Friedman method (1964). Prior to these methods being proposed, Flynn and

Wall stated that cumbersome curve-fitting techniques were typically used to fit kinetics to thermogravimetric data, which often involved fitting for an unknown order n. In many cases where a simple order is not followed, this would lead to poor results. This was in the 1960's and although curve fitting is not the computationally expensive process it used to be, these alternative isoconversional methods are still of interest. These two methods were independently proposed to provide a model independent estimate of the activation energy without any assumptions regarding the form of the kinetic equation, other than that the system is of Arrhenius type temperature dependence.

The Friedman method can be described as a differential isoconversional method, whilst the Ozawa-Flynn-Wall approach can be described as an isoconversional integral approach. Both of these approaches were originally proposed as thermogravimetric analysis (TGA) methods, based on sample weight loss with increasing temperature, but they can also be used with differential scanning calorimetry (DSC). In doing so the degree of conversion of the reaction is used.

Both of these approaches are based on the following single-step reaction:

$$\frac{d\alpha}{dt} = f(\alpha)k(T) \tag{2-61}$$

Where α is the degree of conversion, $f(\alpha)$ is the kinetic model, and $k(T)$ is the rate constant which can be substituted for the Arrhenius equation:

$$k(T) = -A\, e^{-\frac{E}{RT}} \tag{2-62}$$

2.4.4.1. The Friedman Method

The Friedman method is the more straightforward of the two methods to derive mathematically, but requires more mathematical manipulation of the data to determine the results. The Friedman method uses the logarithmic form of equation (2-61) as the basis of its approach, and in originally proposing it Friedman used the sample mass instead of the conversion:

$$\ln\left[\left(-\frac{1}{w_0}\right)\left(\frac{dw}{dt}\right)\right] = \ln f\left(\frac{w}{w_0}\right) + \ln A - \frac{E}{RT} \tag{2-63}$$

In terms of conversion this can be expressed as:

$$\ln\frac{d\alpha}{dt} = \ln f(\alpha) + \ln A - \frac{E}{RT} \tag{2-64}$$

Using the method, the kinetics can be found by plotting $\ln\left[\left(-\frac{1}{w_0}\right)\left(\frac{dw}{dt}\right)\right]$ or $\ln\frac{d\alpha}{dt}$ against $1/T$ for mass loss curves at different heating rates, and for isoconversional fractions, i.e. constant values of conversion w/w_0. From this plot, the activation energy can be found from the slope of the line, $-E/R$, while the pre-exponential factor can be found from the intercept, $\ln A + \ln f(w/w_0)$. In proposing this approach, Friedman (1964) measured the kinetics of the thermal degradation of Fibreglass-reinforced CTL 91-LD phenolic resin. 12 conversional values were chosen at equal intervals and the value of the activation energy, E, measured.

In order to determine the pre-exponential factor, A, Friedman plotted the intercept $\ln A + \ln f(w/w_0)$ against the conversion α. Although not a straight line, the smooth curve produced confirmed that the kinetics were consistent. For this material $f(w/w_0)$ was assumed to take the form:

$$f\left(\frac{w}{w_0}\right) = \left[\frac{w - w_f}{w_0}\right]^n$$

It this holds true, then a plot of the intercept $\ln A + \ln f(w/w_0)$ against $\ln\left[\left(w - w_f\right)/w_0\right]$ should give a straight line of slope n and intercept $\ln A$. For the resin used, a straight line was formed, although there was some deviation at higher weights, attributed to contributions of early weight loss, allowing the order of the reaction, n, and the pre-exponential factor, A, to be measured. These results compared well with other methods and proved this to be a valid approach.

2.4.4.2. The Ozawa-Flynn-Wall Method

The Ozawa-Flynn-Wall approach was a method proposed independently by Ozawa (1965) and by Flynn and Wall (1966) and requires some more mathematical manipulation. For measurements with a constant heating rate, β, (i.e. $T = T_0 + \beta t$), integrating equation (2-61) gives:

$$G(\alpha) = \int_0^\alpha \frac{d\alpha}{f(\alpha)} = \frac{A}{\beta}\int_{T_0}^{T} e^{-\frac{E}{RT}}\,dt \tag{2-65}$$

Taking the logarithm of this gives:

$$\ln G(\alpha) = \ln\left(\frac{AE}{T}\right) - \ln\beta + \ln p(x) \tag{2-66}$$

In this equation $x = E/RT$ and:

$$p(x) = \frac{\mathrm{e}^{-\mathrm{x}}}{x} - \int_{\infty}^{x} \frac{e^{-x}}{x} dx \tag{2-67}$$

Doyle (1962) proposed the following approximation for the solution to this expression:

$$\ln p(x) \approx -5.3305 + 1.052x \tag{2-68}$$

Applying this approximation to equation (2-66) gives:

$$\ln\beta = \ln\left(\frac{AE}{R}\right) - \ln G(\alpha) - 5.3305 + 1.052\frac{E}{RT} \tag{2-69}$$

It can be seen from this expression that when $\ln\beta$ is plotted against $1/T$ for isoconversional fractions and a series of measurements at heating rates of $\beta_1 \dots \beta_j$, a straight line is formed with a slope of $1.052E/R$. The temperature T_{jk} at which the conversion α_k is achieved is taken at the heating rate β_j. Ozawa applied this approach to two reactions: the decomposition of calcium oxalate into calcium carbonate and carbon monoxide, and the thermal degradation of nylon 6. The results from using this approach are in agreement with values reported in literature.

The approximation of the exponential integral in equation (2-67) has significant errors associated with it. For values of $31 < x < 47$ the errors are smaller than 1%, but for values of $x < 25$ or $x < 100$ these errors are in excess of 3%. A correction for this was suggested by Flynn (1983). Flynn provided a table of values from which to determine the correction, while Opfermann and Kaisersberger suggest the empirical correction factor in equation (2-70). Firstly E is estimated using equation (2-69), the mean temperature T_m is determined, and from this the mean value for $x_m = E/RT_m$ is determined. This is used to determine the empirical correction factor $F(x)$;

$$F(x) = a_0\left(1 + \frac{a_1 + x}{1 + a_2x + a_3x^2}\right). \tag{2-70}$$

Where $a_0 = 0.94961$, $a_1 = 7.770439$, $a_2 = 4.56092$, and $a_3 = 0.48843$. The corrected activation energy, E_{corr}, is calculated by dividing the first estimate of E by the correction factor $F(x_m)$.

Venkatesh *et al.* (2013) compared these two approaches in determining the kinetics of decomposition of Nitroimidazoles. They noted that the Ozawa-Flynn-Wall method is

suited to measuring kinetics of systems where multiple reactions are occurring, such that the activation energy is observed to vary with time. If these reactions are of widely different types, such that they have largely different activation energies, then this method may fail. They also noted that the Ozawa-Flynn-Wall method is less accurate than the Friedman method. This may be because of the approximations associated with the Ozawa-Flynn-Wall method. If the activation energy, E, is dependent on the conversion, α, or if competitive reactions are occurring then the values obtained using these methods are found to be different. On the other hand, if the activation energy is independent of the conversion, then these two methods should measure the same values.

2.4.4.3. Applications of these Methods

As mentioned Venkatesh *et al.* (2013) used both of these methods to analyse the thermal decomposition of Nitroimidazoles. They showed that multi-step reactions were occurring, evident from the nonlinear relationship observed between the activation energy and the conversion. They also showed the two methods to have variations in their results, and attributed this to the approximations used for the temperature integral in the Ozawa-Flynn-Wall method. This may also be because they did not use the correction factor proposed by Flynn (1983) for the Ozawa-Flynn-Wall method.

Pielichowski *et al.* (1998) used these two methods to determine the kinetics of gelatinisation of potato starch using DSC. Although both methods were used, the comparison of the two methods was never mentioned, and only one set of results was shared. Again it is worth noting that they did not use the correction factor in the Ozawa-Flynn-Wall method. The results showed that E changed with conversion, suggesting that a single-step reaction model was not appropriate. Instead a double-step reaction was fitted using non-linear regression, where the first reaction is of n^{th} order scheme, and the second is of three-dimensional diffusion Jander's type. This model was found to approximate the reaction very well.

Opfermann and Kaiserberger (1992) simulated reactions and used the Ozawa-Flynn-Wall and Friedman methods to characterise them. In doing so, two reactions were simulated, a single step reaction, and a double step reaction. For the single step reaction, both methods accurately measured the kinetics. The double step reaction was not so

simple. These methods measured the kinetics well in the regions where the two reactions were sufficiently isolated, i.e. $\alpha < 0.3$ and $\alpha > 0.8$. Unlike the work of Venkatesh *et al.* (2013), Opfermann and Kaiserberger showed the Ozawa-Flynn-Wall method to be more reliable. They also showed this method to be less sensitive to noise due to its integral nature. However, the Friedman method was showed to provide better visual separation of the different reaction steps, and more detail with regards the presence of an auto-catalytically activated process.

As mentioned in section 2.4.3, Malow and Krause (2004) compared the basket heating method with DSC methods for determining overall activation energies for self-heating materials. The DSC methods used were the Ozawa-Flynn-Wall and Kissinger-Akahira-Sunose methods. The materials tested were a German lignite coal dust, a cork dust, a riboflavin (vitamin B2), and a detergent powder. The results of the DSC methods were all in reasonable agreement with the results from the basket heating methods, except for the riboflavin. This was possibly due to a phase transition underlying the decomposition reaction. The DSC curves for cork dust had a second peak. This suggested that consecutive reactions may be occurring in this sample, a feature that would be difficult to measure using the basket heating methods. Despite this, the activation energy was not shown to be dependent on the conversion, and suggested that no consecutive reactions were occurring. The other samples shown a similar lack of conversion dependence. DSC based methods may prove to be a good alternative to the basket heating methods, although the erroneous results of riboflavin, and the possibility of consecutive reactions, shows that a degree of caution is required.

2.4.5. DTG Curve Fitting Method for determining n^{th} Order Reaction Kinetics

The DTG (differential thermogravimetry) curve fitting method is a means of measuring apparent kinetics proposed by Yang *et al.* (2001). This approach measures the apparent kinetic parameters from the overall weight loss behaviour of polymers undergoing thermal decomposition, although this approach can be adapted for other materials. Yang *et al.* noted that researchers are often more interested in weight loss behaviour rather that the complex chemical mechanisms at work during thermal decomposition.

The following Arrhenius expression is fitted to experimentally measured weight loss data to determine the kinetic parameters:

$$\frac{dW}{dt} = Ae^{-\frac{E}{RT}}(1-W)^n \tag{2-71}$$

W is the sample weight, E is the apparent activation energy, A is the pre-exponential factor, and n is the order of the reaction. The advantage of this method is that only one DTG curve is required to determine the kinetic parameters. They used this method to measure the apparent kinetics of six plastics: HDPE, LDPE, PS, PP, PVC, and PET. The DTG measured kinetics were compared with those measured using the Friedman method.

The DTG curve fitting method follows the workflow documented in Figure 2-9. The software iterates through all possible combinations of E and n, determining the best fit parameters using the method of least squares. The least square method uses the following equation:

$$\varepsilon = \sum \left[\left(\frac{dW}{dt}\right)_{exp} - \left(\frac{dW}{dt}\right)_{fit} \right]^2 \tag{2-72}$$

$(dW/dt)_{exp}$ is the experimentally measured DTG data, and $(dW/dt)_{fit}$ is the fitted value. The start and end temperature of the thermal decomposition, and the peak of the maximum decomposition rate were all input into the software. It is unclear how Yang *et al.* determine the best fit value of A as it is not included in their workflow. This approach is also inefficient in that it fits every combination of E and n instead of applying a different approach where the best fit parameters are closed in on. Other software packages with curve fitting software such as MATLAB may be more appropriate.

This method was used to measure the thermal decomposition kinetics of high-density polyethylene (HDPE). Using a Seiko 220 TG/DTA instrument, the mass loss of a sample between 3 and 5mg was measured at constant ramped heating rates. For experiments carried out at heating rates of 2, 5, 10, and 20°C/min, the fittings determined the apparent activation energies to be 242, 262, 242, and 264 kJ mol^{-1} respectively. Using an activation energy of 242 kJ mol^{-1} the simulated curves fitted very well to the experimental data for the 0-80% portion of the curve. When using an activation energy of 262 kJ mol^{-1} the simulated curves fitted very well to the experimental data for the 20-100% portion of the curve. Although Yang *et al.* did not note it, this may be due to a temperature dependence of the activation energy, or due to a two-step reaction

occurring. These results compared very well to those measured using the Friedman method, which exhibit the same temperature dependence feature. This is to be expected given that the two methods are derived from the same equations. They did note that the Friedman method required 10 hours of computation time, in comparison to the 1 hours required by the DTG curve fitting method, although this does not make sense, as the Friedman method is in no way computationally difficult. The DTG curve fitting method was successfully used to measure the apparent kinetics of other plastics. This shows that the DTG curve fitting approach should be considered as a possible alternative to the Ozawa-Flynn-Wall and Friedman methods for determining these kinetics.

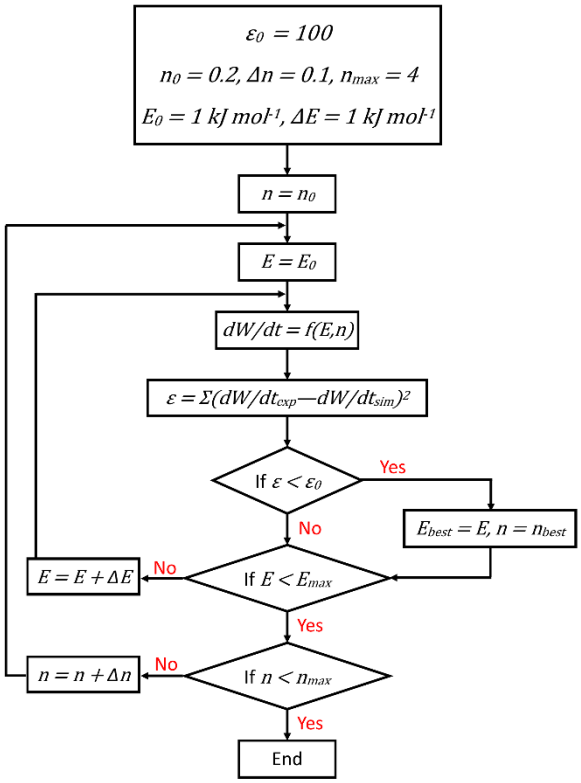

Figure 2-9: The workflow of the DTG curve fitting program used by Yang *et al.* (2001).

2.5. Numerical Modelling of Self-Heating Powder Systems

Ignition in self-heating systems can be difficult to predict and analytical solutions to the equations governing their behaviour can only be found for the simplest of cases. In order to effectively predict the behaviour of these systems it is necessary to model the complex processes that occur in these systems. The self-heating of detergent powders

has not been explored in the literature and as such it is necessary to explore other applicable areas which can be used to model these systems. Additionally the problem of self-heating has not be explored from the point of view of limiting the charring of material, and instead the focus is typically on predicting thermal runaway or the smouldering behaviour of materials. The models in literature are used to predict the evolution of temperature, moisture content, vapour concentration, and reaction species concentrations as a function of space and time. One approach explored is that taken by Chen (1994) (2001), and Chong and Chen (1999), in which the self-heating of physical entities such as a coal stockpiles or baskets of milk powder are subjected to cross-point temperature method testing. Another approach explored is taken by Krause and Schmidt (2001), Krause et al. (2006), and Muramatsu et al. (1979) in which models are used to replicate the smouldering behaviour of some materials, where more complex reactions and species transfer are modelled, with less of an emphasis on particle drying.

2.5.1. Modelling of Zero-Order Reactions in Stockpiles and Baskets

For some materials, being able to effectively model the drying is key to being able to accurately predict self-heating. In the modelling of self-heating in coal stockpiles, Chen (1994) stated that previous studies have shown that the heat of drying increases with reducing moisture content of the coal. It was observed that there are three distinctive energy levels, each corresponding to the vaporisation of different types of moisture (from lowest heat of drying to highest): free moisture, loosely bound moisture, and tightly bound moisture. This drying is expected to impact on the temperature-time profiles during the self-heating process. A simple model of self-heating in coal was proposed which follows the following assumptions:

- The moisture in the gas stream is in equilibrium with the moisture in the coal.
- Heat transfer in the bed is by conduction, and in the gas stream by convection.
- Mass transfer of oxygen is by diffusion and convection. Mass transfer of moisture is by convection.
- The dry gas flow-rate is constant, and independent of space and time.
- The local temperatures of the solid and gaseous are equal.

- The heat of oxidation is constant. The heat of drying/wetting is dependent on the moisture content of the coal.

Using this model, Chen solved for steady-state solutions to determine the maximum possible temperatures at different moisture contents. A qualitative plot of the predicted maximum temperatures as a function of moisture contents for three different heats of drying is shown in Figure 2-10. $H_{w,1}$ is the lowest heat of drying while $H_{w,3}$ is the highest. As free moisture is evaporated first, the temperature rise would follow curve 1. Once enough moisture has been evaporated, a stepwise change would occur and the temperature rise would follow curve 2, before doing the same with regards curve 3. This change in the temperature rise as moisture content reduces is represented by the red line. It is possible that as moisture content decreases the heat generated by the oxidation of the coal may slow down or even stop because it is not sufficient to drive off the remaining moisture. This model was shown to be capable of predicting self-heating and spontaneous ignition in moist coal. Without this stepwise change, the model does not agree with observations as well.

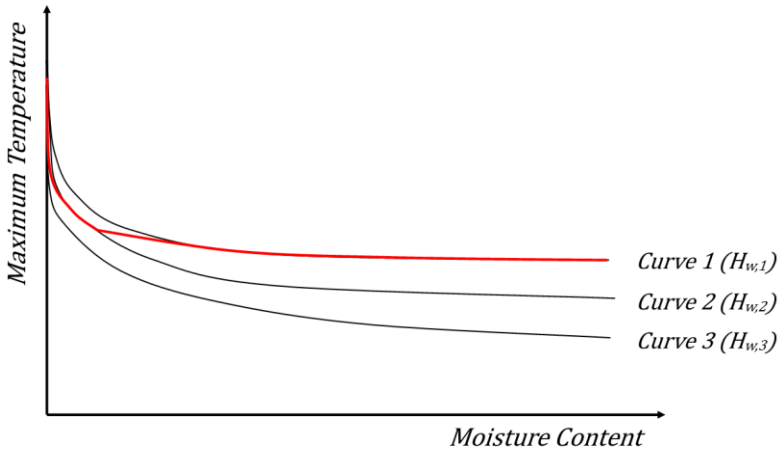

Figure 2-10: Maximum possible temperatures as a function of the moisture content of the coal and for the three different heats of drying. The red line indicates the stepwise change in the heat of drying as the moisture content of the coal decreases.

In this later work Chen (2001), and Chong and Chen (1999) built on this work to propose a model for predicting the self-heating behaviour of spray dried food powders. Chen (2001) aimed to model the basket heating procedure and cross point behaviour as observed in the novel method of Chong *et al.* (1996), while Chong and Chen (1999) explored the influence that different parameters have on the model heat and mass

transfer predictions. Effectively the same model is used in both of these works. This model does not account for oxygen transport, but instead has a more complex model of moisture transport.

For this model, the moisture transport within the system involves the evaporation of moisture from the particles to the void in the powder mass. This moisture then diffuses through the voids, out towards the outer boundary of the powder domain, where it is carried into the ambient air by means of convection. Similar to the previous model, a number of assumptions are applied, these are:

- Reactant consumption (i.e. oxygen and solid reactants) is assumed negligible.
- No convection occurs within the powder mass.
- Newtonian cooling is assumed at the outer boundary.
- The thermal conductivity and diffusion coefficient of water vapour in air is assumed constant.
- The solid particle, moisture, and gas in the voids are assumed to be at the same local temperature.
- Negligible moisture transfer occurs via solid contacts, and the moisture transfer from the inner powder mass to the outer boundary is assumed to occur by diffusion of water vapour.

With these assumptions in place, the following governing equation for energy conservation in the powder mass, accounting for drying of the powder, is defined as:

$$\rho C_p \frac{\partial T}{\partial t} = k\nabla^2 T + \rho_{sd} Q A e^{-\frac{E}{RT}} + \rho_{sd} H_v \frac{\partial X}{\partial t} \tag{2-73}$$

Here the first term is the local rate of enthalpy change in the solid, the second is the conductive heat transfer in the solid, the third is the heat generation term of the lumped exothermic reactions, and the fourth is the rate of heat release due to drying. With regards the parameters, ρ is the density (kg m^{-3}), C_p is the specific heat capacity (J kg^{-1} K^{-1}), k is the thermal conductivity (W m^{-1} K^{-1}), ρ_{sd} is the solid density (kg m^{-3}), Q is the heat of reaction (J kg^{-1}), A is the pre-exponential factor (s^{-1}), E is the activation energy (J mol^{-1}), H_v is the heat of drying/wetting (J kg^{-1}), and X is the moisture content of the solid on a dry basis (kg kg^{-1}). The Laplacian of the second term can be expanded for regular geometries to:

$$k\nabla^2 T = k\left(\frac{\partial^2 T}{\partial x^2} + \frac{j}{x}\frac{\partial T}{\partial x}\right) \quad (2\text{-}74)$$

Here, j is the shape factor and is equal to 0 for an infinite slab, 1 for an infinite cylinder, 2 for a sphere, 3.28 for a cube, or 2.728 for an equi-cylinder (cylinder of equal height and diameter). This shape factor is the same as that used by Boddington *et al.* (1971) in determining the critical parameter δ_{cr} for arbitrary geometries. This was shown to gives values of δ_{cr} that did not agree with those determined analytically. Although the shape factor leads to the correct Laplacian term for an infinite slab, infinite cylinder, and sphere, it is unclear as to why these shape factors can be used as an approximation to reduce 3-dimensional heat transfer to 1-dimensional for an equi-cylinder or cube. This approach is questionable and needs to be validated by comparing a 2D axisymmetric or 3D models with this shape factor based model.

Unlike the model of Chen (1994), oxygen consumption is assumed negligible, meaning only the mass transfer of the moisture in the system needs to be accounted for. There are two mass conservation equations in this model, the first representing the liquid water within the solid particles, and the second representing the water vapour in the voids between the particles. The first of these is given by:

$$-\rho_{sd}\frac{\partial X}{\partial t} = h_{m,in}A_p n_p\left(Y_{s,in} - Y\right) \quad (2\text{-}75)$$

Where $h_{m,in}$ is the effective mass transfer coefficient between the particles and the gas in the voids (m s^{-1}), A_p is the surface area of one particle (m^2), n_p is the number of particles per unit volume (m^{-3}), $Y_{s,in}$ is the vapour concentration at the surface of the particle (kg m^{-3}), and Y is the vapour concentration in the voids (kg m^{-3}). The effective mass transfer coefficient in the above equation is chosen such that it reflects the influence of the diffusivity of water on the solid particles. The diffusivity of water in the solid particles is of the order of 1x10^{-10} to 1x10^{-12} m^2 s^{-1} at low water contents, in comparison to the diffusivity of water vapour in air which is of the order of 2x10^{-5} m^2 s^{-1}. Taking $h_{m,in}$ as the overall mass transfer coefficient through a solid and air layer, and assuming a stagnant layer of 50µm, the effective mass transfer coefficient is of the order of 2x10^{-6} to 2x10^{-8} m s^{-1}.

In defining the vapour concentration at the surface of the particles, $Y_{s,in}$, it is necessary to first define the relative humidity at the surface of these particles, RH_s, as:

$$RH_s = \frac{p_{s,in}}{p_{sat}} \approx \frac{Y_{s,in}}{Y_{sat}} \tag{2-76}$$

Where $p_{s,in}$ and p_{sat} are the partial pressures at the surface of the particle and at saturation respectively (Pa), and can be approximated by the ratio of vapour concentrations. The temperature dependence of Y_{sat} can then be expressed as:

$$Y_{sat}(T) = K_v e^{-\frac{E_v}{RT}} \tag{2-77}$$

Where K_v is the apparent reaction frequency for evaporation (kg m^{-3}), and E_v is the activation energy for pure water evaporation (J mol^{-1}). Substituting this into equation (2-75) gives the following expression for the conservation of water in the particles:

$$\frac{\partial X}{\partial t} = \frac{h_{m,in} A_p n_p}{\rho_{sd}} \left(RH_s K_v e^{-\frac{E_v}{RT}} - Y \right) \tag{2-78}$$

In this expression the relative humidity needs to be calculated. In this work, Chong and Chen correlated this value using a Reaction Engineering Approach (REA). The REA was proposed by Chen (1997) and is a means of modelling drying kinetics by applying chemical reaction engineering principles. This approach assumes that evaporation is a first order activation process with an energy barrier to overcome, taking the form of an activation energy. Condensation is assumed to be a zero order process without such a barrier. The dynamic process of drying and the equilibrium state of drying are then unified in this approach. In this approach, the following Arrhenius equation is used to express the relative humidity at the particle surface:

$$RH_s = e^{-\frac{\Delta E_v}{RT}} \tag{2-79}$$

Where ΔE_v is the apparent activation energy (J mol^{-1}), although Chen (1997) (1998) often refers to this as an additional activation energy or the activation energy correction factor, which seems more appropriate. It is so called because it is effectively energy required in addition to the activation energy of pure water evaporation, which accounts for the added difficulty in removing water as the water content decreases. The equation for ΔE_v is a purely empirical fitting and the self-heating model of Chen (2001), and Chong and Chen (1999) was defined as:

$$\Delta E_v = \frac{a X^{-b}}{T^{n-1}} \tag{2-80}$$

Where a, b, and n are positive constants, with n reflecting the strength of the temperature dependence of this expression. These coefficients are different for whole and skimmed milk powders and reflect the difference in drying of the two powders. This is not the only expression used to define ΔE_v. Chen (1997) used the following expression in addition to that in equation (2-80) in correlating the additional activation energy for Bambara groundnut:

$$\Delta E_v = \frac{a\, e^{-bX^j}}{T^{n-1}} \tag{2-81}$$

This expression is more difficult to fit. n and j are value found by trial and error, while a and b are fitting parameters greater than zero. n was found to be the most important parameter in collapsing the data at different temperatures onto a single curve. Chen (1998) used the following expressions, which are solely a function of moisture content:

$$\begin{gathered} \Delta E_v = \frac{a}{X} + b, \\ \Delta E_v = aX - b, \\ or\ \Delta E_v = \frac{a}{X^2} + \frac{b}{X} + c \end{gathered} \tag{2-82}$$

These polynomials were used to successfully examine the isotherms of 19 different materials from other literature, including rice, peppers, and yoghurt. A ratio of the additional activation energy to the equilibrium activation, ΔE_v the maximum of the drying air, $\Delta E_{v,\infty}$, is also used:

$$\begin{gathered} \frac{\Delta E_v}{\Delta E_{v,\infty}} = a \cdot \exp\left(-b(X - X_\infty)^j\right), \\ or\ \frac{\Delta E_v}{\Delta E_{v,\infty}} = a(X - X_\infty)^3 + b(X - X_\infty)^2 + c(X - X_\infty) \end{gathered} \tag{2-83}$$

Where $\Delta E_{v,\infty}$ is defined as:

$$\Delta E_{v,\infty} = RT_\infty \ln(RH_\infty) \tag{2-84}$$

These expressions have been used by Chen (2008) and Chen and Xie (1997) in measuring the drying of pulped kiwifruit, apple and potato slices, silica gel, and single milk powder droplets, and by Putranto *et al.* (2011) in the drying of mango and apple tissue.

The additional activation energy accounts for the added difficulty in drying at low moisture contents. From the outlined equations, it can be seen that when water covers the entire surface of the solid this correction term reduces to zero, with relative humidity increasing to unity and drying reducing to evaporation from a pure water surface. The REA is a simple and robust approach capable of describing drying behaviour with minimal experiments required to yield the necessary model parameters. There is no evident relationship between the REA and other drying theory. However, in modelling self-heating powder this approach was considered sufficient.

Returning to the self-heating models of Chen (2001), and Chong and Chen (1999), the heat of wetting/drying, H_v, the heat required to remove water from the solid particles, or the heat released when wetting occurs, is correlated to the oven temperature and the relative humidity as follows:

$$H_v = L_v - f\frac{RT}{M_{H_2O}}\ln(RH_s) \tag{2-85}$$

L_v is the latent heat of vaporisation of water (J kg^{-1}) and M_{H_2O} is the molecular mass of water (kg mol^{-1}). In this model, f is assumed to be the same as n used in the relative humidity correlation.

The mass balance for the water vapour in the voids between the particles, Y, is given by;

$$\frac{\partial Y}{\partial t} = \varepsilon D\left(\frac{\partial^2 T}{\partial x^2} + \frac{j}{x}\frac{\partial Y}{\partial x}\right) - \rho_{sd}\frac{\partial X}{\partial t} \tag{2-86}$$

Where ε is the porosity/void fraction of the powder bed, and D is the diffusion coefficient for water in air (m^2 s^{-1}). In this expression the last term represents the addition/removal of vapour to the voids due to the rate of decrease/increase of moisture content in the solid particles.

A symmetrical boundary condition is applied at the basket centre:

For $x = 0$

$$\frac{\partial T}{\partial x} = 0 \tag{2-87}$$

At the external boundary, the body is subjected to Newtonian cooling, such that;

For $x = r$

$$-k\frac{\partial T}{\partial x} = h(T - T_\infty) \tag{2-88}$$

Where h is the heat transfer coefficient between the bulk solid and the ambient air at the interface (W m^{-2} K^{-1}), and T_∞ is the ambient air temperature (K). Similarly boundary conditions are applied to the mass transfer in the system. At the centre of the body, because of symmetry:

For $x = 0$

$$\frac{\partial Y}{\partial x} = 0 \tag{2-89}$$

At the boundary, the diffusion of vapour from the system is driven by the vapour concentration gradient between the boundary and the ambient air. This is expressed as:

For $x = r$

$$\varepsilon D\frac{\partial Y}{\partial x} = h_{m,out}\left(\rho_{s,out} - \rho_\infty\right) \tag{2-90}$$

Where $h_{m,out}$ is the mass transfer coefficient between the outer surface and the ambient air (m s^{-1}), $\rho_{s,out}$ is the vapour concentration at the outer surface of the powder mass (kg m^{-3}), and ρ_∞ is the vapour concentration of the ambient air (kg m^{-3}). $\rho_{s,out}$ at $x = r$ is found from:

$$\rho_{s,out} = \left.\frac{Y}{\varepsilon}\right|_{x=r} \tag{2-91}$$

Using a series of water evaporation tests the heat and mass transfer coefficients were correlated empirically to the oven temperature. Similarly the specific heat capacity of the powder was correlated to the oven temperature for both whole and skimmed milk powder, as a sum of the fractions of the specific heat capacities of the individual components of the powder (i.e. fat, protein, carbohydrates, moisture, and ash). The heat capacity was then determined based on the porosity of the powder:

$$C_p = \varepsilon C_{p,air} + (1 - \varepsilon)C_{p,solids} \tag{2-92}$$

This system of equations, consisting of the energy balance (2-73), the mass conservation equation for moisture in the solid particles (2-75), and the mass conservation equation for the vapour in the voids between the particles (2-86), were coupled together and

solved using the standard explicit method of finite differences. The model solver was written in FORTRAN. Using this method, the energy balance is expressed as:

$$\rho C_p \frac{T_i^m - T_i^{m-1}}{\Delta t} = k\left(\frac{T_{i+1}^{m-1} - 2T_i^{m-1} + T_{i-1}^{m-1}}{\Delta x^2} + \frac{j}{x_i}\frac{T_{i+1}^{m-1} - T_i^{m-1}}{\Delta x}\right) + \rho_{sd} Q A e^{-\frac{E}{RT_i^{m-1}}} + \rho_{sd} H_{v,i}^{m-1}\left(\frac{X_i^m - X_i^{m-1}}{\Delta t}\right) \quad (2\text{-}93)$$

Where Δx is the distance increment, Δt is the time increment, superscript m represents elements of the current time increment, superscript $m-1$ represents elements of the previous time increment, subscript i represents the current nodal element, and $i-1$ and $i+1$ represent the directly adjacent nodes. $i\Delta x$ can be used in place of x_i. Chen (2001) used a forward difference for the first order difference in temperature. A central difference scheme for this term would reduce the order of the error from $O\Delta x$ to $O\Delta x^2$. Stability, convergence and compatibility for this model was not discussed but is an issue that should be examined. A quasi-steady-state assumption was applied, assuming that $\partial Y/\partial t = 0$, thus implying that the moisture transfer from the solid particles to the voids is the limiting process.

In solving the model the approach outlined in Figure 2-11 was followed. After retrieving the input data and initial conditions, the physical properties correlated to the oven temperature are calculated and the mesh is created. Once all required data is calculated the iterative process begins. First the boundary values of temperature, T, and vapour concentration, Y, are calculated, followed by the values for relative humidity, RH_s, and heat of wetting/drying, H_v, for the entire mesh. Finally the internal values of temperature, T, vapour concentration, Y, and moisture content, X are calculated. After writing these results to the output file, they are checked against the pre-set limits such that the iterative process is stopped if thermal runaway occurs or the time limit is exceeded. If these pre-set limits are not exceeded then the time increments by Δt and the iterative procedure is repeated for the next time step.

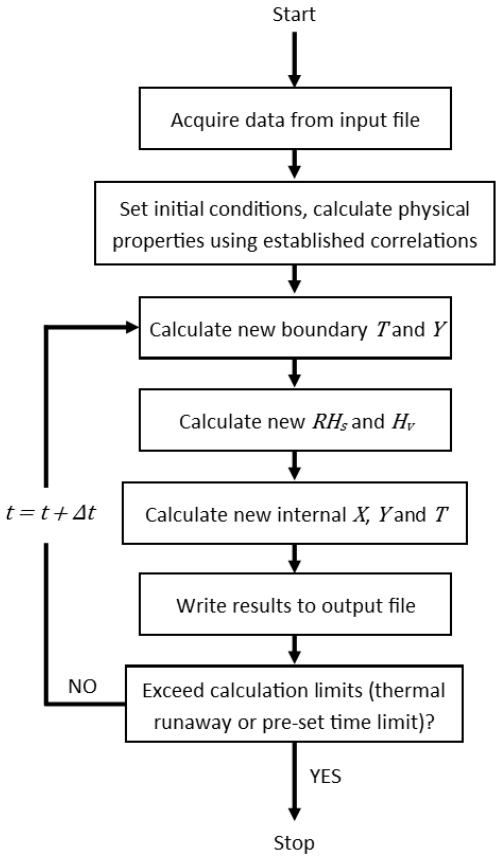

Figure 2-11: Flow diagram of the method taken in solving the sets of equations outlined as part of the model proposed by Chen (2001) and Chong and Chen (1999).

Using standard explicit finite differences to solve the system of partial differential equations is an inefficient, and potentially problematic approach. This explicit approach is only valid for $0 < \Delta t/\Delta x^2 \leq 0.5$, and as such requires small time steps to be stable. Implicit methods with approximations for the non-linear terms would be much more suitable for solving this system of equations, as will be discussed later.

Chong and Chen (1999) used to model to explore the sensitivity of the model parameters, and after having determine the most appropriate set of parameters, this model was used to simulate oven heated baskets of milk powder. The effect of the internal mass transfer coefficient, $h_{m,in}$, was explored. As mentioned, this value was to be considered as an overall mass transfer coefficient for a solid and air layer. This parameter determined the temperature at which the majority of the moisture evaporated, effectively creating a plateau in the temperature-time profile. As $h_{m,in}$ increases, the plateau temperature decreases. By plotting moisture content-time curves, it can be seen that as $h_{m,in}$ increases the rate of evaporation increases, as would

be expected. For particularly high values of $h_{m,in}$, the moisture content at the basket centre was found to increase initially. This was because moisture that evaporates at the basket edges diffuses into the central region.

The influence of surface relative humidity was determined by adjusting the parameter n in equation (2-80). As n increases the "curvature" of the evaporation region is seen to increase, with higher values leading to thermal runaway faster. The heat of drying was adjusted by varying the parameter f in (2-85). As f increases, H_v increases more sharply with falling moisture contents, and the rate of temperature rise in the evaporation region decreases.

Finally the thermal conductivity, k, was adjusted. The influence of this can be easily seen from equation (2-73). Higher values of k lead to a sharper temperature rise in the basket, although for all values of k a lag in temperature rise is seen in the initial stages of the heating, relative to the experimentally measured basket central temperature. This difference was attributed to the fact that the oven was pre-heated before the basket was placed in it. This meant that the thermocouple was pre-heated before it was placed into the sample and thus may be giving false readings initially.

Having determine the parameters which best reflected the observed behaviour, Chong and Chen compared this model to a greater range of experiments. For samples heated above 150°C, the model predicts the temperature profiles in the drying region reasonably well, but over predicts the temperatures after this. It was suggested that this may be because the thermal properties of the milk powder change at these higher temperatures. Similarly for ambient temperatures below 150°C, the model under-predicted the temperatures at all stages. The lower temperatures in the drying region suggest that a lower value of $h_{m,in}$ is required here, suggesting that $h_{m,in}$ is also temperature dependent. The model was shown to at least quantitatively predict the temperature-time profiles observed experimentally, although more work is required to be able to accurately model this behaviour for a range of different conditions.

Chen (2001) used this model to look at the cross-point temperature method. It was shown that this model replicates the experimentally measured basket temperatures for two thermocouples inserted at the centre and at 6mm from this. Having validated the model against this experimental data, Chen noted that the model accurately predicts

the cross-over behaviour observed. It was also seen that the difference between the cross-point temperature and the oven temperature increases with an increase in oven temperature. This again shows that the Heat Release method of Jones *et al.* (1996) may lead to significant errors.

Secondly, Chen looked to confirm the premise that cross-points can be found "everywhere". Essentially, along the same horizontal plane of the basket, different placements of the second thermocouple will exhibit their own cross-points, i.e. $\partial^2 T/\partial x^2 = 0$. Chen showed this to be the case, and suggested that by using more of thermocouples in the sample, more cross-points can be measured, with each experiment yielding multiple data points. This approach may be problematic. There are assumptions with regards the cross-point. Firstly conduction is not considered in the basket axial direction. Secondly a simple finite difference approximation is used which may not adequately represent the temperature derivative term. With these assumptions, particularly the second, it may not be correct to use cross-points for different spacings of Δx in the same plot. Also as Δx approaches the basket radius, the cross-point temperature becomes more similar to the heat-release method, particularly for high Biot numbers. Ideally Δx should be kept small.

2.5.2. Implicit Finite Difference Methods

The models of Chen (2001), and Chong and Chen (1999) were solved using a standard explicit finite difference scheme. As discussed, this approach may be problematic because it is only valid for $0 < \Delta t/\Delta x^2 \leq 0.5$, and as such requires small time steps to be stable. Instead an implicit finite difference scheme would be much more robust. For a one-dimensional model the Crank-Nicolson implicit method or the fully implicit backwards method would be suitable, and much more stable.

The Crank-Nicolson method is an approach that considers the partial differential equation to be satisfied at the mid time step $n + 1/2$ (Smith, 1985). It is based on the trapezoidal rule and can be described by the stencil in Figure 2-12.

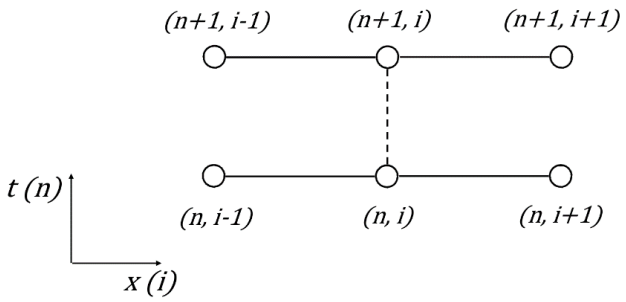

Figure 2-12: The stencil for a one-dimensional problem using the Crank-Nicolson method.

Whereas the standard explicit scheme solves for one unknown point at the next time step of $n+1$ using three known points at the current time step of n, the Crank-Nicolson scheme solves for three unknown points at the next time step of $n+1$ using three known points from the current time step of n. Using this method, the basic energy balance, consisting of only the transient and conduction terms can be solved as:

$$\rho C_p \frac{T_i^{n+1} - T_i^n}{\Delta t} = k\left(\frac{(T_{i-1}^{n+1} - 2T_i^{n+1} + T_{i+1}^{n+1}) + (T_{i-1}^n - 2T_i^n + T_{i+1}^n)}{2\Delta x^2}\right) \quad (2\text{-}94)$$

The fully implicit backwards method is similar but does not rely on three known points at the current time step n, instead solving for for three unknown points at the next time step of $n+1$ using one known point from the current time step of n. It can be described by the stencil in Figure 2-13.

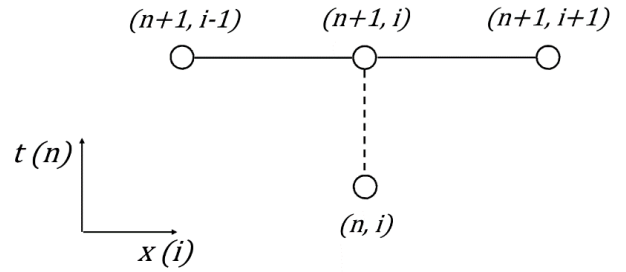

Figure 2-13: The stencil for a one-dimensional problem using the fully implicit backwards method.

Using this method, the basic energy balance, consisting of only the transient and conduction terms can be solved as:

$$\rho C_p \frac{T_i^{n+1} - T_i^n}{\Delta t} = k\left(\frac{T_{i-1}^{n+1} - 2T_i^{n+1} + T_{i+1}^{n+1}}{\Delta x^2}\right) \quad (2\text{-}95)$$

These equations consist of $I-1$ internal mesh points along each time row. These equations can be expressed in form of a tri-diagonal matrix on the left of size ($I-1, I-1$), and a matrix of size ($I-1, 1$) on the right hand side. This takes the general form:

$$\begin{bmatrix} a_{1,1} & a_{1,2} & & & & & & & \\ a_{2,1} & a_{2,2} & a_{2,3} & & & & & & \\ & \cdot & \cdot & \cdot & & & & & \\ & & \cdot & \cdot & \cdot & & & & \\ & & & a_{i,i-1} & a_{i,i} & a_{i,i+1} & & & \\ & & & & \cdot & \cdot & \cdot & & \\ & & & & & \cdot & \cdot & \cdot & \\ & & & & & & a_{I-2,I-3} & a_{I-2,I-2} & a_{I-2,I-1} \\ & & & & & & & a_{I-1,I-2} & a_{I-1,I-1} \end{bmatrix} \cdot \begin{bmatrix} T_1 \\ T_2 \\ \cdot \\ \cdot \\ T_i \\ \cdot \\ \cdot \\ T_{I-2} \\ T_{I-1} \end{bmatrix} = \begin{bmatrix} b_1 \\ b_2 \\ \cdot \\ \cdot \\ b_i \\ \cdot \\ \cdot \\ b_{I-2} \\ b_{I-1} \end{bmatrix} \quad (2\text{-}96)$$

Using Gaussian elimination, this set of matrices can be solved. At the boundaries, applying equations like equation (2-95) leaves imaginary temperature beyond the matrix bounds, T_0 and T_I. These points are eliminated by using central difference equations for the boundary conditions which can be rearranged to give an equation in terms of T_1 and T_2 in the first row, and in terms of T_{I-1} and T_{I-2} in the final row.

If a two-dimensional model is to be solved then a different approach is required. One such approach is the alternating difference implicit method. In this method the time step is divided in two to give a half time step $n+1/2$. The first step, in a similar way to the previous method, involves solving for three points in the i dimension at the half time step $n+1/2$ using three points in the j dimension at the current time step n. Having done this, three points are then solved for in the j dimension at the full time step $n+1$, using three points in the i dimension previously solved for at the half time step $n+1/2$. This can be seen from the stencil in Figure 2-14.

In this case the energy balance for the first step would be given by:

$$\rho C_p \frac{T_{i,j}^{n+\frac{1}{2}} - T_{i,j}^n}{\Delta t/2} = k\left(\frac{T_{i-1,j}^{n+\frac{1}{2}} - 2T_{i,j}^{n+\frac{1}{2}} + T_{i+1,j}^{n+\frac{1}{2}}}{\Delta x^2} + \frac{T_{i,j-1}^n - 2T_{i,j}^n + T_{i,j+1}^n}{\Delta y^2}\right) \quad (2\text{-}97)$$

Then in the second step, this energy balance would be given by:

$$\rho C_p \frac{T_{i,j}^{n+1} - T_{i,j}^{n+\frac{1}{2}}}{\Delta t/2} = k\left(\frac{T_{i-1,j}^{n+\frac{1}{2}} - 2T_{i,j}^{n+\frac{1}{2}} + T_{i+1,j}^{n+\frac{1}{2}}}{\Delta x^2} + \frac{T_{i,j-1}^{n+1} - 2T_{i,j}^{n+1} + T_{i,j+1}^{n+1}}{\Delta y^2}\right) \quad (2\text{-}98)$$

This approach could also be adapted to solve a three dimensional model by solving in the i dimension at the time step $n + 1/3$, in the j dimension at the time step $n + 2/3$, and in the k dimension at the time step $n + 1$.

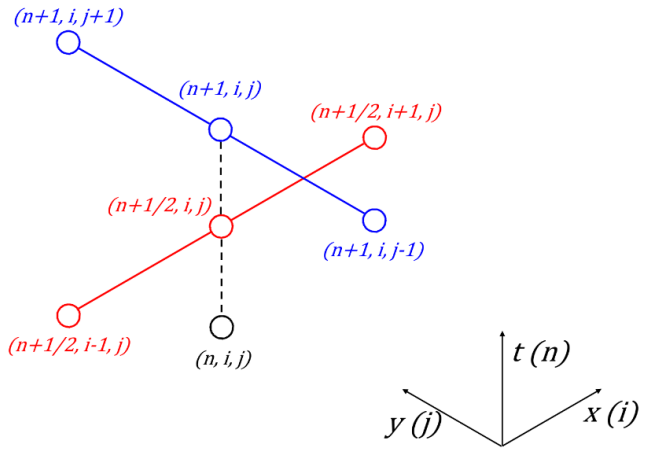

Figure 2-14: The stencil for a two-dimensional problem using the alternating difference implicit method.

When applying these approaches to the problem of self-heating, the non-linearity of the temperature in the Arrhenius term is problematic. A means of linearizing this term is required in order to solve this set of equations. One such approach is that used by Shepherd *et al.* (2015) in modelling the pre-oxidation of a uranium carbide fuel pellet. In this case the numerator and denominator of the heat of reaction term is multiplied by T_i^{n+1}. An iterative procedure is then used where the numerator temperature is solved for as it is now a linear term, and the denominator and exponent temperatures use the value from the previous iteration. If the iteration is given by z and for the first iteration it is assumed that $T_i^{n+1,z} = T_i^n$, then the heat of reaction term can be solved using:

$$\ldots + \left(\frac{T_i^{n+1,z+1}}{T_i^{n+1,z}}\right) \rho Q A \exp\left(-\frac{E}{R T_i^{n+1,z}}\right) \quad (2\text{-}99)$$

This process is iterated until the following condition is met, where the tolerance is typically set to around 0.1% of the temperature, with the solution becoming more stable for a decreasing tolerance.

$$\frac{T_i^{n+1,z+1} - T_i^{n+1,z}}{T_i^{n+1,z+1}} < Tolerance \tag{2-100}$$

Once the tolerance is met, the solver can continue to the next time step.

2.5.3. Smouldering Models with Higher Order Reactions

In the literature there are a number of papers that report on the modelling of smouldering in materials such as dust accumulations, tobacco, biomass, and generalised carbonaceous materials. In general these models are of the same form as those of Chen (2001), and Chong and Chen (1999). The main difference in these models is that moisture is not modelled here and a much more complex reaction model is used.

Krause and Schmidt (2001) presented a model incorporating the combined phenomena of heat and species transfer occurring in the smouldering of dust accumulations. They used this model to predict the self-ignition temperatures of a number of dust accumulations, out of an economic need to address the issue of smouldering fires occurring in bulk materials. Krause and Schmidt built a model capable of modelling using three-dimensional equations whereby the evolution of the scalar quantities of heat and species transfer can each be described by Fourier's Equation, provided that the transport coefficient Γ does not vary with time or space:

$$\frac{\partial \phi}{\partial t} = \Gamma\left(\frac{\partial^2 \phi}{\partial x^2} + \frac{\partial^2 \phi}{\partial y^2} + \frac{\partial^2 \phi}{\partial z^2}\right) + S_\phi \tag{2-101}$$

Here t is the time, x, y, and z are the spatial coordinates and S_ϕ is the source term for the scalar quantity ϕ. For the case of heat transfer the scalar quantity is temperature and the transport coefficient is the thermal diffusivity of the medium. For the case of species transfer the scalar quantity is the concentration of the species in question, and assuming the species to be gaseous, the transport coefficient is the diffusion coefficient through the porous medium.

For the purpose of simplicity, but yet to make the model as comprehensive as possible for a generalised case, the reaction was modelled as a single step reaction as follows;

$$SF + \nu_{Ox} Ox \rightarrow \nu_{SP} SP + \nu_{GP} GP + Q \tag{2-102}$$

Where SF is the solid fuel, Ox is the oxidiser, SP is a fictitious solid product and GP is a fictitious gaseous product. The stoichiometric coefficients are given by ν_i for each species i, and Q is the heat of the reaction. In this reaction, the fictitious species are representative of a mixture of real reactants or products, with the coefficients chosen to match these.

Choosing the solid fuel to be the leading species, the reaction rate was determined using a second-order Arrhenius law of the form;

$$S_{C,SF} = -c_{SF}^{a} c_{Ox}^{b} A e^{-\frac{E}{RT}} \tag{2-103}$$

Where C_{SF} is the concentration of solid fuel, C_{Ox} is the concentration of the oxidiser, a and b are the reaction orders. This second-order expression is dependent on the concentrations of both the fuel and the oxidiser, such that as these deplete the rate of the reaction changes accordingly. Additionally if the oxidiser is chosen to be gaseous, then the rate of diffusion of this gas into the porous medium will also be of influence.

The reaction rate of the other species involved in the reaction is dependent on reaction rate of the fuel, and is given by:

$$S_{C,i} = sign(\nu_i) \frac{\nu_i}{\nu_{SF}} \frac{M_i}{M_{SF}} S_{C,SF} \tag{2-104}$$

Where the index i refers to the species in question, ν_i is the corresponding stoichiometric coefficient, and M_i the molecular weight. The function $sign(\nu_i)$ is equal to 1 for reactants and -1 for products. This is so that the source term is negative for reactants, corresponding to a depletion, and positive for products, to correspond to an increase. For the case of nitrogen this function is 0.

The source term for temperature, corresponding to a generation of heat proportional to the rate of reaction, is given by:

$$S_T = \frac{1}{\rho C_p} \Delta H_R \left| S_{C,SF} \right| \tag{2-105}$$

This set of model equations was solved by Krause and Schmidt using a finite element method (FEM), whereby the control volume in question is overlaid with node points. The connections between these nodes form the finite elements. Each of these nodes exhibits six degrees of freedom, one of which is the temperature, with the other five occupied by the other chemical species.

Hot storage experiments were performed for four different powders: cork dust, wood dust, lignite coal dust, and dyestuff powder. These samples were analysed and the measured self-ignition temperatures compared to those predicted by this model.

Analysing the measured core temperature profiles of the samples showed that smouldering fires follow the behaviour outlined in Figure 2-15.

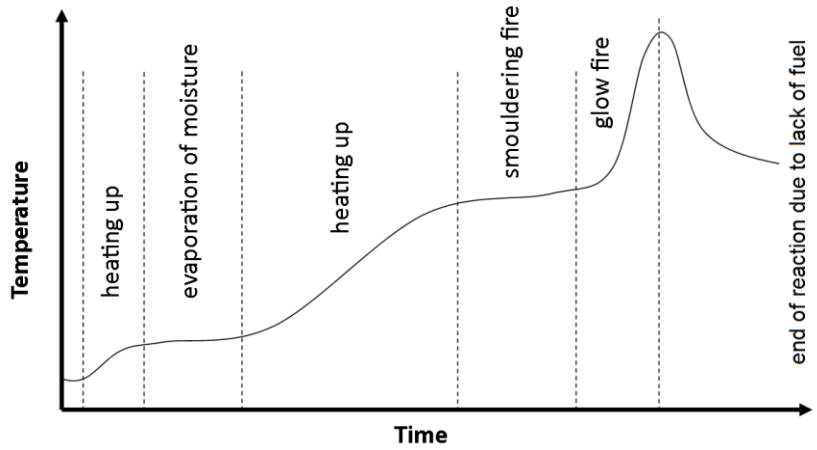

Figure 2-15: Temperature profile as a function of time followed by a material undergoing smouldering as documented by Krause and Schmidt (2001).

Initially the temperature increases to that of the evaporation temperature of the residual moisture. Once the dust has dried the temperature increases again until a characteristic smouldering temperature is reached, which is maintained for the entire smouldering period. Once the smouldering front reaches the sample of the surface, a glowing fire occurs, which may or may not by accompanied by a flame. This occurs from the surface and propagates inwards and results in a significantly higher temperature. Finally, once the fuel has depleted, the temperature begins to drop.

Using the model, the self-ignition temperatures for different volumes of deposits were calculated and compared to experimentally measured values. The model exhibited the same relationship between deposits volume and self-ignition temperature. Despite this,

the model over-predicted these temperatures consistently by 50 to 60°C. This was attributed to inaccuracies in the experimentally measured activation energies, such that the validity of the model is highly dependent on the reliability of the experiments.

Krause *et al.* (2006) followed up on this model with improvements to the modelling of the reaction. In this case the modelling of heat transfer was unchanged but a specific reaction was instead modelled. A fictitious "fuel molecule" was assumed. This molecule was based on an elemental analysis of German lignite coal used. The first step of the reaction, the decomposition of the fuel, can be expressed as:

$$C_{241}H_{228}O_{46} \rightarrow 213C + 18CO_2 + 10CO + 114H_2 \tag{2-106}$$

This is followed by char combustion, oxidation of carbon monoxide, and the oxidation of hydrogen, given by:

$$\begin{gathered} C + O_2 \rightarrow CO_2 \\ 2CO + O_2 \rightarrow 2CO_2 \\ 2H_2 + O_2 \rightarrow 2H_2O \end{gathered} \tag{2-107}$$

It can be seen that the evolution of seven species is followed using this model. Each reaction has its own leading species, and the reaction rate of each of the other constituent parts of that reaction is determined as before, in accordance with equation (2-104), but relative to the leading species of that reaction. This model is useful in that it applies molecules to the generalised model used before, and by treating it as a multiple step reaction, different conditions will lead to different final concentrations of each product.

This model was used to explore a number of problems. Firstly the influence of different oxygen fractions on the self-ignition was determined. Experimentally it has been shown that the self-ignition temperatures of this coal increases for a decrease in the oxygen fraction. The model predictions agreed with observation for the most part. For very low oxygen fractions (below 5%) the predicted values massively exceeded those measured experimentally, although this was attributed to the difficulty in experimentally differentiating between ignition and non-ignition at these low oxygen fractions. Similar to the previous model, Krasue *et al.* states that the model is capable of qualitatively modelling these systems, noting that the accuracy of the measured kinetics limits the ability of the model to quantitatively model these systems.

Another smouldering model worth noting is that of Muramatsu *et al.* (1979). This model predicts pyrolysis and evaporation in a naturally smouldering cigarette. The interesting element of this model is the mass balance used. Here the concentrations of a solid, a char and water are modelled. The solid concertation is modelled using a normalised conversion approach similar to that used in DSC and TGA methods. The conversion, α, is defined relative to the reactant concentration, c_{rc}, as:

$$\alpha = \frac{c_{rc,0} - c_{rc}}{c_{rc,0}} \tag{2-108}$$

Using this, the rate of change of conversion, relative to the reaction order, n, is given by:

$$\frac{\partial \alpha}{\partial t} = -A(1-\alpha)^n e^{-\frac{E}{RT}} \tag{2-109}$$

Relating this back to the concentration of the solid gives:

$$\frac{\partial c_{rc}}{\partial t} = -A c_{rc,0} \left(\frac{c_{rc}}{c_{rc,0}}\right)^n e^{-\frac{E}{RT}} \tag{2-110}$$

By relating the reaction to the conversion instead of purely the concentration means that the approach could still be compatible with the zero-order kinetics measured using the basket heating methods, unlike the other smouldering models. The problem with this equation is that it may fail to model situations where the initial concentration of reactive component is different. However, in such cases, the reaction kinetics may also be different and they themselves may not be applicable.

2.6. Conclusions

The literature relevant to the problem of self-heating in spray dryer wall deposits was explored here. This literature was not exclusive to detergent powder, but instead covered materials such as coal, milk powder, and sawdust, and the problems that self-heating causes in the spray drying and storage of these materials. It can be seen from the first section that self-heating is a problem in spray dryer wall accumulations, with deposition and re-entrainment rates meaning that an active layer is formed. With these deposits falling from the wall, it is evident as to why an understanding of self-heating is required. With significant self-heating comes charring, and having charred particles fall from the wall with affect the finished product quality. The literature has shown that this

is not a problem limited to detergents, and that this is also a significant issue in the spray drying of milk powders, which are subject to strict hygiene standards. There has been little work done to look at the problem of self-heating in detergent powders, with Malow and Krause (2004) the only evident example. This will be addressed in this investigation by extensively exploring this problem exclusively for detergent powders.

Frank-Kamenetskii's Theory of Thermal Explosions (Frank-Kamenetskii, 1969), and the subsequent analytical solutions developed using this theory helped to provide a basic understanding of the mathematics behind the problem of self-heating. The parameter δ, defined by Frank-Kamenetskii as a dimensionless parameter containing all the parameters required to fully describe the problem of self-heating, is of particular importance. Knowing the critical value, δ_{cr}, whether this is determined analytically or numerically, allows predictions of thermal runaway and the extent to which self-heating will occur to be made. Values of δ_{cr} have been numerically solved for at a range of values for φ $(= E/RT)$, and for a number of different geometries by Parks (1961). However, there is much room for improvement here. In this investigation, values of δ_{cr} will be solved for more accurately, for a number of geometries, and for varying values of φ and Biot numbers. This will allow more representative values of δ_{cr} to be applied throughout this investigation. This parameter can then be used as an effective means of comparing results, and of making predictions for thermal runaway in oven heated baskets.

The δ parameter is also the basis of the steady-state basket heating method, which has been extensively used to measure the self-heating reaction kinetics of different materials. Here, this will be used to measure the self-heating reaction kinetics of different detergent powders.

The steady-state method is a slow, yet frequently used approach for measuring these kinetics, as it is a relatively simple and accurate method. The cross-point temperature method was developed as a faster alternative based on the existence of a "cross-point", whereby conduction across a portion of a heated basket is hypothesised to cease. In more recent years, this approach has been successfully applied as an alternative to the much slower steady-state method. The CPT method will be explored further as part of this investigation and will be applied to measure the self-heating reaction kinetics of detergent powders. Different thermocouple setups and cross-point approximations will be applied, building upon the three thermocouple setups used by Chen and Chong

(1995) and Sujanti *et al.* (1999). A novel 5-point finite difference stencil for the second order temperature derivative will be used instead of the incorrectly applied 3-point stencil applied in these previous works.

Differential Scanning Calorimetry (DSC) and Thermogravimetric Analysis (TGA) will also be used, and the methods such as the Ozawa-Flynn-Wall method, Friedman method, and the DTG curve fitting applied.

The numerical models explored, which predicted self-heating in stockpiles and baskets, have provided a good basis from which to develop a model of self-heating detergent powder in oven heated baskets and in spray dryer wall deposits. The models explored were capable of modelling the oven heated basket experiments to explore some of the phenomena of these methods. The model developed in this investigation will be applied to explore aspects of the baskets heating methods that have not been previously explored. Having a model that is able to accurately replicate the basket heating experiments will allow issues such as thermocouple placement, the form of the cross-point temperature assumption, and errors in thermocouple readings to be explored. Exploring these phenomena will allow a more quantitative analysis of the issues in the CPT method to be undertaken.

These models all focused on modelling heat transfer in self-heating materials, but they also explored different aspects. Some of these models focused on the drying aspect and how this influenced the observed self-heating. Other focused on the reaction and the depletion and production of reactants and products. In developing the model in this investigation, the inclusion of powder drying and of an n^{th} order reaction model will also be explored. The value of these different aspects of the model will be evaluated.

3. Evaluation of Self-Heating in Detergent Powders

3.1. Introduction

Due to the lack of information regarding self-heating in detergent powders in the literature, it was decided that an initial evaluation of self-heating in detergent powders must be conducted. A model detergent formulation was produced by Procter and Gamble, designed to be representative of the spray-dried detergents typically produced. The self-heating in this formulation was evaluated using oven heat basket experiments, differential scanning calorimetry (DSC), and thermogravimetric analysis (TGA). In doing so, the following aspects of self-heating were evaluated:

- The influence of self-heating on the core temperature profiles of oven heated baskets full of this formulation of detergent powder.
- The detrimental effects of excessive self-heating and thermal runaway in oven heated powder baskets.
- Localised self-heating in layer-like geometries of oven heated powder.
- Initial cross-point temperature experiments for an equi-cylindrical basket (cylinder of equal diameter and height) and a cubic basket.
- Heat flow profiles for samples of different particle size ranges using DSC.
- Mass loss profiles for samples of different particle size ranges using TGA.
- Influence of oxygen on the self-heating reaction using DSC and TGA.
- Variability in reactivity across different size ranges of particles due to variability in powder composition.

This size distribution of this formulations was first determined. This also allowed the sample to be sieved into individual size fractions, allowing some experiments to be performed on individual fractions.

Chapter 5 explores the basket heating experiments, such as the steady-state, cross-point temperature, and heat release methods, in a considerable amount of detail. Before this is done, an initial evaluation of the oven heating of these baskets is performed here. Baskets of powder in this section are heated and temperature profiles recorded to help understand how self-heating occurs in these systems. Equi-cylindrical and cubic baskets were heated at sub-critical and super-critical temperatures and the different aspects of

the temperature profiles at the basket core evaluated. The slow increase in core temperature, the delays in temperature increase due to drying, and the increase in temperature above the ambient temperature due to self-heating are all discussed. The discolouration of particles, and in extreme cases burning, of these powder baskets are discussed, as is the problem of localised thermal runaway in layer-like geometries.

Initial cross-point temperature experiments were conducted using a simple two thermocouple setup. This is done for an equi-cylindrical and cubic basket. Evaluating this method here will help in improving the methodology in later chapters, and will give an indication as to whether this approach is suitable for measuring the self-heating reaction kinetics of detergent powders.

Differential scanning calorimetry (DSC) and thermogravimetric analysis (TGA) were used to evaluate the heat flow and mass loss associated with the self-heating reaction. Different size fractions of detergent were heated to determine reactivity variability with particle size. These experiments were also conducted under nitrogen, rather than air, such that the role of oxygen on the reaction could be determined. The oxygen dependency of the reaction is important should the reaction be modelled as n^{th} order rather than zero order.

3.2. Detergent Powder Composition and Physical Properties

In this chapter, an evaluation of self-heating was performed on a single detergent powder formulation. This formulation was produced by Procter and Gamble, and consisted of surfactant, polymer, and inorganic salts. This formulations was designed to be a model formulation that is representative of the spray-dried powder present in a commercial laundry detergent products.

This formulation's primary components are sodium sulphate and linear alkylbenzene sulphonate (LAS). A finer grade of sodium sulphate was used to reduce the composition variability that can be seen between particles and between different sizes of particles. The surfactant LAS is present at a level of 17% in the spray dried powder and causes the majority of the observed self-heating behaviour. The powder also contains lower levels of sodium silicate, sodium carbonate, and polycarboxylate polymer. Few other details regarding the detergent formulation can be shared.

The particle size distribution of the detergent powder was measured by sieving. Sieving the sample also allowed the subsequent DSC and TGA experiments to be carried out on different size fractions of the powder. In doing so, the reactivity of the different size fractions can be evaluated. 9 sieve were used: 150µm, 212µm, 300µm, 425µm, 600µm, 710µm, 1.1 mm, 1.60mm, and 2.36mm. The sieves were stacked, a powder sample between 99g and 108g placed into the top sieve, and the stack shook using an automated stack shaker for 5 minutes. This was repeated 4 times to account for any variability in the powder sample used in the each run. The particle size distribution by mass is shown in Figure 3-1.

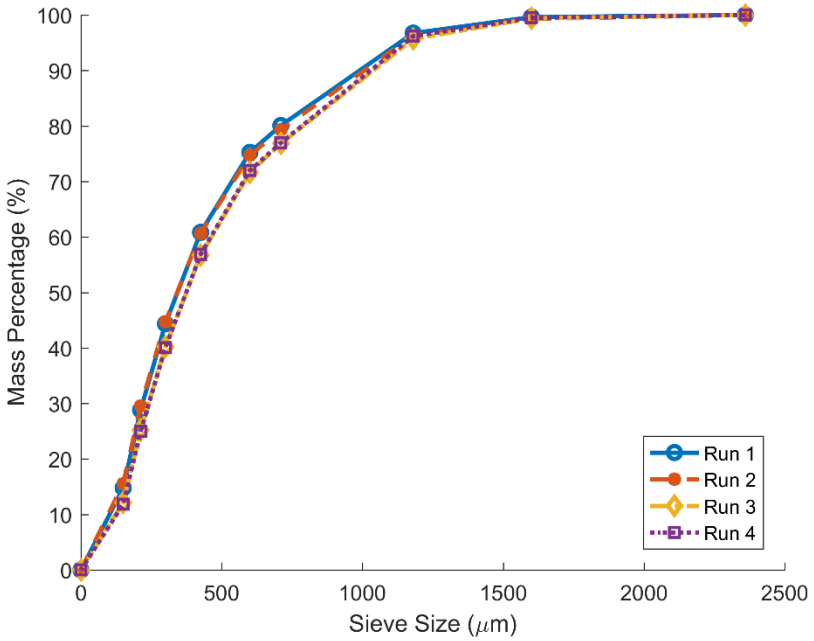

Figure 3-1: Cumulative size distribution by mass of the detergent powder for 4 separate samples.

All four runs are seen to agree very well. The mass median particle diameter, D_{50}, of the detergent was measured as 343µm. This is the diameter for which 50% of the mass of particles are smaller. Also measured were the D_{10} of 101µm, and the D_{90} of 990µm. The percentage contribution of each of these size ranges to the overall composition can also be seen in Table 3-1. The largest particle is smaller than 2.36mm, while 99.6% of particles are smaller than 1.6mm.

Table 3-1: Percentage contribution by mass of each size range to the overall powder size distribution.

	Percentage of Overall Sample Mass
0 µm - 150 µm	14.8%
150 µm – 212 µm	14.0%
212 µm – 300 µm	15.5%
300 µm – 425 µm	16.5%
425 µm - 600 µm	14.4%
600 µm - 710 µm	4.8%
710 µm – 1.18 mm	16.7%
1.18 mm – 1.60 mm	2.9%
1.60 mm – 2.36 mm	0.4%
> 2.36 mm	0%

This powder is not entirely dry when it is produced, with some residual moisture present in the particles. The moisture content varies between samples and for most samples it was found to be approximately 0.025 kg kg^{-1}. This value is also influenced by exposure to the ambient air. The moisture content of the sample was found to increase with longer exposure to the ambient air, suggesting that the relative humidity of the ambient air is greater than the equilibrium relative humidity of the particles.

3.3. Self-Heating in Detergent Powder Baskets

3.3.1. Initial Basket Heating of Detergent Powder

In order to evaluate the self-heating in bulk detergent powder systems, samples of this powder were oven heated. This was done for an equi-cylindrical basket (cylinder of equal height and diameter), a cubic basket, and a layer-like, tray full of powder. The equi-cylinder had a diameter and height of 60mm while the cube had a side length of 50mm. The baskets were filled and tapped, such that they were consistently filled to the same mass, ensuring the same density for each experiment. The equi-cylindrical basket was filled to a mass of approximately 135g, while the cubic basket was filled to a mass of approximately 99g.

Initially the sample were heated with a single type K thermocouple (RS Pro 363-0294) embedded at the basket centre. This thermocouple was glass fibre insulated with a welded exposed junction and supplied with a working range of -60° to 350°C. This thermocouple was inserted after the basket was filled with powder to ensure the basket was filled to a consistent mass for each experiment. As such it was difficult to verify its placement exactly at the basket centre. All these samples were heated in a Memmert UF 75 forced convection oven, shown in Figure 3-2. This oven's control system allowed the temperature to be controlled to within 0.5°C, while also allowing control over fan speed, exhaust opening size, and duration of heating.

Figure 3-2: Memmert UF 75 forced convection oven used to heat the powder samples. 1) Oven controls. 2) Variable outlet vent. 3) Variable speed fan.

The two baskets of powder, prior to heating, can be seen in Figure 3-3. These baskets were made of SS304 grade stainless steel with apertures of 0.223mm and a wire diameter of 0.14mm. In filling these baskets only some of the smaller particles would escape through the mesh apertures, yet this porosity allowed free movement of gas through the basket. This is important because air needs to be able to reach to powder in order for the self-heating reaction to occur, gaseous products of the reaction must be allowed to escape, and the basket itself should impact minimally on the experiment.

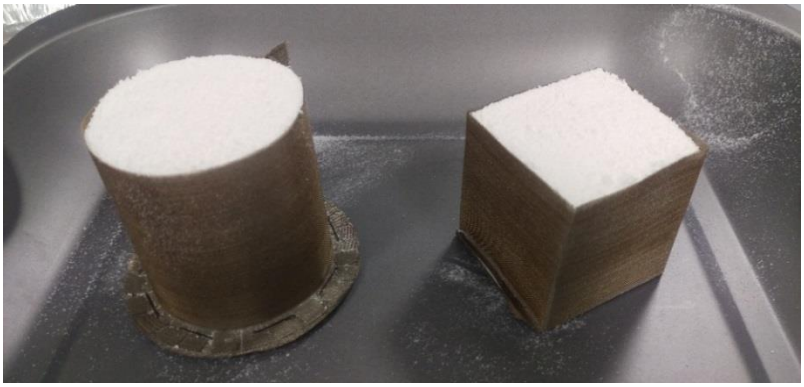

Figure 3-3: Equi-cylindrical basket (cylinder of equal height and diameter) and cubic basket of detergent powder prior to oven heating.

The central temperature profiles of these baskets, as measured by a thermocouple embedded at the core of each basket, can be seen in Figure 3-4 and Figure 3-5. These temperature profiles were used to evaluate the different aspects of the heating of these powders, and how self-heating in particular influences the measured temperature profiles. Figure 3-4 shows the central temperature profiles at a sub-critical ambient temperature of 223°C (496K). Initially, both baskets start at the room temperature, as does the oven. The oven heats up to its set temperature within about 15 minutes, and after some small fluctuations it stabilises. The baskets slowly begin to heat up and after about 25 – 30 minutes, the baskets both reach a temporary plateau. This plateau occurs at approximately 100°C (373K) and is caused by the drying of the powder. This powder is not entirely dry when it is produced, with some residual moisture present in the particles. The energy in this time region is used to evaporate the residual moisture which diffuses out of the powder basket. Once drying has completed, the temperature is again seen to rise, continuing up to the set ambient temperature and increasing further above this ambient temperature due to self-heating.

Although a significant increase in temperature above the ambient temperature occurs at the basket centre in this case, thermal runaway does not occur. At this temperature the heat generation due to the reaction is balanced out by the heat dissipation from the basket, and thus this system is stable. Similar profiles are observed in the two geometries, but by the end the cubic basket has increased to a higher temperature than the equi-cylindrical basket. It is thought that the set ambient temperature of 223°C (496K) is too low to cause thermal runaway of this baskets, but this experiment was stopped too early to be sure.

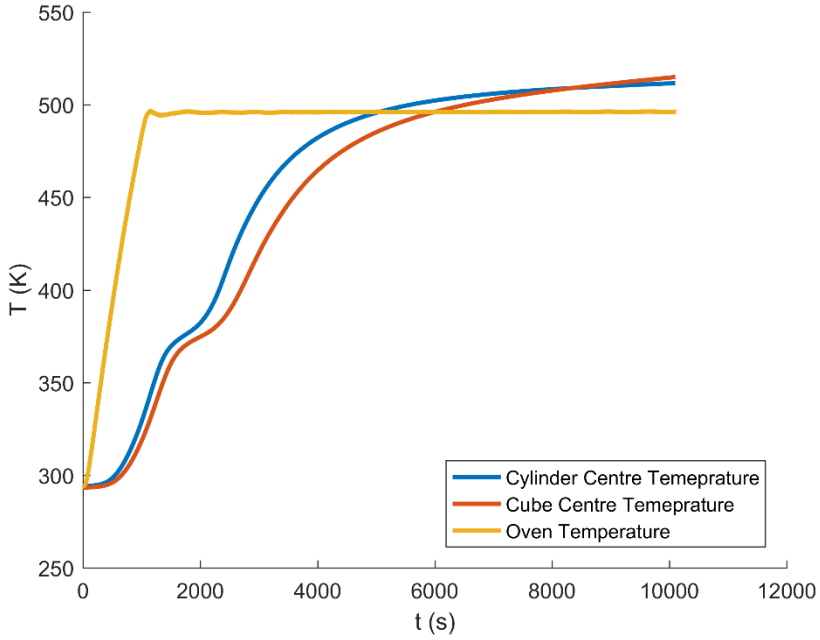

Figure 3-4: Central temperatures of the equi-cylindrical and cubic baskets for a sub-critical ambient temperature of 223°C (496K).

Figure 3-5 shows the central temperature profiles at a super-critical ambient temperature of 239°C (512K). Similar profiles can be observed initially, but as the basket reaches the ambient temperature the core temperature is seen to continue to rise rapidly, rather than slow down as in the previous case. This increase in temperature continues, and even accelerates as these baskets culminate in thermal runaway. The ambient temperature in this case is considerably higher than that of the previous case, with a difference in ambient temperature of 16°C. Although the difference in ambient temperatures between these cases is quite high, only a small difference in ambient temperature is needed for a stable system to become unstable and lead to thermal runaway. When this happens an increase in core temperature of several hundreds of degrees can occur.

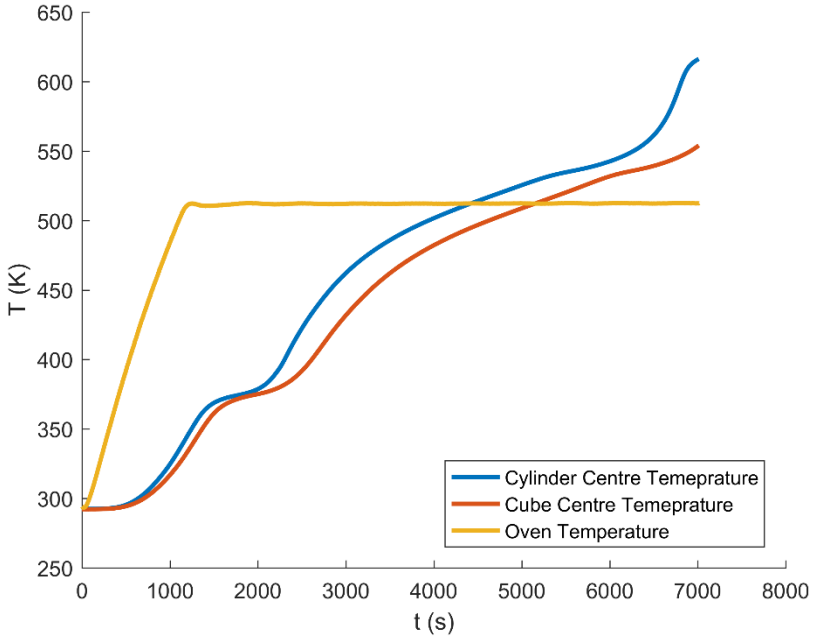

Figure 3-5: Central temperatures of the equi-cylindrical and cubic baskets for a super-critical ambient temperature of 239°C (512K).

Thermal runaway at the basket core is evident by looking at the powder following the experiment. The core of a similar experiment that culminated in thermal runaway can be seen in Figure 3-6. The core of the basket is very clearly burnt and black. From this it is obvious as to why charred particles that can form in spray dryer wall accumulations are a problem. Should these charred particles fall from the wall accumulations and make their way into the finished detergent product, then they would be immediately obvious and detrimental to the product quality. The considerable heat generated when these charred particle are produced is also a significant risk to process safety. This was discussed by Beever (1985) who noted that this self-heating can serve as an ignition source for dust explosions in the spray drying of milk powders.

Figure 3-6: Basket of powder that has undergone thermal runaway at its core. This experiment was stopped before the entire basket was allowed to thermally runaway.

Once it had become evident that the sample in Figure 3-6 had undergone thermal runaway, the oven was switched off and the sample removed to prevent further burning of the powder. If the sample was left to continue burning, then the sample in Figure 3-7 would be found in the oven. The high degree of self-heating at the core eventually leads to an increase in self-heating across the rest of the basket, and a completely burnt sample. Interestingly it can be seen that the entire basket is not black in colour. When broken open, the core is seen to have become a white, brittle, crystalline, hollow sphere. It is not known why this is, but this degree of self-heating is unlikely to be reached in practice, and as such is not explored further.

Figure 3-7: Equi-cylindrical basket of detergent powder that has completely thermally runaway. (left) Before breaking open. (right) After breaking open to show basket core.

3.3.2. Self-Heating in Layer-Like Geometries of Detergent Powder

A tray full of powder was heated to simulate layer-like systems similar to those that may accumulate on the inner walls of the spray drying tower. When a layer of powder is heated it is unclear where thermal runaway will occur, unlike a basket of powder which will typically undergo thermal runaway at the basket centre. This can be seen in Figure 3-8 where localised thermal runaway occurs in one corner of the tray. This localisation may be due to variations in layer thickness across the tray, heterogeneity in powder composition of size across the layer, or variations in temperature in the oven. The thermal runaway is also seen to occur at a central point, and propagate outwards from this in a circular pattern. The rest of the powder, where some degree of self-heating but not thermal runaway has occur, can be seen to be slightly discoloured and “browned”. This “browning” is consistently seen across all basket experiments where thermal runaway does not occur, and is still detrimental to the product quality.

Figure 3-8: Tray of powder used to simulate powder layers, exhibiting thermal runaway in one corner, possible due to heterogeneity or difference in layer thickness.

3.3.3. Initial Cross-Point Temperature Method Experiments

By inserting a second type K thermocouple into the equi-cylindrical and cubic baskets used in the previous section, similar oven heating experiments can be used as part of the cross-point temperature method. This method can then be used to estimate the kinetics of this detergent powder. The first thermocouple was inserted at half height at the centre of each basket, and a second was inserted at approximately 6mm from the first in the same horizontal plane. 6mm was chosen as the spacing as it was thought that this spacing was large to allow for a noticeable difference in recorded temperature

between the thermocouples, but not so large that it impacts heavily on the finite difference approximation used to determine the cross-point temperature. These thermocouples were connect to a Pico Technology USB TC-08 data logger and sampled at a rate of 1 measurement per second. Experiments were run for 9 different ambient temperature between 216°C (489K) and 234°C (507K).

In these initial tests, the thermocouples were simply twisted together. Because of the rigidity of these thermocouples, twisting them together helped to maintain a constant 6mm spacing between them. Although the spacing could be ensured, it was difficult to ensure the placement of these thermocouples, and in particular difficult to ensure that one of these is at the basket geometric centre. The basket setup can be seen in Figure 3-9.

Figure 3-9: Equi-cylindrical and cubic basket setup for the initial cross-point temperature experiments.

The oven controller controls the temperature by measuring the ambient temperature using the thermocouple at position 1 in Figure 3-10, which is integrated with the oven's temperature control system. This thermocouple is shielded by a metallic tube and is at the top of the oven. Experiments indicated that the temperature measured by this thermocouple was lower than that at the level where the baskets are placed by between 3 and 4°C. For this reason an additional thermocouple, denoted by 2, was placed on the level of the two baskets to measure a more representative ambient temperature, as can be seen in Figure 3-10.

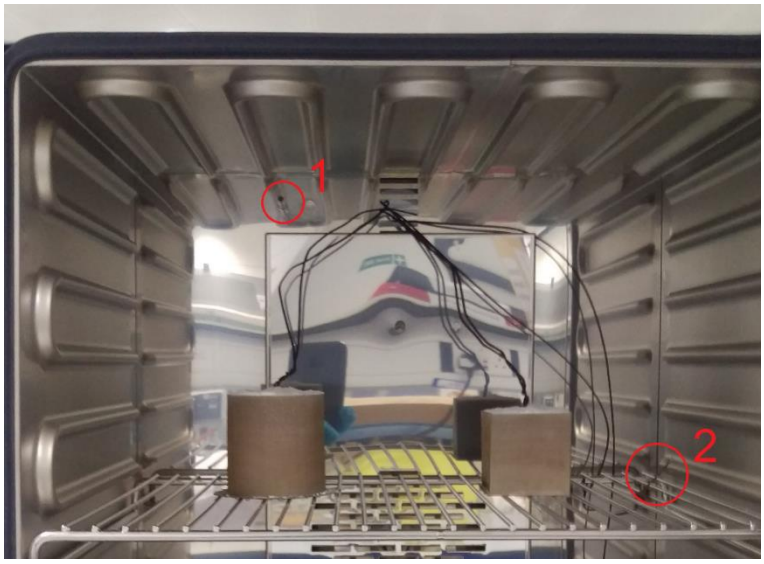

Figure 3-10: Oven setup and additional thermocouples. The thermocouple at 1 is used by the oven temperature controller. The thermocouple at 2 was used to measure a more representative ambient temperature.

The cross-point temperature method is a mean of determining zero-order self-heating reaction kinetics in self-heating materials. The literature related to this was method was discussed Section 2.4.2. It was developed by Chong et *al.* (1996) and is based on the following energy balance for a self-heating body given by equation (2-47).

As a basket of powder is heated in an oven the peripheral regions of the basket reach the oven temperature first. Heat conducts slowly into the centre of the basket and as self-heating begins the core temperature rises above that of the periphery, such that at some time the thermocouple at the basket centre the thermocouple offset from this by 6mm are at the same temperature. At this time the conduction between these two points is assumed to be zero. The temperature at which this occurs is known as the cross-point temperature (CPT) and at this point equation (2-47) reduces to:

$$\ln\left(\frac{dT}{dt}\right)\Big|_{T=T_{CPT}} = \ln\left(\frac{QA}{C_p}\right) - \frac{E}{RT_{CPT}} \tag{3-1}$$

For each set ambient temperature the basket is heated and the temperature is recorded at the centre and offset point for the duration of the experiment. From this, the cross-point temperature, T_{CPT}, and heating rate at basket centre, dT/dt, is noted. This is repeated for a range of ambient temperatures. By plotting T_{CPT} and dT/dt values for each test, the self-heating reaction kinetics can be measured using equation (3-1). The

activation energy, E, and logarithmic term, $\ln(QA/C_P)$, are determined from the slope and intercept respectively.

Firstly the results are discussed for the equi-cylindrical basket. Temperature-time profiles were recorded at the basket centre and at the 6mm offset point and are shown in Figure 3-11. These profiles are for four different ambient temperatures: (a) 218°C (491K), (b) 222°C (495K), (c) 228°C (501K), and (d) 232°C (505K). These experiments were stopped once the central temperature increased above the offset temperature. For each experiment it can be seen that the basket temperature rises from room temperature to some temperature in excess of the oven temperature. In doing so, the baskets can again be seen to undergo drying, as seen before in Figure 3-4 and Figure 3-5. A more significant step is seen on the central thermocouple in each case, but this is simply because drying takes longer at the basket centre.

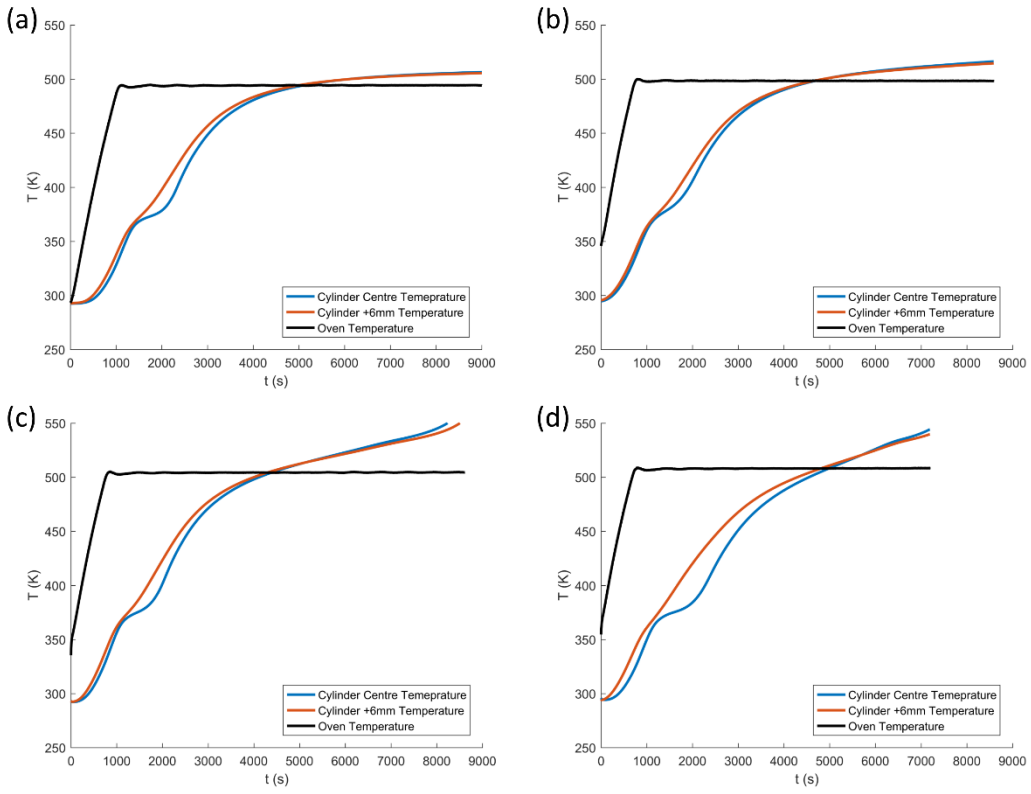

Figure 3-11: Equi-cylindrical basket temperature profiles at ambient temperatures of (a) 218°C (491K), (b) 222°C (495K), (c) 228°C (501K), and (d) 232°C (505K).

It can be seen that the difference between the ambient and the basket central temperature increases with an increase in ambient temperature, indicating an increase in self-heating. It can also be seen that the experiments at 218°C (491K) and 222°C

(495K) do not seem as though they will lead to thermal runaway, while the experiments at 228°C (501K) and 232°C (505K) are already beginning to thermally runaway when they are stopped.

In this case, where two thermocouples are used, the cross-point is based on the following finite difference approximation for the conduction term in equation (2-47):

$$\frac{T_{i-1} - 2T_i + T_{i+1}}{\Delta x^2} = 0 \tag{3-2}$$

If T_i is taken as the thermocouple at the basket centre, and T_{i+1} is taken as the offset thermocouple, then because of symmetry the cross-point reduces to:

$$T_i = T_{i+1} \tag{3-3}$$

To determine the cross-point temperature a MATLAB script was employed. This script firstly determined the instance where the central temperature first exceeds the offset temperature. The temperature at which this occurs is the cross-point temperature. At this point the heating rate dT/dt at the central thermocouple, corresponding to the centre of the finite difference in equation (3-2), was also recorded using the MATLAB script. A degree of smoothing was applied to the dT/dt data to improve the results.

The cross-points at two ambient temperatures are shown in Figure 3-12. It can be seen that in this region there is little difference between the two measured temperatures. This is problematic because any small errors in thermocouple readings or any errors in thermocouple placement could lead to significant differences in the measured cross-point temperature and heating rate. This problem is discussed later in the uncertainty analysis of this method in Section 5.3.2 and in the model simulations of this method in Section 5.4.

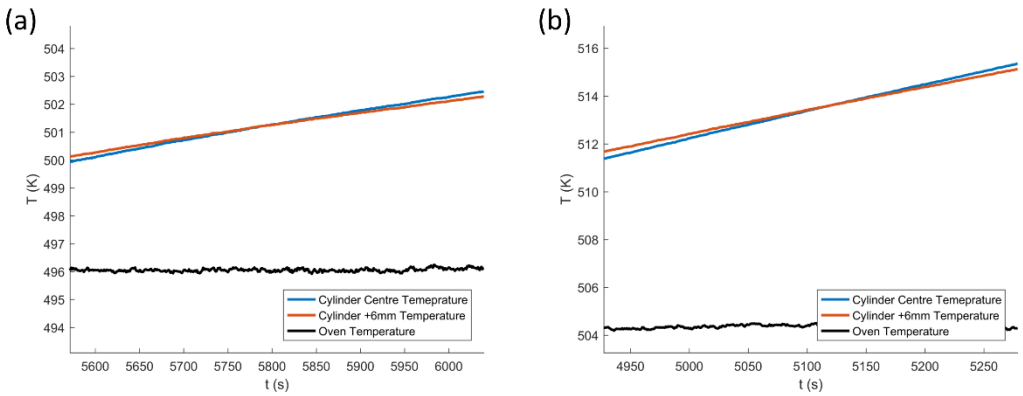

Figure 3-12: Cross-points for equi-cylindrical baskets at ambient temperatures of (a) 220°C (493K) and (b) 228°C (501K).

Plotting the T_{CPT} and dT/dt for each experiment in accordance with (3-1) gives the plot shown in Figure 3-13. Experiments were run for 9 different ambient temperatures between 216°C (489K) and 234°C (507K), with each experiment yielding a data point. A reasonably linear plot is formed with only a couple of outliers. These outliers are probably due to poor thermocouple placement, spacing, or powder variability. These issues can be addressed by developing a new and improved means of accurately inserting the thermocouples into the baskets.

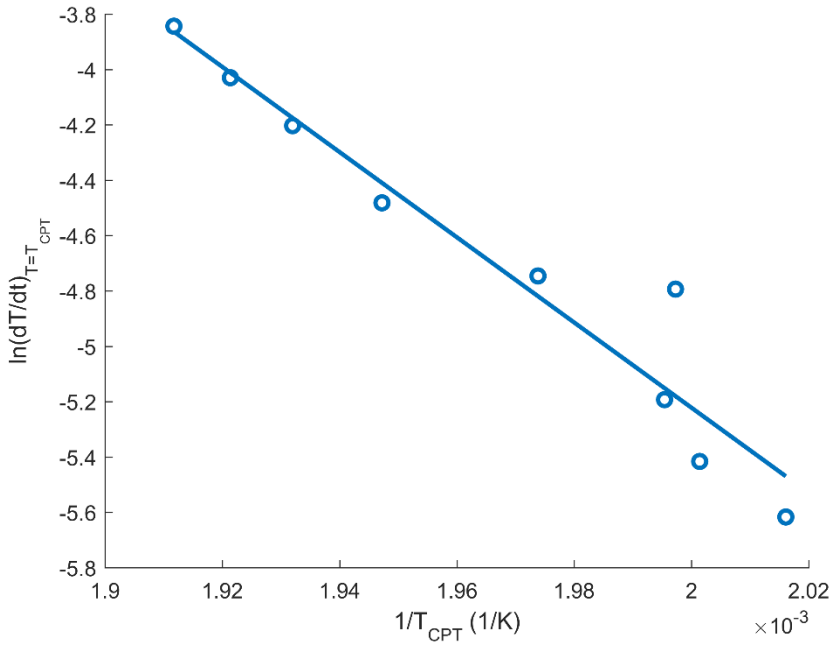

Figure 3-13: Cross-point temperature results for an equi-cylindrical basket of detergent powder run at 9 ambient temperatures between 216°C (487K) and 234°C (507K).

From this plot, the self-heating reaction kinetics can be estimated. Using these data, the activation energy, E, was estimated as 128(±31)x10^3 J mol^{-1}. The error associated with these term shown in brackets are the 95% confidence interval of the linear regression to these data points. The logarithmic term, $\ln(QA/C_P)$, encapsulating the pre-exponential factor, A, the heat of reaction, Q, and the specific heat capacity, C_p, was estimated from the intercept as 25.6(±7.4). It can be seen that the confidence intervals associated with these kinetics are relatively large. Again, this can be improved by developing an improved means of inserting the thermocouples that allows repeatable and accurate insertion at the desired points.

Previous work has not commented on the problems of thermocouple placement, other than noting that a ±1mm error is typically associated with thermocouple placement (Chen & Chong, 1995). In originally using this method, Chong *et al.* (1996) halved the sample after each experiment to verify the positioning of the thermocouples, with experiments repeated if either thermocouple was found to be out of position. This is only possible if the sample is left to burn and form a solid mass. This was not done here because not every temperature tested would culminate in thermal runaway. Additionally such temperature rises can be dangerous and risk damaging the oven and thermocouples. The cross-point method will be explored in much more detail in Section 5.3 of this thesis, but for now this shows that this method may be a suitable means of determining the self-heating kinetics of detergent powders.

The cross-point temperature method was also performed for a cubic basket, although the results were considerably poorer. Temperature profiles recorded during these experiments are shown in Figure 3-14, whilst the results of the cross-point method are shown in Figure 3-15. No linear regression of the data can be seen in the results plot, while from the temperature profiles it is unclear as to why the results are so poor. Again the problem may be due to thermocouple placement. Unlike the cylindrical basket, the cubic basket is not axisymmetric, and as such basket orientation must be considered when inserting the thermocouples. Following these poor results, it was decided that cubic baskets would no longer be used for cross-point temperature experiments, and that differently sized equi-cylindrical baskets would be used instead. Cubic baskets have been previously used in literature, but the majority of baskets used are cylindrical in shape, as discussed in the literature review Section 2.4.2.

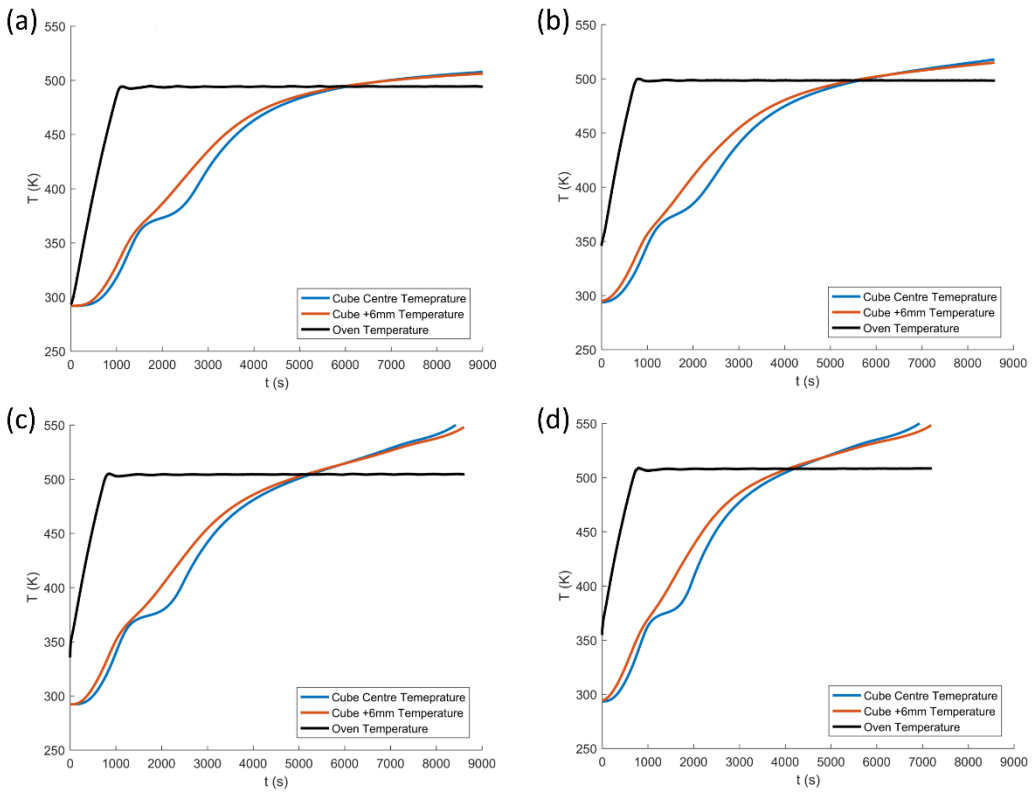

Figure 3-14: Cubic basket temperature profiles at ambient temperatures of (a) 218°C (491K), (b) 222°C (495K), (c) 228°C (501K), and (d) 232°C (505K).

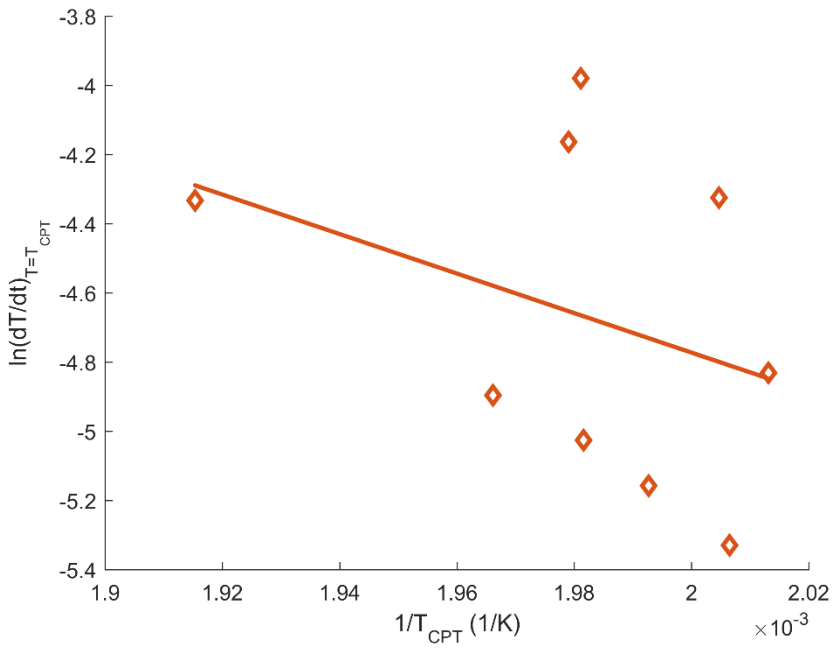

Figure 3-15: Cross-point temperature results for a cubic basket of detergent powder.

3.4. Self-Heating as Evaluated using Differential Scanning Calorimetry (DSC)

It was thought that smaller scale experiments may help to give more indication as to the nature of these reactions. The two techniques used were differential scanning calorimetry (DSC) and thermogravimetric analysis (TGA). In later sections these techniques will also be explored as a means of determining the self-heating reaction kinetics. In this section DSC is applied to help gain an understanding of the heat flow profiles during the self-heating reaction. Tests were run for samples of different size ranges such that the variability of reactivity with particle size could be evaluated. Finally the role that oxygen plays in this reactions was explored.

DSC is a technique in which the difference in supplied heat required to raise the temperature of a sample and a reference material is measured as a function of temperature. In this study the TA Instruments DSC Q2000 was used. This equipment uses an auto-sampler capable of running 50 experiments without human intervention. Open aluminium pans of sample powder were loaded in the auto-sampler along with an empty reference pan. The auto-sampler would load a sample pan and the reference pan into the heating cell. Each pan was placed onto a chromel area thermocouple and the heating cell lid closed. The DSC could then be programmed to heat the cell under different isothermal, ramped, or modulated heating rates, depending on what is being measured.

For this part of the study, the DSC was programmed to hold an isothermal temperature of 50°C (323K) for 5 minutes before increasing in temperature up to 500°C (773K) using a constant ramped heating rate of between 5°C min^{-1} and 10°C min^{-1}. This samples were heated in an atmosphere of air. Open pans containing approximately 8mg of different size ranges of particles were tested such that the difference in reactivity of differently sized particles, which may vary in composition, can be determined. This was done for six size ranges of particles: >150µm and <212µm, >212µm and <300µm, >300µm and <425µm, >425µm and <600µm, >60µm and <710µm, and >710µm and <1.18mm

Figure 3-16 shows the auto-sampler tray with 7 sample pans and two reference pans. These samples have already been heated and they are seen to be discoloured. All samples are seen to be similarly discoloured, which gives an initial indication that

reactivity is similar across all particles sizes. As mentioned previously, a finer grade of inorganic salt was used in this formulation, and that should help to reduce variability in reactivity.

Figure 3-16: DSC sample pans of different size ranges heated from 50°C (323K) to 500°C (773K) and showing discolouration, with particle size increasing from pan 1 to pan 7.

The measured heat flow for samples of 6 different particle sizes can be seen in Figure 3-17. Firstly it can be seen that the heat flow for all particle size ranges are in agreement, and react almost identically. This confirms, at least for this formulation of detergent where a finer grade of inorganic salt was used, that reactivity is consistent across all particle sizes. This is important because if different particle sizes were found to exhibit different reactions, then this would have implications in the basket heating experiments and in modelling these systems. Consistent packing of the baskets would be much more important, and the modelling of particle size distributions would be required.

Looking in more detail at these profiles, it can be seen that there is a small endotherm at approximately 100°C (373K). This endotherm would be consistent with the energy required to evaporate any residual moisture in the detergent particles. Nothing is seen to happen after this until a sharper endotherm at around 540K (267°C). It is unknown as to what causes this endotherm, but it is seen to occur immediately prior to the start of the sharp exothermic reaction peak. This endotherm may be due to a phase change in the material, but it is thought that it does not impact on the reaction. The self-heating reaction is evident as the sharp exothermic peak seen in the heat flow curve. From the

magnitude of this peak it is clear as to why the self-heating reactions that occur in these materials can be problematic. The reaction can be seen to output a significant amount of heat for a relatively small change in temperature.

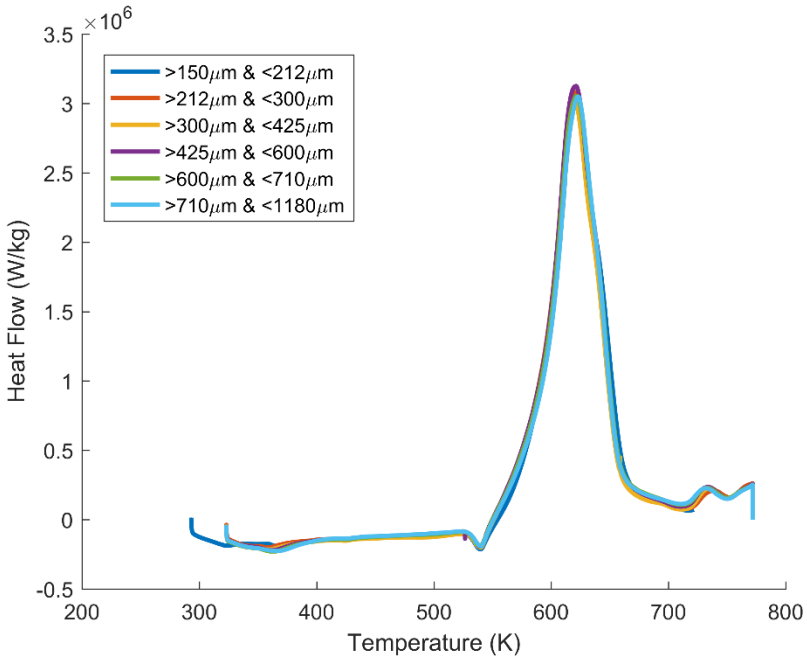

Figure 3-17: DSC heat flow plots for samples of different particle size ranges at a heating rate of 5°C min^{-1} in air.

The temperatures at which the reactions occur in the DSC are significantly higher than the ambient temperatures required to induce thermal runaway in the basket experiments. This is because the detergent powder has a low thermal conductivity, so the rate of heat dissipation is relatively low, and only a small amount of self-heating is required to induce thermal runaway. In the small sample pans used in the DSC, the problem of conduction of heat out of the sample is not as much of an issue.

The previous DSC experiments were run with air as the gas in the heating cell. Following this, a sample was run using nitrogen, under the same program settings, such that the effect this has on the reaction can be observed. The resulting plot can be seen in Figure 3-18. The endotherm due to evaporation of residual moisture seen in Figure 3-17 is also present in this profile. The endotherm that occurs immediately prior to the reaction in Figure 3-17 is also seen here. As was expected though, the reaction itself does not occur in the absence of oxygen. Instead, little activity in seen above temperatures 570K (297°C), when the self-heating reaction would typically start. This confirms that the

reaction is an oxidation reaction, which is worth considering when it comes to modelling this reaction.

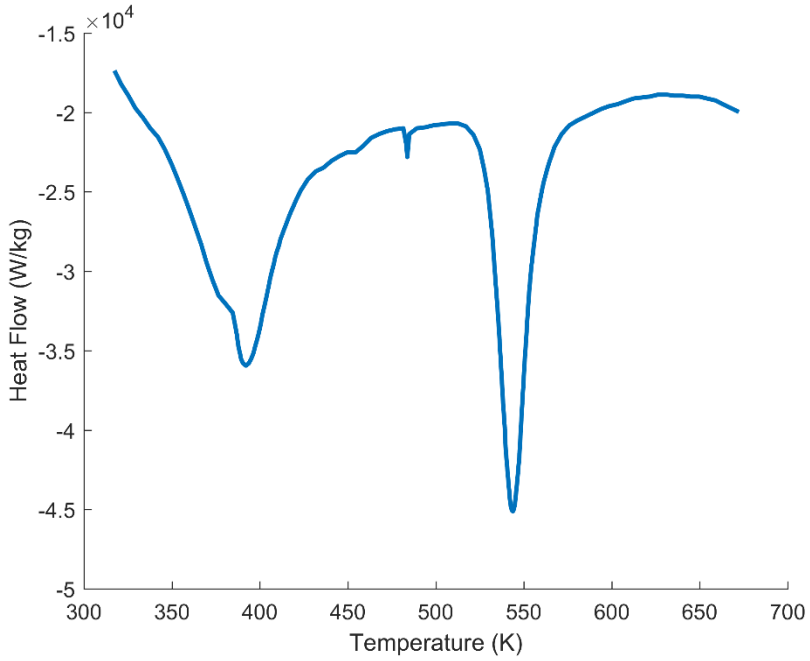

Figure 3-18: DSC heat flow plots at a heating rate of 5°C min^{-1} in nitrogen, which inhibits the self-heating reaction seen to occur in air.

3.5. Self-Heating as Evaluated using Thermogravimetric Analysis (TGA)

The second technique used was thermogravimetric analysis. TGA is a technique whereby the mass change of a sample is measured as a function of temperature, or time if the experiments are run isothermally. In this study the TA Instruments Discovery TGA was used. This equipment uses an auto-sampler capable of running 25 experiments without human intervention. Reusable aluminium pans of sample were loaded in the auto-sampler along with an empty reference pan. The auto-sampler would load a sample pan and the reference pan into the heating cell. Each pan was hung from a mass balance integrated into the heating cell and the chamber closed. This mass balance then weighs the sample as it is heated under different conditions. The TGA can be programmed to heat the cell under different isothermal or ramped heating rates, depending on what is being measured.

For this part of the study, the TGA was programmed to hold an isothermal temperature of 50°C (323K) for 5 minutes before increasing in temperature up to 500°C (773K) using

constant ramped heating rates between 5°C min^{-1} and 20°C min^{-1}. These samples were heated in an atmosphere of air. Pans were run containing approximately 12mg of different size ranges of particles such that the difference in reactivity of differently sized particles can again be determined. Again this was done for six size ranges of particles: >150µm and <212µm, >212µm and <300µm, >300µm and <425µm, >425µm and <600µm, >60µm and <710µm, and >710µm and <1.18mm. Figure 3-19 shows the auto-sampler tray with 6 sample pans.

Figure 3-19: TGA sample pans of different size ranges heated from 50°C (323K) to 500°C (773K) and showing discolouration. Sample 5, 6, 8, and 10 were heated in air, whilst samples 7 and 9 were heated under nitrogen and show a much darker discolouration.

These sample have already been heated and they are all seen to be discoloured. Sample pan 5, 6, 8, and 10 were all heated in air and show a similar discolouration as those heated in air in the DSC, again giving an indication that reactivity is similar across all particles sizes. The samples in pans 7 and 9 were heated in nitrogen rather than air. These samples can be seen to be very discoloured, and almost black in colour. The self-heating reaction was shown not to occur in the absence of oxygen in the DSC. The sample were also cooled before removed from the heating cell, and as such sudden exposure to air while hot was not the cause. This discolouration must be due to a form of non-oxidative degradation.

Figure 3-20 shows the normalised sample mass of samples containing particles of different size ranges as a function of temperature. The shape of these profiles are all in agreement with one another, but there is an offset between the curves. It can be seen that the large particle sizes have a greater normalised mass loss in the initial period. This occurs at around 100°C (373K) and is due to the evaporation of residual moisture in the particles. The larger particles contain more moisture, and as such have a greater mass loss initially as this evaporates. Again the agreement in profile of all these curves confirms, at least for this formulation, that the reactivity is consistent across all particle sizes.

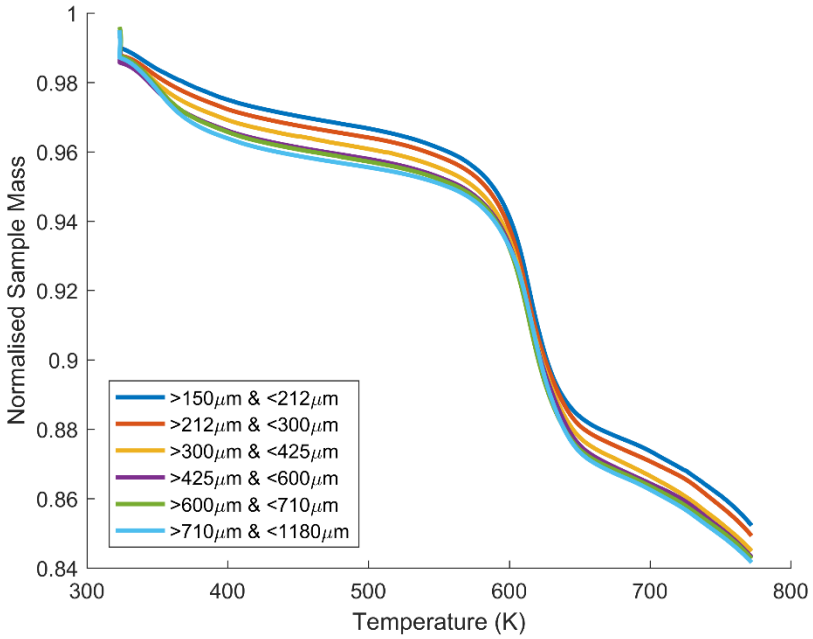

Figure 3-20: TGA normalises sample mass plots for samples of different particle size ranges at a heating rate of 5°C min^{-1} in air.

As shown in Figure 3-19, some of the TGA samples were run in nitrogen to see what affect this has on the reaction. These experiments were run under the same program settings as those under air (isothermal at 50°C (323K) for 5 minutes, then ramped at 5°C min^{-1} up to 500°C (773K)). This normalised mass loss profiles are shown in Figure 3-21 and the presence of air is seen to have a significant effect. Again the reaction is seen not to occur without the presence of oxygen, but instead, at a very high temperature of approximately 700K (427°C), the sample is seen to undergo a rapid and substantial mass loss. It is not known what causes this mass loss, but it is probably what

leads to the dark discolouration seen in these samples. However, these temperatures are well in excess of any temperatures relevant to this study, and as such this unexplained behaviour will not be explored any further.

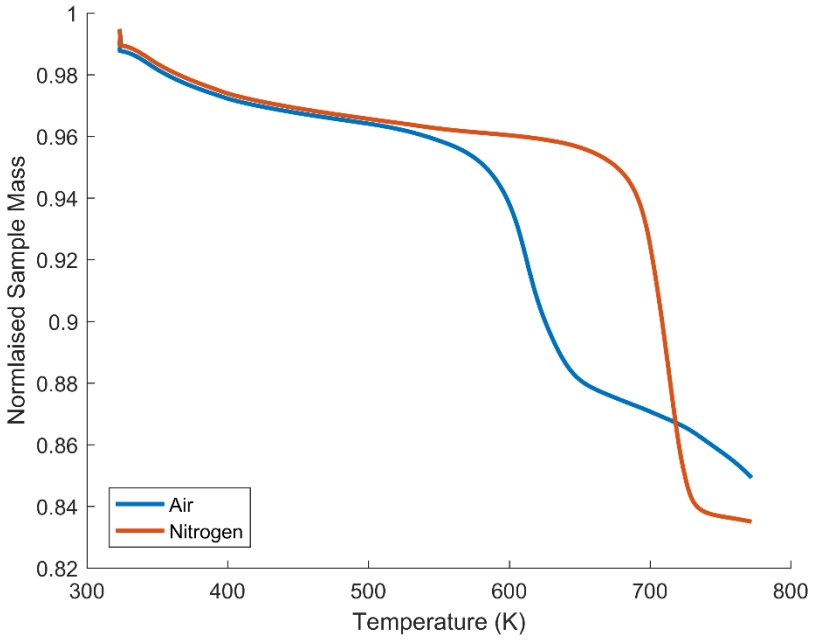

Figure 3-21: TGA normalised sample mass plots for samples of particle size range >212µm and < 300µm at a heating rate of 5°C min^{-1} in air and nitrogen.

3.6. Conclusions

An initial assessment of the self-heating behaviour of a typical detergent powder was conducted. It was shown that this formulation undergoes an exothermic oxidative reaction. For an equi-cylinder of diameter and height 60mm, this formulation is shown to generate a considerable amount of heat for ambient temperatures in excess of 216°C (489K). At some ambient temperature between 222°C (495K) and 228°C (501K), these baskets are seen to go from stable to unstable, with the unstable cases culminating in thermal runaway.

The initial basket heating experiments conducted here have shown the detrimental effects that self-heating can have on detergent formulations. Even if the powder does not completely thermally runaway, localised thermal runaway at the basket core, or at particular points in a layer can be damaging. Even when thermal runaway does not

occur, the discolouration or “browning” seen in the sample may be enough to compromise the quality of the finished product.

The cross-point temperature method experiments conducted here show that this method shows promise as a means of estimating self-heating reaction kinetics. Using this approach and a 60mm equi-cylinder, kinetics of E = 128(±31)x10^3 J mol^{-1} and $\ln(QA/C_P)$ = 25.6(±7.4) were estimated. However, there are a number of issues that need to be addressed before this approach can be effectively used. The main issue is that of thermocouple placement. In these experiments, the thermocouples were simply twisted together and inserted approximately at the basket centre. A new, and improved means of inserting these thermocouples, which ensure repeatable and accurate placement and spacing of the thermocouples is required, and this will be addressed in later sections. Considerably poorer results were achieved when using a cubic basket rather than an equi-cylindrical basket. It is unclear as to why this is, but it is though that the orientation of the thermocouples within the cubic basket was an issue. In subsequent cross-point temperature experiments, only equi-cylindrical baskets are used.

The DSC and TGA experiments have shown, at least for this formulation, that variability in reactivity is not present across different size fractions. This was expected due to the finer grade of sodium sulphate used in this formulation. The DSC heat flow profile showed the large amount of energy produced by the self-heating reaction and why it can be such an issue. The TGA showed a large mass loss corresponding to this reaction. These techniques produced repeatable profiles which are used in later sections to characterise the self-heating reaction using a number of different methods.

Performing these experiments under nitrogen, rather than air, showed that the self-heating reaction is dependent on oxygen. Without oxygen, the reaction was seen not to occur in the DSC and TGA profiles in the temperature range of interest, confirming that the self-heating reaction in this detergent formulation is an oxidative reaction. Although the self-heating reaction did not occur in nitrogen, the TGA profile showed a different, non-oxidative, mass loss at a temperature in excess of the usual reaction onset temperature. It is not known what causes this non-oxidative degradation but it occurs at a temperature outside of the temperature range of interest, and as such is not explored further.

4. Numerical Model of Self-Heating Detergent Powder Systems

4.1. Introduction

This chapter outlines the numerical model that is used throughout this investigation. Three different variants of this model are used depending on what aspects of self-heating are being explored. Typically these are modelled in 2D axisymmetric cylindrical coordinates, although the model equations also allow the coordinate system to be varied. These variants are:

- A model of heat transfer with a zero order self-heating reaction.
- A model of heat transfer with a zero order self-heating reaction and mass transfer of moisture used to model particle drying. Moisture is modelled as liquid moisture in the solid particles as vapour in the voids between the particles.
- An n^{th} order, reactant concentration dependent, self-heating reaction model which can used instead of the zero order reaction model used in the previous two variants.

These models were initially built in MATLAB and solved using custom-built, finite difference based solvers. This was later improved by transferring this model in gPROMS ModelBuilder, an advanced process modelling environment, which allows for easier editing and faster solving of the model, due to the more efficient in-built solvers available. The in-built solvers of gPROMS that were used and the adaptive approach to discretising time were outlined.

This model was validated by comparing the numerical solutions to analytical solutions for a finite slab and infinite cylinder. The validation included the following comparisons:

- 1D numerical model of a finite slab compared with analytical solutions for a finite slab.
- 1D numerical model of an infinite cylinder with varying boundary conditions compared with analytical solutions for an infinite cylinder.

- 2D numerical model of a finite cylinder, using a high axial length to radius ratio such that the model is analogous to an infinite cylinder, with varying boundary conditions compared with analytical solutions for an infinite cylinder.

The developed 2D model was also used to refute the shape factor approximation used by Chen (2001), and Chong and Chen (1999). They used this shape factor to approximate heat transfer in an equi-cylinder using 1D equations, but this approach is problematic. A comparison is made of the 1D model using this shape factor approximation and the 2D axisymmetric model used to discuss the problems of this approximation.

The model boundary conditions require the convective heat transfer coefficient to the oven to be known. The effective heat transfer coefficient was measured using the transient temperature measurement method, used by both Sato *et al.* (1987) and Carson *et al.* (2006). From this the convective heat transfer coefficient could be correlated, and applied in the boundary conditions of this model.

4.2. Modelling Heat and Mass Transfer in Self-Heating Systems

4.2.1. Governing Equations for Heat Transfer in Self-Heating Systems

These self-heating problems were modelled using a set of 2D-axisymmetric partial differential equations in the radial direction, r, and axial direction, z. These equations describe the heat transfer and mass transport in a cylindrical basket of powder. Within the powder, heat transfer is by conduction, while at the outer boundary the heat transfer to the ambient is by convection. A number of assumptions are applied to this model, these are:

- Reactant consumption (i.e. oxygen and solid reactants) is assumed negligible, such that the reaction is modelled as zeroth order.
- No convection occurs within the powder mass.
- Newton's Law of Cooling is applied at the outer boundary.
- The thermal conductivity and specific heat capacity are assumed constant.

The transient energy conservation equation for a generic geometry, and in a generic coordinate system, is given by:

$$\rho C_p \frac{\partial T}{\partial t} = k\nabla^2 \mathrm{T} + \rho Q A e^{\frac{-E}{RT}} \quad (4\text{-}1)$$

In this energy balance the left hand term denotes the local rate of enthalpy change in the solid, the first right hand side term denotes the conductive heat transfer in the solid, and the final term denotes the heat generation of a single zero-order exothermic reaction, or several simultaneous zero-order reactions assumed to be one overall reaction.

In this model, the Laplacian conduction term is replaced with 2D cylindrical coordinates modelling heat transfer in a basket of radius R (m) and half-height Z (m), giving:

$$\rho C_p \frac{\partial T}{\partial t} = k\left(\frac{\partial^2 T}{\partial r^2} + \frac{1}{r}\frac{\partial T}{\partial r} + \frac{\partial^2 T}{\partial z^2}\right) + \rho Q A e^{\frac{-E}{RT}} \quad (4\text{-}2)$$

Here, ρ (kg m^{-3}) is the bulk density of the powder, C_p (J kg^{-1} K^{-1}) is the specific heat capacity, k (W m^{-1} K^{-1}) is the thermal conductivity, Q (J kg^{-1}) is the heat of reaction, A (s^{-1}) is the pre-exponential factor of the zero-order Arrhenius reaction, E (J mol^{-1}) is the activation energy, R (J mol^{-1} K^{-1}) the universal gas constant, t (s) the time, and T (K) the temperature.

In previous work, Chen (2001), and Chong and Chen (1999) used a similar equation but with a shape factor, j, to approximate 2D heat transfer using a 1D model. In doing so, the conduction term is replaced with:

$$k\nabla^2 T = k\left(\frac{\partial^2 T}{\partial x^2} + \frac{j}{x}\frac{\partial T}{\partial x}\right) \quad (4\text{-}3)$$

Where the shape factor and is equal to 0 for a finite slab, 1 for an infinite cylinder, 2 for a sphere, 3.28 for a cube, or 2.728 for an equi-cylinder. However, this shape factor approximation leads to incorrect results when modelling heat transfer in equi-cylindrical geometries. The refuting of this shape factor for equi-cylindrical geometries is shown in Section 4.4.

This model was validated against analytical solutions for heat transfer in an infinite cylinder documented by Carslaw and Jaeger (1959). This was done by using a large ratio of axial to radial length such that this model can be assumed to be for an infinite cylinder. The heat of reaction and drying terms were removed for this validation. The model

solution agreed with the analytical solution for the discretisation in space and time used. This validation will be discussed in Section 4.3.

Symmetrical boundary conditions apply along the central axes of the cylinder in both the radial and axial directions, and these are expressed as:

$$\left.\frac{dT}{dr}\right|_{r=0} = 0, \qquad \left.\frac{dT}{dz}\right|_{z=0} = 0. \tag{4-4}$$

At the exposed boundaries Newton's Law of Cooling is applied, whereby heat transfer is dependent on the effective heat transfer coefficient, h (W m^{-2} K^{-1}), and the ambient temperature, T_∞ (K), such that:

$$-k\left.\frac{dT}{dr}\right|_{r=R} = h(T|_{r=R} - T_\infty), \qquad -k\left.\frac{dT}{dz}\right|_{z=Z} = h(T|_{z=\mathrm{Z}} - T_\infty). \tag{4-5}$$

For simplicity, it is assumed that there is no thermal boundary layer at the cylinder boundary, such that the temperature immediately adjacent to the cylinder edge is equal to the ambient temperature. The heat transfer coefficient for the oven was determined by using the transient temperature measurement method used by Carson *et al.* (2006). This is discussed in detail in Section 4.5.

4.2.2. Inclusion of Powder Drying Equations

A variation of this model was developed which includes the equations required to model the drying of the powder. This model is largely based on that of Chen (2001), and Chong and Chen (1999). The moisture movement within the system involves the evaporation of moisture from the particles to the void in the powder mass. This moisture is then diffused through the voids, out towards the outer boundary of the powder domain, where it is carried into the ambient air by means of convection. A number of additional assumptions are applied to this model, these are:

- The solid particle, moisture, and gas in the voids are assumed to be at the same local temperature.

- Negligible moisture transfer occurs via solid contacts, and the moisture transfer from the inner powder mass to the outer boundary is assumed to occur by diffusion of water vapour.
- The vapour diffusion coefficient is assumed to be constant.

The transient energy conservation equation in 2D cylindrical coordinates, modelling heat transfer in a basket of radius R (m) and height Z (m), and with the inclusion of drying is given by:

$$\rho C_p \frac{\partial T}{\partial t} = k\left(\frac{\partial^2 T}{\partial r^2} + \frac{1}{r}\frac{\partial T}{\partial r} + \frac{\partial^2 T}{\partial z^2}\right) + \rho Q A e^{\frac{-E}{RT}} + \rho_{sd} H_v \frac{\partial X}{\partial t} \qquad (4\text{-}6)$$

Here, ρ_{sd} (kg m^{-3}) is the solid density of the powder particles, H_v (J kg^{-1}) is the heat of vaporisation of the liquid water in the particles, and X (kg kg^{-1}) is the moisture content of the particles on a dry basis. The final term denotes the heat of wetting or drying of the powder.

The moisture in the system is modelled in two states, firstly as liquid moisture in the particles and secondly as vapour in the voids between the particles. The first of these is described by the following:

$$-\rho_{sd}\frac{\partial X}{\partial t} = h_{m,in} A_p n_p \left(Y_{s,in} - Y\right) \qquad (4\text{-}7)$$

Where $h_{m,in}$ is the effective mass transfer coefficient between the particles and the gas in the voids (m s^{-1}), A_p is the surface area of one particle (m^2), n_p is the number of particles per unit volume (m^{-3}), $Y_{s,in}$ is the vapour concentration at the surface of the particle (kg m^{-3}), and Y is the vapour concentration in the voids (kg m^{-3}).

To solve the above equation, the vapour concentration at the particle surface, $Y_{s,in}$ (kg m^{-3}), is required. This is achieved by first defining the surface relative humidity, RH_s:

$$RH_s = \frac{p_{s,in}}{p_{sat}} \approx \frac{Y_{s,in}}{Y_{sat}} \qquad (4\text{-}8)$$

The surface relative humidity, RH_s, is defined as the ratio of the internal partial pressure, $p_{s,in}$ (Pa), to the saturated partial pressure, p_{sat} (Pa). This can be approximated by the ratio of vapour concentrations, where Y_{sat} is the saturated vapour concentration (kg m^{-3}). Y_{sat} was determined using the following correlation used by Putranto *et al.* (2011):

$$Y_{sat} = 4.844 \times 10^{-9}(T-273)^4 - 1.4807 \times 10^{-7}(T-273)^3 + 2.6572 \times 10^{-5}(T-273)^2 - 4.8613 \times 10^{-5}(T-273) + 8.342 \times 10^{-3} \quad (4\text{-}9)$$

Using this expression, and rearranging equation (4-8), the mass conservation equation (2-75) can now be expressed as:

$$-\rho_{sd}\frac{\partial X}{\partial t} = h_{m,in}A_p n_p(RH_s \mathrm{Y_{sat}} - Y) \quad (4\text{-}10)$$

Now the surface relative humidity needs to be calculated. This was done by applying the Reaction Engineering Approach (REA), proposed by Chen (1998), which is a means of modelling drying kinetics by applying chemical reaction engineering principles. This approach assumes that evaporation is a first order activation process with an energy barrier to overcome, taking the form of an activation energy. The dynamic process of drying and the equilibrium state of drying are then unified in this approach. The REA is a simple and robust approach capable of describing drying behaviour with minimal experiments required to yield the necessary model parameters (Putranto, et al., 2011). The relationship between the REA and other drying theories, such as the characteristic drying curves model and the distributed-parameter models, are unclear, but for this self-heating model where drying is not of critical importance this approach is sufficient. The following Arrhenius expression is used to describe the relative humidity at the particle surface:

$$RH_s = e^{-\frac{\Delta E_v}{RT}} \quad (4\text{-}11)$$

Where ΔE_v (J mol^{-1}) is the additional activation energy to that of pure water evaporation, which accounts for the added difficulty in removing water at low water contents. When water covers the entire surface of the solid this correction term reduces to zero, with relative humidity increasing to unity and drying modelled as evaporation from a pure water surface. This value is determined through a purely empirical fitting to sorption isotherms.

It was found in evaluating the drying model parameters used, in Section 5.7.3, that the value of the internal mass transfer coefficient, $h_{m,in}$, and the vapour diffusion coefficient, D_{vap}, have as much of an influence on the predicted behaviour as the correlation of ΔE_v used. As such, only a single experiment was used to determine the

correlation for ΔE_v. Using an approach based on that of Chen (1997) this REA model was fitted to sorption isotherm data at a temperature of 25°C (298K) determined using dynamic vapour sorption (DVS) equipment. The correction factor was assumed to take the form:

$$\Delta E_v = a \cdot \exp[b(X^c)] \tag{4-12}$$

The change in mass relative to a completely dried sample was plotted against $\ln(RH) \cdot RT$ to which this equation (4-13) was fitted using the MATLAB curve fitting toolbox. This fitting can be seen in Figure 4-1, and from this the correlation for the correction factor was approximated as:

$$\Delta E_v = 4.68 \times 10^6 \exp[-9.43(X^{0.0613})] \tag{4-13}$$

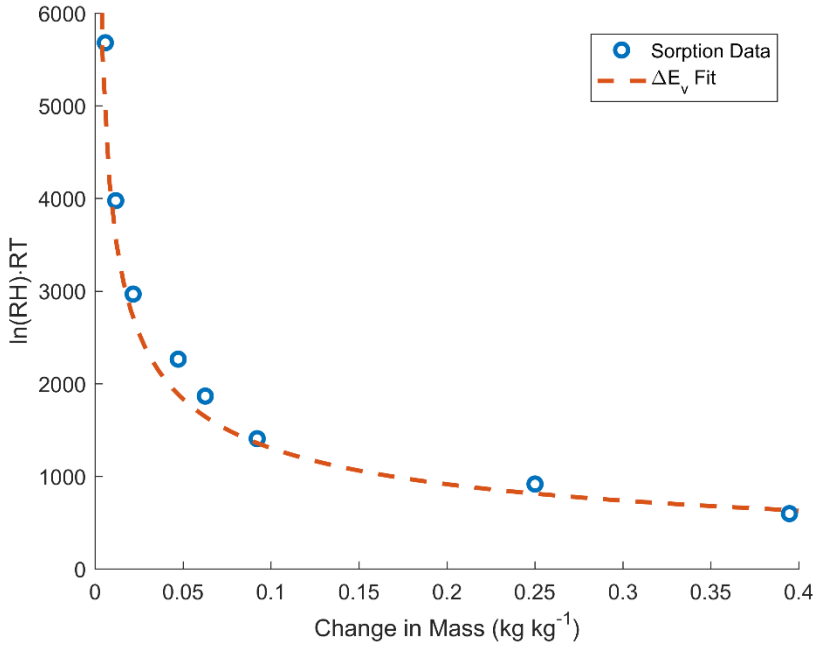

Figure 4-1: Correction factor, ΔE_v, fitted to DVS sorption data for a sample of detergent heated at 25°C under different ambient relative humidifies, RH.

Chen (2001), and Chong and Chen (1999) used equation (2-85) to determine the heat of wetting or drying, H_v, in their models which essentially corrected the heat of vaporisation of water with a term that was a function of the surface relative humidity and temperature. The value of H_v changed very little and in this model the value of H_v was assumed constant and taken as the heat of vaporisation of water, with a value of 2257x10^3 J kg^{-1}.

The transport of water vapour through the voids in the basket of particles is described by the following equation in 2D cylindrical coordinates:

$$\frac{\partial Y}{\partial t} = \varepsilon D_{vap}\left(\frac{\partial^2 Y}{\partial r^2} + \frac{1}{r}\frac{\partial Y}{\partial r} + \frac{\partial^2 Y}{\partial z^2}\right) - \rho_{sd}\frac{\partial X}{\partial t} \tag{4-14}$$

Y is the water vapour concentration (kg m^{-3}), ε is the void fraction or porosity, and D_{vap} is the diffusion coefficient of vapour through the powder voids (m^2 s^{-1}). The last term in this equation represents the addition/removal of vapour to the voids due to the rate of decrease/increase of moisture content in the solid particles.

Similar to the temperature boundary conditions, symmetrical boundary conditions for the vapour concentration are applied along the central axes of the cylinder. In the radial direction this is expressed as:

$$\left.\frac{dY}{dr}\right|_{r=0} = 0 \tag{4-15}$$

A similar gradient applies in the axial direction apply at $z = 0$.

$$\left.\frac{dY}{dz}\right|_{z=0} = 0 \tag{4-16}$$

At the exposed boundaries heat transfer was defined using the effective heat transfer coefficient, h. Here the mass transfer is dependent on the mass transfer coefficient, h_m (m s^{-1}), such that in the radial direction:

$$-\varepsilon D_{vap}\left.\frac{dY}{dr}\right|_{r=R} = h_m\left(\left.\frac{Y}{\varepsilon}\right|_{r=R} - Y_\infty\right). \tag{4-17}$$

Where Y_∞ is the ambient vapour concentration (kg m^{-3}). Again, a similar gradient applies in the axial direction at $z = Z$.

$$-\varepsilon D_{vap}\left.\frac{dY}{dz}\right|_{z=Z} = h_m\left(\left.\frac{Y}{\varepsilon}\right|_{z=Z} - Y_\infty\right). \tag{4-18}$$

The drying model has been included to allow this model to be more easily compared with experimental results. It was seen that the drying had very little impact on the predicted self-heating behaviour and critical ambient temperatures. As such, little work has been done in characterising the drying of the detergent powders in this investigation. This variant of the model will only be used to qualitatively evaluate the drying behaviour.

4.2.3. Modelling of n^{th} Order Reactions

For the most part, a zero-order reaction model was used in this investigation, using reaction kinetics as measured using the basket heating methods. In Section 5.6 n^{th} order kinetics are estimated using the DTG curve fitting approach. This kinetics are used in the model, but in doing so the heat generation term of the energy balance in equation (4-1) needs to be adjusted accordingly. This term needs to be adjusted to account for the reaction's dependency on the concentration of reactive component, c_{rc} (kg m^{-3}), its initial concentration, $c_{rc,0}$ (kg m^{-3}), and the reaction order, n. As the reactive component depletes, the reaction rate decreases, until all the reactive component has depleted and the reaction ceases. The approach used by Muramatsu *et al.* (1979) was applied in which the following expression is used:

$$\frac{\partial c_{rc}}{\partial t} = -c_{rc,0}\left(\frac{c_{rc}}{c_{rc,0}}\right)^{n} Ae^{-\frac{E}{RT}} \tag{4-19}$$

In this case, the depletion of reactive component is captured as a ratio to the initial concertation of the reactive component. In this model, the value of n influences the "strength" of the reaction with the depletion of reactive component. This is because $\left(\frac{c_{rc}}{c_{rc,0}}\right)^{n}$ will never exceed 1. Using a ratio of the concentration to the initial concentration means that the value of n in this model does not impact on the units of the pre-exponential factor, A. However, this model has issues as discussed in Section 2.5.3.

Similar to equation (4-19), the heat generation term in equation (4-2) is adjusted to account for the reaction's dependency on the concentration of reactive component. This equation now becomes:

$$\rho C_p \frac{\partial T}{\partial t} = k\left(\frac{\partial^2 T}{\partial r^2} + \frac{1}{r}\frac{\partial T}{\partial r} + \frac{\partial^2 T}{\partial z^2}\right) + c_{rc,0}\left(\frac{c_{rc}}{c_{rc,0}}\right)^{n} QAe^{\frac{-E}{RT}} \tag{4-20}$$

4.2.4. Solving the Model using gPROMS ModelBuilder

Originally this model was solved using custom built solvers in MATLAB. The 1D variant of the model was solved using a Fully Implicit Backwards finite difference scheme, while

the 2D variant was solved using an Alternating Difference Implicit (ADI) finite difference scheme. These methods are outlined in Section 2.5.2. The custom built, non-adaptive time, solver used was found to give accurate results which were successfully validated against analytical solutions. However, these solvers could be rather slow and difficult to update given how they were coded in MATLAB.

As this investigation progressed, it was thought that transferring the models to gPROMS ModelBuilder would be beneficial. gPROMS ModelBuilder is an advanced process modelling environment which allows for easier building and solving of models due to its intuitive GUI, in-built solvers, and adaptive approach to the discretisation of time. It also meant that some of the other useful features of gPROMS ModelBuilder could be used. These include:

- Simple GUI with separate scripts for the model and the model parameters. This allows the same model to be easily updated and allows the model to be easily run under different conditions or with different parameter values.
- Improved run time and accuracy. The in-built solvers are much more optimised than the custom built solvers built in MATLAB. An adaptive discretization of time is used that helps to improve on the time required to run the model.
- Easy input of experimental input. Experimentally measured values and control variables can be input into the software for any number of experiments. These can be used to simulate the experiments, or can be used in parameter estimation or the design of experiments.

Having transferred the model to gPROMS ModelBuilder, its in-built solvers were used to solve this set of 2D model equations. The model and process scripts are shown in Appendix B. Most simulations were run for an equi-cylindrical basket of radius and half-height 30mm. The basket radius and half height were each discretized into 31 points. This number of discretised points was chosen so that grid points were spaced by 1mm when modelling an equi-cylindrical basket of diameter 60mm, making simulations of the basket heating methods easier. Having solved this model with discretisations of 61 and 121 points, it was found that 31 points was sufficient to achieve grid independence.

gPROMS ModelBuilder uses a number of different solvers. The default solvers were found to work well for this model. The solvers are separated based on the type of equations they are used to solve. The solvers used for this model were:

Linear Algebraic Equations

- MA48 Solver
    - This solver uses direct LU-factorisation algorithms designed for large, sparse, asymmetric systems of linear equations.

Non-Linear Algebraic Equations

- BDNLSOL Solver
    - This stands for "Block Decomposition Non-Linear Solver". It is a general solver for solving sets of non-linear equations rearranged into block triangular form.

Differential Algebraic Equations

- DASOLV Solver
    - This is a solver that uses variable time step and variable order Backward Differentiation Formulae. For most problems this solver is efficient, but it struggles with highly oscillatory problems or problems with frequent discontinuities.

Both of the Differential Algebraic Equation solvers use a variable time step, and adjust this time step so that the following criterion is satisfied:

$$\sqrt{\frac{1}{n_d}\sum_{i=1}^{n_d}\left(\frac{\epsilon_i}{a + r|x_i|}\right)^2} \leq 1 \qquad (4\text{-}21)$$

Where n_d is the number of differential variables in the problem, ϵ_i is the solver's estimate of the local error in the i^{th} differential variable, x_i is the current value of the i^{th} differential variable, a is the absolute error tolerance, and r is the relative error tolerance. This means that error, ϵ_i, in the variable x_i is not allowed to exceed $a + r|x_i|$ over a single time step, where the default value for a and r of $1\text{x}10^{-5}$ was used.

4.3. Code Validation of Numerical Model against Analytical Solutions

4.3.1. Finite Slab

There exist analytical solutions to the transient temperature profiles for simple geometries such as finite slabs, infinite cylinders, and spheres. A finite solid slab can be defined as occupying the space between $y = -b$ to y$= +b$, and initially being at a temperature of T_0. For this solution, at the time $t = 0$ the surfaces of the slab at $x = \pm b$ are suddenly raised to some temperature T_1 and maintained at this temperature from this time onwards. The solution to this case is outlined by Bird *et al.* (2007) and firstly requires a number of dimensionless variables to be defined.

Dimensionless temperature:

$$\Theta = \frac{T_1 - T}{T_1 - T_0} \tag{4-22}$$

Dimensionless coordinate:

$$\eta = \frac{y}{b} \tag{4-23}$$

Dimensionless time:

$$\tau = \frac{\alpha_T t}{b^2} \tag{4-24}$$

α_T is the thermal diffusivity, equal to $k/\rho C_p$, of the body in question. Using these dimensionless variables, the differential equation outlining the heat transfer in this system can be expressed as:

$$\frac{\partial \Theta}{\partial \tau} = \frac{\partial^2 \Theta}{\partial \eta^2} \tag{4-25}$$

Initially the slab is at temperature T_0, such that the initial conditions can be expressed as:

$$\Theta = 1 \qquad at\ \tau = 0 \tag{4-26}$$

At time $t = 0$ the slab faces at $y = \pm b$ are raised to temperature T_1 such that the boundary conditions can be defined as:

$$\Theta = 0 \qquad at\ \eta = \pm 1 \tag{4-27}$$

The solution to this problem is detailed in Appendix C. From this solution, it was found that the temperature profile in a finite slab under the outlined conditions can be expressed as:

$$\Theta = 2\sum_{n=0}^{\infty} \frac{(-1)^n}{\left(n+\frac{1}{2}\right)\pi} \exp\left[-\left(n+\frac{1}{2}\right)^2 \pi^2 \tau\right] \cos\left(n+\frac{1}{2}\right)\pi\eta \tag{4-28}$$

Using the original variables, this is expressed as:

$$\frac{T_1 - T}{T_1 - T_0} = 2\sum_{n=0}^{\infty} \frac{(-1)^n}{\left(n+\frac{1}{2}\right)\pi} \exp\left[-\left(n+\frac{1}{2}\right)^2 \pi^2 \frac{\alpha_T t}{b^2}\right] \cos\left(n+\frac{1}{2}\right)\frac{\pi y}{b} \tag{4-29}$$

The results of the numerical model for heat transfer, with no heat generation, in a finite slab were compared with analytical solutions using equation (C-22). These solutions are seen to agree and this serves to validate this 1D finite slab model.

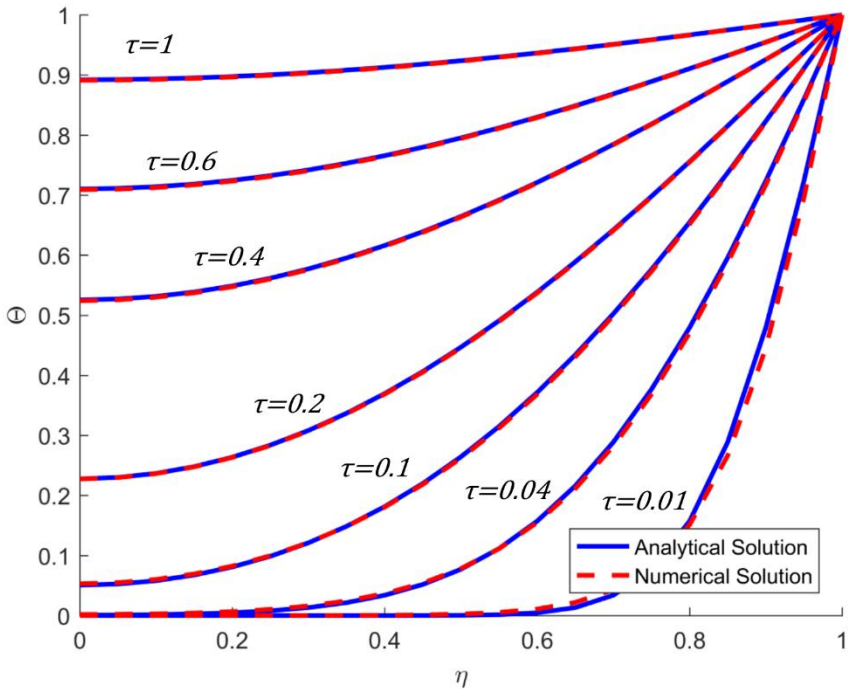

Figure 4-2: Overlay of analytical and numerical solutions ($Bi = \infty$) for transient temperature profiles in a finite slab.

4.3.2. Infinite Cylinder

Similar to the case of the finite slab above, there exist analytical solutions for the temperature profile of an infinite cylinder for some special cases. The solution for the geometry is more complex than the finite slab case outlined above and has been explored by Carslaw and Jaeger (1959). Initially the temperature of the cylinder is a function of the radius and given by $T = f(r)$. The surface, at $r = b$ is at a constant temperature, which may be taken as zero. Based on this, the equations for the temperature of the cylinder are:

$$\frac{\partial T}{\partial t} = \alpha\left(\frac{\partial^2 T}{\partial r^2} + \frac{1}{r}\frac{\partial T}{\partial r}\right) \tag{4-30}$$

$$T = 0 \qquad at\ r = b \tag{4-31}$$

$$T = f(r) \qquad at\ t = 0 \tag{4-32}$$

The solution to this problem is detailed in Appendix D. If the case is similar to that of the slab discussed previously where the initial temperature is zero and the surface is maintained at some higher temperature T_1 for $t > 0$, then the dimensionless temperature can be expressed as:

$$\Theta = 1 - 2\sum_{n=0}^{\infty} e^{-\gamma_n^2 \tau}\frac{J_0(\gamma_n \eta)}{\gamma_n J_1(\gamma_n)} \tag{4-33}$$

Where $J_0(x)$ is the Bessel function of order zero of the first kind, $J_1(x)$ is the Bessel function of order one of the first kind, and $\pm\gamma_n$, $n = 1,2, \ldots$, are the roots of:

$$J_0(\gamma) = 0 \tag{4-34}$$

The results of the numerical model for heat transfer, with no heat generation, in an infinite cylinder were compared with analytical solutions using equation (D-14). These solutions are seen to completely agree and this serves to validate this 1D infinite cylinder model.

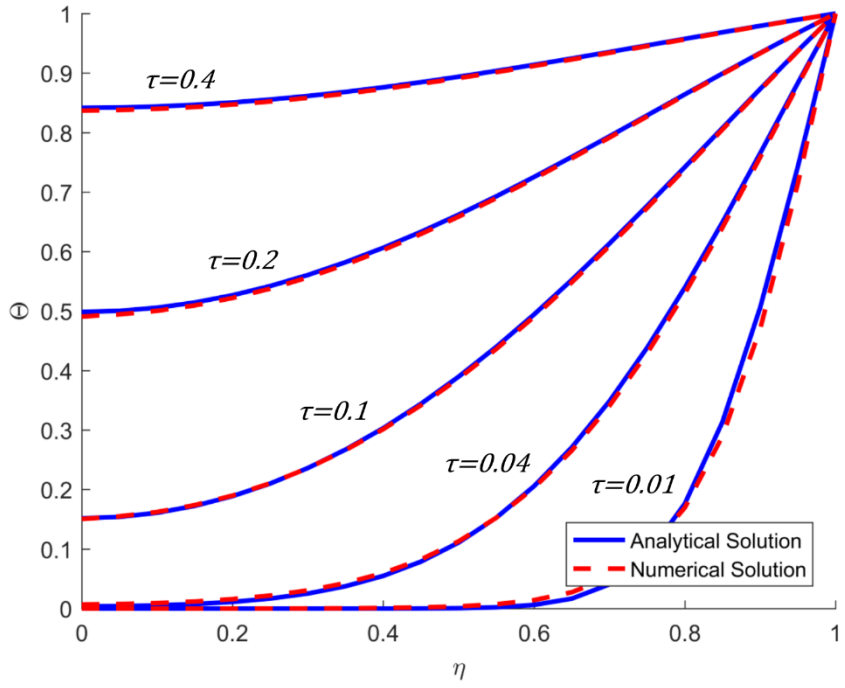

Figure 4-3: Overlay of analytical ($n = 100$) and numerical solutions ($Bi = \infty$) for transient temperature profiles in an infinite cylinder.

The above solutions are for an infinite Biot number. The Biot number, Bi, is the dimensionless ratio of internal to external heat transfer resistance, and is equal to hL/k, where L is some characteristic length. The model solutions for varying values of the Biot number were compared with the analytical solutions. This was done for value of Bi of 2, 10, 20, and 200, and can be seen in Figure 4-4. As expected, it can be seen that the numerical solution for a low Biot number of 2 are very different to the analytical solutions, where an infinite Biot number is used.

For the analytical solutions, the dimensionless temperature, Θ, at all dimensionless times, τ, is equal to 1 at a dimensionless coordinate, η, equal to 1, corresponding to the slab surface. As the time progresses, all points increase in temperature to the steady-state temperature. For the low finite Biot number cases, as expected, the slab surface is seen not to be at a constant temperature and instead increases in temperature as time progresses. As the Biot number increases, and heat transfer at the boundary becomes more pronounced, the numerical model solutions are seen to approach the analytical solutions, with a Biot number of 200 providing sufficient agreement.

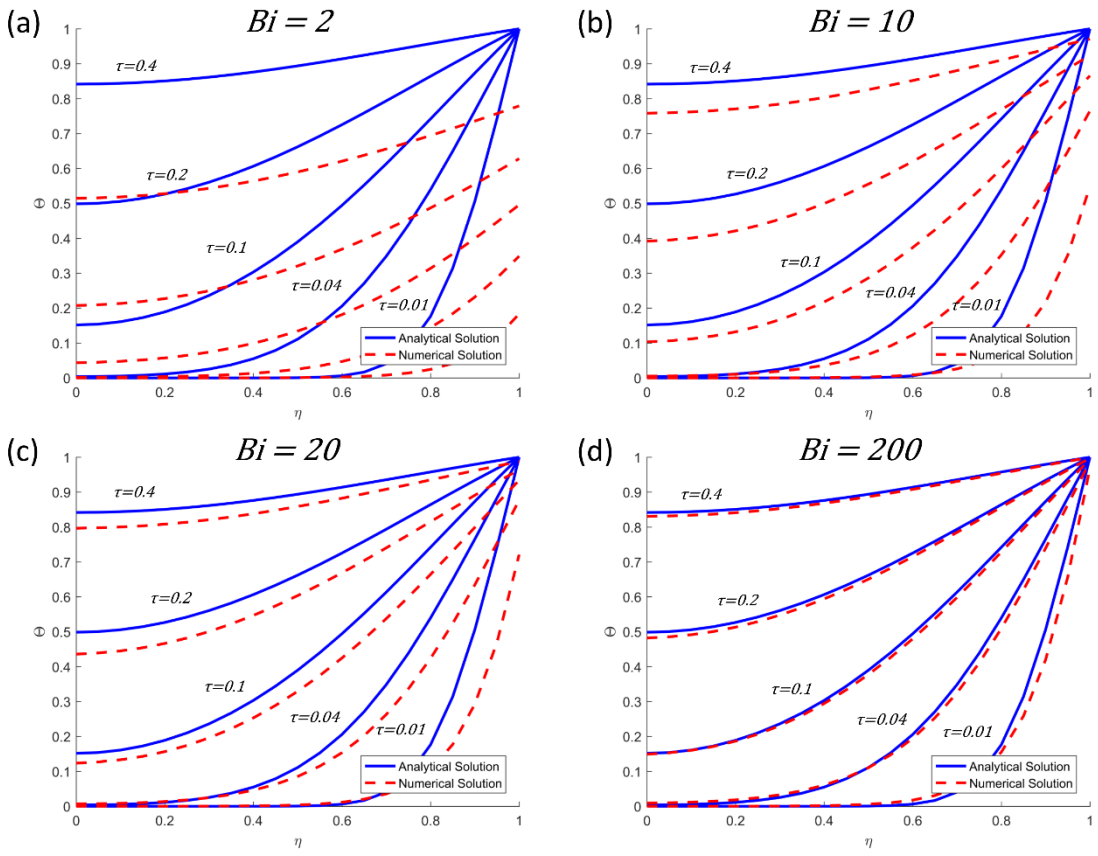

Figure 4-4: Overlay of analytical ($n = 100$) and numerical solutions for transient temperature profiles in an infinite cylinder with Newtonian boundary conditions and a Biot number, Bi, of (a) 2, (b) 10, (c) 20, and (d) 200. The analytical solutions are for an infinite Biot number.

Finally, the 2D numerical model of a finite cylinder was also validated. In this case a high radial to axial length ratio was used such that the finite cylinder becomes analogous to an infinite cylinder. A radius of 0.03m and an axial length of 1m was used. These results can be seen in Figure 4-5. Almost the same results are seen. As the Biot number increase, the numerical results are again seen to approach the analytical solutions.

The numerical model solutions were shown to be in agreement with analytical solutions for the following three variants of the model for increasing Biot numbers:

- 1D finite slab model.
- 1D infinite cylinder model.
- 2D cylinder model using a high axial length to radius ratio, such that the model is analogous to an infinite cylinder.

The agreements for these three cases validates the heat transfer aspect of this numerical model.

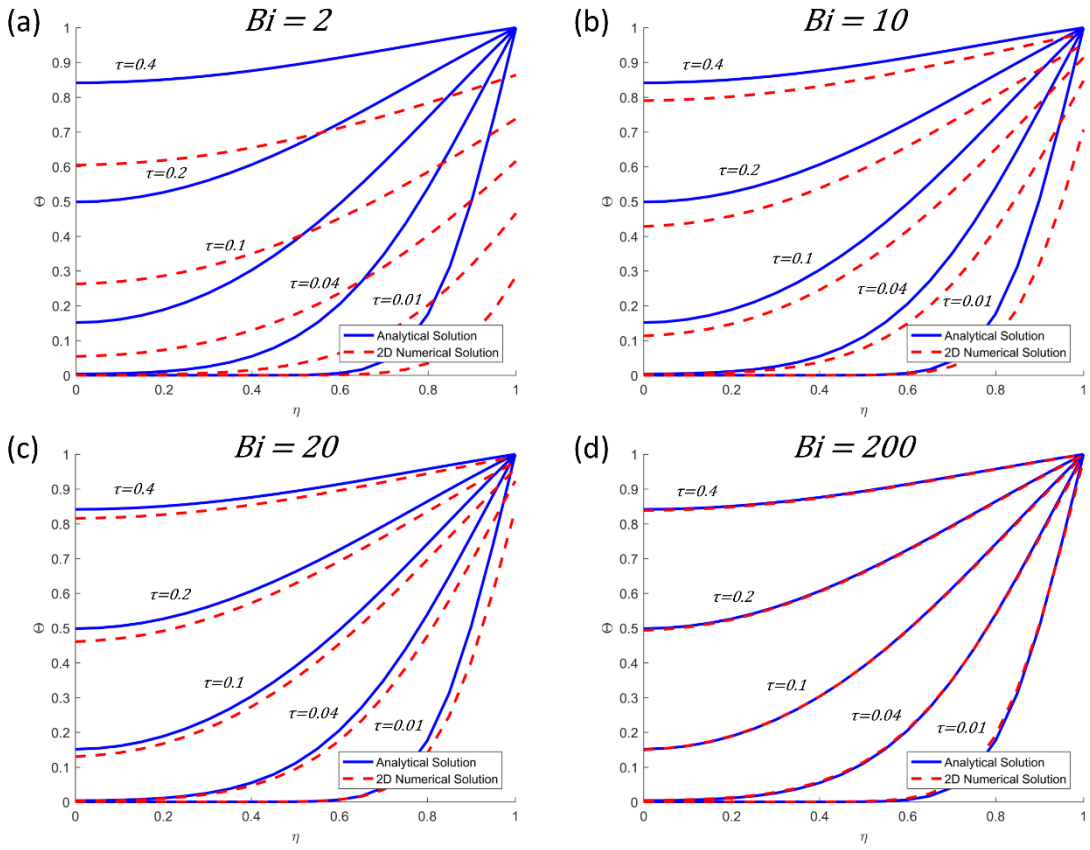

Figure 4-5: Overlay of analytical ($n = 100$) and numerical solutions for transient temperature profiles in a 2D pseudo-infinite cylinder ($r = 0.03m$ and $z = 1m$) with a Biot number, Bi, of (a) 2, (b) 10, (c) 20, and (d) 200.

4.4. Refuting the Pseudo-2D Shape Factor in Modelling Equi-Cylindrical Heat Transfer

4.4.1. Introduction

Chen (2001), and Chong and Chen (1999) proposed a model for predicting the self-heating behaviour of spray dried food powders. In this model the following governing equation for energy conservation in the powder mass, accounting for heat generation and drying of the powder, was used:

$$\rho C_p \frac{\partial T}{\partial t} = k\nabla^2 T + \rho_{sd} Q A e^{-\frac{E}{RT}} + \rho_{sd} H_v \frac{\partial X}{\partial t} \qquad (4\text{-}35)$$

The second term represents the conductive heat transfer in the solid. The Laplacian in this term is dependent on the coordinate system being used and the geometry being modelled. In this model, they used the following expansion of the Laplacian:

$$k\nabla^2 T = k\left(\frac{\partial^2 T}{\partial x^2} + \frac{j}{x}\frac{\partial T}{\partial x}\right) \tag{4-36}$$

Here, j is the shape factor and is changed to reflect the geometry being modelled. For 1D geometries, the exact value of 0 for a finite slab, 1 for an infinite cylinder, and 2 for a sphere can be used. For other geometries, such as a cube and equi-cylinder (cylinder of equal diameter and height), the shape factor was used under the premise that it allows 2D or 3D geometry to be approximated using 1D model equations. A shape factor of 3.28 for a cube, and 2.728 for an equi-cylinder was used.

This shape factor is that first proposed by Boddington *et al.* (1971) in determining the critical parameter δ_{cr} for arbitrary geometries. It was shown in Section 2.4.1.2 that the values of δ_{cr} calculated using this shape factor in other work did not agree with the values of δ_{cr} solved for analytically. This puts the use of this shape factor into doubt. Although the shape factor uses the correct Laplacian term for a finite slab, infinite cylinder, and sphere, it is unclear if this shape factors can be used as an approximation for an equi-cylinder or a cube. In an equi-cylinder, it is though that axial conduction plays a key role, and that modelling in at least axisymmetric 2D is required. No work could be found that validates the use of this shape factor for an equi-cylinder so it was decided that the use of this shape factor needed to be validated or refuted here.

4.4.2. Refuting the Shape Factor Approximation for Equi-Cylindrical Geometries

To do this, the 1D model of heat transfer, with no heat generation or drying, was used. This model uses the conduction term in equation (4-36) with a shape factor value of 2.728 as suggested by Chen (2001), and Chong and Chen (1999) in order to model an equi-cylinder. This model was solved using the Finite Implicit Backwards (FIB) scheme. Dimensionless temperature profiles were determined using this model, similar to those used in validating these models against analytical solutions. These profiles were compared to profiles generated from a 2D axisymmetric model of heat transfer in an equi-cylinder.

Profiles were plotted for dimensionless lengths $0 \leq \eta \leq 1$, for dimensionless temperatures $0 \leq \Theta \leq 1$, and at dimensionless times of $\tau = 0.01, 0.04, 0.1, 0.2$, and 0.4. For a very high Biot number (3000), such that it can be assumed infinite, the comparison of these two models is shown in Figure 4-6.

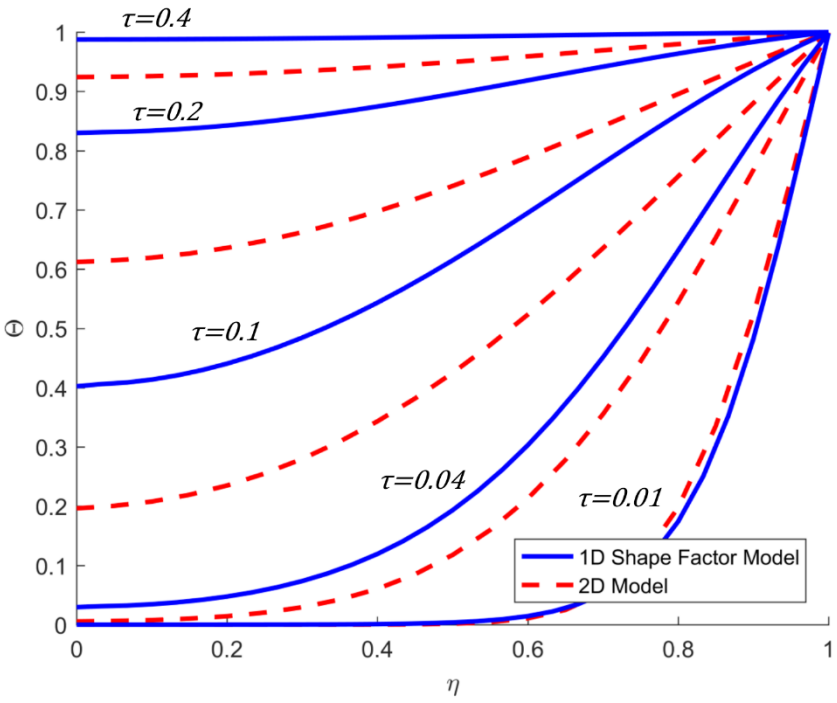

Figure 4-6: Comparison of dimensionless temperature profiles for a 1D heat transfer model using the shape factor, j = 2.728, used by Chen (2001), and Chong and Chen (1999) and a 2D axisymmetric equi-cylinder model.

Both of these models have previously been validated. The 1D model was validated against analytical solutions for transient heat transfer using a shape factor of 0 to model a slab, and a shape factor of 1 to model an infinite cylinder. The 2D model was validated against analytical solutions for transient heat transfer in an infinite cylinder by using a high radial to axial length ratio. Despite this, the results of these two models, when a shape factor of 2.728 is used, are not in agreement. Initially, at a dimensionless time of 0.01, these models are quite similar, yet as time progresses the two models are seen to diverge. The 1D model is seen to approach the steady-state temperature faster than the 2D model. The 1D model profiles are also different in shape. Close to the surface at $\eta = 1$, the 1D model profiles have a greater degree of "curvature". This can be seen particularly well at $\tau = 0.1$ and $\tau = 0.2$. These results suggest that using a 1D model

with this shape factor is not suitable for modelling equi-cylindrical heat transfer, and that a 2D axisymmetric model is required.

This analysis was repeated for finite Biot number values of 3, 15, 30, and 300. These results are shown in Figure 4-7 and the same behaviour as before can be seen. In each case the 1D shape factor model heat up faster than the 2D model. Again these results suggest that using a 1D model with the shape factor approximation, or at least using a shape factor of j = 2.728, is not suitable for modelling equi-cylindrical heat transfer. Although more computationally expensive, and more complex, a 2D axisymmetric model is the minimum required to model such systems. This also suggest that axial conduction has an impact that cannot be approximated. This has implications in the cross-point temperature method, where only radial conduction is considered in determining the cross-point. The effect of axial conduction on the cross-point, and the true form of the cross-point assumption, will be explored later in Section 5.4.2.

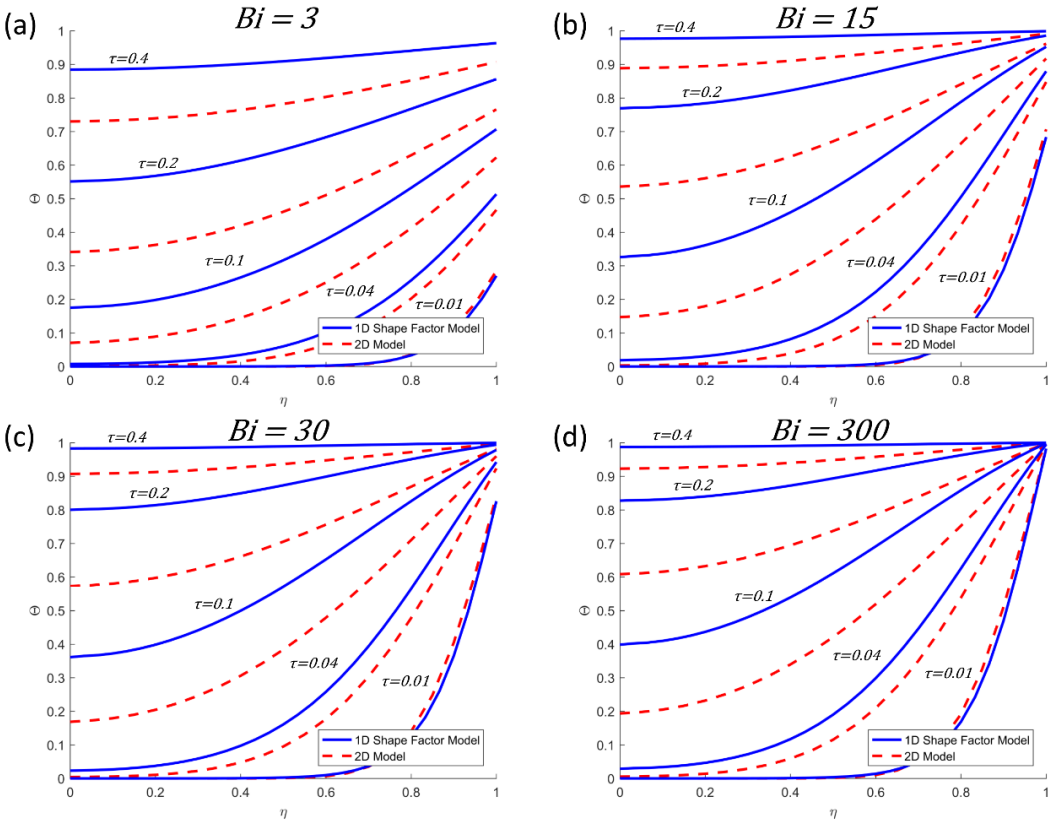

Figure 4-7: Comparison of dimensionless temperature profiles for a 1D heat transfer model using the shape factor of j = 2.728 and a 2D axisymmetric equi-cylinder model for Biot number of (a) 3, (b) 15, (c) 30, and (d) 300.

4.5. Experimentally Measuring the Convective Heat Transfer Coefficient in the Oven

In order to accurately model the heat transfer in oven heated baskets of detergent powder, one must be able to accurately model the heat transfer at the basket boundaries. To do this, the heat transfer coefficient must be known, or rather measured. Firstly, the heat transfer across the boundary is quantified by what is commonly referred to as Newton's Law of Cooling:

$$q = h_{eff}(T_s - T_\infty) \tag{4-37}$$

Where q is the heat flux (W m^{-2}), h is the effective heat transfer coefficient (W m^{-2} K^{-1}), T_s is the surface temperature (K), and T_∞ is the ambient temperature (K). The effective heat transfer coefficient is the sum of the convective heat transfer coefficient, h_{conv}, and the radiative heat transfer coefficient, h_{rad}:

$$h_{eff} = h_{conv} + h_{rad} \tag{4-38}$$

The most common method for measuring the effective heat transfer coefficient is the transient temperature measurement method, used by both Sato *et al.* (1987) and Carson *et al.* (2006). This method consists of fitting a mathematical model to transient temperature vs time data, and using this to back-calculate the heat transfer coefficient. The general solution to the heat transfer equation for a body with convective heat transfer at its surface is defined as:

$$\theta = \sum_{j=1}^{\infty} f_j(Bi)\exp(-g_j(Bi)Fo) \tag{4-39}$$

θ is the dimensionless temperature at some position, defined relative to the temperature at that position, T, as:

$$\theta = \frac{T - T_\infty}{T_0 - T_\infty} \tag{4-40}$$

Here, T_0 is the initial temperature. Bi is the Biot number, the ratio of internal to external thermal resistance, defined as:

$$Bi = \frac{hL}{k} \tag{4-41}$$

Fo is the Fourier number, which is essentially the dimensionless time, defined as:

$$Fo = \frac{kt}{\rho C_p L^2} \tag{4-42}$$

The function $f_j(Bi)$ and $g_j(Bi)$ in equation (4-39) are dependent on the geometry of the body. By plotting the logarithm of the dimensionless temperature change against time, the following can be fitted to the linear region:

$$\ln \theta = B - st \tag{4-43}$$

If the Biot number of the body is less than 0.1, then the lumped heat capacity approximation can be used. This avoids rather complex solutions to equation (4-39). In doing so, and by using the volume to surface area ratio as the characteristic length (i.e. $L = V/A$), equation (4-39) can instead be expressed as:

$$\theta = \exp(-Bi\, Fo) \tag{4-44}$$

Rearranging this allows the effective heat transfer coefficient to be back-calculated from the following:

$$h_{eff} = \rho C_p \frac{V}{A} s \tag{4-45}$$

Where ρ is the density, C_p is the specific heat capacity, and s is the slope of the linear fitting in equation (4-43). By knowing the radiative heat transfer coefficient, h_{rad}, the convective heat transfer coefficient, h_{conv}, can be determined. h_{rad} is defined as:

$$h_{rad} = \sigma \epsilon (T_s + T_{wall})(T_s^2 + T_{wall}^2) \tag{4-46}$$

Where σ is the Stefan Boltzmann constant (5.67x10^{-8} W m^{-2} K^{-4}), ϵ is the emissivity, and T_{wall} (K) is the temperature of the internal oven walls. Here it is assumed that the temperature of the oven walls is equal to the ambient temperature, T_∞. To determine this heat transfer coefficient of the oven in this study, a Memmert UF 75 forced convection oven, an aluminium equi-cylinder of height and dimeter 50mm was used. The thermal conductivity of aluminium (≈215 W m^{-1} K^{-1} at 125°C) is large enough that the temperature of the cylinder can be considered uniform. A hole was drilled into the cylinder to allow a probe-type type K thermocouple to be inserted and the central temperature of the cylinder measured. The cylinder was also painted using matte black, high temperature, spray paint, such that the emissivity of the cylinder could be assumed to be equal to 0.97. A thermocouple is also placed close to the cylinder to allow the true ambient temperature to be recorded. The experimental setup can be seen in Figure 4-8.

Figure 4-8: Setup of black painted aluminium cylinder used in the transient temperature measurement method for determining the convective heat transfer coefficient.

Aluminium was used because a material with known properties is required. The following properties for aluminium were used in this method:

Table 4-1: Properties of aluminium used in this method.

Property	**Value**
Specific Heat Capacity, C_p (J kg^{-1} K^{-1})	910
Density, ρ (kg m^{-3})	2700

In this method, small ambient temperature changes are made and the temperature-time profile at the cylinder centre recorded. Ambient temperature changes of 20°C were made starting from 20°C (293K) and finishing at 240°C (513K), corresponding to 11 experiments. For each temperature change, the cylinder was allowed time to reach a uniform steady-state temperature before proceeding to the next temperature increase. The start and end temperatures for each of the experiments are shown in Table 4-2.

Table 4-2: Start and end temperatures for the 11 transient temperature measurement experiments.

Test Number	Start Temperature	End Temperature
1	20°C	40°C
2	40°C	60°C
3	60°C	80°C
4	80°C	100°C
5	100°C	120°C
6	120°C	140°C
7	140°C	160°C
8	160°C	180°C
9	180°C	200°C
10	200°C	220°C
11	220°C	240°C

The temperature difference between the ambient and cylinder temperature, and cylinder temperature alone can be seen in Figure 4-9 at an ambient temperature of 180°C (453K). It can be seen that the temperature difference is initially equal to 0K because the oven temperature is yet to be increased. The oven temperature is changed, and it takes a short amount of time for the oven to reach this temperature, causing the temperature difference to reach some value between 15 and 20K. The temperature difference then reduces to 0K once again as the cylinder heats up. Some noise can be seen on the latter part of the temperature difference profile. This noise is more pronounced at lower ambient temperatures.

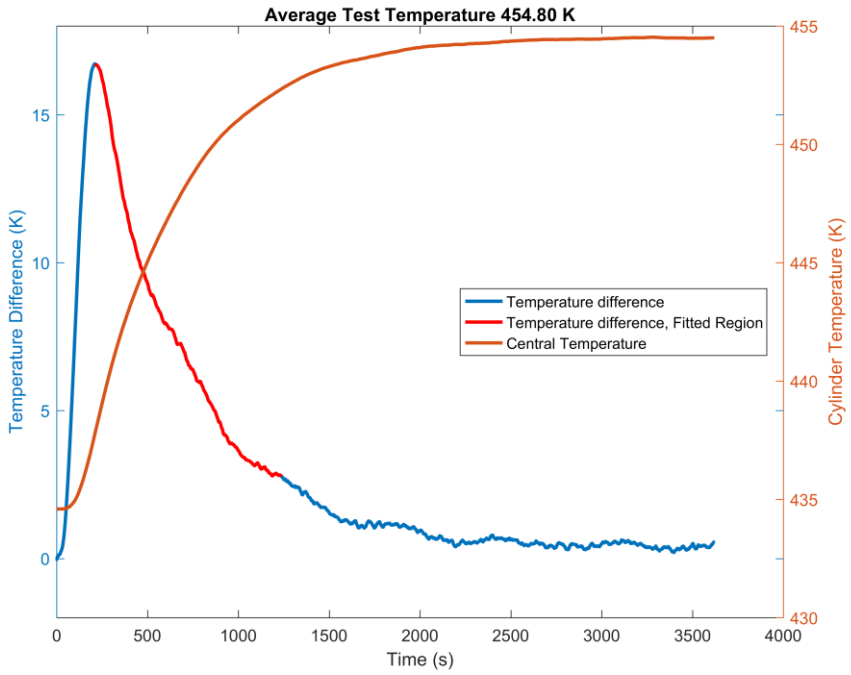

Figure 4-9: Temperature difference and cylinder temperature for an ambient temperature of approximately 180°C (453K).

For each experiment, the recorded cylinder, initial, and ambient temperatures are used to calculate the dimensionless temperature difference, θ, in equation (4-40). This is plotted in Figure 4-10. It can be seen that this value begins at 0, before approaching a final value of approximately -4. There is considerably more noise on this profile, but the initial portion of the profile is reasonably linear. It is to this region that equation (4-43) is fitted. This is done for each of the experiments outlined in Table 4-2, and the heat transfer coefficient for each test calculated from equation (4-45). The results for ambient temperature of approximately 200°C (473K) and 220°C (493K) can be seen in Figure 4-11 and Figure 4-12 respectively. These are temperatures close to those at which the baskets of detergent powders will be heated.

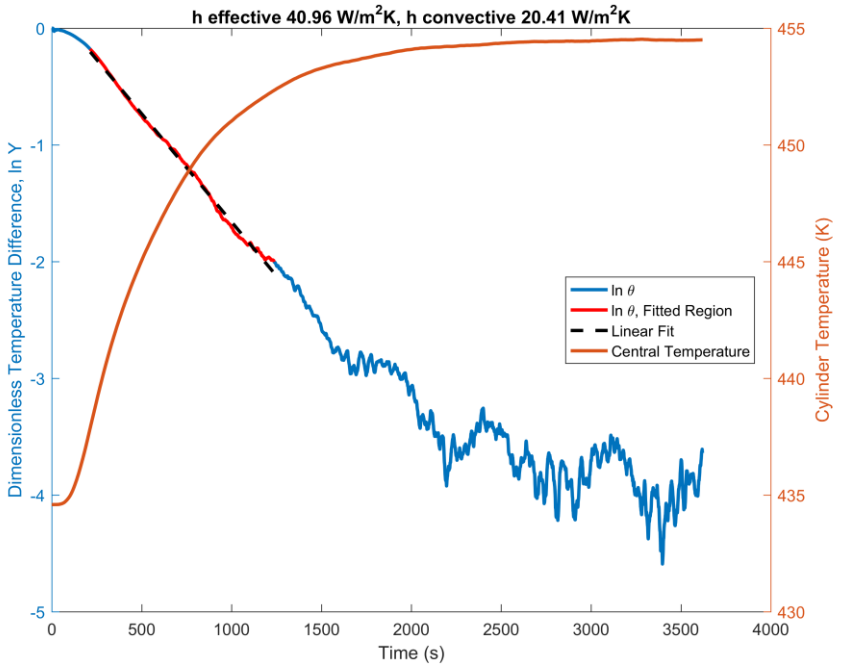

Figure 4-10: Dimensionless temperature difference, fitting region, and linear fit to these data for a cylinder heated at an ambient temperature of approximately 180°C (453K).

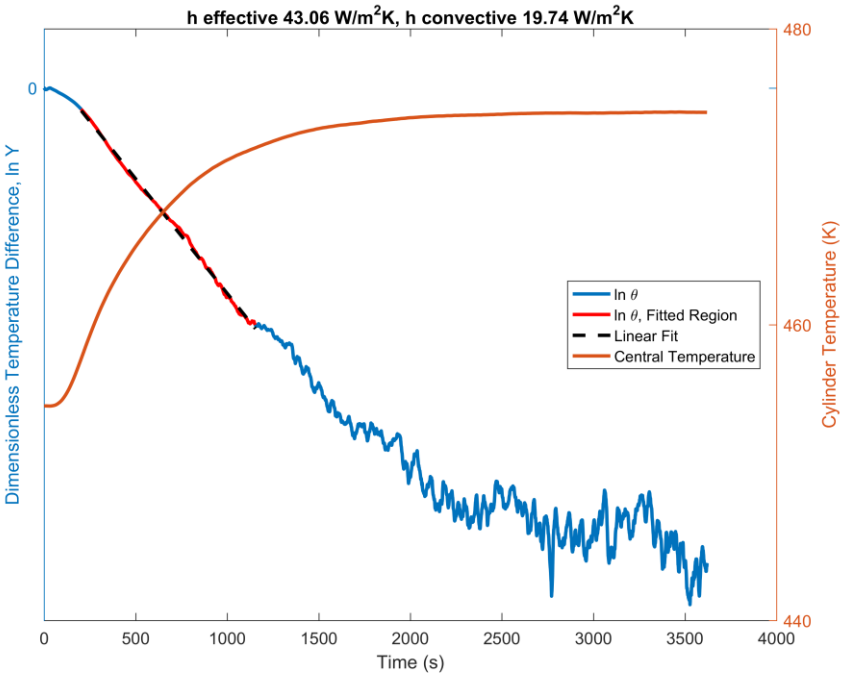

Figure 4-11: Dimensionless temperature difference, fitting region, and linear fit to these data for a cylinder heated at an ambient temperature of approximately 200°C (473K)

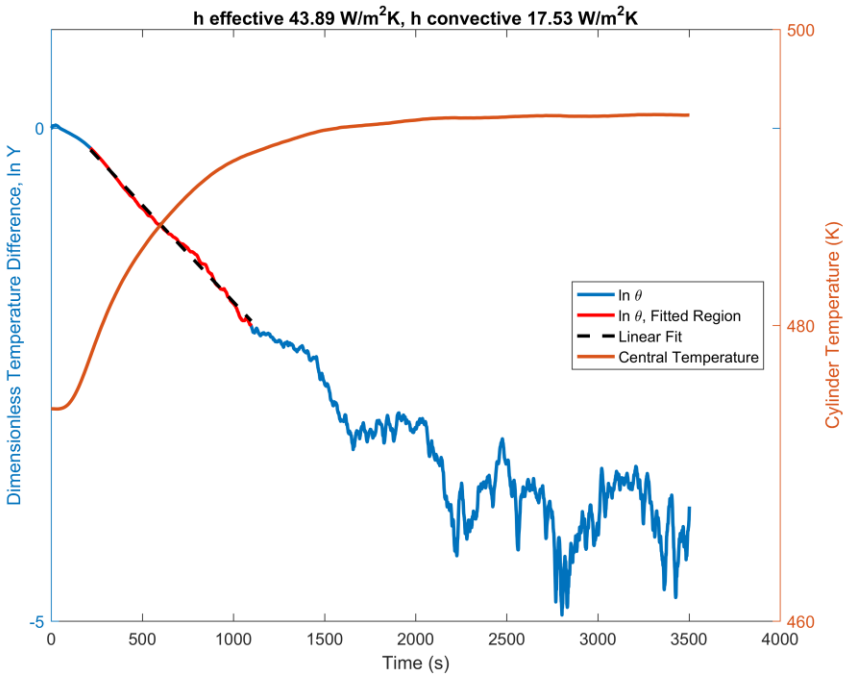

Figure 4-12: Dimensionless temperature difference, fitting region, and linear fit to these data for a cylinder heated at an ambient temperature of approximately 220°C (493K).

The effective heat transfer coefficient, h_{eff}, for each test was plotted as a function of the ambient temperature in Figure 4-13. A relatively good fit is seen that shows how the effective heat transfer coefficient is seen to increase with ambient temperature, from approximately 34 W m^{-2} K^{-1} at 20°C (293K) to approximately 44 W m^{-2} K^{-1} at 220°C (493K).

The following correlation was fitted to allow h_{eff} to be estimated for any ambient temperature:

$$h_{eff} \approx 7.64 \times 10^{-5}\, T^2 - 6.67 \times 10^{-3}\, T + 28.19 \qquad (4\text{-}47)$$

This is the effective heat transfer coefficient for a black aluminium cylinder in this oven. To apply this to other objects heated in this oven, the effective heat transfer coefficient needs to be separated into the radiative and convective heat transfer coefficient. The radiative component will vary from object to object, and is dependent on the surface emissivity, ϵ. By painting this cylinder matte black, the emissivity is assumed equal to 0.97, allowing the radiative heat transfer coefficient to calculated using equation (4-46) for different ambient temperatures. This value, as a function of ambient temperature is

shown in Figure 4-14. Subtracting this from the effective heat transfer coefficient gives the convective heat transfer coefficient, and this can be seen in Figure 4-15.

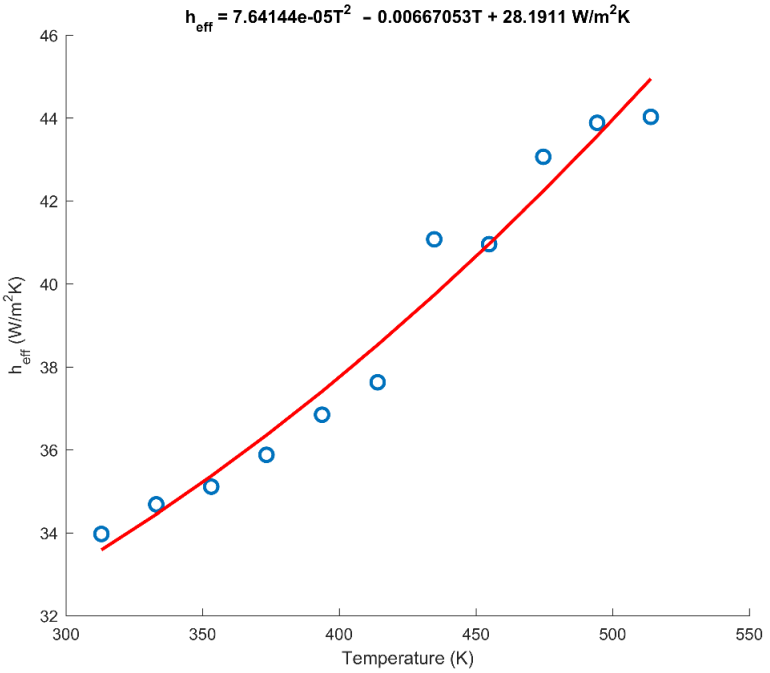

Figure 4-13: Effective heat transfer coefficient as a function of ambient temperature.

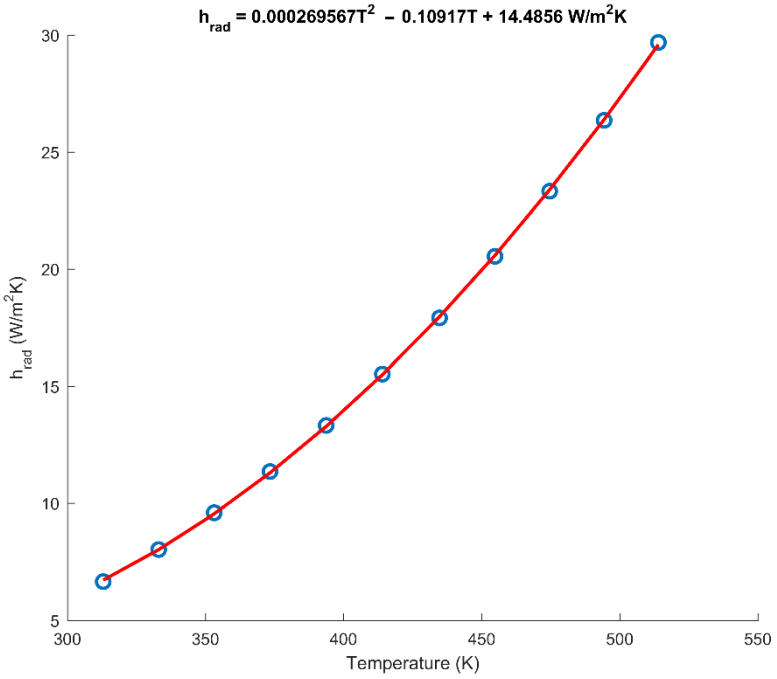

Figure 4-14: Radiative heat transfer coefficient as a function of ambient temperature.

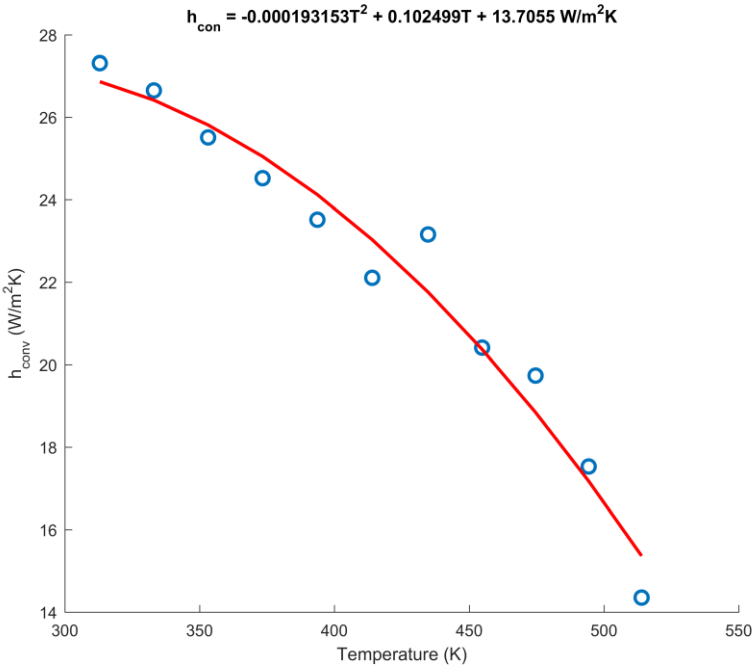

Figure 4-15: Convective heat transfer coefficient as a function of ambient temperature.

The following correlation was fitted to allow h_{conv} to be estimated for any ambient temperature:

$$h_{conv} \approx -1.93 \times 10^{-4}\, T^2 - 0.102\, T + 13.71 \qquad (4\text{-}48)$$

The correlated value of h_{conv} is seen to decrease with a decrease in ambient temperature. This is unexpected and may be due to the radiative heat transfer coefficient. As shown in equation (4-46), the radiative heat transfer coefficient is dependent on the temperature of the internal oven walls. However, it was assumed that this was equal to the ambient temperature. It may be incorrect to assume this, and this may be the reason that the convective heat transfer coefficient decreases with temperature. As such, this correlation is only applicable in the temperature ranges for which it was calculated. This correlation can be used in the numerical model to estimate the convective heat transfer coefficient for a basket of detergent powder in this oven.

4.6. Conclusions

In this chapter, the model equations for three different variants of a numerical model capable of predicting self-heating behaviour in self-heating systems were outlined.

These were modelled using 2D axisymmetric cylindrical coordinates, although the model equations also allow the coordinate system to be varied. These models allow different combinations of heat transfer, mass transport of moisture, zero order self-heating reactions, and n^{th} order reactant concentration dependent reactions, to be modelled.

These models were initially built in MATLAB but transferring these models in gPROMS ModelBuilder allowed for easier editing and faster, and more accurate, solving of these models. The in-built solvers of gPROMS and the adaptive approach to discretising time helped in improving these models.

Different variants of this model were successfully validated by comparing the numerical solutions to analytical solutions for a finite slab and infinite cylinder. Both the 1D and 2D variants of this model were validated against analytical solutions for a finite slab and infinite cylinder. These analytical solutions assumed an infinite Biot number, and using the same assumption, these models agreed very well with the analytical solutions. Model solutions with varying Biot numbers were also compared to analytical solutions. It could be seen that the model solutions approached the analytical solutions for increasing values of the Biot number. As expected, solutions with lower Biot numbers were shown to have a greater difference in surface to ambient temperatures.

This model was successfully used to refute shape factor approximation used by Chen (2001), and Chong and Chen (1999). By comparing a 1D variant of the developed model using this shape factor approximation and the 2D axisymmetric model variant, it was shown that the model with this shape factor gave incorrect results. Chen (2001), and Chong and Chen (1999) suggested that this approximation could be used to model heat transfer in an equi-cylinder using 1D equations. This comparison showed that this shape factor approximation should not be used, at least for the value of j = 2.728 suggested, and that at least a 2D axisymmetric model is required.

Finally, the transient temperature measurement method was used to correlate the convective heat transfer coefficient of the oven to the ambient temperature. This was correlated as:

$$h_{conv} \approx -1.93 \times 10^{-4}\, T^2 - 0.102\, T + 13.71 \qquad (4\text{-}49)$$

This can be summed with the radiative heat transfer coefficient to give the effective heat transfer coefficient. This correlation is applied in simulating the oven heating of detergent powder baskets in later applications of these models.

5. Assessment of Methods for Characterising Detergent Formulations

5.1. Introduction

The self-heating behaviour of materials other than detergent powders have previously been explored using a number of methods. The long established method is the steady-state method based on Frank-Kamenetskii's theory of thermal explosions (Frank-Kamenetskii, 1969). This is a basket heating method which was originally used to estimate self-heating kinetics for activated carbons (Bowes & Cameron, 1971). The steady-state method is an effective approach based on determining the critical ambient temperatures, the temperature above which thermal runaway will occur, for different basket sizes of material. This is a slow method requiring several experiments to yield a single data point. Developed as a faster alternative, the cross-point temperature (CPT) method is another basket heating method, first proposed by Chong *et al.* (1996), and originally used to estimate the self-heating kinetics of skimmed and whole milk powders. Since then, Sujanti *et al.* (1999) has used this approach to study coal, and has shown that the steady-state method and the cross-point temperature method estimate similar kinetics. Malow and Krause (2004) has also compared these two methods, along with the differential scanning calorimetry (DSC) based Ozawa-Flynn-Wall method to estimate the kinetics of coal dust, cork dust, riboflavin and a detergent powder. This is also one of the few studies that addresses self-heating in detergent powders. Few details were given with regards the detergent powder formulation, but it was shown that the steady-state and CPT methods estimated similar kinetics, giving activation energies of $102(\pm30)x10^3$ J mol^{-1} and $112(\pm24)x10^3$ J mol^{-1} respectively. These errors are relatively large but this is possibly due to only 4 and 5 points being determined for the steady-state and CPT methods respectively.

The work presented in this chapter draws on this previous work and seeks to determine the best means of estimating the self-heating reaction kinetics of a typical detergent powder, such that the estimated kinetics can be used in the numerical model developed in Section 4.2 and applied to the study of self-heating in detergent powder accumulations. The reaction kinetics in this chapter have been estimated using three

different methods. Two of these are the previously outlined steady-state and cross-point temperature (CPT) methods, which are used to estimate zero-order reaction kinetics. The third method is a thermogravimetric fitting method, adapted from that of Yang *et al.* (2001). This method is used to fit n^{th} order kinetics to mass loss data from Thermogravimetric Analysis (TGA). The kinetics estimated using these methods are compared and the advantages and disadvantages of each method explored.

The majority of the work in this chapter was done using the detergent formulation used in Section 3.2. This formulation used a finer grade of sodium sulphate to reduce composition variability. As such this formulation will be referred to as Micronized Formulation 1. Cross-point temperature method experiments were also conducted using three other detergent formulations. The first of these formulations is referred to as Non-Micronized Formulation 1. As the name suggests, this formulation uses a non-micronized grade of sodium sulphate, but in all other ways it is the same as Micronized Formulation 1. This means that it also contains LAS surfactant at a level of 17%, which is thought to cause the majority of the observed self-heating behaviour. It also contains low levels of Sodium Silicate, Sodium Carbonate, and Polycarboxylate Polymer at the same levels at Micronized Formulations 1.

The other two formulations, Formulation 2 and Formulation 3, are similar to one another. These formulations have a similar composition to Formulation 1, but vary in the exact level of the individual components. They both contain approximately 17% LAS but their compositions vary from one another in that Formulation 3 contains 1% Polycarboxylate Polymer, whilst Formulation 2 contains 0%. These formulations allow the influence of this polymer on the self-heating to be evaluated. The estimated kinetics of all these formulations are discussed.

These kinetics are applied in the 2D-axistmmetric model of transient heat and mass transfer in a cylindrical basket of detergent powder. This model is adapted from the models of Chen (2001) and Chong and Chen (1999), which were used to model self-heating in milk powders and explore aspects of the cross-point temperature method. The comparison of this model to experimental temperature profiles is explored. Both the numerical model and the two basket heating methods are based on the same energy balance for a self-heating body, given by equation (4-1).

The model based on this energy balance, discussed in detail in Chapter 4, was used to simulate the cross-point temperature method experiments, such that the impact of the form of the cross-point approximation on the results could be explored. The effects of errors in the thermocouple readings were also simulated. This model was then used to predict temperature-time profiles in baskets of detergent powder across a range of ambient temperatures. Critical ambient temperatures for baskets of varying sizes are also predicted. These predictions are then compared with experimental data. The influence of the specific heat capacity, a number of drying parameters, and the differences in predicted temperature profiles from using zero-order and n^{th} order reaction models are also explored.

5.2. Steady-State Basket Method

The steady-state approach, sometimes referred to as the F-K method, initially developed by Bowes and Cameron (Bowes & Cameron, 1971), is based on the steady-state dimensionless form of the energy conservation equation (4-1). It is widely used for determining the zero-order reaction kinetics of self-heating powders and is the basis of the British Standard BS EN 15118:2007 (British Standards Institution, 2007). The dimensionless form is obtained by defining the dimensionless temperature, θ, the dimensionless length, ξ, the dimensionless exponent, φ, and the dimensionless parameter, δ:

$$\theta = \frac{E}{RT_\infty^2}(T - T_\infty) \tag{5-1}$$

$$\xi = \frac{x}{L} \tag{5-2}$$

$$\varphi = \frac{E}{RT_\infty} \tag{5-3}$$

$$\delta = \frac{E}{RT_\infty^2}\frac{\rho Q A L^2}{k} e^{-\frac{E}{RT_\infty}} \tag{5-4}$$

Where x (m) is the position, L (m) is a characteristic length, and T_∞ (K) the ambient temperature. The steady-state energy conservation equation can then be expressed as:

$$\nabla_{\xi}^{2}\theta = -\delta e^{\frac{\theta}{1+\frac{\theta}{\varphi}}} \tag{5-5}$$

The Frank-Kamenetskii parameter, δ, is a dimensionless term that encompasses all the quantities required to describe the problem of self-heating, with a value above the critical value, δ_{cr}, leading to thermal runaway. The value of δ_{cr} is a function of geometry, the dimensionless exponent φ in equation (5-3), and the Biot number, Bi, used in defining the dimensionless boundary conditions of this problem. Rearranging δ in equation (5-4) gives:

$$\ln\left(\frac{\delta_{cr}T_{\infty,cr}^{2}}{L^{2}}\right) = \ln\left(\frac{\rho Q A}{k}\frac{E}{R}\right) - \frac{E}{RT_{\infty,cr}} \tag{5-6}$$

The steady-state approach is based on this equation. A stainless steel equi-cylindrical (cylinder of equal height and diameter) mesh basket was filled with detergent powder and placed in a Memmert UF75 forced convection oven. The baskets were filled and tapped, such that they were consistently filled to the same mass, ensuring the same density for each experiment. A type K thermocouple (RS Pro 363-0294) was inserted into the centre of this basket to measure the core temperature. This thermocouple was glass fibre insulated with a welded exposed junction and supplied with a working range of -60° to 350°C. The oven temperature was set and an additional thermocouple was placed near to the basket to measure the true ambient temperature close to the basket. The temperature was measured over a number of hours to determine if the powder undergoes thermal runaway at the oven set ambient temperature. The test was repeated at different ambient temperatures, in 0.5°C increments, to find the critical ambient temperature, above which the basket of powder undergoes thermal runaway, for the size of basket used. 0.5°C increments were used because that was increment to which the oven temperature could be set. Repeating this for baskets of different sizes and plotting according to equation (5-6) allowed the zero-order activation energy and pre-exponential factor for the self-heating reaction to be estimated. In this investigation three equi-cylindrical baskets were used, with diameters of 50mm, 60mm, and 70mm.

5.2.1. Numerical Solutions for the Frank-Kamenetskii Parameter, δ_{cr}

As mentioned, δ is a dimensionless term that encompasses all the quantities required to describe the problem of self-heating. For a value above the critical value, δ_{cr}, the system will lead to thermal runaway. In order to accurately execute the steady-state method the value of δ_{cr} must be known. δ_{cr} has previously been calculated for common geometries, such as for an infinite slab detailed in Section 2.3. This solution was accompanied by a number of assumptions. It was assumed that Biot number ($Bi = hL/k$) was infinite, such that the edge temperature of the slab is equal to the ambient temperature. It was also assumed that $\Delta T \ll T_\infty$, such that φ was assumed infinite, and a simplified exponential term of e^θ could be used in equation (5-5). These assumptions limit the use of these solved for δ_{cr} values. Chambré (1952) detailed this solution for other geometries but these same assumptions were applied. Parks (1961) used a digital computer to solve for these δ_{cr} values for a range of φ values and for a number of geometries, as detailed in section 2.3.4, but the limitations of 1960s computing means there is scope to expand on this work.

Here δ_{cr} is solved for numerically for four geometries, a finite slab, an infinite cylinder, a sphere, and an equi-cylinder (cylinder of equal diameter and height), for a range of values for φ and the Biot number. Solving in terms of φ allows more material specific values of δ_{cr} to be used, whilst solving in terms of the Biot number allows δ_{cr} for different boundary conditions to be used. To calculate the critical value δ_{cr}, the dimensionless steady-state equation (5-5) is solved for varying values of φ, Bi, and δ. For set values of φ and Bi, the value of δ was increased to find the maximum value for which a steady-state solution exists. This maximum value is the critical value, δ_{cr}. The Laplacian term in equation (5-5) has been expanded to model the four different geometries explored in this investigations. For the 1-dimensional systems the following expanded equations are used:

$$infinite\ slab \qquad \frac{d^2\theta}{d\xi^2} = -\delta e^{\frac{\theta}{1+\frac{\theta}{\varphi}}} \tag{5-7}$$

$$infinite\ cylinder \qquad \frac{d^2\theta}{d\xi^2} + \frac{1}{\xi}\frac{d\theta}{d\xi} = -\delta e^{\frac{\theta}{1+\frac{\theta}{\varphi}}} \tag{5-8}$$

$$sphere \qquad \frac{d^2\theta}{d\xi^2} + \frac{2}{\xi}\frac{d\theta}{d\xi} = -\delta e^{\frac{\theta}{1+\frac{\theta}{\varphi}}} \tag{5-9}$$

To solve for δ_{cr} for an equi-cylinder, a 2D model was required, which requires solving for θ in both the dimensionless radial and axial directions, hereby denoted as ξ_r and ξ_z respectively:

$$equi-cylinder \qquad \frac{d^2\theta}{d\xi_r^2} + \frac{1}{\xi_r}\frac{d\theta}{d\xi_r} + \frac{d^2\theta}{d\xi_z^2} = -\delta e^{\frac{\theta}{1+\frac{\theta}{\varphi}}} \tag{5-10}$$

Boundary conditions are required to solve this problem. A symmetrical boundary condition applies at the centre of the geometry such that:

$$at\ \xi = 0, \qquad \frac{\partial\theta}{\partial\xi} = 0 \tag{5-11}$$

Or in 2D coordinates this boundary condition is expressed as:

$$at\ \xi_r = 0, \qquad \frac{\partial\theta}{\partial\xi_r} = 0 \tag{5-12}$$

$$at\ \xi_z = 0, \qquad \frac{\partial\theta}{\partial\xi_z} = 0 \tag{5-13}$$

At the exposed boundary of the body, heat transfer is dependent on the Biot number, Bi, which is the ratio of the conductive heat transfer resistance within the body to the convective heat transfer resistance at the boundary. This parameter was a specified input parameter in the model. Using this, the boundary condition can be defined as:

$$at\ \xi = 1, \qquad \frac{\partial\theta}{\partial\xi} = -Bi\ \theta \tag{5-14}$$

As the Biot number increases, the temperature at $\xi = 1$ approaches the ambient temperature. For an infinitely high Biot number this boundary condition reduces to $\theta_{\xi=1} = 0$. In 2D coordinates this boundary condition is expressed as:

$$at\ \xi_r = 1, \qquad \frac{\partial\theta}{\partial\xi_r} = -Bi\ \theta \tag{5-15}$$

$$at\ \xi_z = 1, \qquad \frac{\partial\theta}{\partial\xi_z} = -Bi\ \theta \tag{5-16}$$

5.2.1.1. Critical Criterion δ_{cr} Numerically Solved as a Function of φ

Parks (1961) solved for δ_{cr} for φ values from 20 to 100 in increments of 5, and using the boundary condition at $\xi = 1$ of $\theta = 0$. This was replicated here using implicit finite difference models built in MATLAB. The 1D model was discretised in ξ into 21 points. Both the 1D and 2D models were solved for discretisations of 21, 41, and 81 points. All the solved for θ profiles were the same, such that 21 points was sufficient to achieve grid independence. In this method the three values of θ captured in the Laplacian term of the next iteration $(n+1)$, θ_{i-1}^{n+1}, θ_i^{n+1}, and θ_{i+1}^{n+1}, were solved using a single value from the current iteration (n) of θ_i^n in the exponential term. Here i denotes the spatial position in ξ. The MATLAB script of this solver is in Appendix E. The method is illustrated in Figure 5-1, and the discretised model equation is as follows, where κ is varied depending on the geometry that is being solved for (i.e. 0 for a finite slab, 1 for an infinite cylinder, and 2 for a sphere):

$$\frac{\theta_{i-1}^{n+1} - 2\theta_i^{n+1} + \theta_{i+1}^{n+1}}{\Delta\xi^2} + \frac{\kappa}{\xi_i}\frac{\theta_{i+1}^{n+1} - \theta_{i-1}^{n+1}}{2\Delta\xi} = -\delta \exp\left(\frac{\theta_i^n}{1 + \frac{\theta_i^n}{\varphi}}\right) \qquad (5\text{-}17)$$

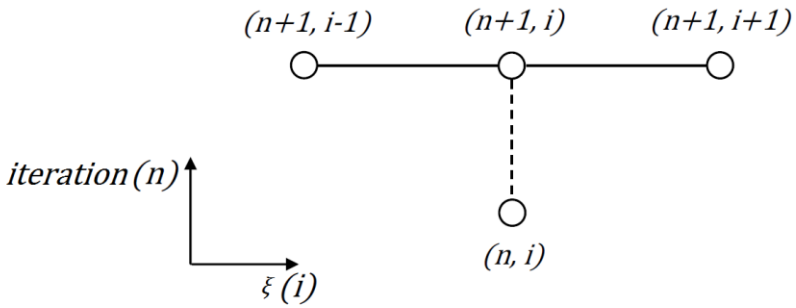

Figure 5-1: Schematic of the 1D finite difference solving procedure.

The 2D model uses a similar approach but it is split into two parts. The model was discretized into 21 points in both ξ_r and ξ_z. Firstly the three values of $\theta_{i-1,j}^{n+1/2}$, $\theta_{i,j}^{n+1/2}$, and $\theta_{i+1,j}^{n+1/2}$ are solved for in the radial direction at the half iteration $(n + 1/2)$, using three values from the current iteration (n) of $\theta_{i,j-1}^n$, $\theta_{i,j}^n$, and $\theta_{i,j+1}^n$. Here i denotes the spatial position in ξ_r and j denotes the spatial position in ξ_z. Secondly the three values of $\theta_{i,j-1}^{n+1}$, $\theta_{i,j}^{n+1}$, and $\theta_{i,j+1}^{n+1}$ are solved for in the axial direction at the full iteration $(n+1)$,

using three values from the half iteration $(n+1/2)$ of $\theta_{i-1,j}^{n+1/2}$, $\theta_{i,j}^{n+1/2}$, and $\theta_{i+1,j}^{n+1/2}$. The MATLAB script of this solver is in Appendix F. The method is illustrated in Figure 5-2, and the discretised model equation is as follows for the first step:

$$\frac{\theta_{i-1,j}^{n+1/2}-2\theta_{i,j}^{n+1/2}+\theta_{i+1,j}^{n+1/2}}{\Delta\xi_r^2}+\frac{1}{\xi_{r,i}}\frac{\theta_{i+1,j}^{n+1/2}-\theta_{i-1,j}^{n+1/2}}{2\Delta\xi_{\mathrm{r}}}$$
$$+\frac{\theta_{i,j-1}^{n}-2\theta_{i,j}^{n+1/2}+\theta_{i,j+1}^{n}}{\Delta\xi_z^2}=-\delta\exp\left(\frac{\theta_{i,j}^{n}}{1+\frac{\theta_{i,j}^{n}}{\varphi}}\right) \quad (5\text{-}18)$$

At the step second it is discretised as follows:

$$\frac{\theta_{i-1,j}^{n+1/2}-2\theta_{i,j}^{n+1}+\theta_{i+1,j}^{n+1/2}}{\Delta\xi_r^2}+\frac{1}{\xi_{r,i}}\frac{\theta_{i+1,j}^{n+1/2}-\theta_{i-1,j}^{n+1/2}}{2\Delta\xi_r}$$
$$+\frac{\theta_{i,j-1}^{n+1}-2\theta_{i,j}^{n+1}+\theta_{i,j+1}^{n+1}}{\Delta\xi_z^2}=-\delta\,exp\left(\frac{\theta_{i,j}^{n+1/2}}{1+\frac{\theta_{i,j}^{n+1/2}}{\varphi}}\right) \quad (5\text{-}19)$$

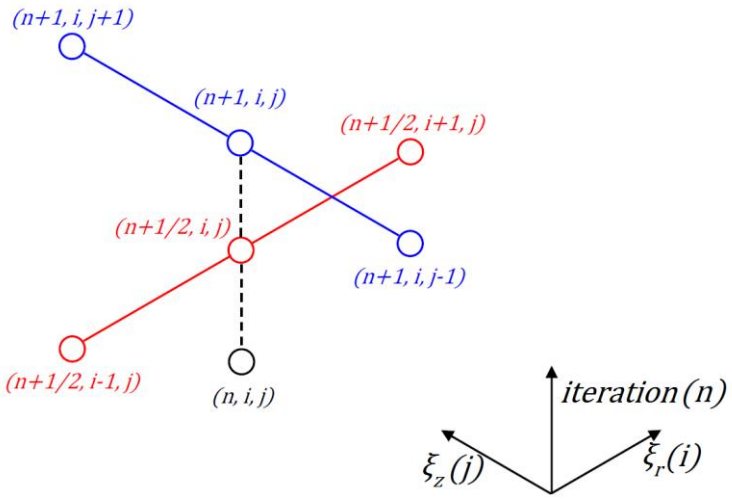

Figure 5-2: Schematic of the 2D finite difference solving procedure.

Using these models, the critical criterion δ_{cr} was found for each of the four geometries. For each geometry a minimum and maximum guess for δ_{cr} was specified. Then average of these two values is taken as the first guess for δ_{cr}. The model then attempts to solve for a steady-state solution. There are two possible outcomes. The first is that a steady-state solution exists, meaning the chosen value of δ_{cr} was too low. The minimum δ_{cr} is

set to this value and the procedure repeated. The second scenario is that there is no steady-state solution. In this case, the chosen value of δ_{cr} was too high, and the maximum δ_{cr} is set to this value, and the procedure repeated. This continues until the value of δ_{cr} changes by less than $1x10^{-6}$ for the 1D model, and by less than $1x10^{-4}$ for the 2D model for consecutive iterations. This was done for a range of different value of φ, with the results tabulated in Table 5-1. These results are also plotted in Figure 5-3 which shows how for all geometries the value of δ_{cr} increases with a decreases in φ, which corresponds to a decrease in activation energy, E.

Table 5-1: δ_{cr} as a function of φ $(= E/RT)$ and for an infinte Biot number, for an infinite slab, infinite cylinder, sphere, and equi-cylinder.

	Infinite Slab	**Infinite Cylinder**	**Sphere**	**Equi-Cylinder**
$\boldsymbol{\varphi}$	$\boldsymbol{\delta_{cr}}$	$\boldsymbol{\delta_{cr}}$	$\boldsymbol{\delta_{cr}}$	$\boldsymbol{\delta_{cr}}$
5	1.207	2.681	4.504	3.719
10	1.023	2.261	3.768	3.127
15	0.980	2.163	3.598	2.987
20	0.960	2.119	3.522	2.924
25	0.949	2.093	3.478	2.888
30	0.942	2.077	3.449	2.864
35	0.937	2.065	3.430	2.848
40	0.933	2.057	3.415	2.836
45	0.930	2.050	3.404	2.827
50	0.928	2.045	3.395	2.819
55	0.926	2.041	3.388	2.813
60	0.925	2.037	3.382	2.808
65	0.923	2.034	3.376	2.804
70	0.922	2.032	3.372	2.801
75	0.921	2.030	3.368	2.797
80	0.920	2.028	3.365	2.795
85	0.920	2.026	3.362	2.792
90	0.919	2.025	3.360	2.790
95	0.918	2.023	3.357	2.788
100	0.918	2.022	3.355	2.787

These results are in agreement with those of Parks (1961) for all cases except the infinite slab. Whereas Parks' results for δ_{cr} for the infinite slab approach the analytical solution value of 0.88 as α approaches infinity, the results of this investigation approach 0.909. The reason for this discrepancy is still unknown. Despite this, the calculated temperature difference at the slab centre, θ_0, approaches the analytically solution value of 1.2.

All other cases approach the δ_{cr} values documented in the literature (Nelson & Chen, 2007). These are a value of 2 for an infinite cylinder, 3.32 for a sphere, and 2.78 for an equi-cylinder. Essentially these results show that the values of δ_{cr} solved for analytically by Frank-Kamenetskii is an approximation which becomes increasingly less accurate as φ decreases. Therefore it is important that these adapted δ_{cr} values are accounted for when measuring kinetics using the steady-state method, or when predicting the criticality of systems.

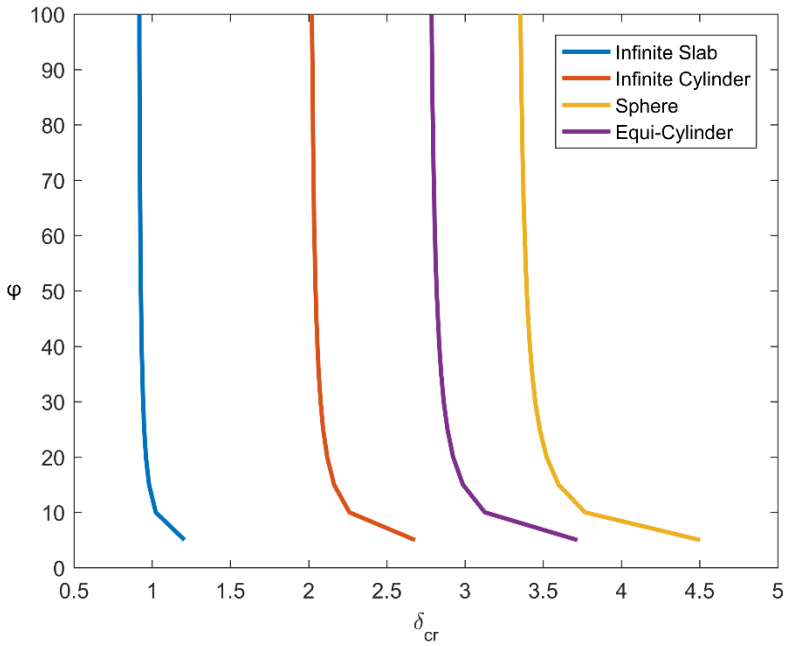

Figure 5-3: δ_{cr} as a function of φ $(= E/RT)$ and for an infinte Biot number, for an infinite slab, infinite cylinder, sphere, and equi-cylinder.

5.2.1.2. Critical Criterion δ_{cr} Numerically Solved as a Function of φ and Bi

The previous case looked to replicate the work of Parks (1961) by assuming an infinite Biot number, such that the surface of the body is at the same temperature as the

surroundings. This greatly simplifying the problem but in reality the Biot number is often so low that it cannot be assumed infinite. In this investigation it typically took a value of between 11 and 15. By adapting this model to account for Newton's Law of Cooling at the boundary, using the boundary conditions outlined in (5-14), (5-15), and (5-16), the value of δ_{cr} can be found as a function of both φ and Bi.

The same solving procedure was used as before, solving for δ_{cr} iteratively by looking for the existence of a steady-state solution, but in this case it was done for a range of values of both φ and Bi. Values of φ between 10 and 100 in increments of 5 were used. Values of Bi between 1 and 10 in increments of 1, and 10 and 100 in increments of 5, were used. Solving for these values is much more computationally expensive than the previous case because 19 values of φ and 28 values of Bi give 532 combinations which need to be solved for. The results are plotted in Figure 5-4 and Figure 5-5. For all four geometries investigated, it was found that for low Biot numbers the value of δ_{cr} decreased substantially, in contrast to low values of φ which caused an increase in the value of δ_{cr} as before.

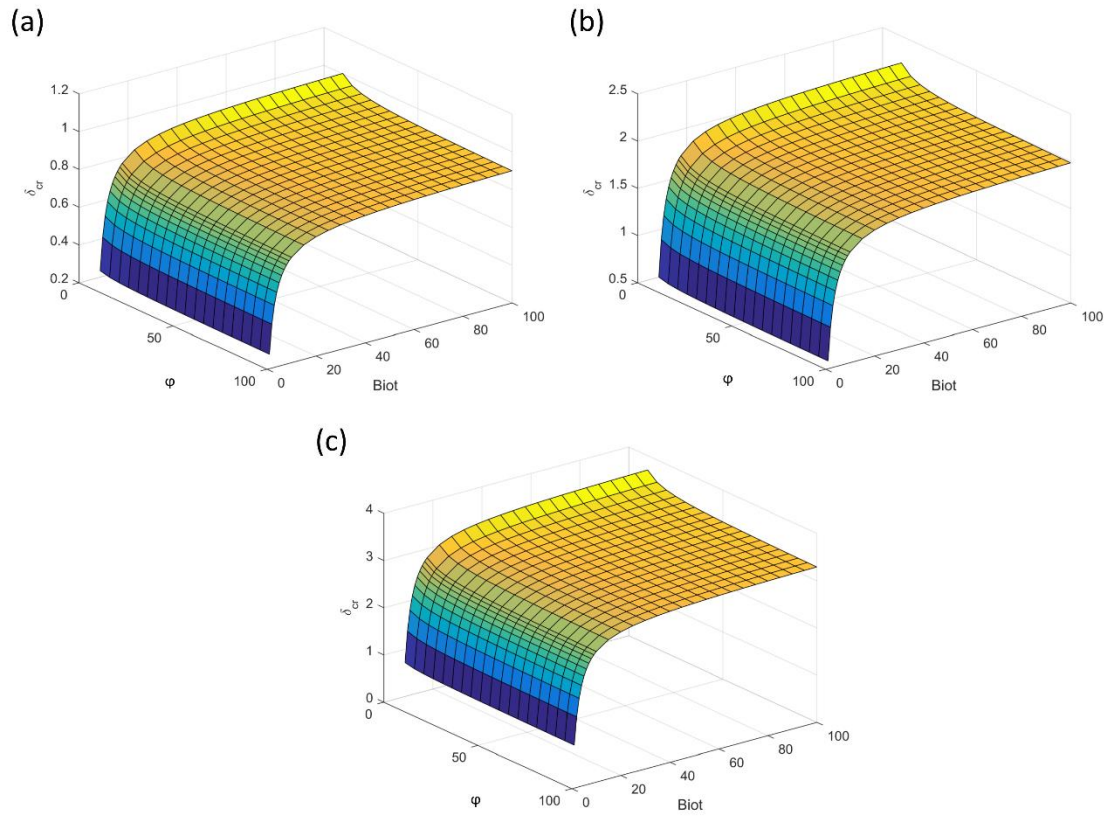

Figure 5-4: δ_{cr} as a function of φ and Bi for (a) an infinite slab, (b) an infinite cylinder, and (c) a sphere.

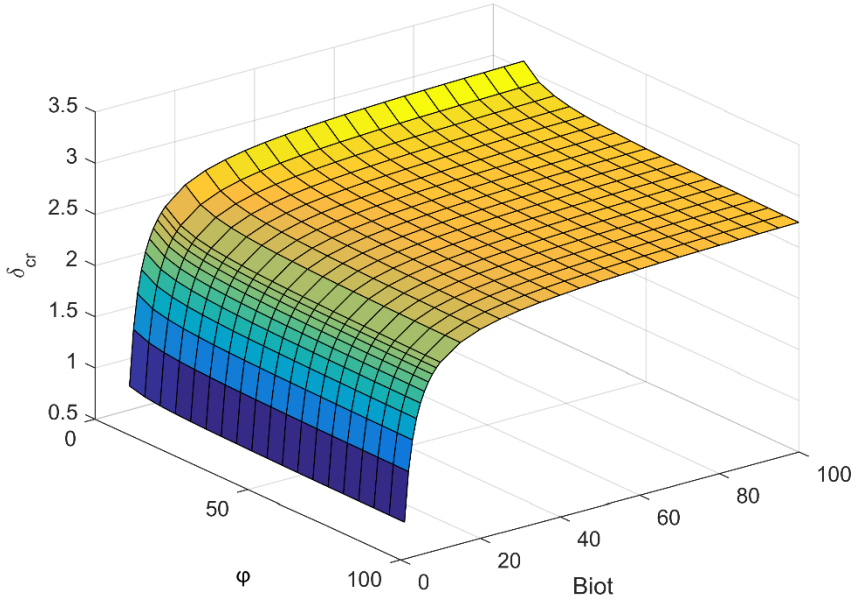

Figure 5-5: δ_{cr} as a function of φ and Bi for an equi-cylinder.

For the equi-cylinder δ_{cr} as a function of Bi at $\varphi = 100$ is plotted in Figure 5-6 (a). At this value it is the value of Bi that has the greatest influence on the calculated value of δ_{cr}. Biot numbers below 30 are seen to have a significant impact on the value of δ_{cr}, with a Biot number of 1 found to decrease δ_{cr} below 1 (note that when $\varphi = \infty$ and $Bi = \infty$ the value of $\delta_{cr} = 2.78$). In contrast to this, δ_{cr} as a function of φ at $Bi = 100$ are plotted in Figure 5-6 (b). In this case, very low values of φ increase the value of δ_{cr}, but its impact is almost an order of magnitude lower than that of the Biot number. These results can also be seen in Table 5-2, which is colour coded to show to gradient seen graphically in the other figures.

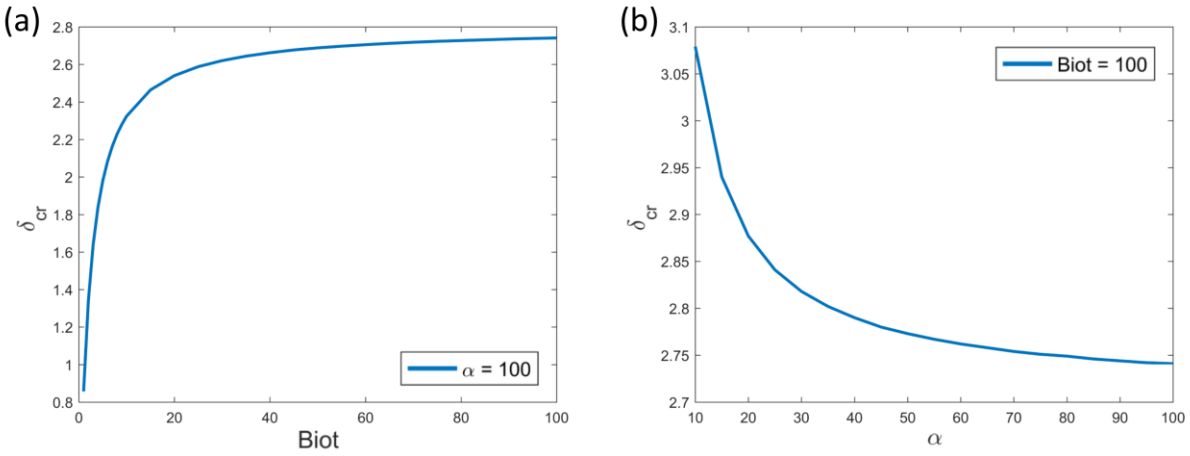

Figure 5-6: (a) δ_{cr} as a function of Bi at $\varphi = 100$ and (b) δ_{cr} as a function of φ at $Bi = 100$.

Table 5-2: δ_{cr} as a function of φ and Bi for an equi-cylinder.

φ \ Bi	1	2	3	4	5	6	7	8	9	10	15	20	25	30	35	40	45	50	55	60	65	70	75	80	85	90	95	100
10	0.95	1.49	1.83	2.05	2.21	2.33	2.43	2.50	2.56	2.61	2.77	2.85	2.91	2.94	2.97	2.99	3.01	3.02	3.03	3.04	3.05	3.05	3.06	3.06	3.07	3.07	3.08	3.08
15	0.91	1.43	1.75	1.97	2.12	2.23	2.32	2.39	2.44	2.49	2.64	2.72	2.78	2.81	2.84	2.86	2.87	2.88	2.89	2.90	2.91	2.92	2.92	2.93	2.93	2.93	2.94	2.94
20	0.89	1.40	1.72	1.92	2.07	2.18	2.27	2.34	2.39	2.44	2.59	2.67	2.72	2.75	2.78	2.79	2.81	2.82	2.83	2.84	2.85	2.85	2.86	2.86	2.87	2.87	2.87	2.88
25	0.88	1.39	1.70	1.90	2.05	2.16	2.24	2.31	2.36	2.41	2.55	2.63	2.68	2.72	2.74	2.76	2.77	2.79	2.80	2.80	2.81	2.82	2.82	2.83	2.83	2.83	2.84	2.84
30	0.88	1.38	1.68	1.89	2.03	2.14	2.22	2.29	2.34	2.39	2.53	2.61	2.66	2.69	2.72	2.74	2.75	2.76	2.77	2.78	2.79	2.79	2.80	2.80	2.81	2.81	2.81	2.82
35	0.87	1.37	1.67	1.88	2.02	2.13	2.21	2.28	2.33	2.38	2.52	2.60	2.65	2.68	2.70	2.72	2.74	2.75	2.76	2.77	2.77	2.78	2.78	2.79	2.79	2.80	2.80	2.80
40	0.87	1.36	1.67	1.87	2.01	2.12	2.20	2.27	2.32	2.37	2.51	2.59	2.63	2.67	2.69	2.71	2.72	2.74	2.75	2.75	2.76	2.77	2.77	2.78	2.78	2.78	2.79	2.79
45	0.87	1.36	1.66	1.86	2.01	2.11	2.19	2.26	2.31	2.36	2.50	2.58	2.63	2.66	2.68	2.70	2.72	2.73	2.74	2.74	2.75	2.76	2.76	2.77	2.77	2.77	2.78	2.78
50	0.87	1.36	1.66	1.86	2.00	2.11	2.19	2.25	2.31	2.35	2.49	2.57	2.62	2.65	2.68	2.69	2.71	2.72	2.73	2.74	2.74	2.75	2.76	2.76	2.76	2.77	2.77	2.77
55	0.86	1.35	1.65	1.85	2.00	2.10	2.18	2.25	2.30	2.35	2.49	2.56	2.61	2.65	2.67	2.69	2.70	2.71	2.72	2.73	2.74	2.74	2.75	2.75	2.76	2.76	2.76	2.77
60	0.86	1.35	1.65	1.85	1.99	2.10	2.18	2.24	2.30	2.34	2.48	2.56	2.61	2.64	2.66	2.68	2.70	2.71	2.72	2.73	2.73	2.74	2.74	2.75	2.75	2.76	2.76	2.76
65	0.86	1.35	1.65	1.85	1.99	2.10	2.18	2.24	2.29	2.34	2.48	2.56	2.60	2.64	2.66	2.68	2.69	2.70	2.71	2.72	2.73	2.73	2.74	2.74	2.75	2.75	2.76	2.76
70	0.86	1.35	1.65	1.85	1.99	2.09	2.17	2.24	2.29	2.34	2.48	2.55	2.60	2.63	2.66	2.68	2.69	2.70	2.71	2.72	2.73	2.73	2.74	2.74	2.74	2.75	2.75	2.75
75	0.86	1.35	1.64	1.84	1.98	2.09	2.17	2.24	2.29	2.33	2.47	2.55	2.60	2.63	2.65	2.67	2.69	2.70	2.71	2.72	2.72	2.73	2.73	2.74	2.74	2.75	2.75	2.75
80	0.86	1.34	1.64	1.84	1.98	2.09	2.17	2.23	2.29	2.33	2.47	2.55	2.60	2.63	2.65	2.67	2.68	2.70	2.71	2.71	2.72	2.73	2.73	2.74	2.74	2.74	2.75	2.75
85	0.86	1.34	1.64	1.84	1.98	2.09	2.17	2.23	2.29	2.33	2.47	2.55	2.59	2.63	2.65	2.67	2.68	2.69	2.70	2.71	2.72	2.72	2.73	2.73	2.74	2.74	2.74	2.75
90	0.86	1.34	1.64	1.84	1.98	2.08	2.17	2.23	2.28	2.33	2.47	2.54	2.59	2.62	2.65	2.67	2.68	2.69	2.70	2.71	2.72	2.72	2.73	2.73	2.73	2.74	2.74	2.74
95	0.86	1.34	1.64	1.84	1.98	2.08	2.16	2.23	2.28	2.33	2.47	2.54	2.59	2.62	2.65	2.66	2.68	2.69	2.70	2.71	2.71	2.72	2.72	2.73	2.73	2.74	2.74	2.74
100	0.86	1.34	1.64	1.84	1.98	2.08	2.16	2.23	2.28	2.32	2.46	2.54	2.59	2.62	2.64	2.66	2.68	2.69	2.70	2.71	2.71	2.72	2.72	2.73	2.73	2.73	2.74	2.74

The values for φ and Bi in this investigation were estimated as 32.64 and 11.57 respectively. These values were estimated for a 60mm equi-cylindrical basket. How this influences the value of δ_{cr} that is to be used in this investigation can be seen in Table 5-3. All geometries are seen to have a considerably lower value of δ_{cr} when the correct values of φ and Bi are used. In reality, the value of δ_{cr} varies with basket size because this changes the value of Bi. Also the value of φ is dependent on the activation energy, E, which is calculated using this value of δ_{cr}, such that these value are inextricably linked. In calculating the kinetics using this method, an iterative procedure is required and this is discussed next.

Table 5-3: δ_{cr} values for common geometries at ideal conditions (left) and at the conditions used in this investigation (right).

	$\boldsymbol{\varphi = \infty, Bi = \infty}$	$\boldsymbol{\varphi = 32.64, Bi = 11.57}$
Infinite Slab	0.878	0.790
Infinite Cylinder	2	1.745
Sphere	3.32	2.891
Equi-Cylinder (height=diameter)	2.844	2.427

5.2.2. Steady-State Method Results

The steady-state approach was performed as outlined previously in Section 5.2. The critical ambient temperature was determined for three equi-cylindrical baskets, of equal height and diameter 50mm, 60mm, and 70mm. A thermocouple was placed close to the basket to measure the true ambient temperature. This was done because the ambient temperature measured close to the basket varied from that measured by the in-built thermocouple, housed towards the roof of the oven, which was used by the oven's temperature controller to set the temperature. In some the set oven temperature and the temperature measured close to the basket could vary by as much as 4°C. The critical ambient temperatures for the three baskets are shown in Table 5-4. Sinusoidal fluctuations were seen in the oven temperature causing this temperature to fluctuate within approximately a 0.5°C ranges. This was probably due to a slow response in the

oven's temperature controller. Because of this, the critical ambient temperatures for each basket were taken as the average oven temperature over the duration of the experiment.

Table 5-4: Critical ambient temperatures for the baskets used in the steady-state method.

Basket Diameter/Height	**Critical Ambient Temperature, T_{crit}**
50mm	227.26°C (500.41K)
60mm	221.30°C (494.45K)
70mm	216.38°C (489.53K)

Using these critical ambient temperatures, the kinetics of this formulation were estimated in accordance with equation (5-6). To estimate these kinetics, a value of δ_{cr} needed to be used. As mentioned, an iterative procedure is required in order to use the correct value of δ_{cr} for each data point. Firstly, using the estimated value of δ_{cr} for an equi-cylinder in Table 5-3, $\frac{1}{T_{\infty,cr}}$ was plotted against $\ln\left(\frac{\delta_{cr}T_{\infty,cr}^2}{L^2}\right)$ and the first guess for the kinetics E and $\ln QA$ were found. Now, using this first guess, an iterative procedure can be implemented.

The Biot number for each basket must next be calculated. The heat transfer coefficient, h, was calculated using the correlation measured using the transient temperature measurement method in Section 4.5. The thermal conductivity, k, was taken as 0.08 W m^{-1} K^{-1}, a value approximated from the novel Parameter Estimation Approach used in the subsequent Chapter 6. The characteristic length was taken as the basket radius or half-height, which are equal for an equi-cylinder. The Biot number, Bi, for each of the baskets is shown in Table 5-5. These value remains constant for each iteration.

Table 5-5: Biot numbers for the baskets used in the steady-state method.

Basket Diameter/Height	**Biot Number, Bi**
50mm	9.64
60mm	11.58
70mm	13.52

The value of φ is calculated next. This value changes with each iteration because it is dependent on the estimated value of the activation energy, E, from the previous iteration. Each basket also has its's own value of φ because each basket has a different value of $T_{\infty,cr}$. Using the values of φ and Bi, a new value of δ_{cr} is interpolated for each basket using Table 5-2, and new values of $\frac{1}{T_{\infty,cr}}$ are plotted against $\ln\left(\frac{\delta_{cr}T_{\infty,cr}^2}{L^2}\right)$. This gives the new values of E and $\ln QA$. This iterative procedure is repeated until little change is seen in the estimated kinetics. In this case, only 4 iterations were required for the estimated values of E and $\ln QA$ to converge to 7 significant figures. The final values of φ and δ_{cr} for each basket are shown in Table 5-6. The results of the final iteration can be seen in Figure 5-7. The resulting kinetics are shown in Table 5-7. The associated errors in Table 5-7 are the 95% confidence intervals of the linear regression to the data.

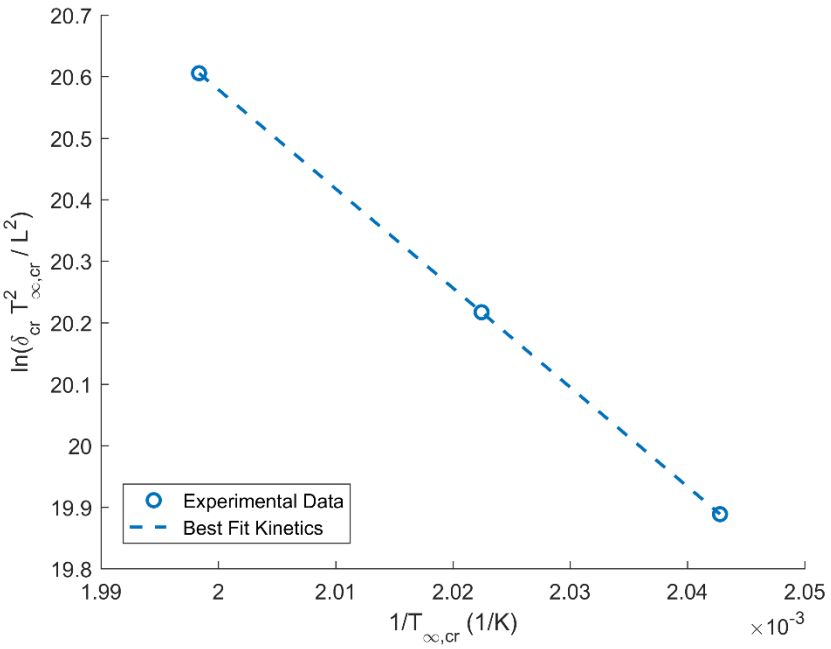

Figure 5-7: Steady-state approach results using 50mm, 60mm, and 70mm equi-cylindrical baskets.

Table 5-6: The final values of φ and δ_{cr} for each basket as calculated using the outlined iterative procedure.

	$\boldsymbol{\varphi}$	$\boldsymbol{\delta_{cr}}$
50mm	30.11	2.372
60mm	30.47	2.434
70mm	30.78	2.490

Table 5-7: Activation energy, E, and the natural logarithm of the product of the heat of reaction and the pre-exponential factor, $\ln QA$, as estimated using the steady-state method.

	$\boldsymbol{E}$ (J mol^{-1})	$\boldsymbol{\ln QA}$
Steady-State Approach	125.3 (±1.0) x10^3	31.90 (±0.25)

How the iterative procedure affects the results can be seen in Figure 5-8. The results are seen to slightly change between the first and final iteration. This is also seen to have an impact on the critical ambient temperature calculated using the resulting kinetics from each of these iterations and the equation for δ (5-4). The results from the first iteration do not compare as well with the actual $T_{\infty,cr}$ values as the final iteration does. The difference in critical ambient temperature is also seen to increase as the basket size increases or decreases considerably beyond the measured sizes. This shows that using the correct value of δ_{cr} for the system, and even each basket used, is important. Equally important is the iterative procedure applied here.

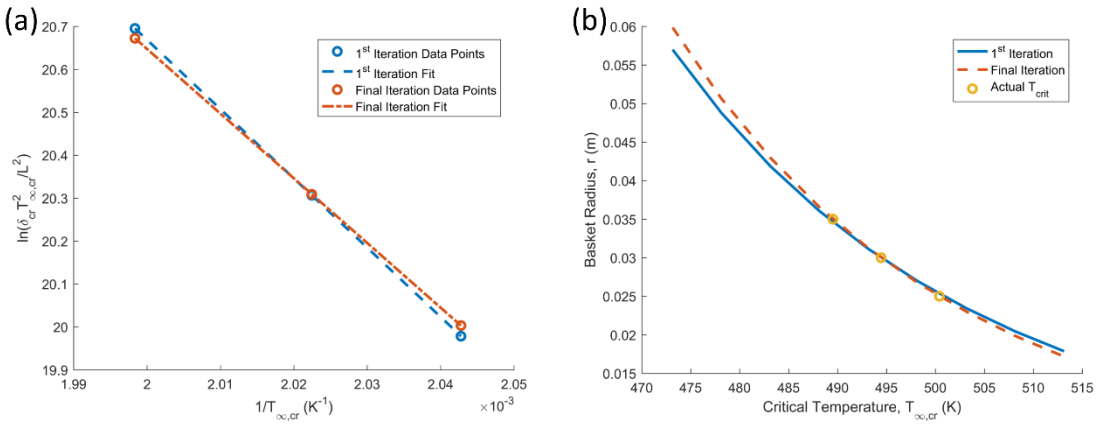

Figure 5-8: Steady-State method results after the first and final iterations. (a) Results plotted in accordance with equation (5-6). (b) Critical ambient temperatures as a function of basket size calculated using the resulting kinetics of each iteration.

Only three baskets were used to produce these results so it is difficult to say definitively that these results are good, but a good fit was found to these three points. This can be seen from the low 95% confidence intervals shown in Table 5-7. This method is relatively easily to perform, with only a single thermocouple required to measure the temperature at the centre of the basket. The accuracy of the placement of this thermocouple is not

of critical importance. So long as it is placed close to the basket centre then it will be easy to see when thermal runaway occurs. The only error is in the measurement of the ambient temperature. Another advantage is that the kinetics measured using this method are based on experimentally measured critical ambient temperatures, such that a model using these kinetics will predict thermal runaway in agreement with experimentally measured runaway.

Despite this, there are a number of disadvantages associated with this method. This method is particularly slow. Experiments for the 50mm equi-cylindrical basket took approximately 5 hours, while experiments for the 70mm equi-cylindrical basket took approximately 8 hours. Larger baskets than this are rather impractical to experiment with. Additionally, each of these experiments does not yield a data point, and it can take a considerable number of experiments to find the critical ambient temperature to within 0.5°C, as was done here. For this reason, a less time consuming method is required.

5.3. Cross-Point Temperature Method

The Cross-Point Temperature (CPT) method is a transient means of determining zero-order self-heating reaction kinetics developed by Chong et *al.* (Chong, et al., 1996), and seen as a faster alternative to the much slower steady-state method. This method was outlined in Section 3.3.3, where initial CPT method experiments were performed using a setup with two thermocouples. These initial experiments showed that this method has promise as a means of measuring the self-heating kinetics of these powders. Errors, and in particular thermocouple placement errors, significantly affected the results. Further experiments and analysis are conducted here to improve upon this method.

As outline in Section 3.3.3, the cross-point temperature method is based around the assumption that at some point the conduction term in equation (4-1) reduces the zero. The temperature at which this occurs is known as the cross-point temperature (CPT) and at this point equation (4-1) reduces to:

$$\ln\left(\frac{dT}{dt}\right)\Big|_{T=T_{CPT}} = \ln\left(\frac{QA}{C_p}\right) - \frac{E}{RT_{CPT}} \qquad (5\text{-}20)$$

In this chapter, two equi-cylindrical baskets of diameter 50mm and 60mm were used with an array of three thermocouples placed within the powder. Type K thermocouples (RS Pro 363-0294) were used. These thermocouples were glass fibre insulated with a welded exposed junction and supplied with a working range of -60° to 350°C. Of these thermocouples, one was placed at the centre of the basket at the basket half-height. The other two were offset from this at spacings of 6mm and 12mm from the centre, as can be seen in Figure 5-9.

For each experiments the baskets were filled to the same mass of powder. The baskets were filled and tapped. The 60mm basket was filled to a mass of approximately 118.5(±0.5)g and the 50mm basket to a mass of approximately 68.5(±0.5)g, corresponding to a density of approximately 698.5 kg m^{-3}.

This setup also included a new approach to thermocouple placement. In the initial experiments carried out in Section 3.3.3, two thermocouples were used that were simply twisted together. Twisting them together helped to ensure that a constant spacing of 6mm was achieved, but made accurate placement of these thermocouples difficult. As can be seen in Figure 5-9, a spacer above the basket was used to ensure the thermocouples were at positions of 0mm, 6mm, and 12mm. Once the basket was filled, the spacer was attached to the top of the basket and the thermocouples inserted down to the basket half-height. The thermocouples were rigid enough that they did not bend when inserted into the powder. This method improves upon the previous approach, but it is still not possible to verify the placement of the thermocouples once inserted, such that there are still errors associated with this method.

These baskets were heated in a Memmert UF75 forced convection oven. The thermocouples were connected to a Pico Technology USB TC-08 data logger and sampled at a rate of 1 measurement per second. These baskets were heated at temperatures ranging from 222°C (495K) to 235°C (508K). An additional thermocouple is placed close to the basket to measure the true ambient temperature, which varied from the in-built thermocouple used by the oven's temperature controller to set the oven temperature. In some cases these measured temperatures varied by as much as 4°C.

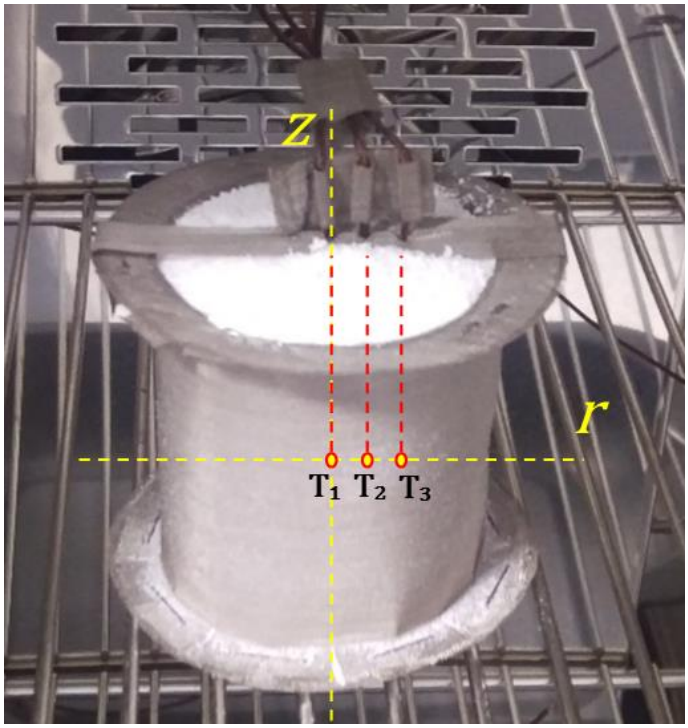

Figure 5-9: Basket of detergent powder and thermocouple setup.

5.3.1. Cross-Point Temperature Method Results

In this investigation an array of three radially spaced thermocouples was used. These thermocouples, as labelled in Figure 2, are T_1 at 0mm, T_2 at 6mm, and T_3 at 12mm from the centre. The temperature-time profiles measured by these three thermocouples at ambient temperatures ranging from 225°C to 231°C are shown in Figure 5-10.

It can be seen in each of these plots that the basket starts at a uniform temperature close to room temperature. As time progresses the basket is seen to increase in temperature, with the outermost thermocouple at 12mm increasing in temperature first, as would be expected. The plateau seen to occur in each of the plots is due to the evaporation of the residual moisture in the detergent powder particles. The central temperature is seen to stagnate longest, and this is because of the slow diffusion of the evaporated moisture out of the basket, limiting the temperature rise at the centre.

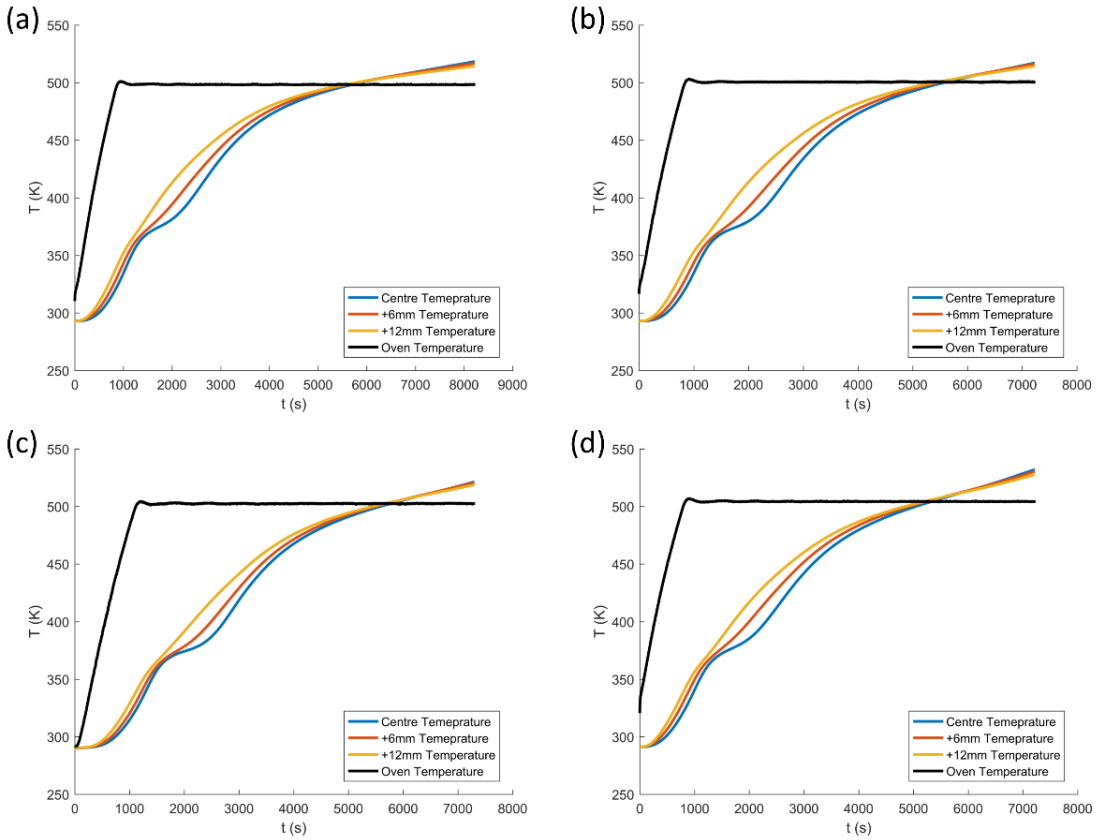

Figure 5-10: Temperature-time profiles for a 60mm basket as measured by thermocouples at the basket centre, +6mm, and +12mm for ambient temperatures of approximately (a) 225°C (498K), (b) 227°C (500K), (c) 229°C (502K), and (d) 231°C (504K).

By having an array of three thermocouple it is possible to evaluate three different cross-point temperatures. The first case (case 1) is taken when the centre (0mm) and thermocouple offset at 6mm are at the same temperature, with the temperature rate, dT/dt, taken at the basket centre point. A three point, central, second order, finite difference approximation is used to approximate the conduction term at this cross-point. At some position i, this approximation is expressed as:

$$\frac{d^2T}{dr^2} = \frac{T_{i-1} - 2T_i + T_{i+1}}{\Delta r^2} \tag{5-21}$$

If i is taken as the basket centre, then because of symmetry about the central axis in an equi-cylinder, $T_{i-1} = T_{i+1}$, where $i-1$ and $i+1$ are two points equally spaced by a distance of Δr either side of the basket centre. Substituting for the thermocouples at 0mm and 6mm, it can be seen when these temperatures are equal, the conduction term can be approximated as equal to zero:

$$\frac{d^2T}{dr^2} = \frac{2(T_{6mm} - T_{0mm})}{\Delta r^2} = 0 \quad \rightarrow \quad T_{0mm} = T_{6mm} \tag{5-22}$$

The second case (case 2) uses the same equation but measures the conduction between the central thermocouple and the thermocouple at 12mm from the basket centre.

$$\frac{d^2T}{dr^2} = \frac{2(T_{12mm} - T_{0mm})}{\Delta r^2} = 0 \quad \rightarrow \quad T_{0mm} = T_{12mm} \tag{5-23}$$

The third case (case 3) is somewhat more complex. Whereas the previous two cases use the three point stencil for the second order temperature difference term in equation (5-21), the conduction term here is approximated using a five point stencil for the second order finite difference approximation. This stencil makes use of the temperatures at five points, instead of three, centrally spaced about the temperature T_i. The temperature rate, dT/dt, is again taken at the centre. This difference approximation is given by:

$$\frac{d^2T}{dr^2} = \frac{-T_{i-2} + 16T_{i-1} - 30T_i + 16T_{i+1} - T_{i+2}}{12\Delta r^2}, \tag{5-24}$$

Again, because of symmetry, $T_{i-2} = T_{i+2}$ and $T_{i-1} = T_{i+1}$, and substituting for the thermocouples at 0mm, 6mm, and 12mm, this equation reduces to:

$$\frac{d^2T}{dr^2} = \frac{-15T_{0mm} + 16T_{6mm} - T_{12mm}}{6\Delta r^2} = 0. \tag{5-25}$$

In a perfect system a five point stencil reduces the order of the error in approximating the second order derivative term from an order of $O(\Delta r^2)$ to $O(\Delta r^4)$. It is worth noting that a similar three thermocouple setup has been used in previous investigations (Chen & Chong, 1995), but in each case a three-point second order finite difference approximation was applied to the three thermocouples. In doing this the cross-point was measured at the position of T_2. This is not incorrect, and the cross-point can be measured here, but the problem was that the temperature rate, dT/dt, was measured at the position of T_1 (i.e. the basket centre), instead of at the centre of the finite difference. In this approach, using symmetry, case 3 measures both the cross-point temperature and the temperature rate, dT/dt, at the position of T_1.

At each of the cross-points, the corresponding temperature rate dT/dt is measured. These values are plotted in accordance with equation (5-20) to estimate the kinetics. For a 50mm equi-cylindrical basket at an ambient temperature of approximately 229°C

(502K), the case 1 cross-point and temperature rate are shown in Figure 5-11 (a). It can be seen in Figure 5-11 (b) that the temperature difference between the central and 6mm thermocouple is very small, making it very difficult to accurately measure the cross-point. This small temperature difference makes thermocouple placement very important, with any error in placement and readings impacting on the result.

A similar plot, but for the case 2 cross-point, consisting of the central and 12mm thermocouple, is shown in Figure 5-12. It can be seen that at this distance, although still small, the difference is considerably larger. This makes reading this cross-point much easier, and in theory less susceptible to errors in thermocouple placement and readings. Again, this will be discussed in the upcoming uncertainty analysis.

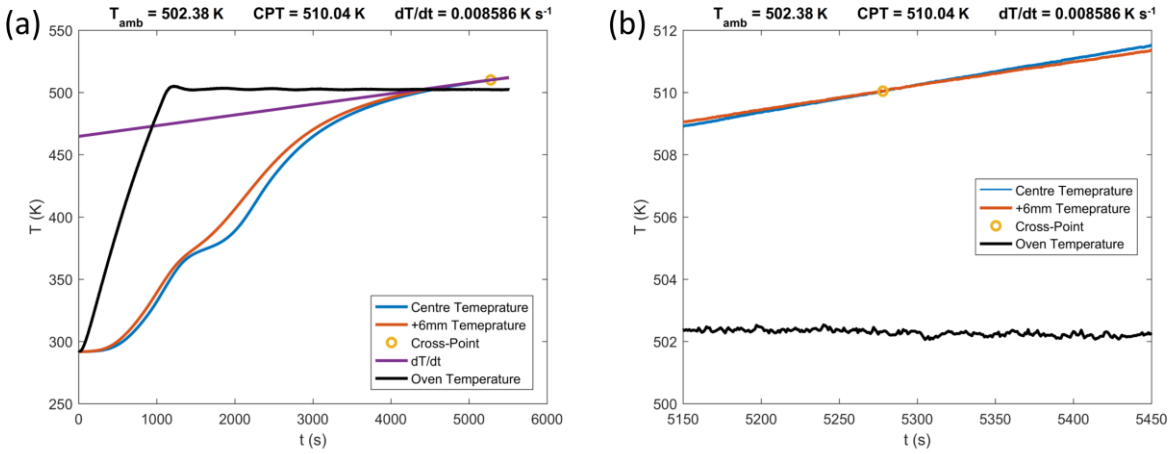

Figure 5-11: Case 1 cross-point for a 50mm basket at an oven temperature of approximately 229°C (502K).

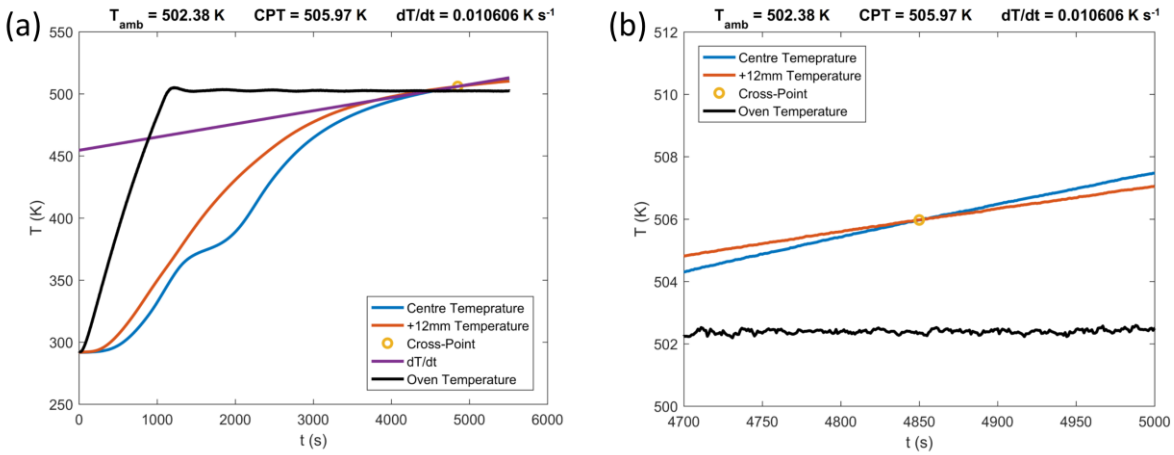

Figure 5-12: Case 2 cross-point for a 50mm basket at an oven temperature of approximately 229°C (502K).

Finally, the case 3 cross-point has also been plotted, and this can be seen in Figure 5-13. In this case, the close-up of the cross-point is not included because the equation used to calculate this cross-point means that it does not coincide with the crossing of two of the temperature profiles. This case looks very similar to that of case 1, and this is found for all ambient temperatures. This is because case 3 is more heavily influenced by the thermocouple at 6mm (T_2) used in case 1, than by the thermocouple at 12mm (T_3) used in case 2. Again the influence of this is discussed in the upcoming uncertainty analysis.

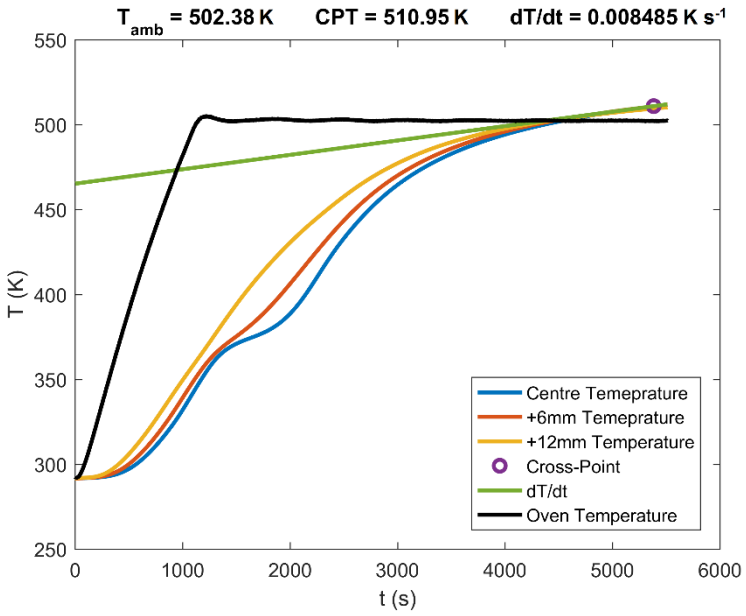

Figure 5-13: Case 3 cross-point for a 50mm basket at an oven temperature of approximately 229°C (502K).

In this investigation, a 50mm and a 60mm equi-cylindrical basket was used. Cross-points are only evident over a narrow band of ambient temperatures, so using two basket sizes allowed more cross-points to be determined. In both baskets, the same thermocouple setup was used. These baskets were run at ambient temperatures between 222°C (495K) and 235°C (508K). The ambient temperatures at which each basket was run is detailed in Table 5-8. At the lower of these ambient temperatures, little self-heating is exhibited, while the baskets at the higher ambient temperatures culminate in thermal runaway. Additional experiments were run at oven temperatures below 222°C (495K), but they were seen exhibited very little self-heating, making the cross-point temperatures

difficult to measure and more sensitive to errors in thermocouple readings and placement.

The results for this method have been calculated for each basket separately, and for both baskets together, and these results explored. The results for the two baskets separately, showing the three cases and the best fit linear regression to each case from which the kinetics are estimated, are shown in Figure 5-14. Figure 5-14 (a) shows the results for the 50mm basket, while Figure 5-14 (b) shows the results for the 60mm basket. Figure 5-15 shows the results for each case where the results of both baskets are combined.

Table 5-8: Temperatures at which the 50mm and 60mm equi-cylindrical baskets were run.

	50mm Basket	**60mm Basket**
222°C		✓
223°C		✓
224°C	✓	✓
225°C	✓	✓
226°C	✓	✓
227°C	✓	✓
228°C	✓	
229°C	✓	✓
230°C	✓	
231°C	✓	✓
232°C	✓	
233°C	✓	✓
235°C	✓	

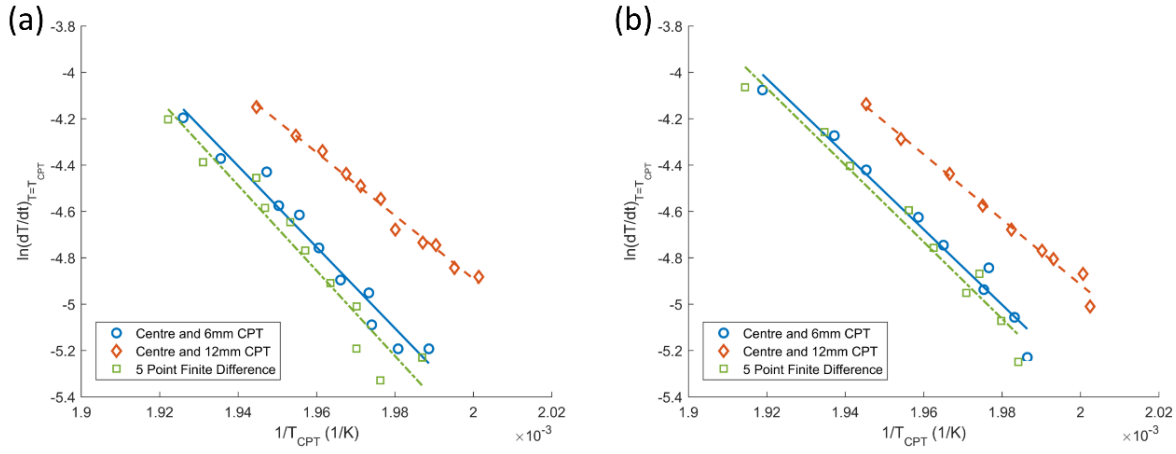

Figure 5-14: CPT method results for a (a) 50mm equi-cylindrical basket and (b) 60mm equi-cylindrical basket.

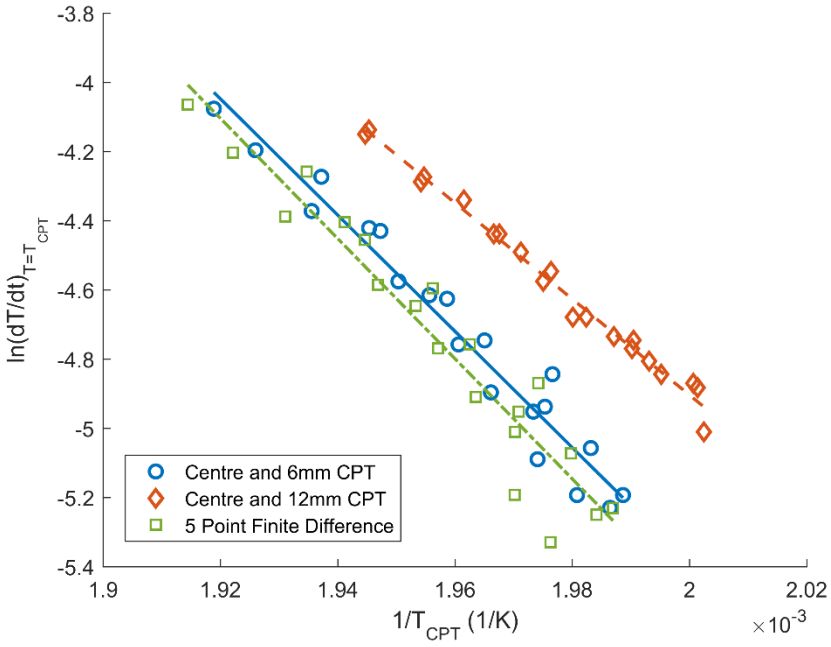

Figure 5-15: Combined results for the CPT method using both a 50mm and 60mm baskets.

The resulting kinetics for the three cases where both the 50mm and 60mm baskets are considered are shown in Table 5-9. It can be seen that each case gives different results. The activation energies of case 1 and 3, 139.7x10^3 J mol^{-1} and 144.4x10^3 J mol^{-1} respectively, are very different to the activation energy estimated using the steady-state approach, 125.3x10^3 J mol^{-1}. The kinetics of case 2, with an activation energy of 115.5x10^3 J mol^{-1} and $\ln(QA/C_p)$ value of 22.88, are more similar to the steady-state approach kinetics. They also predict a much closer critical ambient temperature, 223.9°C

(497.1K), to that observed experimentally for a 60mm equi-cylindrical basket, 221.3°C (494.5K). Case 1 and 3 over predict this with values of 229.1°C (502.3K) and 229.9°C (503.1K) respectively. Other work (Sujanti, et al., 1999) (Malow & Krause, 2004) has shown that the steady-state approach and CPT method yield comparable results for coal, cork dust, riboflavin, and a detergent powder. The activation energies for this detergent formulation are greater than those of Malow and Krause (2004), who measured values of 102(±30)x10^3 J mol^{-1} and 112(±24)x10^3 J mol^{-1} using the steady-state approach and CPT method respectively. Details of the detergent powder formulations used by Malow and Krause were not given, and as such it is difficult to draw comparisons between the kinetics. However, the associated error, which is the 95% confidence interval of the linear regression to the data, for the steady-state and case 2 results in particular are considerably smaller than those of Malow and Krause.

Table 5-9: Summary of estimated kinetics for the two basket heating methods and the corresponding critical ambient temperature for a 60mm equi-cylindrical basket.

	E (J mol^{-1})	$\ln QA$	$\ln \frac{QA}{C_p}$	60mm T_{crit} (°C)
Steady-State Approach	125.3 (±1.0) x10^3	31.90 (±0.25)	-	221.3
CPT Case 1	139.7 (±14.9) x10^3	-	28.21 (±3.51)	229.1
CPT Case 2	115.5 (±6.4) x10^3	-	22.88 (±1.53)	223.9
CPT Case 3	144.4 (±21.2) x10^3	-	29.24 (±4.99)	229.9

Figure 5-16 shows the three cases separately and from this it can be seen that the data points for case 2 are much less scattered than the other two cases. This is echoed in the confidence intervals for case 2 which are considerably smaller than those of case 1 and 3, with the confidence intervals of case 3 found to be particularly large.

These experiments were simulated using the numerical model and the cross-point temperatures determined for the same three cases. This analysis is discussed in detail in the next section. The results of this analysis are shown in Figure 5-17 and suggest that there should not be such a large discrepancy between the results of these three cases. It does, however, show that a small difference should exist between the cases. This difference is found to increase with an increase in thermocouple spacing. The

approximation associated with the cross-point temperature assumption and the finite difference approximation used in equation (5-21) is thought to be the reason for this difference.

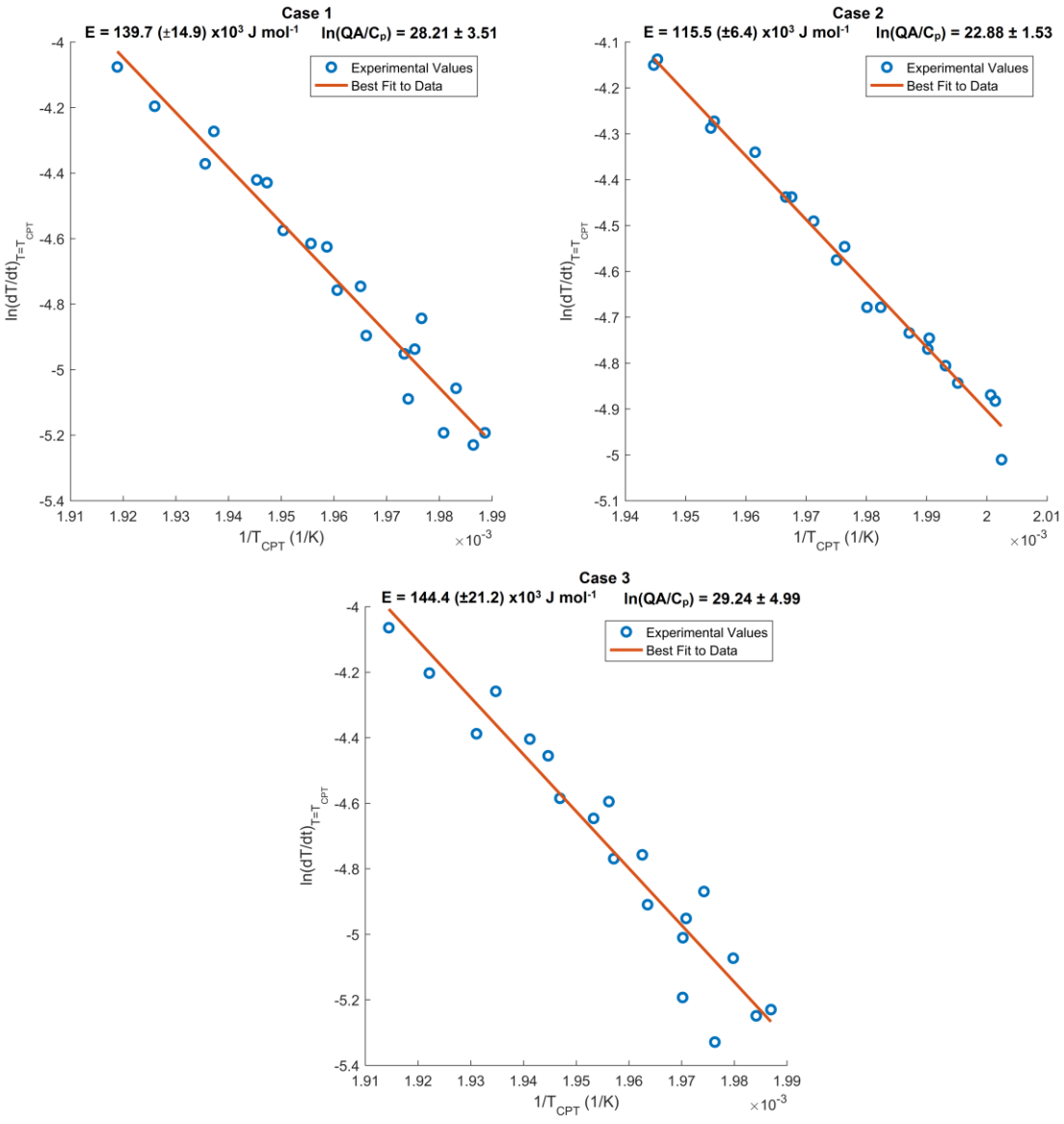

Figure 5-16: CPT method results separated by case using both a 50mm and 60mm baskets.

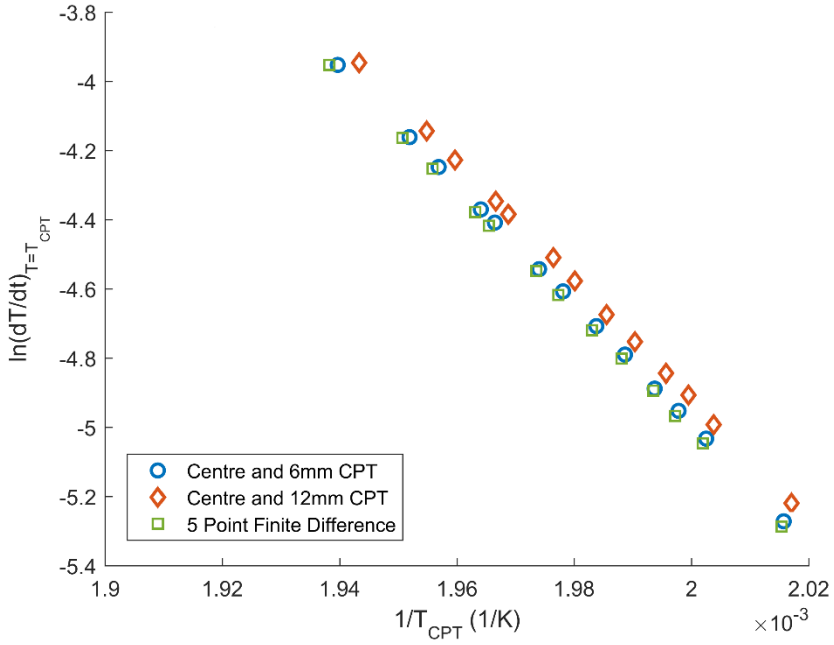

Figure 5-17: Model simulated cross-point temperature method experiments simulating the same three thermocouple pairing cases as measured experimentally.

The kinetics from the three cases were compared by using the kinetics in the equation for δ (5-4). The critical ambient temperature for equi-cylindrical baskets of a range of sizes were predicted using the kinetics measured for the 50mm and 60mm baskets both separately and together. This can be seen in Figure 5-18. It can be seen that none of these cases agree exactly with the experimentally measured critical ambient temperatures, with case 1 and case 3 over predicting the critical ambient temperatures, and case 2 under predicting. It can be seen that the case 2 results are better, particularly for smaller basket sizes, and that the kinetics from all three methods (50mm basket, 60mm basket, and both) are in agreement. This coincides with the reduced scatter seen for the case 2 results in the previous plots. Again there is a big difference in the predictions of each of the cases.

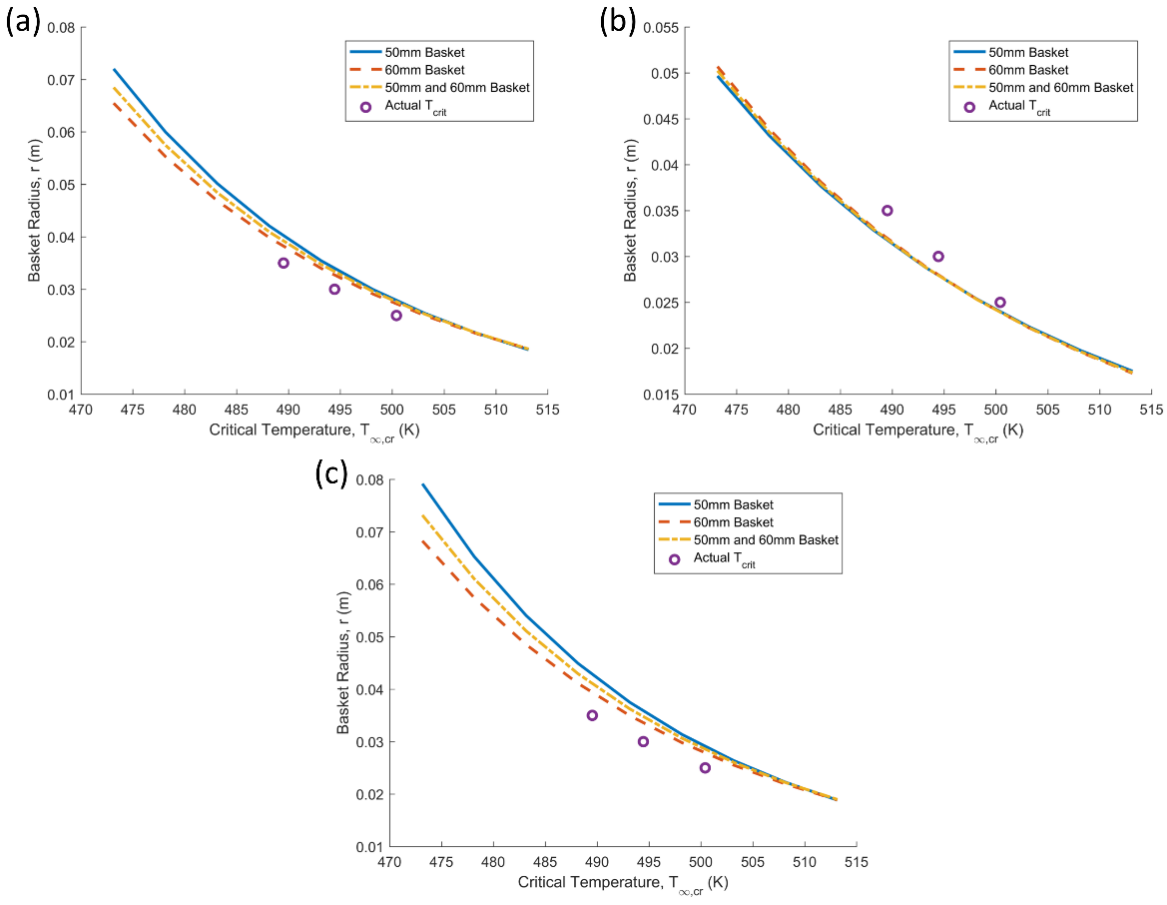

Figure 5-18: Critical ambient temperature for a ranges of equi-cylindrical basket sizes, using the kinetics for the 50mm and 60mm baskets both separately and together, for (a) case 1, (b) case 2, and (c) case 3.

5.3.2. Uncertainty Analysis

The errors in the cross-point temperature method can be attributed to a combination of the error in thermocouple readings (±0.25°C) and error in thermocouple placement (±1mm). In the cross-point region, the difference in temperatures across the three thermocouples is quite small, and thus any error in the measured temperatures, be it due to error in thermocouple readings or errors in placement, will have a significant impact on the measured cross-points. Looking across all the 50mm basket experiments, an increase in oven temperature of 1°C corresponds to an average increase in the case 2 cross-point temperature of 1.32°C. With such small differences in cross-point temperatures it is evident that an error in thermocouple readings of ±0.25°C will have a significant impact. Errors in thermocouple placement are difficult to quantify. It is difficult to verify their position because the thermocouples are inserted into the powder

after the basket is filled, and thus the approximated error in placement of ±1mm could have a significant impact on the measured cross-points.

These issues account for the errors in the measured values, but do not explain why the three cross-point cases estimate different kinetics. The difference between the three cases may be due to the spacing between the 0mm and 6mm thermocouple being too small. Only a small number of particle diameters would fit into the 6mm gap between thermocouples T_1 and T_2. The mass median particle diameter is 328µm, such that 19 median particles would fall within this space. Although micronized sodium sulphate was used in this formulation in an effort to reduce composition variability, some variability in composition will still exist between the particles. The packing of the baskets, which were simply filled to a consistent density, will also impact on the variability, and with an average of 19 particles in the 6mm spacing, these sources of variability with impact on the results. In particular, this would heavily influence the case 1 results, whereas the larger spacing of 12mm used for the case 2 cross-point means that these results are not a susceptible to this variability.

The susceptibility of the case 1 results to this variability explains why the confidence intervals associated with the case 2 results are much smaller than those of case 1. Similar experiments conducted using other detergent formulations are shown in Section 5.5. These formulations do not make use of micronized sodium sulphate, and as such may have a greater degree of composition variability. These formulations have much more pronounced issues when using the same thermocouple spacing of 6mm, and for each of the three formulations tested, this variability made it impossible to fit kinetics to the case 1 results.

It can been seen from the equation for case 3 in (5-25) that the thermocouple T_2 has a much greater influence than T_3 on the five point finite difference approximation for the second order temperature derivative. This explains why the case 3 results are more similar to the case 1 results, with case 3 also being affected by the issues of variability that impacted on the case 1 results, and the problem of the small number of particle diameters that would fit between the thermocouples T_1 and T_2.

5.4. Model Analysis of the Cross-Point Temperature Method

5.4.1. Simulation of the Performed Cross-Point Temperature Method Experiments

The kinetics measured using the steady-state method, shown in Table 5-7, were used in the numerical model. Using these kinetics gives a model that predicts critical ambient temperatures in almost exact agreement with the experimentally measured values, so long as the correct value for δ_{cr} is used, which reflects the self-heating reaction kinetics and model boundary conditions. This is because the dimensionless equations used to derive the steady-state method are the exact dimensionless equivalents of the numerical model equations.

Using the kinetics from the cross-point temperature method, the predicted critical ambient temperature were very different. It is thought that this is because the CPT method is more susceptible to errors. In a perfect system, one would expect the results of these two methods to be identical. This was explored numerically using the heat transfer model outline in Section 4.2, making use of the kinetics determined using the steady-state method. The drying equations are excluded from this model, such that only heat transfer and heat generation are modelled. The model is used to predict temperature-time profiles for a 60mm equi-cylindrical basket of powder, heated from room temperature to a range of different ambient temperatures.

The model was used to replicate the performed experiments. An equi-cylindrical basket of diameter and height 60mm was simulated with thermocouples at radial distances of 0mm, 6mm, and 12mm from the basket centre and at the basket half-height, as shown in Figure 5-19. Using this setup it is possible to predict the temperatures at the three thermocouple positions and therefore calculate the three different cross-point temperatures identified by equations (5-22), (5-23), and (5-25).

The model was simulated at 10 ambient temperatures between 493K (220°C) and 502K (229°C). In each simulated experiment the oven starts at the same temperature as the powder basket, 293K (20°C), and is ramped up to its final temperature.

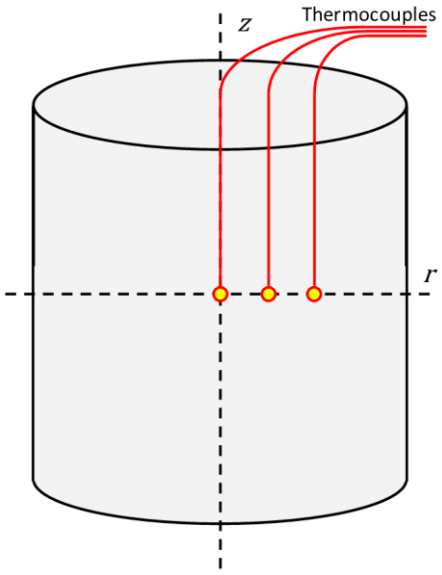

Figure 5-19: Experimental basket setup replicated numerically. Three thermocouples were simulated at radial distances of 0mm, 6mm, and 12mm.

The profile of the second order temperature derivative term was calculated for each case, and for the duration of the experiment. This profile allows the cross-point to be identified by determining the point at which these temperature derivatives are equal to zero. This can be seen along with the simulated basket core temperature in Figure 5-20.

It can be seen that all these profiles start at zero and then increase in value to some peak. This is because the basket starts at a uniform temperature, then as the oven temperature increases the basket heats from the basket edges inwards, increasing the temperature gradient. The basket then approaches a steady-state temperature, reducing this temperature gradient back towards zero. As the temperature in the basket increases, the reaction rate increases, and self-heating increases the temperature at the core above the temperatures of the surrounding regions. This can be seen in how the temperature gradient falls below zero. The cross-point for each case is the point at which this gradient equals zero.

The temperature gradient for case 1 and 3 are almost identical. The 5 point stencil used for case 3 should in theory reduce the order of the error of the finite difference approximation. Case 2 measures the gradient across a greater distance, and this is reflected in the greater temperature gradient seen at the profile peak.

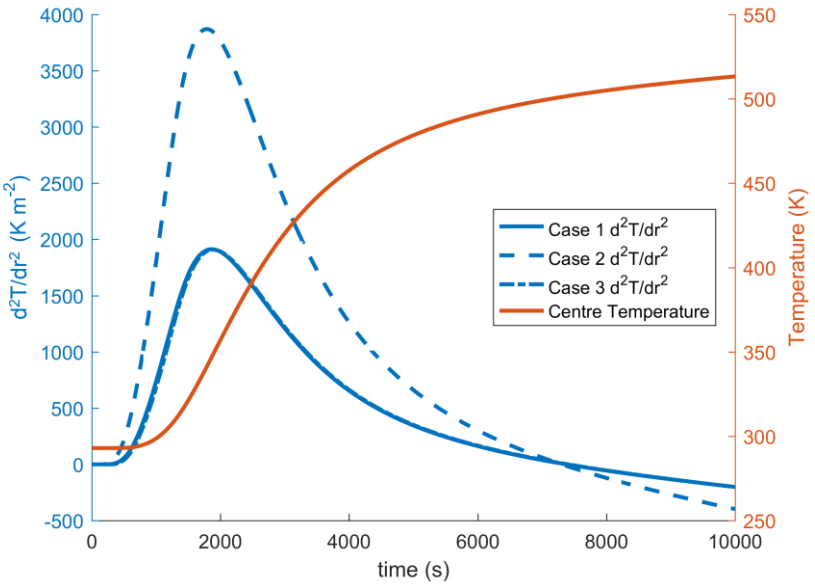

Figure 5-20: The profile of the second order temperature derivative term for three cross-point cases, and the simulated basket core temperature at an ambient temperature of 497K (224°C).

The radial temperature profiles at each of the three cross-points are shown in Figure 5-21 (a). The profile close to the central axis is relatively flat at these points, but it is thought that if larger thermocouple spacing are used, then this radial temperature profile may not be entirely flat at the cross-point. Figure 5-21 (b) confirms this problem, showing that for a very large thermocouple spacing the temperature profile would not be flat, even though the thermocouples may be at the same temperature. In this case it would be wrong to assume that conduction across that region has ceased.

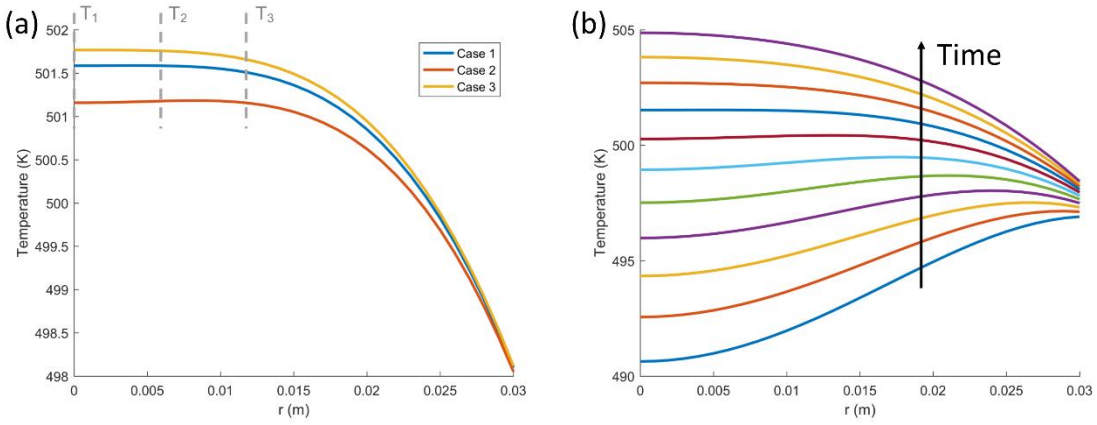

Figure 5-21: (a) Radial temperature profile at each of the three cross-points for an ambient temperature of 497K (224°C). (b) Radial temperature profiles at $z = 0mm$ as

time progresses throughout the experiment, simulated at an ambient temperature of 497K (224°C).

Using these data, the three different cross-points were found for each experiment. The results, plotted as they would be in the cross-point temperature method, can be seen in Figure 5-22. A slight difference can be seen across the three cases. They all have a similar slope, which would lead to all cases measuring similar activation energy values, E, but they have slightly different intercepts, which influences the measured values of the logarithmic term $\ln(QA/C_p)$.

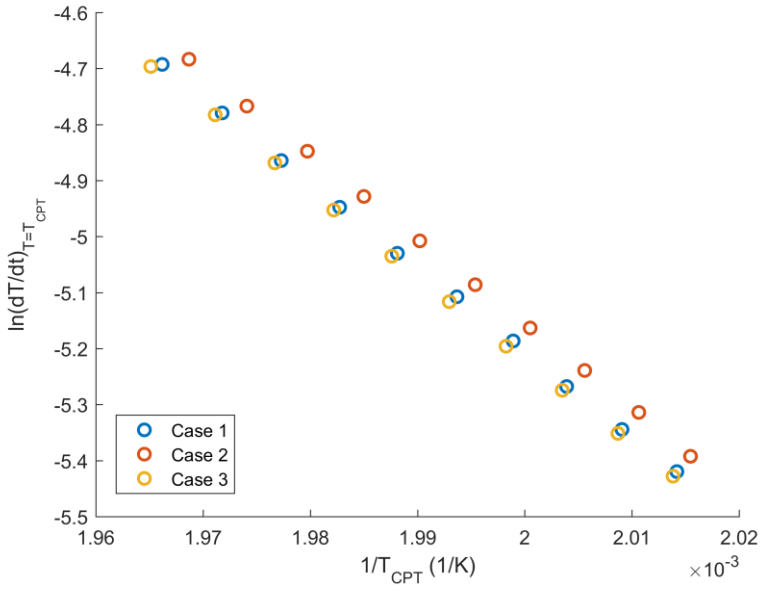

Figure 5-22: Results of the simulated cross-point temperature method experiments, measuring the same three cross-point cases as measured experimentally.

The kinetics from each of these three simulated cases are shown in Table 5-10. It can be seen that there is little difference between the kinetics of each case. However, these kinetics were also used to predict the critical ambient temperature of a 60mm equi-cylindrical basket, and there is some discrepancy between these values. The simulated case 3 predicted critical ambient temperature is over 1°C higher than that of case 2. For an ideal system, this is a notable difference, and warrants further investigation.

Table 5-10: Simulated cross-point temperature method results and the predicted critical ambient temperature for a 60mm equi-cylindrical basket using these kinetics.

	E (J mol^{-1})	$\ln\left(\frac{QA}{C_p}\right)$	T_{crit} for 30mm radius basket
Simulated Case 1	125.7x10^3	25.04	220.59°C
Simulated Case 2	125.5x10^3	25.03	219.72°C
Simulated Case 3	125.4x10^3	24.95	220.89°C
Model Input Kinetics	125.3x10^3	24.89	221.38°C

Using the equation for δ_{cr} in (5-4), critical ambient temperatures for a range of basket sizes were calculated. This allows the kinetics to be compared with those from the steady-state method, and this comparison can be seen in Figure 5-23.

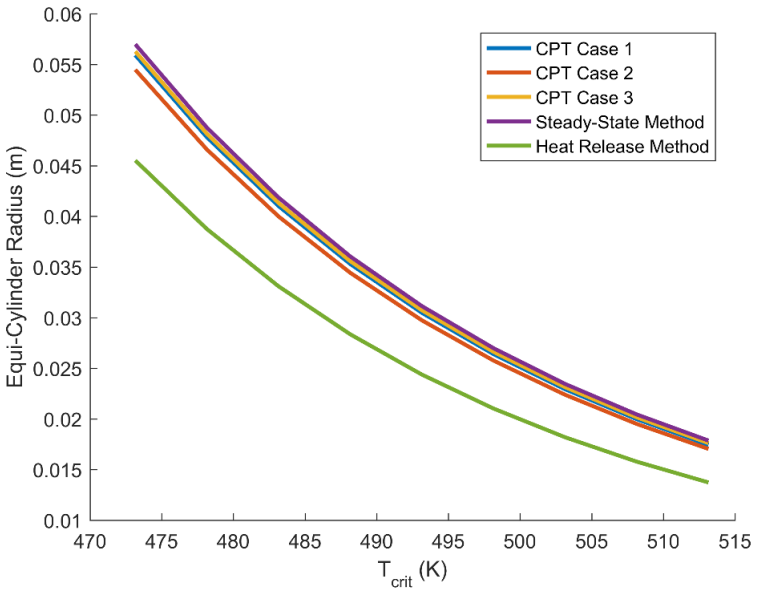

Figure 5-23: Critical ambient temperatures for a range of basket sizes, calculated using the kinetics for each case as measured from the simulated experiments.

The predicted critical ambient temperatures for each case are similar, although there exists a difference as shown in Table 5-10. They are also similar to those calculated using the steady-state method kinetics. The case 3 results are the most similar, as would be expected because of the reduced error of the 5 point stencil used in the finite difference approximation. The other results are similar but not exactly the same, implying that the cross-point approximation used influences the measured kinetics.

Also included in this plot are the results of the heat release method, discussed in Section 2.4.3, which predict very different critical ambient temperatures. This method is similar to the cross-point method, but conduction is assumed to cease when the core temperature equals the ambient temperature. The radial temperatures in Figure 5-21 (b) show why this method is flawed. This model uses the heat transfer coefficient correlation in equation (4-49), such that a finite Biot number is used. For a system with a near infinite Biot number, the difference in results of the heat release method may not be as pronounced as in this case.

5.4.2. Analysis of the Cross-Point Assumption

Having analysed the cross-point temperature method for the thermocouple setup used experimentally, the next step is to explore why a difference is seen between each of the cases. This was done by exploring the form of the cross-point approximation used and the spacing of the thermocouples used.

5.4.2.1. Approximating the Conduction Term with a Three Point Stencil in the Radial Direction

The first form of the cross-point approximation explored was that used in case 1 and 2 of the experiments, a three point stencil for the second order temperature difference in the radial direction. Despite being a three point stencil, because of symmetry one of the outer thermocouples is not needed. This layout can be seen in Figure 5-24.

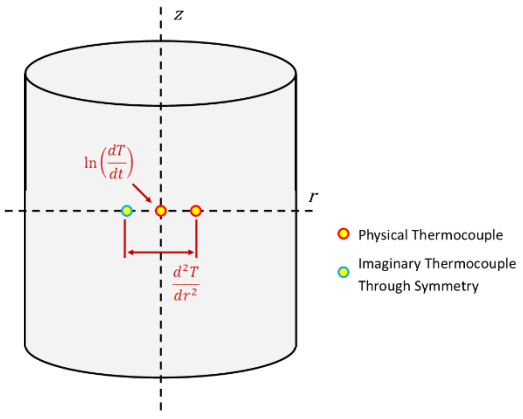

Figure 5-24: Three point stencil in the radial direction used to approximate the second order temperature difference term.

The cross-point using this form of the approximation is given by the following:

$$\frac{d^2T}{dr^2} = \frac{T_{i-1} - 2T_i + T_{i+1}}{\Delta r^2} = \frac{2(T_{i+1} - T_i)}{\Delta r^2} = 0. \qquad (5\text{-}26)$$

The same model simulated experiments, run at 10 ambient temperatures between 493K and 502K, were used and the cross-point was calculated as before using this equation. Results were measured for thermocouple spacings from 1mm to 15mm in 1mm increments. The results are shown in Figure 5-25.

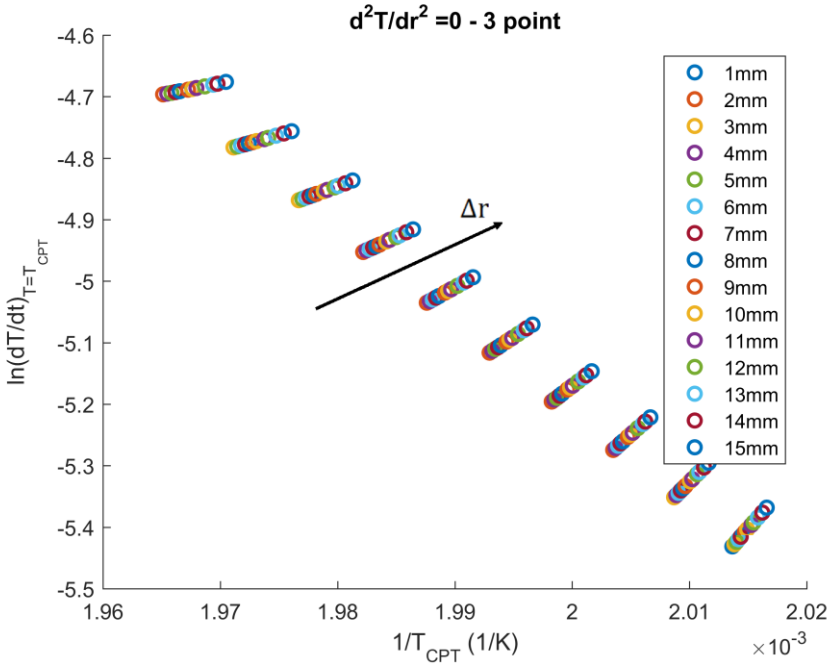

Figure 5-25: Simulated cross-point temperature method results using a three point stencil in the radial direction.

The results vary with thermocouple spacing. The slopes of each spacing are similar, from which similar activation energy values, E, are measured, with the difference coming from the intercept, which influences the measured value of $\ln QA/C_p$. Although it is not shown here, increasing the thermocouple spacing up to 30mm further increases the difference in results.

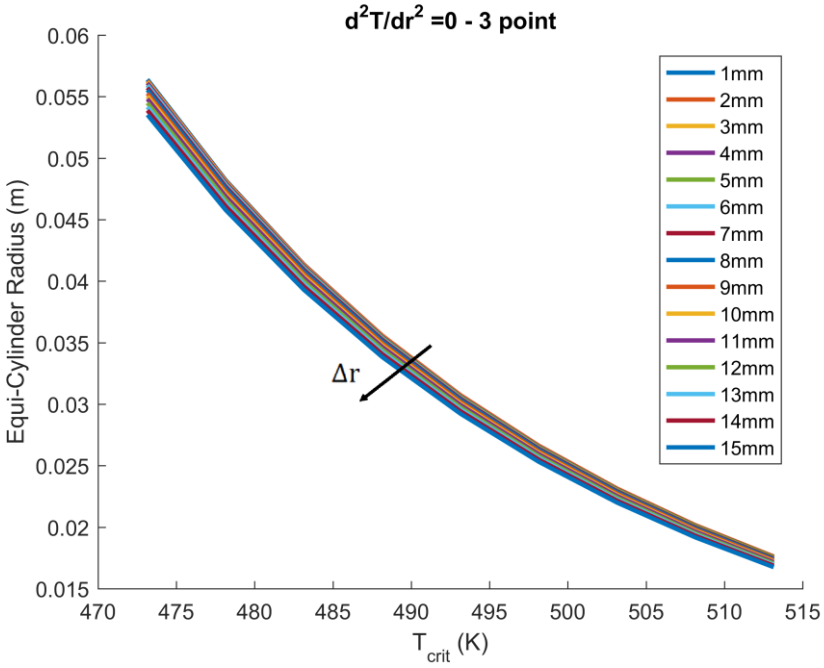

Figure 5-26: Critical ambient temperatures for a range of basket sizes calculated using the kinetics for different thermocouple spacings.

The kinetics measured from each thermocouple spacing was used to calculate critical ambient temperatures for a range of basket sizes as before. These results can be seen in Figure 5-26. Some variation can be seen between the predicted critical ambient temperatures for the different thermocouple spacings. An increase in thermocouple spacing is seen to decrease the predicted critical ambient temperature for any basket size. The finite difference approximation in equation (5-26) becomes more accurate with decreasing values of Δr. The error is of the order Δr^2, and as $\Delta r \rightarrow 0$, this approximation approaches the exact value of d^2T/dr^2. This implies that the smallest possible values of Δr would produce the best results, but practically speaking, this value of Δr is impossible to achieve. Instead, more practical spacings are used, such as 6mm, but with this approximation, the results for such a spacing would under predict the critical ambient temperatures. Using more accurate approximations for the temperature difference term would improve these results.

5.4.2.2. Approximating the Conduction Term with a Five Point Stencil in the Radial Direction

The second form of the cross-point approximation explored was that used in case 3 of the experiments, a five point stencil for the second order temperature difference in the radial direction. In theory, using a five point stencil instead of a three point stencil will reduce the order of the finite difference approximation from an order of $O(\Delta r^2)$ to $O(\Delta r^4)$. The required thermocouple layout can be seen in Figure 5-27.

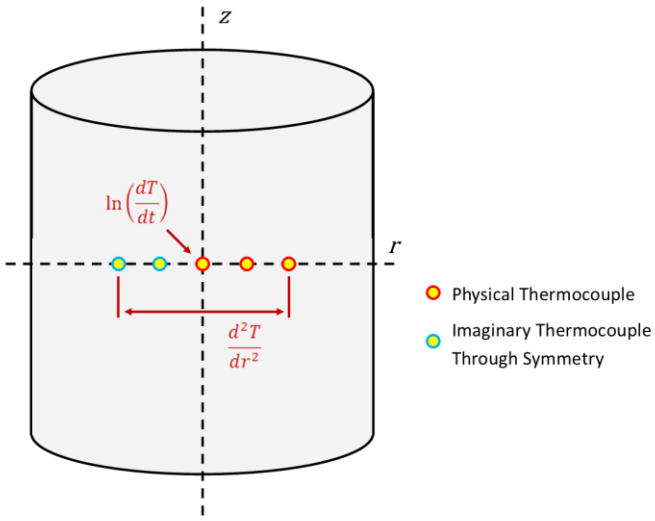

Figure 5-27: Five point stencil in the radial direction used to approximate the second order temperature difference term.

The cross-point using this form of the approximation is given by the following:

$$\frac{d^2T}{dr^2} = \frac{-T_{i-2} + 16T_{i-1} - 30T_i + 16T_{i+1} - T_{i+2}}{12\Delta r^2} = \frac{-15T_i + 16T_{i+1} - T_{i+2}}{6\Delta r^2} = 0. \quad (5\text{-}27)$$

The cross-point was calculated as before using this equation. Results were measured for thermocouples spacings between T_i and T_{i+1} from 1mm to 15mm in 1mm increments. 15mm was used as the largest spacing because for a spacing of 15mm between T_i and T_{i+1}, the spacing between T_i and T_{i+1} was 30mm.

The results for spacings between 1mm and 15mm are shown in Figure 5-28. The results do not vary largely with thermocouple spacing as in the previous case. The similarity of

the results for all thermocouple spacings means that similar values for the activation energy, E, and the logarithmic term, $\ln QA/C_p$, are measured.

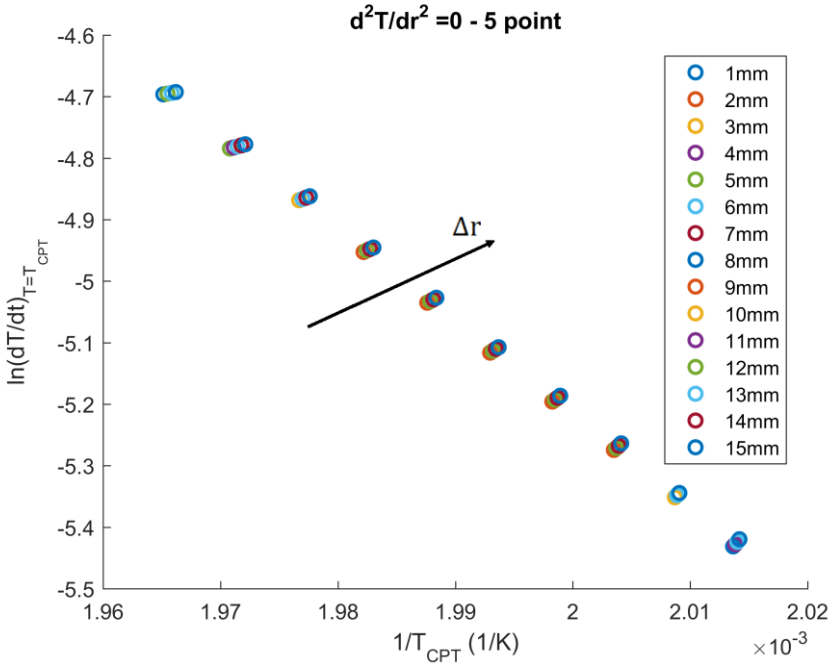

Figure 5-28: Simulated cross-point temperature method results using a five point stencil in the radial direction.

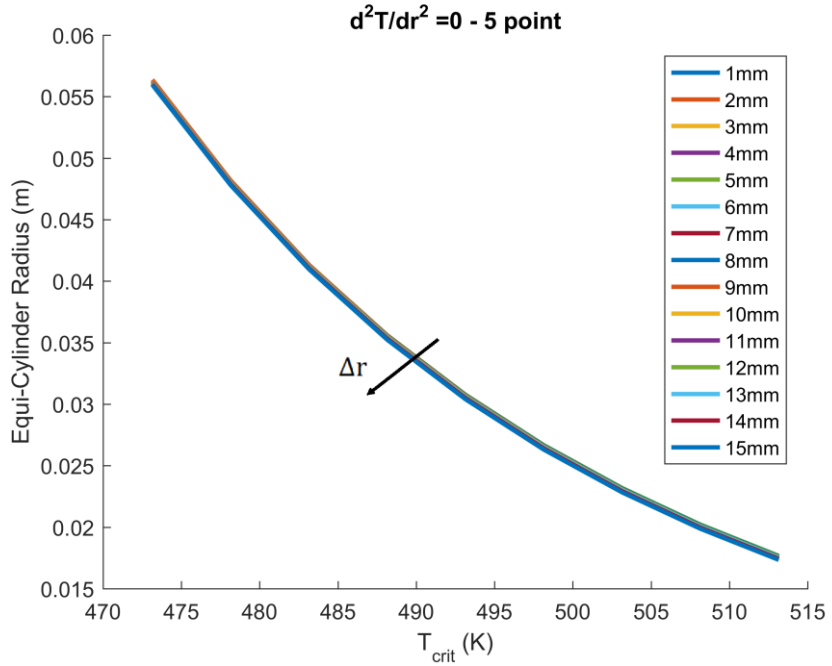

Figure 5-29: Critical ambient temperatures for a range of basket sizes calculated using the kinetics for different thermocouple spacings.

As before, the measured kinetics from these simulated experiments were used to calculate critical ambient temperatures for a range of basket sizes. As would be expected, based on the results plot in Figure 5-28, the predicted critical ambient temperatures are consistent across all the thermocouple spacings simulated. This can be seen in Figure 5-29, and implies that using a five point stencil makes this an accurate approximation of the conduction term and the cross-point assumption. This also implies that no matter the thermocouple spacing, the measured kinetics from case 3 in the experiments should be consistent, but evidently, the errors discussed in the uncertainty analysis of Section 5.3.2 have a significant influence on these results. The kinetics of these different approximation will be compared in Section 5.4.2.5.

5.4.2.3. Approximating the Conduction Term with a Three Point Stencils in the Radial and Axial Directions

Although the previous approximation form predicted consistently measured kinetics for all thermocouple spacings, it was not an entirely accurately approximation of the conduction term. For pseudo-one-dimensional geometries such as an infinite slab, infinite cylinder, or sphere, approximated conduction in one dimension is sufficient. However, for an equi-cylinder a more accurate representation of the conduction term would include conduction in both the radial and the axial directions. At the cross-point, even if conduction in the radial direction is zero, it does not necessarily mean conduction in the axial direction is zero. For this reason, conduction in both directions is considered in this form of the approximation, although this setup is difficult to implement experimentally.

Figure 5-30 shows the simulated axial temperatures profiles at $r = 0mm$ of the basket throughout the experiment. These profiles are very similar to those in the radial direction. At no point is this profile flat, and for a large thermocouple spacing this may be an issue.

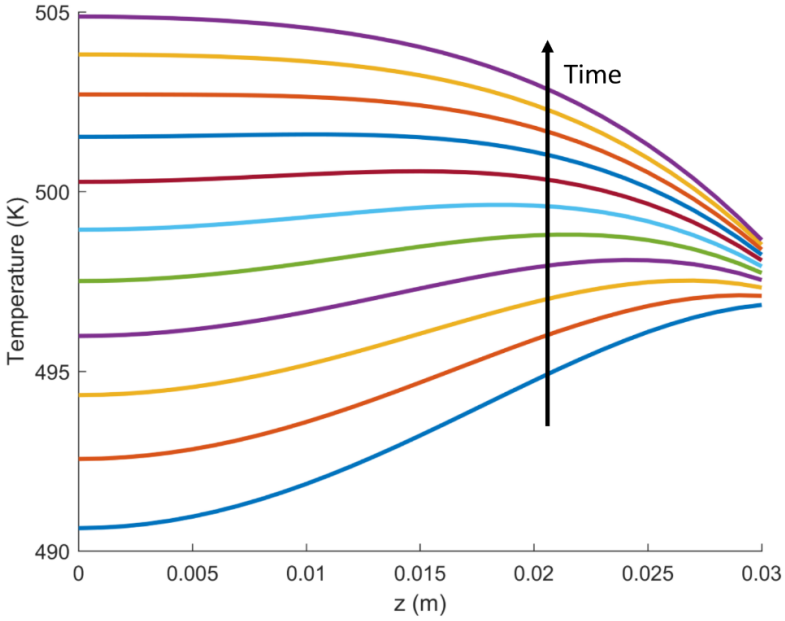

Figure 5-30: Axial temperature profiles at $r = 0mm$ as time progress throughout the experiment, simulated at an ambient temperature of 497K (224°C).

To explore the influence of axial conduction, the value of axial conduction term d^2T/dz^2 was calculated at the previous cross-point, where a five point stencil in the radial direction only was used. This value was calculated using a consistent thermocouple spacing of 6mm at the 10 different ambient temperatures simulated and can be seen in Figure 5-31.

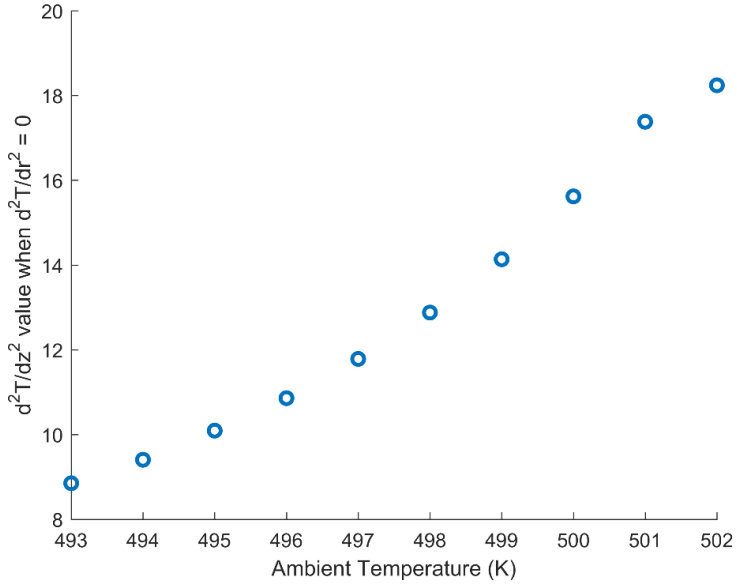

Figure 5-31: Axial conduction value calculated at the cross-points as measured using a five point stencil in the radial direction only.

It can be seen that axial conduction still exists at the cross-point, and that it increases with an increase in ambient temperature. Considering at its peak, the second order temperature derivative reached a value of almost 2000 K m^{-2}, the magnitude of the axial conduction may turn out to be negligible, but this will not be known until this is explored further.

The form of the cross-point approximation used here is a three point stencil for the second order temperature difference in both the radial and axial directions. Again symmetry is used to eliminate two of the thermocouples. This layout can be seen in Figure 5-32.

The cross-point using this form of the approximation is given by the following:

$$\frac{d^2T}{dr^2}+\frac{d^2T}{dz^2}=\frac{T_{i-1,j}-2T_{i,j}+T_{i+1,j}}{\Delta r^2}+\frac{T_{i,j-1}-2T_{i,j}+T_{i,j+1}}{\Delta z^2}$$
$$=\frac{2\left(T_{i+1,j}-T_{i,j}\right)}{\Delta r^2}+\frac{2\left(T_{i,j+1}-T_{i,j}\right)}{\Delta \mathrm{z}^2}=0. \quad (5\text{-}28)$$

The cross-point was calculated as before using this equation. Results were measured for thermocouples spacings between $T_{i,j}$ and $T_{i+1,j}$ from 1mm to 15mm in 1mm increments. The spacings in the axial direction, between $T_{i,j}$ and $T_{i,j+1}$, were incremented in the same way as the spacings in the axial radial direction, such Δr was always equal to Δz.

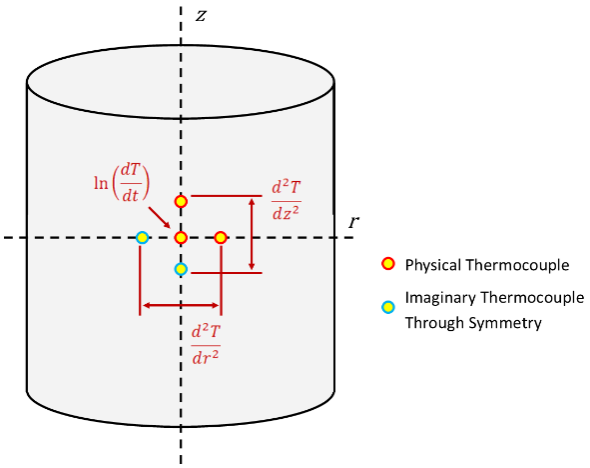

Figure 5-32: Three point stencils in the radial and axial directions used to approximate the second order temperature difference term.

The results for spacings between 1mm and 15mm are shown in Figure 5-33. It was thought that including axial conduction would improve the results, but instead the results are seen to vary with thermocouple spacings, as they did when the approximation of conduction solely in the radial direction using a three point stencil was used. This implies that the error induced by the stencil of the finite difference approximation used is more influential than including axial conduction in the approximation, at least for an equi-cylindrical basket. This may not be the case for cylinders where the height and diameter and not equal.

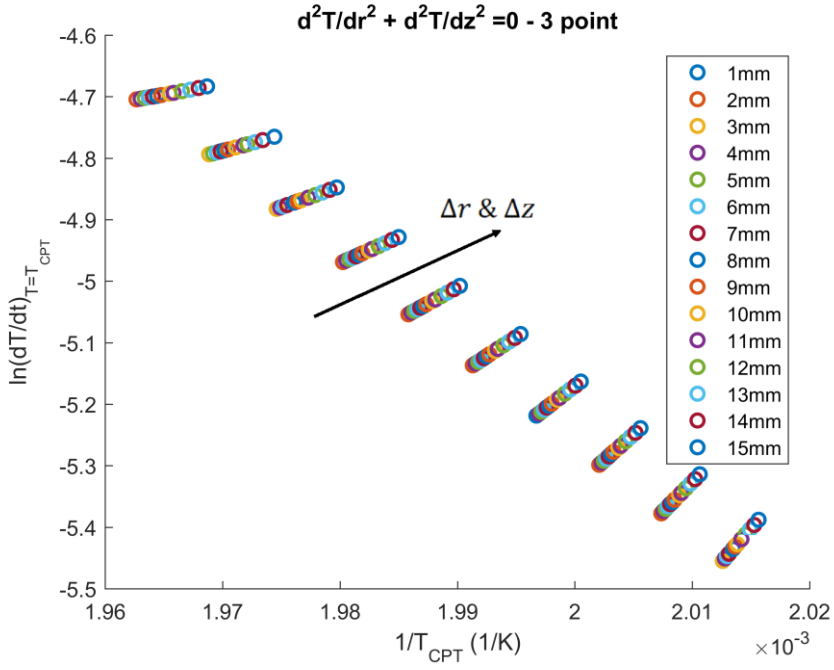

Figure 5-33: Simulated cross-point temperature method results using a three point stencil in both the radial and axial directions.

The measured kinetics from these simulated experiments were used to calculate critical ambient temperatures for a range of basket sizes as seen in Figure 5-34. Some variation can be seen between the predicted critical ambient temperatures for the different thermocouple spacings. An increase in thermocouple spacing is seen to decrease the predicted critical ambient temperature for any basket size. This same behaviour was seen for the results when the three point stencil for conduction solely in the radial direction was used, again emphasising that the error induced by the stencil of the finite difference approximation used is more influential than including axial conduction in the approximation.

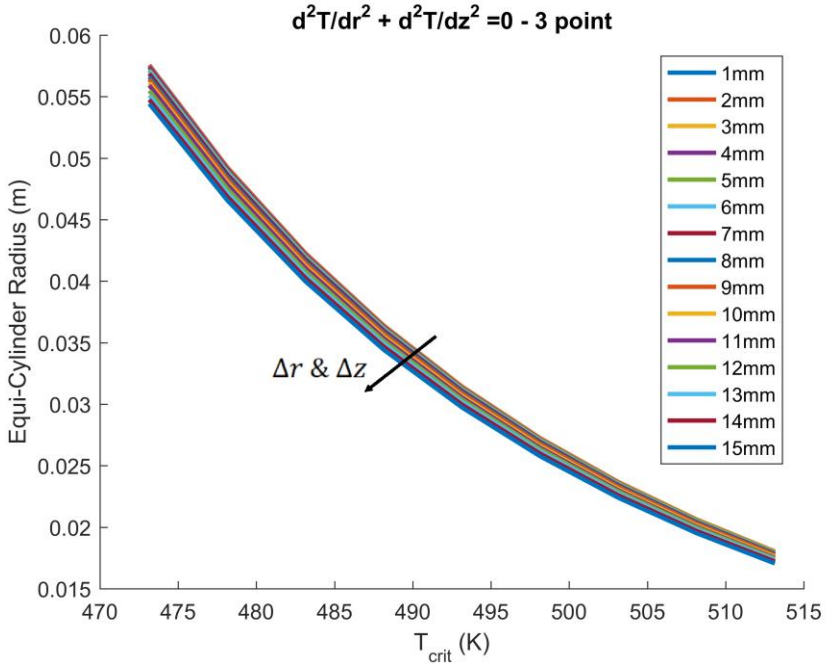

Figure 5-34: Critical ambient temperatures for a range of basket sizes calculated using the kinetics for different thermocouple spacings.

5.4.2.4. Approximating the Conduction Term with a Five Point Stencils in the Radial and Axial Directions

This approximation looks to combine the best elements of the previous approximations, the five point stencil for the finite difference term and the inclusion of axial conduction. Conduction in both the radial and axial directions is considered in this form of the approximation, with both approximated using a five points stencil. Again this would be difficult to implement experimentally, but is being explored anyway to help understand the implications of the approximations used. Because of symmetry, two thermocouples in both directions are not required for this stencil. This layout can be seen in Figure 5-35.

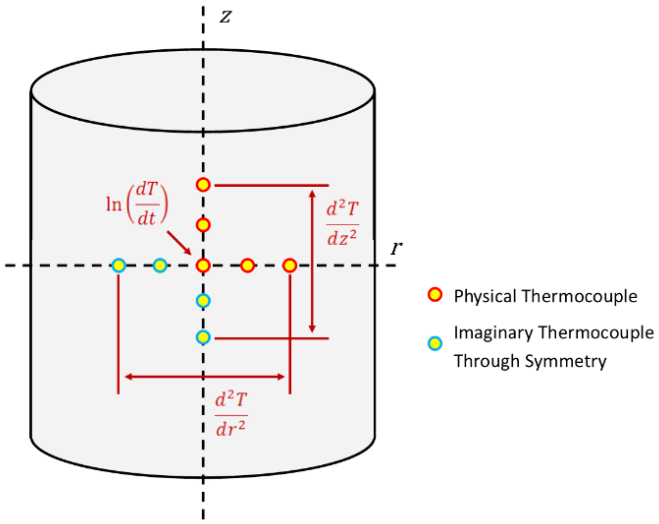

Figure 5-35: Five point stencils in the radial and axial directions used to approximate the second order temperature difference term.

The cross-point using this form of the approximation is given by the following:

$$\frac{d^2T}{dr^2}+\frac{d^2T}{dz^2}=\frac{-T_{i-2,j}+16T_{i-1,j}-30T_{i,j}+16T_{i+1,j}-T_{i+2,j}}{12\Delta r^2} + \frac{-T_{i,j-2}+16T_{i,j-1}-30T_{i,j}+16T_{i,j+1}-T_{i,j+2}}{12\Delta z^2}=0 \tag{5-29}$$

Applying symmetry this reduces to:

$$\frac{d^2T}{dr^2}+\frac{d^2T}{dz^2}=\frac{-15T_{i,j}+16T_{i+1,j}-T_{i+2,j}}{6\Delta r^2} + \frac{-15T_{i,j}+16T_{i,j+1}-T_{i,j+2}}{6\Delta z^2}=0. \tag{5-30}$$

The cross-point was calculated as before using this equation. Results were measured for thermocouples spacings between $T_{i,j}$ and $T_{i+1,j}$ from 1mm to 15mm in 1mm increments. The spacings in the axial direction, between $T_{i,j}$ and $T_{i,j+1}$, were incremented in the same way as the spacings in the axial radial direction, such Δr was always equal to Δz. The results for spacings between 1mm and 15mm are shown in Figure 5-36. The results do not vary largely with thermocouple spacing as in the previous case where only three point stencils were used. The similarity of the results for all thermocouple spacings means that similar values kinetics are always measured.

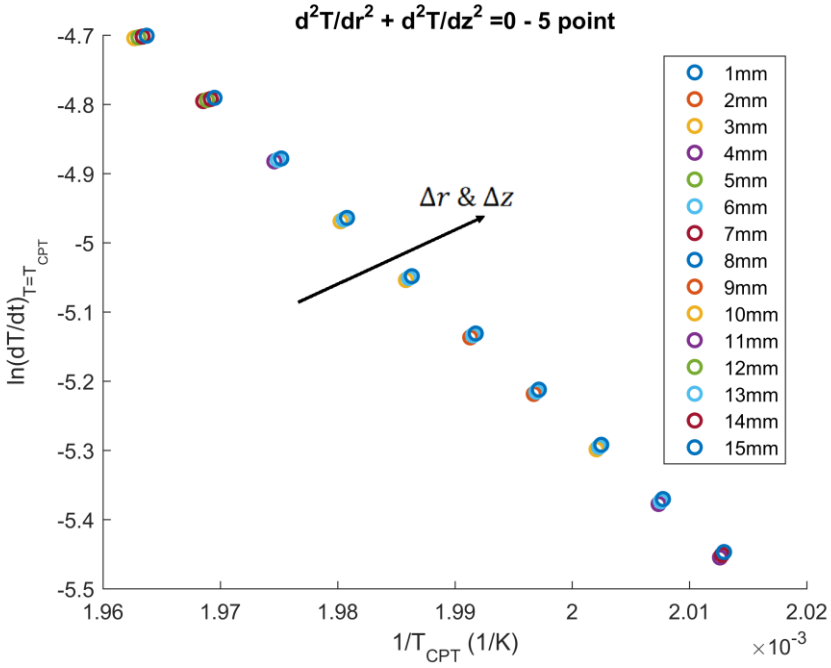

Figure 5-36: Simulated cross-point temperature method results using a five point stencil in both the radial and axial directions.

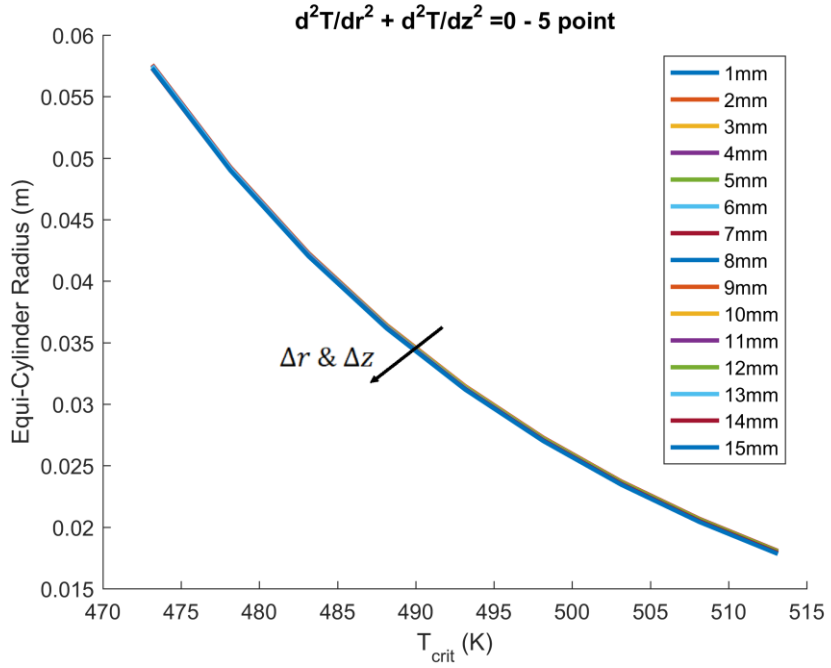

Figure 5-37: Critical ambient temperatures for a range of basket sizes calculated using the kinetics for different thermocouple spacings.

The measured kinetics from these simulated experiments were used to calculate critical ambient temperatures for a range of basket sizes, and can be seen in Figure 5-37. For

this approximation, as was the case when conduction was accounted for in only the radial direction but using a five point stencil, there is little variation across the predicted critical ambient temperatures for different thermocouple spacings. This behaviour implies again that the error induced by the stencil of the finite difference approximation used is more influential than including axial conduction in the approximation, although this approximation can be considered the most thorough of the approximations used.

5.4.2.5. Comparison of the Different Approximations for the Conduction Term

The previous analysis has suggested that the stencil of the finite difference approximation has more of an influence on the cross-point temperature method results than the thorough inclusion of conduction in both the radial and axial directions. This section compares the four approximations explored, and looks to confirm if these results agree with those from the Steady-State method, which are based on measured critical ambient temperatures. Plotting the simulated experimental results for these four approximations can be seen in Figure 5-38. A slight difference in results can be seen for each of the four approximations. All results have similar slopes, which would lead to similar values for the activation energy, E, and the difference primarily comes for the intercepts, which influences the measured value of $\ln QA/C_p$.

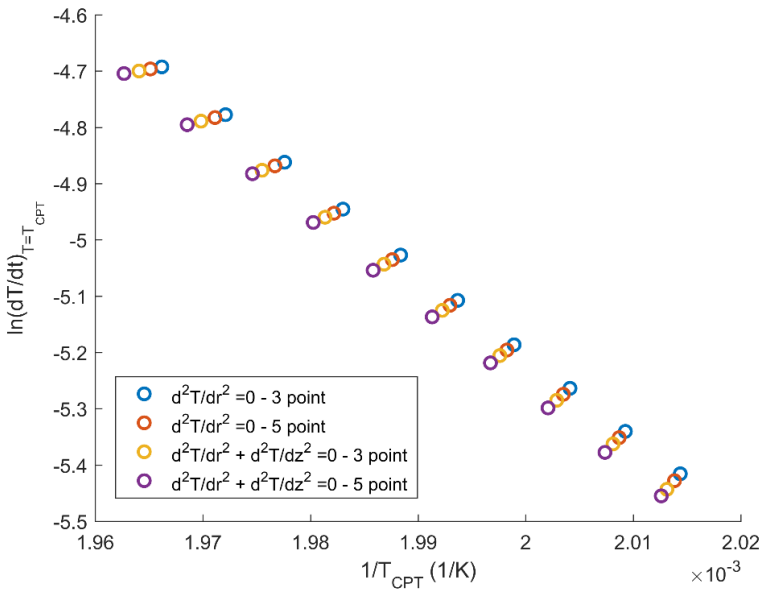

Figure 5-38: Comparison of the results from the four cross-point approximations used for a thermocouple spacing of 6mm.

The kinetics for each approximation as determined from the plot in Figure 5-38 were used to predict critical ambient temperatures for a range of basket sizes. These values have been plotted in Figure 5-39 and shows that all these cases predict similar critical ambient temperatures, at least for the thermocouple spacing of 6mm compared here. The kinetics for each approximation are shown in Table 5-11. For a basket of radius 30mm, less than 2°C difference is predicted in critical ambient. This shows that the difference in measured kinetics is not significant, and that even the simplest setup of two radially spaced thermocouples would produce good results. Axially spaced thermocouples would be difficult to implement experimentally, and this shows that they are not required to obtain good results.

These results were also compared with the critical ambient temperatures predicted by the kinetics measured using the steady-state method. These kinetics were used in the numerical model, and as such if the cross-point approximation is accurate then the simulated results should agree with the steady-state method results. The results for all four approximations agree very well with steady-state method results, but in particular the results when both radial and axial conduction is accounted for. This is not a surprise as including conduction in the axial direction makes this a much more accurate approximation. However, the difference is not sufficient to justify the added complexity of using both radially and axially spaced thermocouples.

The previous analysis has showed that the error induced by the finite difference approximation used is of more importance than including conduction in the axial direction. Using a five point stencil for the finite difference approximation instead of a three point stencil reduces the order of the error from an order of $O(\Delta r^2)$ to $O(\Delta r^4)$.

Experimentally, of the three cases used in this investigation, case 3 is the best approximations for the conduction term. However, it was seen that the errors induced by errors in thermocouple readings and placement overshadow the benefits of this approximation.

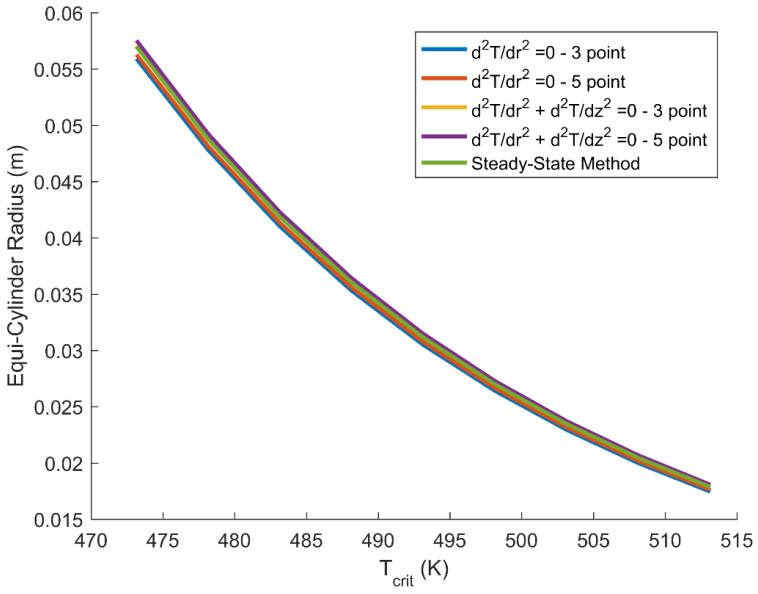

Figure 5-39: Comparison of the four cross-point approximations using a thermocouple spacing of 6mm.

Table 5-11: Kinetics as predicted from simulated experiments using the four different cross-point temperature approximations.

		E (J mol^{-1})	$\ln\left(\frac{QA}{C_p}\right)$	T_{crit} for 30mm radius basket
$\frac{d^2T}{dr^2}=0$	**3 point stencil**	125.7x10^3	25.04	220.59°C
	5 point stencil	125.4x10^3	24.95	220.89°C
$\frac{d^2T}{dr^2}+\frac{d^2T}{dz^2}=0$	**3 point stencil**	125.3x10^3	24.89	221.41°C
	5 point stencil	125.1x10^3	24.83	221.75°C
Input Model Kinetics		125.3x10^3	24.89	221.38°C

5.4.3. Model Analysis of the Effects of Thermocouple Reading Errors on the Measured Cross-Point Temperature

It is thought that the measured cross-point temperatures are influenced not only by the errors in the placements of the thermocouples, but by the errors in the thermocouple readings. As such, the effects of errors in the thermocouple readings were also explored using the model simulated CPT method experiments. The experimental temperature-time profiles in Figure 5-40 show how an error of ±0.25°C on the thermocouple at the basket centre could affect the measured cross-point. The band of error effectively

means that the cross-point temperature can now occur anywhere within the highlighted range. It can be seen that there is little difference between the gradients of the temperature-time profiles of the thermocouple at 0mm and at 6mm, and this makes this case particularly susceptible to errors in thermocouple readings. For case 1, where these two thermocouples are used, the range in which the cross-point temperature can occur spans over 400s. Within this range the cross-point temperature could be anywhere between 510.7K (237.5°C) and 514.7K (241.5°C). This 4°C difference may have a large impact on the measured kinetics.

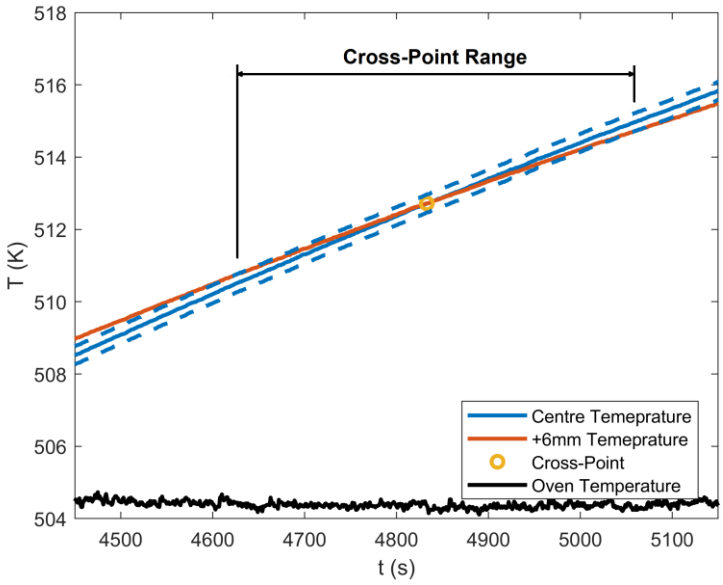

Figure 5-40: The influence of a thermocouple reading error of ±0.25°C on the measured case 1 cross-point temperature of a 50mm equi-cylindrical basket heated at 231°C (504K).

The effects of this error on the case 2 results was also explored, as can be seen in Figure 5-41. In this case, the gradients of the two temperature-time profiles are not as similar as before. This makes this case much less susceptible to errors in thermocouple readings. This can also be seen in the range of possible cross-point temperatures highlighted. For case 2, this only spans a range of approximately 150s, which corresponds to a cross-point temperature between 508.0K (234.8°C) and 509.5K (236.3°C), a difference of only 1.5°C. This again shows why the experimental case 2 kinetics are more accurate than those of case 1 and case 3.

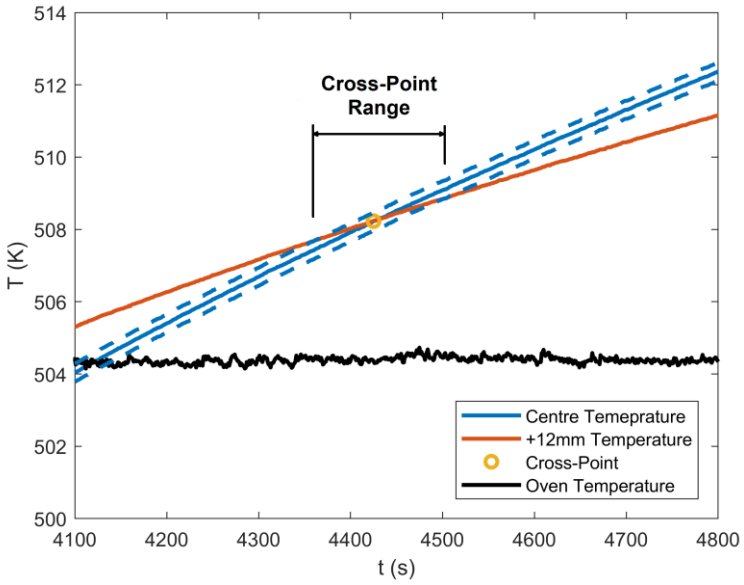

Figure 5-41: The influence of a thermocouple reading error of ±0.25°C on the measured case 2 cross-point temperature of a 50mm equi-cylindrical basket heated at 231°C (504K).

The model simulated experiments used in the previous section were also used to explore the effects of thermocouple reading errors in the measured CPT method kinetics. To do this, after the experiments had been simulated, an error of +0.25°C was applied to each of the thermocouples individually. The three different cross-point cases were then evaluated from the simulated thermocouples, and the influence of the simulated errors explored. The combinations of thermocouple errors detailed in Table 5-12 were applied.

Table 5-12: Simulated errors applied to the thermocouples of the simulated experiments.

Error on T_1 (0mm) (°C)	**Error on T_2 (6mm) (°C)**	**Error on T_3 (12mm) (°C)**
0	0	0
+0.25	0	0
0	+0.25	0
0	0	+0.25

The results of the simulated experiments without any error applied can be seen in Figure 5-22. Here it can be seen that all three cases have similar results. The offset between

the three different cases can be attributed to the cross-point assumption and the form of the second order temperature derivative term as shown in Section 5.4.2.

Firstly, an error of +0.25°C was applied to the thermocouple T_1 at the basket centre (0mm). The CPT method results for these data can be seen in Figure 5-42. This error can be seen the affect the results of all three cross-point cases. This was expected because T_1 is the only thermocouple that is used by all three of the cross-point cases. The kinetics as measured from these data can be seen in Table 5-13. The kinetics for each case are seen to change relative to where no error was applied. This effect is even more pronounced for cases 1 and 3, with a significantly larger decrease in the kinetics of these case relative to case 2. This was expected based on what was seen when applying an error to the experimental temperature-time profiles in Figure 5-40 and Figure 5-41.

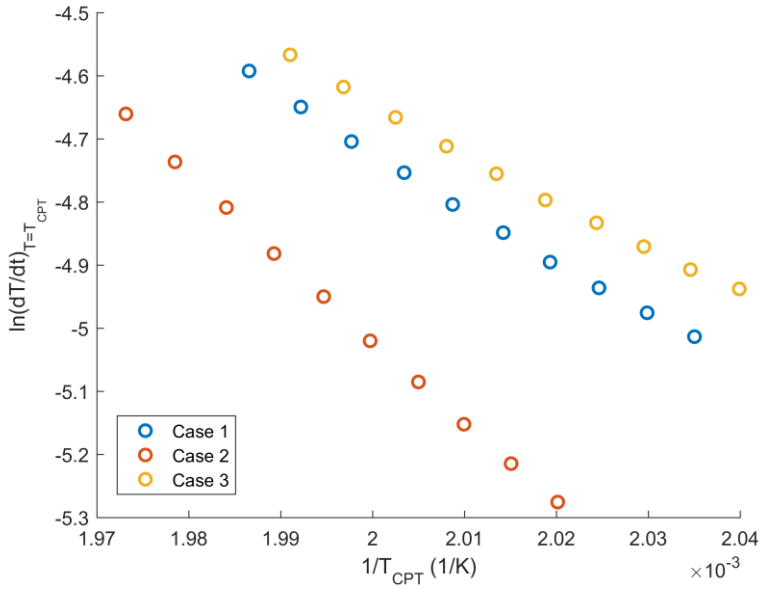

Figure 5-42: Simulated CPT method experiments with a thermocouple reading error of +0.25°C applied to thermocouple T_1 at the basket centre.

The next step was to apply an thermocouple reading error of +0.25°C to the thermocouple T_2 at 6mm from the basket centre. The CPT method results for these data can be seen in Figure 5-43. For this error, it can be seen that the case 1 and 3 results are again affected. However, the case 2 results are not affected because case 2 does not involve the thermocouple T_2. The kinetics as measured from these data can again be seen in Table 5-13. The case 1 and 3 kinetics are now seen to increase significantly for this error, whereas they decreased when the error was applied to the thermocouple T_1.

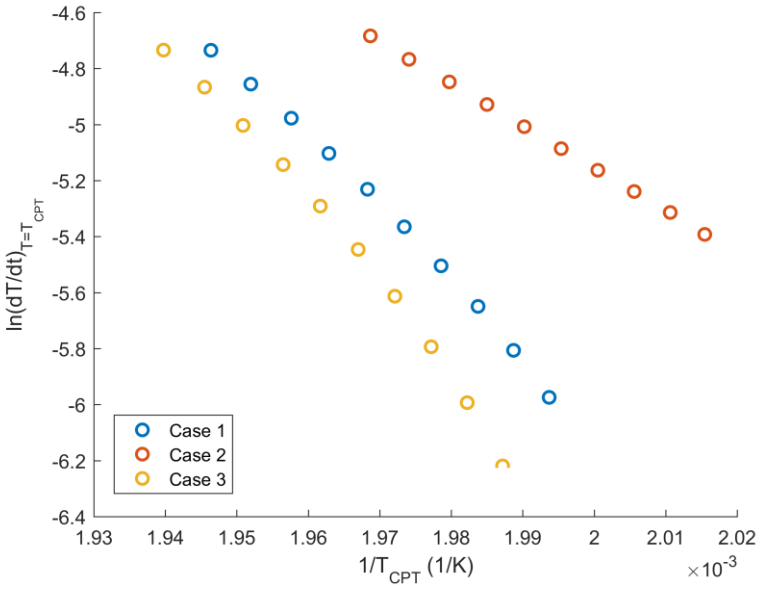

Figure 5-43: Simulated CPT method experiments with a thermocouple reading error of +0.25°C applied to thermocouple T_2 at 6mm from the centre.

Finally, a thermocouple reading error of +0.25°C to the thermocouple T_3 at 12mm from the basket centre. The CPT method results for these data can be seen in Figure 5-44. For this error, much less difference in the results can be seen. Case 2 and 3 are affects by this error, with case 1 unaffected as this case does not use the thermocouple T_3. The kinetics as measured from these data can again be seen in Table 5-13. The case 2 kinetics are seen to increase relative to the kinetics where no error was applied. However, this difference is considerably smaller than that seen in the case 1 kinetics where previous errors were applied. Again, this was expected based on the analysis in Figure 5-40 and Figure 5-41, and shows why the experimental case 2 kinetics are more accurate than those of case 1 and 3.

The case 3 kinetics exhibit a much smaller decrease relative to the kinetics where no error was applied. This is because case 3 is more heavily influence by the thermocouples T_1 and T_2 than by the thermocouple T_3, as discussed in Section 5.3.2.

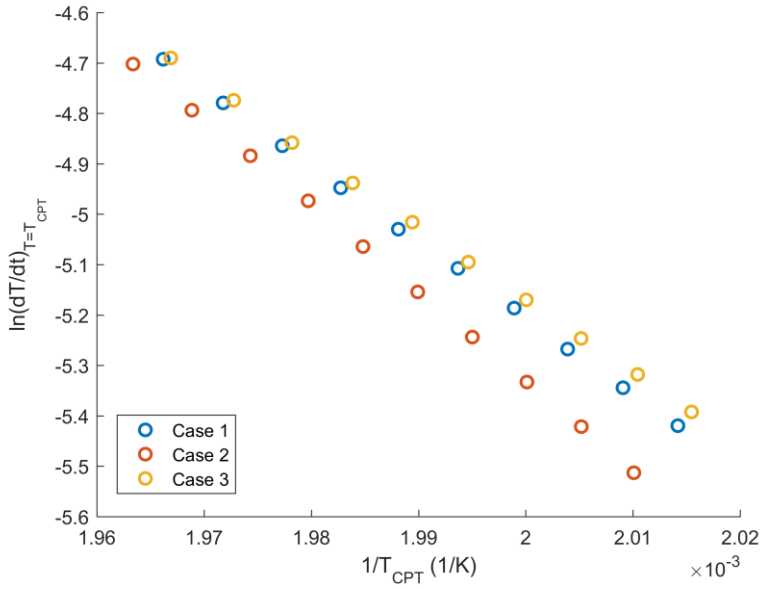

Figure 5-44: Simulated CPT method experiments with a thermocouple reading error of +0.25°C applied to thermocouple T_3 at 12mm from the centre.

Table 5-13: Results of the simulated CPT method experiments with different combinations of errors applied to the thermocouples. The results in red highlight the cases affected by the error applied in each combination.

Simulated Thermocouple Error $[T_1, T_2, T_3]$ (°C)	**Case 1**		**Case 2**		**Case 3**	
	E (J mol^{-1})	$\ln\left(\frac{QA}{C_p}\right)$	E (J mol^{-1})	$\ln\left(\frac{QA}{C_p}\right)$	E (J mol^{-1})	$\ln\left(\frac{QA}{C_p}\right)$
[0, 0, 0]	125.7x10^3	25.04	125.5x10^3	25.03	125.4x10^3	24.95
[+0.25, 0, 0]	72.2x10^3	12.64	109.0x10^3	21.21	63.3x10^3	10.58
[0, +0.25, 0]	215.8x10^3	45.82	125.5x10^3	25.03	255.9x10^3	55.03
[0, 0, +0.25]	125.7x10^3	25.04	144.3x10^3	29.38	120.1x10^3	23.71

These simulated experiments illustrate that the errors in the thermocouple readings heavily influence the measured kinetics using the CPT method. This shows that the CPT method is very susceptible to errors in comparison to the steady-state method. It also shows that both the thermocouple placement and thermocouple readings errors are important and where possible, all efforts to alleviate these errors must be applied.

5.5. Application of the Cross-Point Temperature Method to Other Detergent Formulations

The cross-point temperature method was applied to three other formulations outlined in the introduction of this chapter. The first of these formulations is referred to as Non-Micronized Formulation 1. As the name suggests, this formulation uses a non-micronized grade of sodium sulphate, but in all other ways it is the same as Micronized Formulation 1. The other two formulations, Formulation 2 and Formulation 3, are similar to one another, with Formulation 3 containing 1% Polycarboxylate Polymer, whilst Formulation 2 contains none. This is discussed in more detail in Section 5.1.

These formulations were characterised using the same three thermocouple setup, with the first at the centre (0mm), the second offset at 6mm, and the third offset at 12mm. The results shown in Figure 5-45, Figure 5-46, and Figure 5-47 are for the case 1 and case 2 kinetics. It can be seen for all formulations that the case 1 kinetics are poor results. All of these formulations contained non-micronized sodium sulphate, unlike the previously analysed formulation which used a micronized variant. It is thought that without micronized sodium sulphate there is too much variability in the particles, and coupling this with the errors in thermocouple readings and placement has led to these poor results for case 1. Nonetheless, the results of case 2 are significantly better. This case used the larger 12mm spacing, and it is thought that this spacing help to alleviate some of the problems of composition variability and the impact of thermocouple errors.

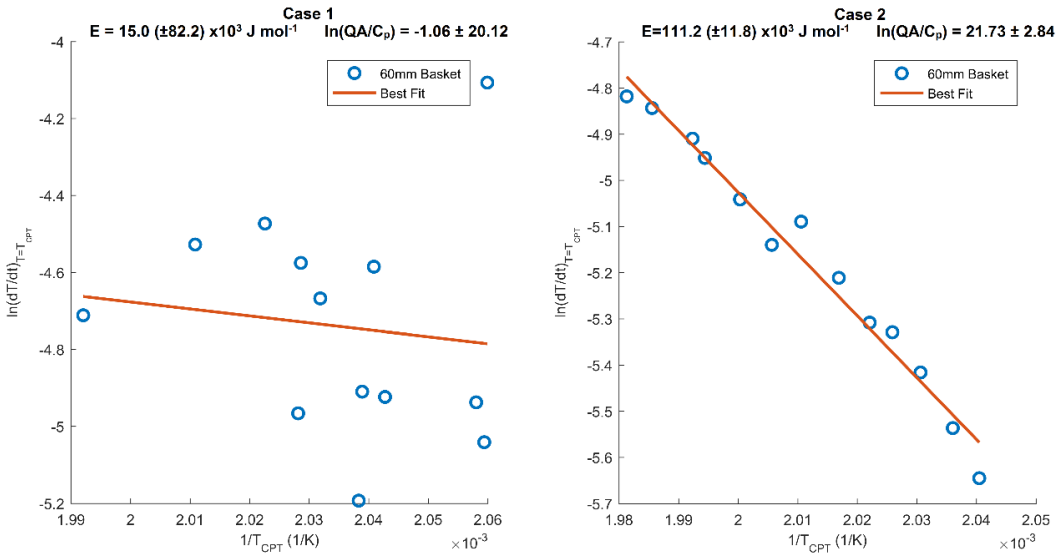

Figure 5-45: CPT method results for Non-Micronized Formulation 1, separated by case using both a 60mm baskets.

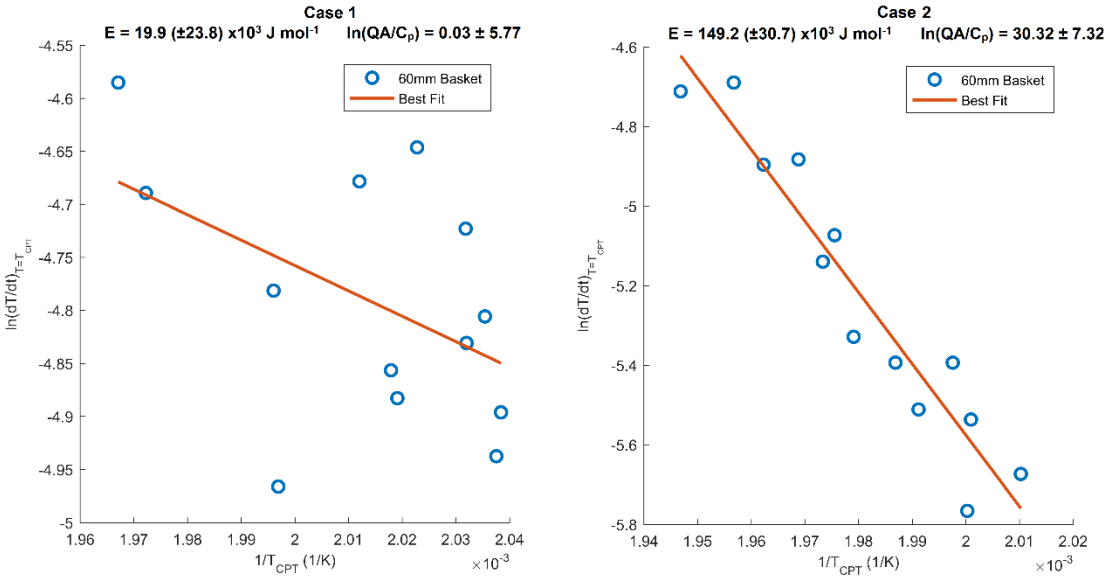

Figure 5-46: CPT method results for Formulation 2 separated by case using both a 60mm baskets.

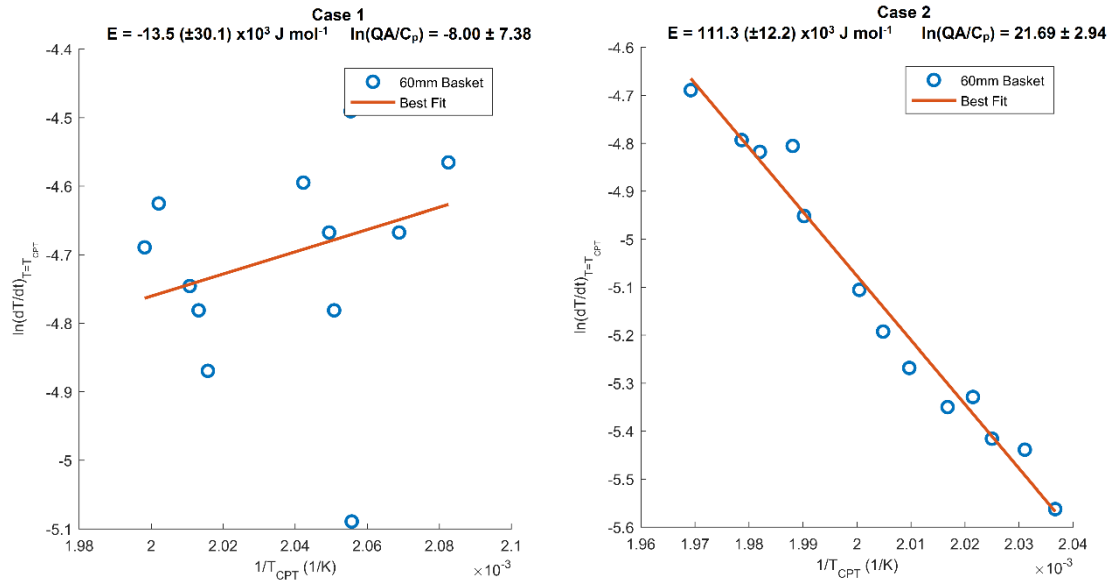

Figure 5-47: CPT method results for Formulation 3, separated by case using both a 60mm baskets.

Differential Scanning Calorimetry (DSC) was used to explore the problem of composition variability in these three formulations where non-micronized sodium sulphate was used. The powder samples were sieved into four different particle size ranges: >150µm and <250µm, >250µm and <355µm, >355µm and <425µm, and >425µm and <600µm. Heat

flow profiles as a function of temperature were measured for each of these four particles size ranges and compared. These comparisons can be seen in Figure 5-48.

Non-Micronized Formulation 1 is seen to react similarly to Micronized Formulation 1, as discussed in Section 3.4, in that low variability in reactivity is seen across the differently sized particles. However, Formulation 2 and Formulation 3 do not exhibit this behaviour. Instead, it can be seen that the smaller particles react less than the larger particles. This variability will impact on the cross-point temperature case 1 results because of the small number of particles that on average are between the thermocouple at 0mm and 6mm. This explains why the case 1 results for these two formulations are so poor, and helps to verify that composition variability needs to be considered when choosing the spacing between thermocouples in this method. However, this does not explain why the results for Non-Micronized Formulation 1 are also poor.

These results will be discussed again in Section 7.2 where they are compared with the kinetics estimated using the new Parameter Estimation Approach.

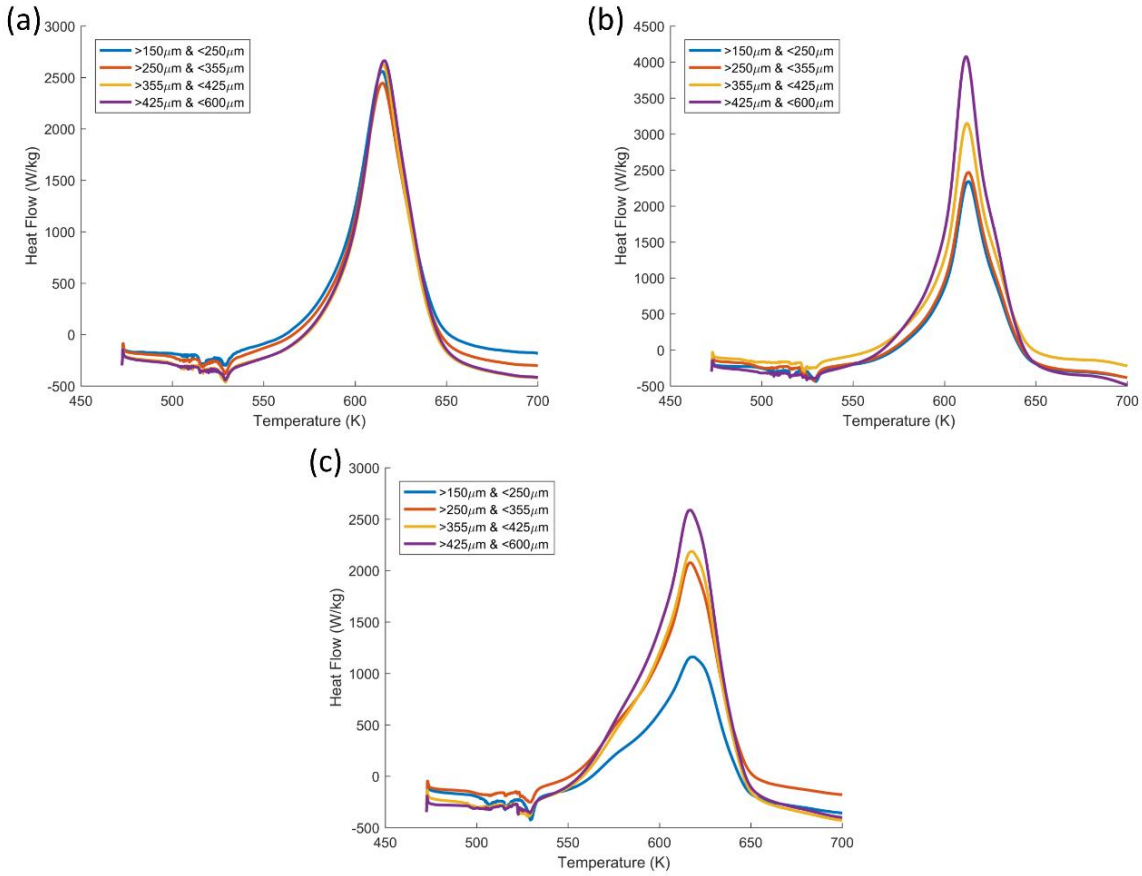

Figure 5-48: DSC measured heat flow profiles at a ramped heating rate of 4°C min^{-1} for four particle size ranges and for (a) Non-Micronized Formulation 1 (b) Formulation 2, and (c) Formulation 3.

5.6. DTG Method for Estimating n^{th} Order Kinetics

A method adapted from the DTG (differential thermogravimetry) method of Yang et al. (2001) was used to fit n^{th} order kinetics to the mass loss curves of samples of Micronized Formulation 1 measured using thermogravimetric analysis (TGA) under ramped heating conditions. A sample of powder was sieved into a number of size ranges such that the kinetics of different size ranges could be compared. Samples of detergent powder, approximately 11mg in mass, were placed into aluminium pans and loaded into the TA Instruments Discovery TGA. These pans were hung from a mass balance integrated into the heating cell of the TGA, such that the mass loss of the sample throughout the experiment could be measured. These samples were heated from 50°C (323K) to 500°C (773K) in an environment of air at a heating rate of 5°C min^{-1}. Data were sampled by the equipment at a rate of 1 measurement every 0.5 seconds. The normalised mass loss curves for the samples of different particle sizes at a heating rate of 5°C min^{-1} are shown in Figure 3-20.

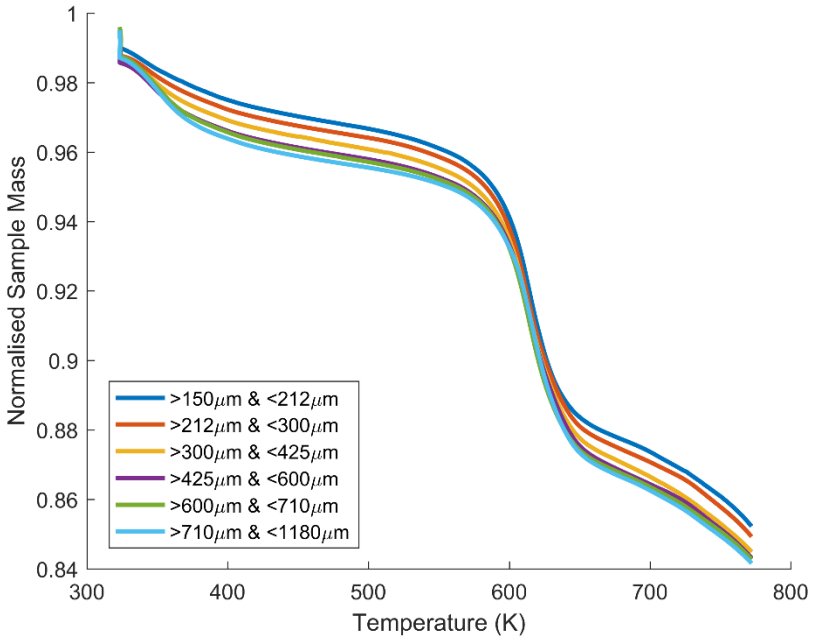

Figure 5-49: TGA normalises sample mass plots for samples of different particle size ranges at a heating rate of 5°C min^{-1} in air.

It can be seen that all samples react similarly which confirms that there is little difference in reactivity across the different particle sizes of this formulation. This has also been explored in Section 3.5. Despite this, it can be seen that there is an offset which develops in the initial period of the curves. It can be seen that the large particle sizes have a greater mass loss in the initial period, and that this occurs at around 100°C (373K). This behaviour can be attributed to the evaporation of residual moisture in the particles, with the larger particles having a greater amount of residual moisture.

The data were normalised by picking a start and end point of the reaction. This allowed the initial mass loss due to water evaporation and mass loss to occur after the reaction to be removed. These data were then normalised. To these normalised curves, the following equation for conversion rate during the reaction was fitted, where α is the normalised conversion of the sample:

$$\frac{d\alpha}{dt} = (1-\alpha)^n A e^{-\frac{E}{RT}} \tag{5-31}$$

Here, E is the activation energy (J mol^{-1}), A is the pre-exponential factor (s^{-1}), and n is the reaction order. Measurements were made by the TGA every 0.5 seconds, such that approximately 2400 points were included in the fitting. Yang *et al.* used an inefficient approach whereby every combination of E and n is fit to the experimental data, with the best fitting parameters by chosen by the method of least squares. It is also unclear as to how A was fitted as it was not included in the flowsheet of their fitting procedure. In this study, the curve fitting toolbox built into MATLAB was used to fit this equation to the experimental data. This toolbox uses optimised solvers to efficiently determine the best fitting parameters. This toolbox also uses the method of least squares in fitting to these data, in which the software attempts to minimise the following parameter S:

$$\mathrm{S} = \sum \left[\left(\frac{d\alpha}{dt}\right)_{exp} - \left(\frac{d\alpha}{dt}\right)_{fit} \right]^2 \tag{5-32}$$

The best fitting values for the activation energy, E, the pre-exponential factor, A, and the order of the reaction, n, were determined for each of the TGA experiments.

5.6.1. DTG Method Results

As mentioned, samples of different particle size ranges were tested, these ranges being: >150µm and <212µm, >212µm and < 300µm, >300µm and <425µm, >425µm and 600µm, >600µm and <710µm, and >710µm and <1.18mm. As shown there was little difference in the reactivity of these samples. The four smallest size ranges were tested further, and at a heating rate of 5°C min^{-1}. The normalised conversion curves for each of these four samples were overlaid in Figure 5-50. It can be seen that all four samples have similar conversion profiles. Kinetics were fitted to these normalised conversion curves.

The best fit kinetics using this approach were found to be dependent on the initial guess for the pre-exponential factor, A. The best fit kinetics for five different initial guesses of A are shown in Table 5-14. It can be seen that for initial guesses of A above 1x10^8 s^{-1}, that the fit value of A are close to the initial guess. This shows the difficulty in fitting for three parameters simultaneously, and suggests that a lower initial guess of A should be used. However, each fitting has a R^2 value of 0.999. This shows that the fittings are still good, and that the difference in parameters is due to the correlation between them, which allows them to compensate for one another.

Table 5-14: Best fit kinetics for a sample of particle sizes >212µm and < 300µm for five different initial guesses for the pre-exponential factor, A.

Initial Guess A (s^{-1})	Best Fit Kinetics			R^2
	E (J mol^{-1})	A (s^{-1})	n	
1x10^7	136.6x10^3	6.10x10^8	1.36	0.999
1x10^8	137.0x10^3	6.56x10^8	1.37	0.999
1x10^9	139.1x10^3	9.98x10^8	1.39	0.999
1x10^{10}	150.6x10^3	9.93x10^9	1.49	0.999
1x10^{11}	161.9x10^3	9.51x10^{10}	1.60	0.999

Using an initial guess for A of 1x10^8 s^{-1}, the best fit of the n^{th} order conversion equation (5-31) to these normalised conversion curves can be seen in Figure 5-51. All four samples have a good fit, with an R^2 value in excess of 0.998 achieved for each fit. Similar kinetics were also measured for each of the four samples, with activation energies, E, of approximately 137x10^3 J mol^{-1}, pre-exponential factors, A, ranging from 5.99x10^8 s^{-1} to 7.02x10^8 s^{-1}, and orders of the reaction, n, ranging from 1.24 to 1.38. Because the

conversion curves in Figure 5-50 are the same, it would be expected that the kinetics for each fitting would be the same. Although similar, the kinetics are not the same and it is thought that again this is because of the difficulty in fitting three parameter simultaneously.

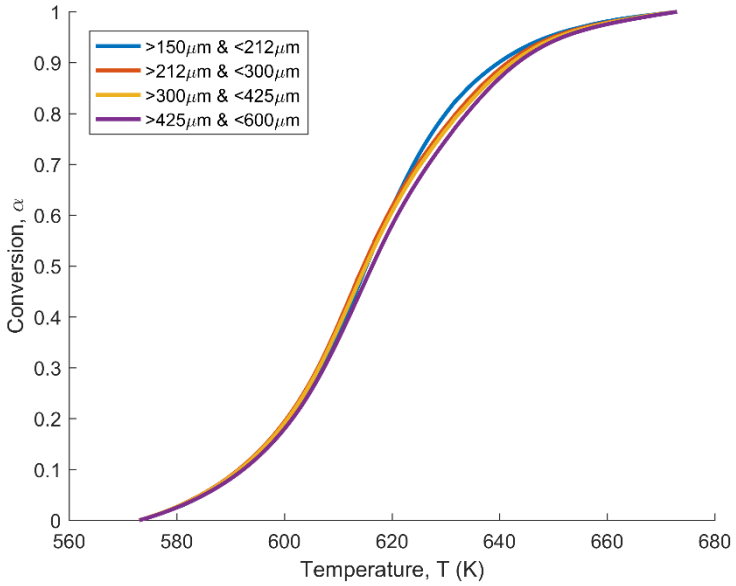

Figure 5-50: Normalised conversion curves for four particle size ranges at a heating rate of 5°C min^{-1}.

These n^{th} order kinetics are difficult to compare with those from the steady-state method and the cross-point temperature method as these two methods measure zero-order kinetics. However, the activation energies are somewhat comparable, and it can been seen that the activation energies in this method are slightly larger. These kinetics are used in the numerical model to understand the impact that this difference in activation energy will have on the self-heating reaction.

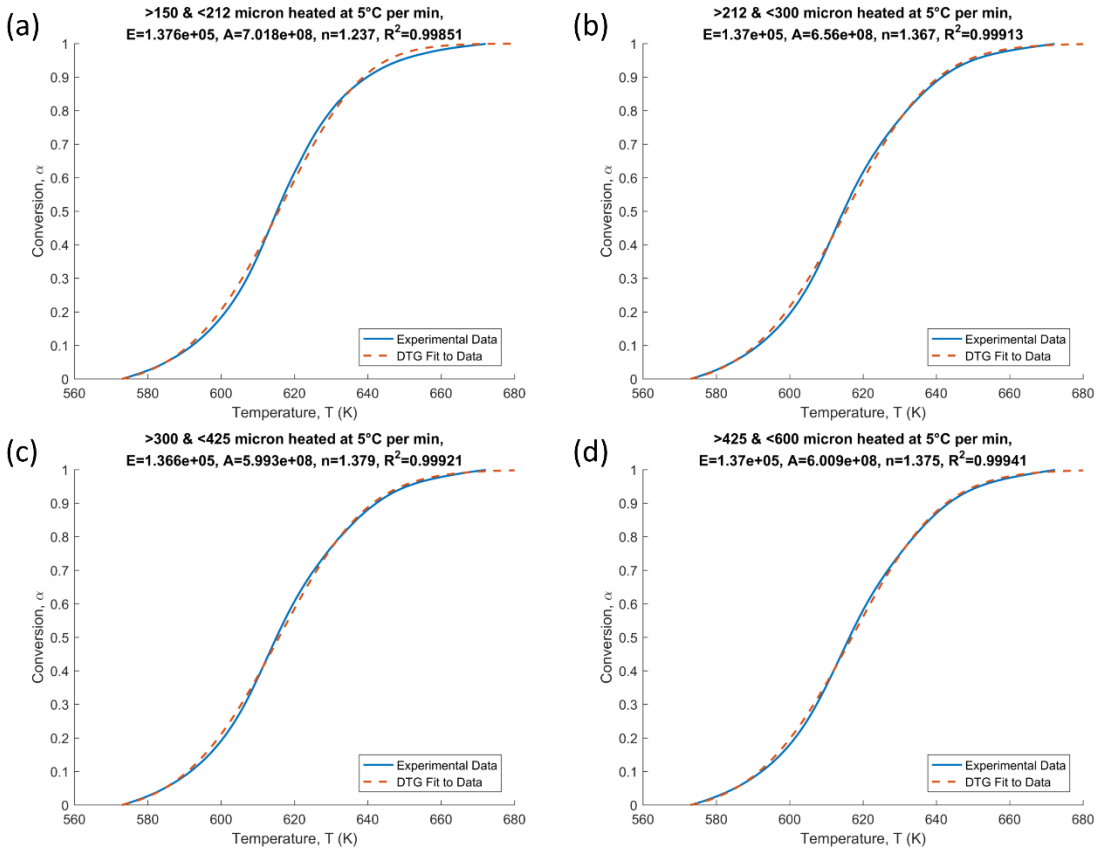

Figure 5-51: DTG fitted results for samples heated at a ramped heating rate of 5°C min^{-1} of particle size (a) >150 and <212µm, (b) >212 and <300µm, (c) >300 and <425µm, and (d) >425 and <600µm.

The temperatures at which these reaction occurs in the TGA experiments are in excess of the temperatures reached in the basket heating experiments. This lead to speculation that the kinetics estmated using the DTG method may not be representative of those seen in the basket heating experiments. A 50mm equi-cylindrical baskets of powder heated at a sub-critical temperature of approximately 500K (227°C), was seen to reach a maximum core temperature of 541K (268°C). This core temperature of 541K (268°C) is still below the reaction onset temperature seen in these TGA experiments. For this reason it was thought that the self-heating seen to occur in the baskets is largely caused by the initial portion of the reaction observed using TGA. As such, a second DTG approach was applied where the fitting was applied only to the initial portion of the normalised conversion curve, for $0 \geq \alpha \geq 0.4$. The normalised conversrions curves for the four samples can be seen in Figure 5-52.

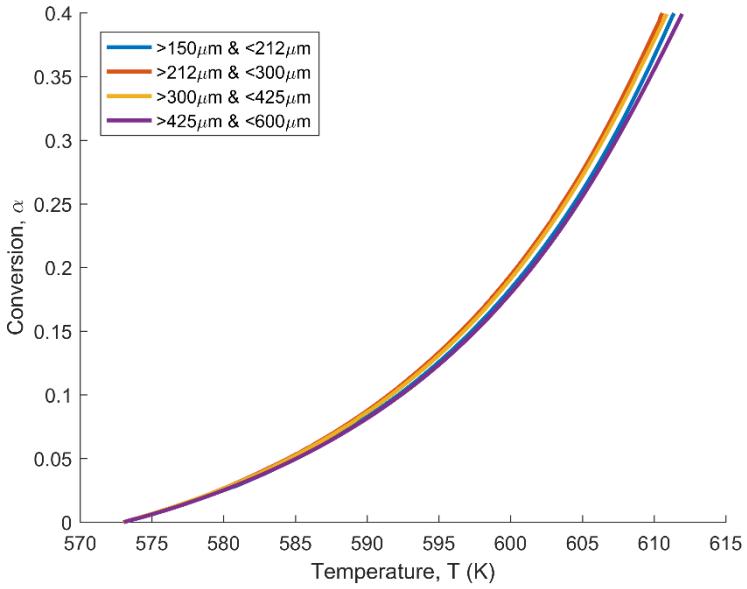

Figure 5-52: The initial portion of the normalised conversion curves for four particle size ranges at a heating rate of 5°C min^{-1}, to which kinetics are fitted.

Again the same problem was found whereby the initial guess of A influenced the best fit kinetics. The fittings to this initial portion for the four different size ranges and an initial guess for A 1x10^{8} s^{-1} can be seen in Figure 5-53. All four samples are found to have good fittings with all R^2 values in excess of 0.998. The fitted kinetics to each sample are again similar, with activation energies, E, of approximately 129x10^{3} J mol^{-1} and a consistent pre-exponential factors, A, of 1.17x10^{8} s^{-1}. Fittings were attempted over a range of values for the order of the reaction, n, but the best fit value would always tend towards the lower fitting bound value, with little change in the shape of the profile. For this reason n in these fittings was fixed to a value of 1. The effects of mass loss on the reaction are much less pronounced in this fitted region, and it is though that this causes the software to have difficulty in fitting a value of n. The activation energies of these fittings are more similar to those found using the basket heating methods shown in Table 5-9.

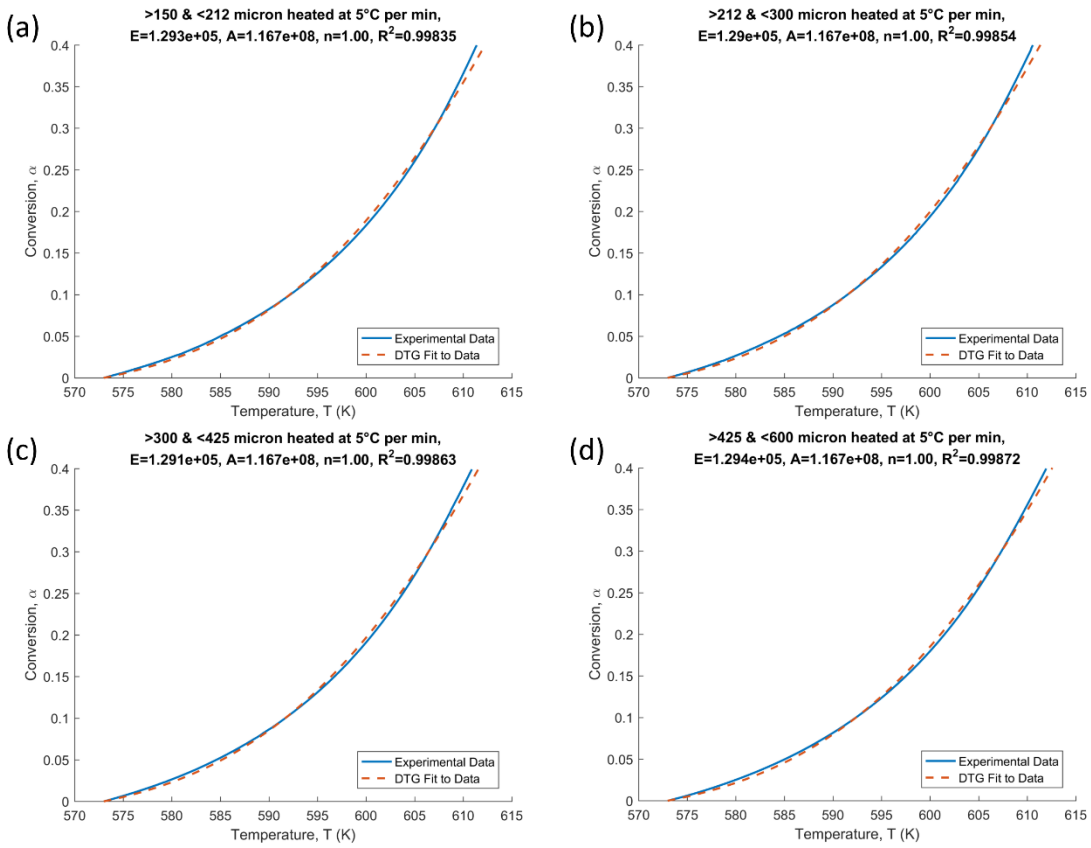

Figure 5-53: Kinetics fitted to the initial degradation profile of samples heated at a ramped heating rate of 5°C min^{-1} of particle size (a) >150 and <212µm, (b) >212 and <300µm, (c) >300 and <425µm, and (d) >425 and <600µm.

The kinetics for these two approaches are summarised in Table 5-15 for samples of particle size >212 and <300µm. These kinetics are used in the numerical model to explore the effects of n^{th} order kinetics.

Table 5-15: Kinetics estimated using the DTG approach for samples of particle size >212 and <300µm and at a heating rate of 5°C min^{-1}.

	$\boldsymbol{E}$ (J mol^{-1})	$\boldsymbol{A}$ (s^{-1})	$\boldsymbol{n}$
Full Profile Fitting	$137x10^3$	$6.56x10^8$	1.367
Initial Profile Fitting	$129x10^3$	$1.17x10^8$	1

5.7. Model Simulations of the Basket Experiments

The model developed as part of the investigation is discussed in Section 4.2. This model is capable of predicting temperature, moisture content, and vapour concentration

profiles in the radial and axial directions of a quarter portion of a cylindrical basket. The predicted temperature profiles are of most interest in this investigation and have already been used to explore aspects of the cross-point temperature method. In this section the drying behaviour is included in the model. The drying of the powder is not of importance to this study as does not impact on the self-heating behaviour of the detergent, but it has been included to allow for a better comparison with experimental data. It also illustrates the capabilities of the model, should drying need to be included in modelling spray dryer wall deposits, which will have a higher moisture content than these powders.

The evolution of temperature across the 2D basket domain with time can be seen in Figure 5-54. This plot shows the capabilities of the model and illustrates how the core of the basket increases in temperature due to self-heating in a typical basket heating experiment. In this model the reaction kinetics were taken as those measured using the steady-state method. These kinetics were used because they predict the same critical ambient temperatures as measured experimentally, and as such are considered the most representative set of kinetics. The model parameters are summarised in Table 5-16.

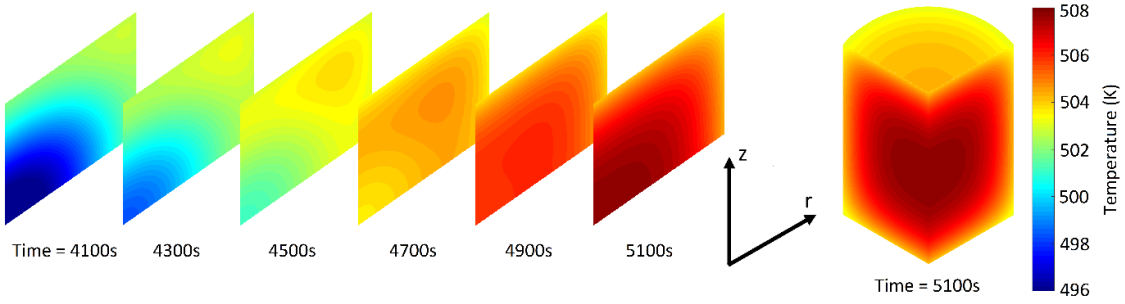

Figure 5-54: 2D model calculated temperature evolution in 50mm equi-cylindrical basket at and ambient temperature of 502.5K as self-heating causes the core temperature to rise.

Table 5-16: Parameters used in the numerical model of a self-heating basket of Micronized Formulation 1 detergent powder.

Parameter	Symbol	Value
Basket Radius	R	0.025m
Basket Half-Height	Z	0.025m
Powder Density	ρ	683.8 kg m^{-3}
Thermal Conductivity	k	0.08 W m^{-1} K^{-1}
Activation Energy	E	125.3x10^3 J mol^{-1}
Logarithmic Product of the Heat of Reaction and Pre-Exponential Factor	$\ln QA$	32.11
Emissivity	ϵ	0.5

The correlation for the heat transfer coefficient is given in equation (4-49), while other parameters are determined through qualitatively fitting. These parameters are the specific heat capacity, C_p (J kg^{-1} K^{-1}), the initial moisture content, X_0 (kg kg^{-1}), the internal mass transfer coefficient, $h_{m,in}$ (m s^{-1}), and the vapour diffusion coefficient, D_{vap} (m^2 s^{-1}). Best fit values of these parameters are shown in Table 5-17. The process by which these values were determined is discussed in Sections 5.7.2 and 5.7.3.

Table 5-17: Parameters used in the numerical model determined through qualitative fitting in Sections 5.7.2 and 5.7.3.

Parameter	Symbol	Value
Specific Heat Capacity	C_p	1350 J kg^{-1} K^{-1}
Initial Moisture Content	X_0	0.025 kg kg^{-1}
Internal Mass Transfer Coefficient	$h_{m,in}$	6x10^{-5} m s^{-1}
Vapour Diffusion Coefficient	D_{vap}	0.08 m^2 s^{-1}

5.7.1. Comparison of Model Predicted and Experimental Temperature Profiles

The model predicted central temperature-time profile using the parameter values in Table 5-16 and Table 5-17, and how this compares to the experimental data can be seen in Figure 5-55. For each experiment, the model ambient temperature profile is imported

from experimental data. The model predicted temperature profile is seen to compare well with the experimental data.

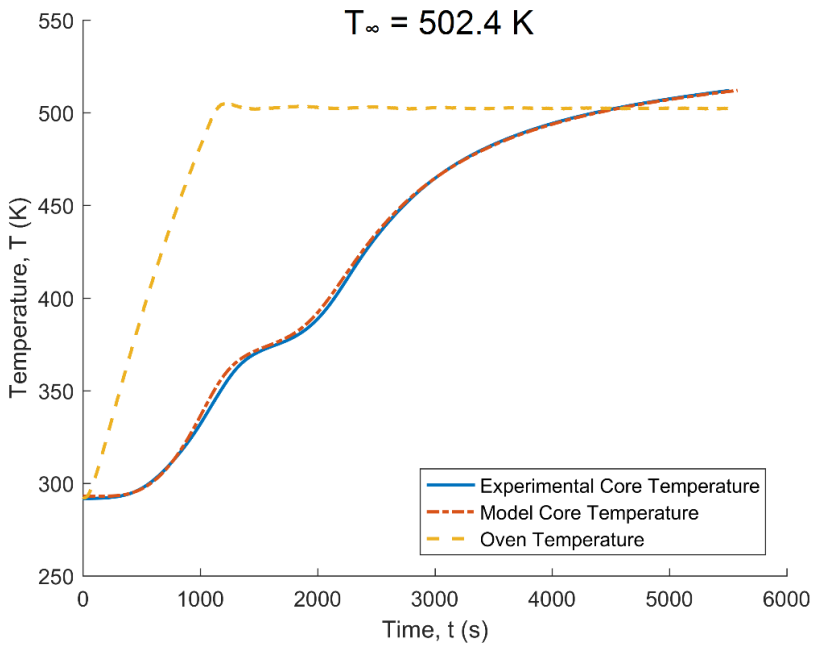

Figure 5-55: Comparison of model predicted basket core temperature profile and experimental data at an oven temperature of 502.5K (229.3°C). Kinetics for this model were estimated using the steady-state method.

The increase in temperature of the powder basket above the oven temperature is of most interest as this is an indication of the self-heating occurring. The agreement in this region is an indication that the kinetics determined using the steady-state method which were applied in this model are correct, and a good representation of this system. Additionally, it shows that a zero-order reaction model, at least up to this point in the temperature-time profiles, is a suitable model for predicting this behaviour.

Further comparisons of the model predicted temperature profiles with experimental data at a range of different ambient temperatures were made. These are shown in Figure 5-56 and show the comparison of the model predictions to the three thermocouples at radial distances of 0mm, 6mm, and 12mm. These plots are for four experiments run at oven controlled ambient temperatures from 498.5K (225.3°C) to 504.4K (231.2°C). Again good agreement is seen across these experiments, suggesting that this model is very capable of predicting these temperature profiles. This also validates the use of this model in simulating these basket heating experiments.

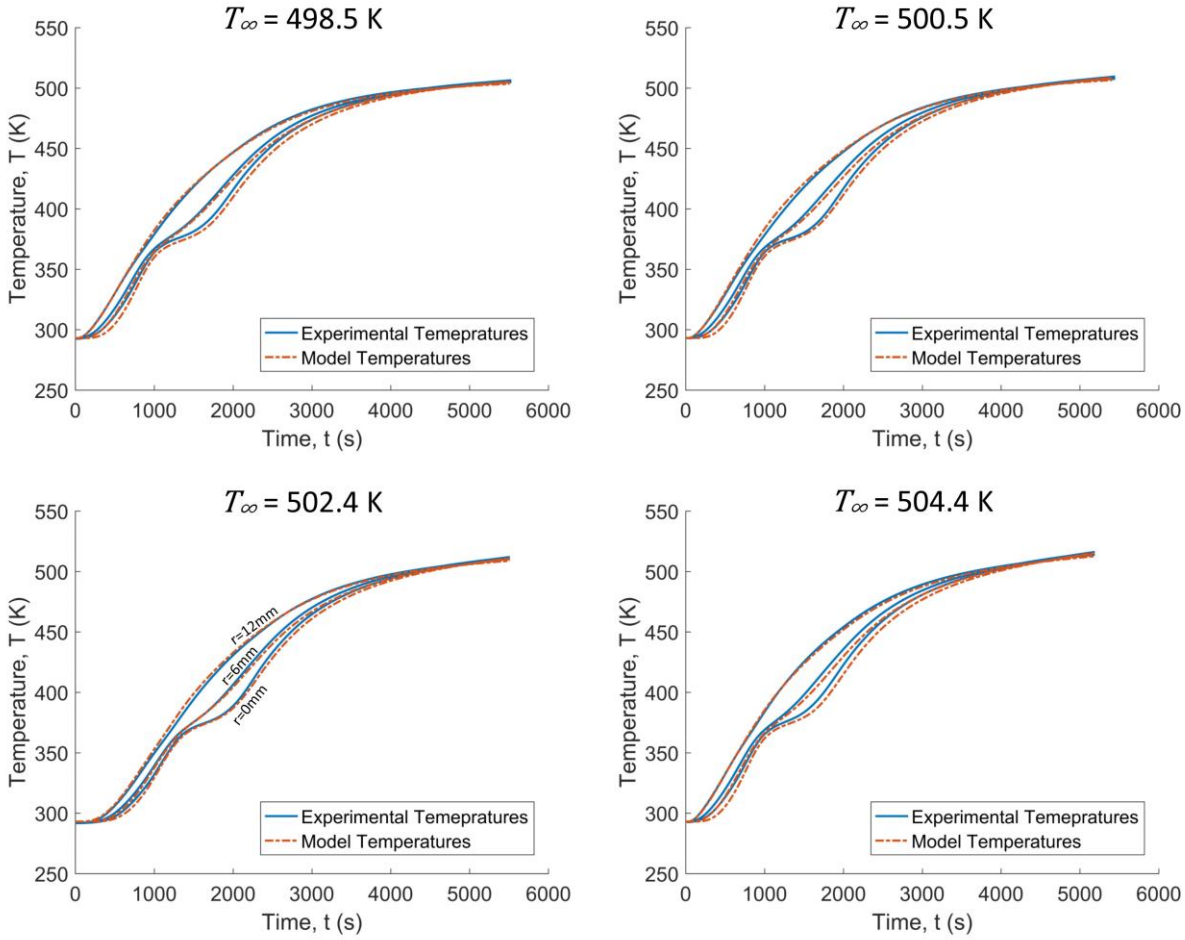

Figure 5-56: Comparison of model predicted temperature profiles to experimental data from an array of three thermocouples at radial distances of 0mm, 6mm, and 12mm, and at oven temperatures from 498.5K (225.3°C) to 504.4K (231.2°C). Kinetics for this model were estimated using the steady-state method.

5.7.2. Influence of Specific Heat Capacity on Model Predicted Temperature Profiles

In this study, the influence of the specific heat capacity, C_p, of the powder was also explored. C_p is calculated in the next chapter, Chapter 6, as part of the parameter estimation approach as approximately 1350 J kg^{-1} K^{-1} using modulated differential scanning calorimetry. The specific heat capacity, and thermal conductivity, k, are highly correlated values, as will also be seen in Chapter 6. This correlation leads to a corresponding thermal conductivity value of approximately 0.08 W m^{-1} K^{-1}. k was fixed here while C_p was varied. This effectively changes the value of the thermal diffusivity ($k/\rho C_p$), which dictates the rate of thermal response of the powder.

The specific heat capacity does not feature in equation (5-4), the equation for the Frank-Kamenetskii parameter, δ. Therefore its value does not influence the critical ambient temperature, merely the thermal response time. The effect of varying the specific heat capacity is shown in Figure 5-57. This figure shows the model predicted core temperature profile of the basket using varying values of C_p and how this compares to the experimentally measured temperature. Using these values outlined previously, the temperature profile using a C_p value of 1350 J kg^{-1} K^{-1} is seen to compare best with the experimental data. Higher values than this giving a slower thermal response, but this slower thermal response will impact on the basket's tendency to thermally runaway.

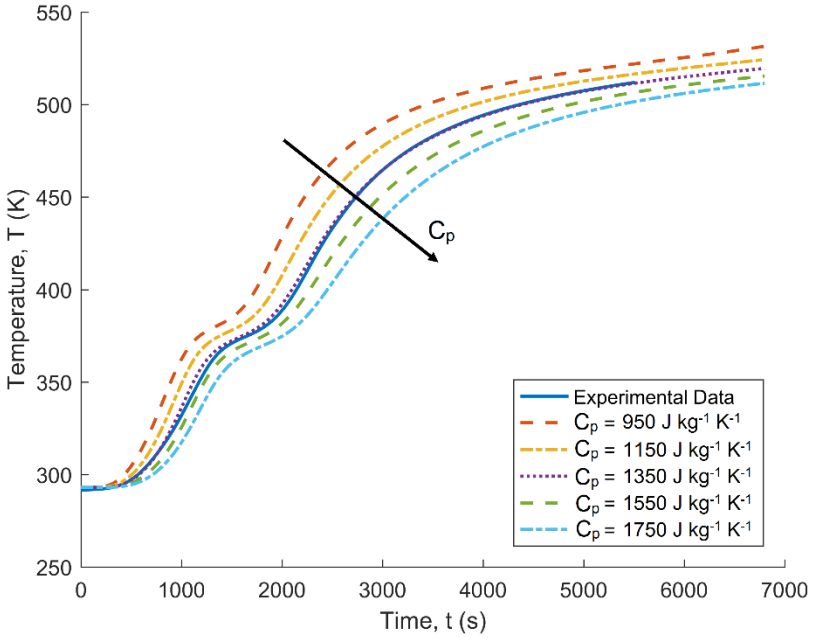

Figure 5-57: Comparison of model predicted basket core temperature profiles to experimental data using different specific heat capacity values.

5.7.3. Influence of Drying Parameters on Model Predicted Temperature Profiles

In this study, the prediction of drying behaviour was not considered important. Instead of predicting this, an established model was fitted to the observed drying behaviour. The drying does not impact on the models ability to predict self-heating behaviour, and as such, only a qualitative fit for the drying model parameters was required.

A Reaction Engineering Approach (REA) was taken to modelling the drying kinetics. These kinetics were determined by fitting a simple model to sorption isotherm data as

discussed in Section 4.2.2. A correlation for the apparent activation energy correction factor, ΔE_v, was calculated as:

$$\Delta E_v = 8.36x10^7 \exp[-13.65(X^{0.09928})] \quad (5\text{-}33)$$

Despite having these drying kinetics, parameters such as that vapour diffusion coefficient, D_{vap}, the initial moisture content, X_0, and the internal mass transfer coefficient, $h_{m,in}$, were found to largely influence the drying behaviour. The influence of each of these parameters on the predicted drying behaviour was explored by varying these parameters and plotting the model predicted temperature profiles along with experimental data. Figure 5-58 shows the influence of X_0, Figure 5-59 shows the influence of $h_{m,in}$, and Figure 5-60 shows the influence of D_{vap} in comparison to the experimental measured central temperature profile.

An approximate value of X_0 was known from measuring the mass loss of samples following drying in the oven, varying slightly between samples. The comparison in Figure 5-58 was used to determine the best fitting value for this sample.

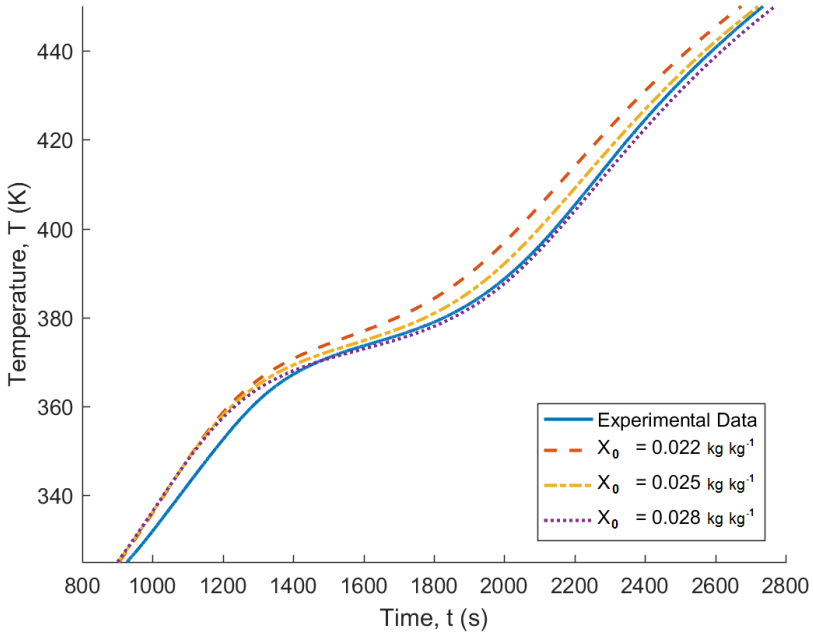

Figure 5-58: Effects of initial moisture content on the fitting of the model to the experimental core temperature profile in the drying region.

Values for $h_{m,in}$ and D_{vap} similar to those of Chen (2001) and Chong and Chen (1999), used in the modelling of heat and mass transfer in oven heated baskets of milk powder,

were used. It was found that above a value of 5x10^{-5} m s^{-1} for the internal mass transfer coefficient, $h_{m.in}$, there is little change in the core temperature profile in the drying region of the curve, as can be seen in Figure 5-59. This is due to the drying behaviour being limited by the value of the vapour diffusion coefficient, D_{vap}.

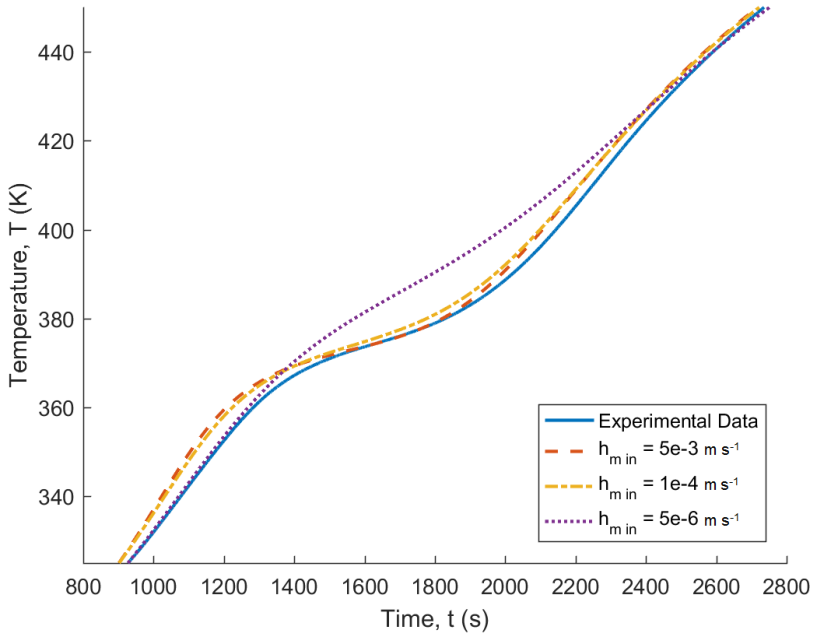

Figure 5-59: Effects of internal mass transfer coefficient on the fitting of the model to the experimental core temperature profile in the drying region.

For decreasing values of D_{vap} the plateau in the core temperature profile, where the majority of the drying happens, is seen to occur later. This is shown in Figure 5-60. This is caused by the slow diffusion of vapour to the boundary. Drying is known to be slowest at the basket centre. The low diffusion coefficient means that the evaporated moisture at the basket centre takes longer to reach the basket edges where is can be transferred to the ambient air. This is also why a more severe “step” is seen in the temperature profiles of the central thermocouples, relative to those of the thermocouples at 6mm and 12mm. This can be seen in Figure 5-56.

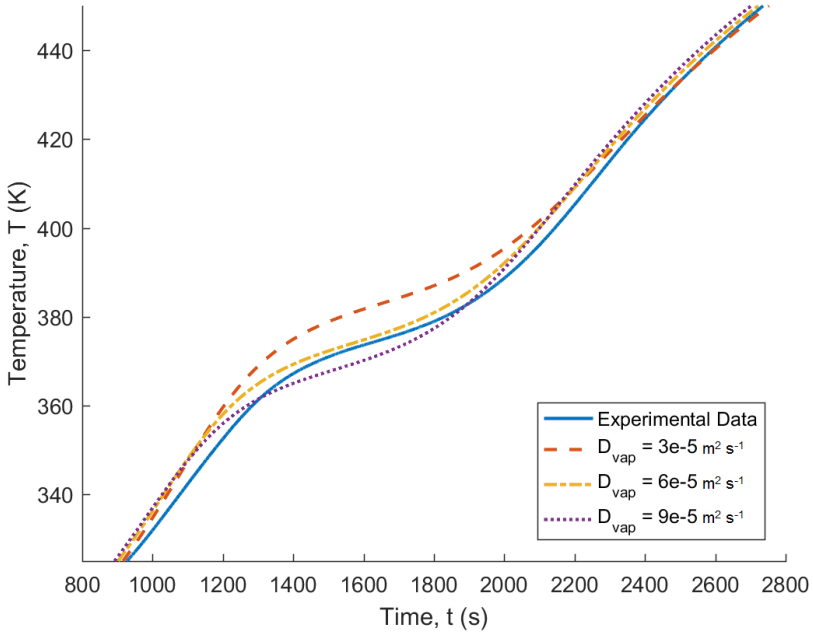

Figure 5-60: Effects of vapour diffusion coefficient on the fitting of the model to the experimental core temperature profile in the drying region.

5.7.4. Model Results Comparison using Zero-Order vs. n^{th} Order Reaction Kinetics

Two different sets of kinetics and their accompanying models were used in this investigation, these being zero-order kinetics as estimated using the steady-state approach and the cross-point temperature method, and n^{th} order kinetics as estimated using the Thermogravimetric approach. The steady-state approach kinetics were fitted to the experimentally determined critical ambient temperatures, with the equation using an exact dimensionless manipulation of the governing equation of this model. This means that, so long as the correct value of δ_{cr} is used in measuring these kinetics, the thermal runaway as predicted by the model will occur at the same temperatures as in the experiments. This can be seen in the plot of the basket core temperature profile at a sub-critical ambient temperature in Figure 5-61 and at a super-critical ambient temperature in Figure 5-62. These comparisons are made over a longer time period than those in Figure 5-56, such that thermal runaway can be observed. This agreement also serves as a validation of the heat generation aspect of the model. The model and experimental temperature profiles agree very well in the initial period of self-heating, but after about 2.5 hours (9000 seconds) the profiles diverge. The model predicted temperature reaches a steady-state, a feature only possible because a zero-order kinetic model is used. The experimental data continue to increase in temperature before

reaching a temperature peak after about 4.5 hours (16200 seconds), and then falling in temperature. This temperature peak exists because in reality the reaction rate is influenced by the concentration of reactive component, with depletion of this causing this reaction rate to eventually begin to fall. The concentration of reactive component is not accounted for in the zero-order kinetics model and is why the use of an n^{th} order model was explored.

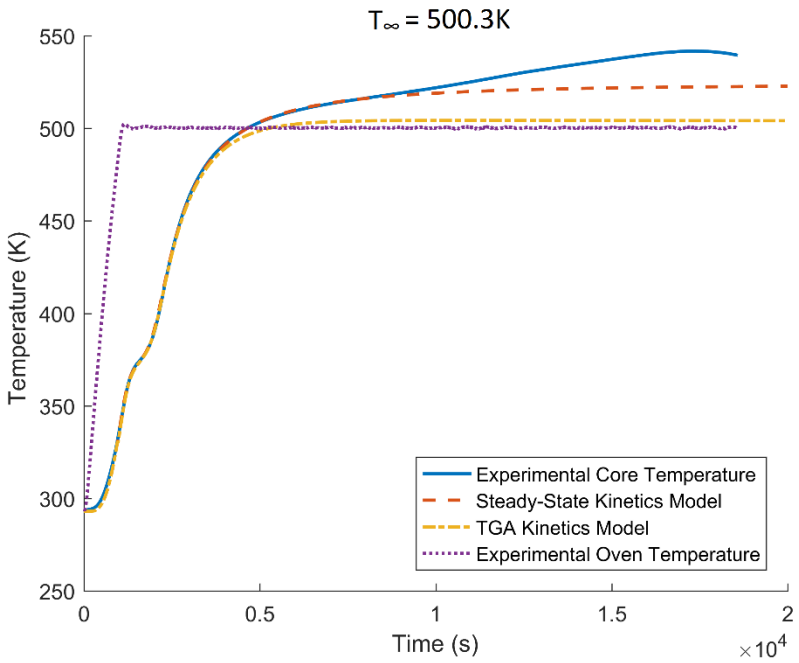

Figure 5-61: Comparison of model temperature profiles using zero- and n^{th} order kinetics to experimental data for a 50mm equi-cylindrical basket at a sub-critical temperature of 500.3K (227.1°C).

The kinetics determine using the DTG method were used to model n^{th} order reactions using the equations outlined in Section 4.2.3. This kinetics determined from fitting to the initial portion of the degradation were used here. The heat of reaction, Q, was determined using DSC by measuring the area under the reaction heat flow profile. A value of 1.6×10^6 J kg^{-1} was used. The model predicted temperature profiles using this set of n^{th} order kinetics are significantly different to the experimental profiles, as can be seen in Figure 5-61 and Figure 5-62. Using these kinetics, the model predicts very little self-heating in these oven heated baskets. This is not surprising, given that the TGA reaction is seen to have a higher reaction onset temperature. Similarly, little self-heating was exhibited when using the kinetics determined from fitting to the entire degradation

profile. For this reason, it was thought that this ambient temperature was too low to initiate the reaction using these kinetics.

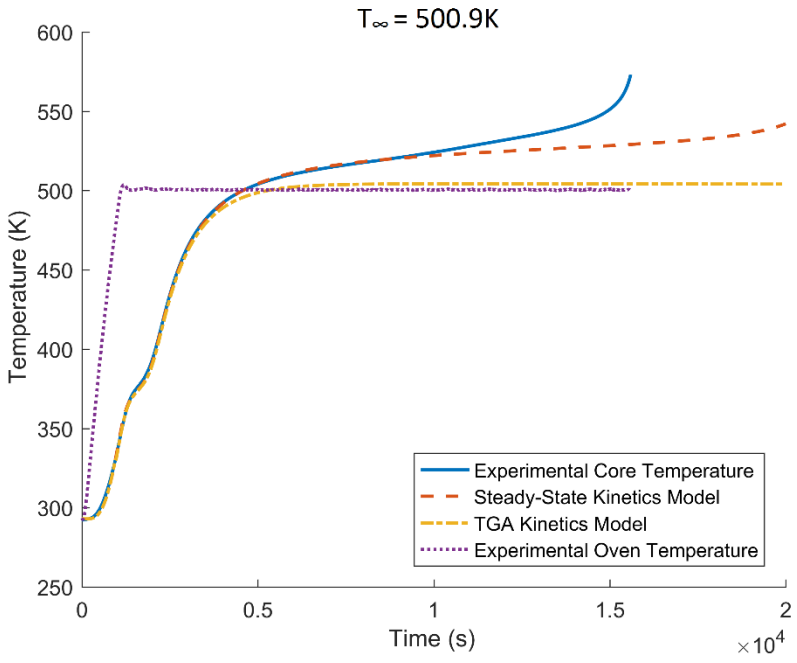

Figure 5-62: Comparison of model temperature profiles using zero-order and n^{th} order kinetics to experimental data for a 50mm equi-cylindrical basket at a super-critical temperature of 500.9K (227.7°C).

Higher ambient temperature were modelled so that the predicted temperature profiles when self-heating is exhibited could be analysed. This was done for two sub-critical ambient temperatures of 515K (242°C) and 518K (245°C), and a super-critical temperature of 519K (246°C), as shown in Figure 5-61. These ambient temperatures are significantly higher than the experimentally measured critical ambient temperature, 500.4K (227.2°C).

At a sub-critical temperature of 518K (245°C), the powder is seen to react quicker than in the experiments, but as the reactive component depletes the reaction slows quickly and the temperature falls towards the oven temperature. At a super-critical temperature, the powder is seen to suddenly spike in temperature, as happens in the experiments and zero-order model. With regards the initially quick reaction rate increase, inclusion of the observed oxygen dependency of the reaction may improve the results. The reaction is known to be oxygen dependent from previous TGA and DSC experiments in Sections 3.4 and 3.5, and the slow diffusion of oxygen into the basket core may inhibit this rapid increase in temperature seen.

Only the initial portion of the reaction was accounted for when fitting these kinetics. Isoconversional DSC experiments carried out later in Chapter 6 show that the reaction activation energy changes as a function of conversion. Characterising these reactions and modelling a multi-step reaction may help in replicating the experimental behaviour.

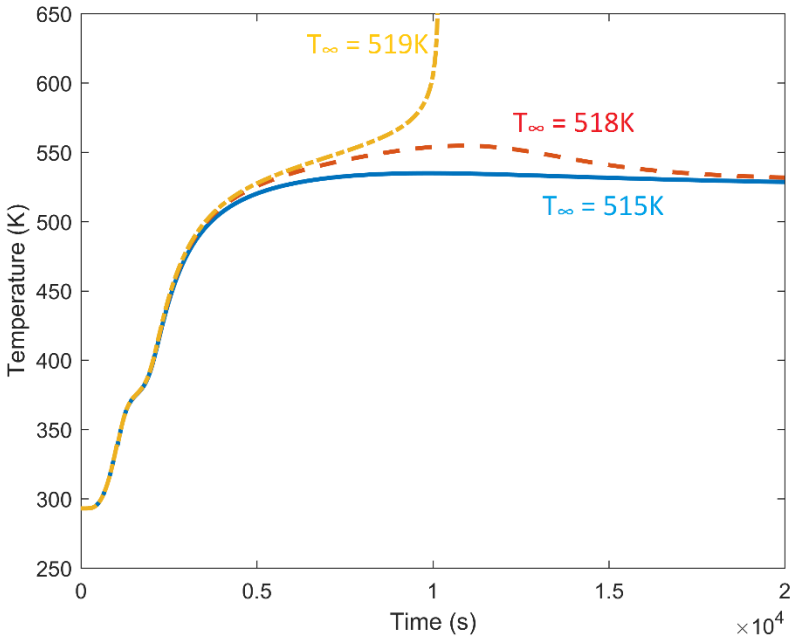

Figure 5-63: Model predicted central temperature of a 50mm equi-cylindrical basket of powder using an n^{th} order reaction model at different ambient temperatures.

The added complexity of the n^{th} order model, the difficulty in getting the model to replicate the observed behaviour, and the fact that it over predicts thermal runaway by almost 20°C, makes the zero-order model the preferred choice for modelling these systems. The zero-order model predicted the same critical ambient temperature, and was found to fit very well with the self-heating period, only deviating in the peak temperature reached. When modelling self-heating in oven heated baskets or in spray dryer wall accumulations such complexity is typically not required and it is thought that the zero-order models used here will provide good, representative results.

5.8. Conclusions

This aspect of the study sought to determine the best means of estimating the self-heating reaction kinetics of detergent powders. The first method discussed was the steady-state method. This method is based around the critical criterion δ_{cr}. This

parameter is a function of the dimensionless exponent, φ ($= E/RT$), and the Biot number, Bi, and has been previously solved for analytically for ideal conditions, such that $\varphi = \infty$ and $Bi = \infty$. Parks (1961) numerically calculated δ_{cr} for a range of values for φ, but there was scope for improvement. 1D and 2D dimensionless numerical models were used here to calculate δ_{cr} as a function of φ and Bi. It was shown that using incorrect values for δ_{cr} can impact strongly on the results. If the correct value for δ_{cr} is used in estimating the self-heating reaction kinetics of the powder using the steady-state method, then a model can be developed which agrees almost exactly with the experimentally measured critical ambient temperatures. This was what was done here. The model predictions using these kinetics fitted very well with observed temperature profiles for the majority of the reaction period. The steady-state method however is slow with each test taking between 4 and 8 hours, and a number of tests required to obtain a single data point.

The cross-point temperature method is a faster alternative, but this approach was seen to be more susceptible to errors. The estimated kinetics using this approach varied depending on the spacing of the thermocouples used. Model simulations showed that some variation should exist between the cases, but not to the extent seen here. In fact, model simulations have shown that similar results should be achieved no matter the thermocouple spacing, so long as it is not greater than half the radius.

Further simulations of the method were conducted to evaluate the impact of the finite difference approximation for the conduction term on the results. The impact of thermocouple spacing and the inclusion of axial conduction were also explored. It was found that using a more accurate finite difference stencil (i.e. 5 point instead of a 3 point stencil) had more of an impact than the inclusion of axial conduction. Ideally a five-point stencil in both the radial and axial directions should be used to approximate the second order temperature derivative. In reality this involves five thermocouples and is impractical to apply experimentally. Instead, a five-point stencil in the radial direction, consisting of three thermocouples, as used here for case 3, should be sufficient. However, it was shown both in the experiments and with the model, that errors in thermocouple readings overshadowed the improvements in the accuracy of this setup.

In the experiments, a relatively large spacing of 12mm was found to give to best results. The kinetics estimated using this spacing predicted thermal runaway for a 60mm equi-

cylindrical basket at 223.9°C (497.1K), only 2.6°C greater than the experimentally measured critical ambient temperature of 221.3°C (494.5K). A smaller spacing of 6mm produced more variability and kinetics that significantly over-predicted this temperature at 229.0°C (502.2K). A slight discrepancy in estimated kinetics is expected, as shown using model simulated experiments, but the large discrepancy observed experimentally could be due to a combination of errors in thermocouple placement (±1mm), thermocouple readings (±0.25°C), and the variability caused by the small number of particle diameters that fits in the smaller thermocouple spacing of 6mm.

The numerical model developed as part of this study allowed predictions in temperature profiles and critical ambient temperatures to be made. Having estimated a number of parameters, in particular the drying parameters, and using a zero-order reaction model with the kinetics estimated using the steady-state method, the predictions of this model were found to agree well with the experimentally measured temperature profiles. This agreement was shown for baskets at a range of ambient temperatures.

In this study, n^{th} order kinetics were found using a TGA based method, whereby kinetics were fitted to the normalised mass loss data observed in the sample across the reaction. Applying these kinetics in an n^{th} order model exhibited little self-heating, with critical ambient temperatures under predicted by almost 20°C. This is not surprising given that the TGA reaction onset temperature was found to be considerably in excess of the onset temperature in the basket tests. Even at higher ambient temperatures, the n^{th} order model predicted behaviour was different to that observed experimentally. The reaction was seen to occur much quicker using this model. It may be that this model can be improved by including a multi-step reaction or oxygen dependency of the reaction and oxygen diffusion. However, this will not improve this models predictions of critical ambient temperatures.

The much simpler zero-order model compared considerably better to experimental data. It is also thought that a zero-order model is sufficient when it comes to predicting self-heating in these systems. The next chapter will look at improving the basket heating methods discussed here using a novel parameter estimation approach, whereby the zero-order model is fitted to the temperature profiles measured in the oven heated baskets.

6. Novel Parameter Estimation Approach for Characterising Self-Heating Powders

6.1. Introduction

The characterisation of the self-heating behaviour of detergent powders has thus far been done using the steady-state method and the cross-point temperature method. The steady-state method was shown to give good results, allowing accurate model predictions of self-heating to be made. However, this method is particularly slow. The cross-point temperature is a faster method, but it was shown that this method is susceptible to errors. Building on these methods, a novel approach was developed which was used to characterise the self-heating reaction kinetics, and the powder thermal conductivity and specific heat capacity. This novel approach is developed from the same basket setup as the cross-point temperature method but uses the numerical model of a self-heating basket of detergent powder, outlined in Section 4.2.1, to determine these parameters through parameter estimation.

Parameter estimation is the process of fitting a number of model parameters to experimental data in order to make the model predictions match the observed data. This was done using the parameter estimation features of gPROMS ModelBuilder, where parameters are estimated using maximum likelihood formulation. The results of this methods, as well as the advantages and disadvantages in comparison to the existing methods explored, are discussed in this chapter.

The parameter estimation approach uses a 2D-axisymmetric model of heat transfer with heat generation in an equi-cylindrical (cylinder of equal height and diameter) basket of detergent powder. This model is simultaneously fit to temperature profiles from a number of basket experiments. The experiments consists of oven heated basket experiments which follow the same procedure as the cross-point temperature method experiments, whereby an equi-cylindrical basket full of detergent powder is heated to some high temperature with an array of three thermocouples embedded within the powder. These thermocouples provide three temperature profiles for each experiment, to which the model can be fitted.

This approach was used to fit the activation energy, E, and logarithmic term capturing the pre-exponential factor and heat of reaction, $\ln QA$. However, the thermal conductivity, k, and specific heat capacity, C_p, of the powder are also required to predict self-heating behaviour. To reduce the number of experiments required to characterise these powders, these parameters were also estimated using this method.

The powder thermal conductivity and specific heat capacity are highly correlated parameters. As such, Modulated Differential Scanning Calorimetry (Modulated DSC or MDSC) was used to determine the specific heat capacity value prior to fitting. It was also thought that the correlation between the activation energy and the logarithmic term may be an issue, and as such the activation energy was also determined prior to fitting using DSC and the Ozawa-Flynn-Wall and Friedman approaches. The effects of fixing these values in the fittings is explored. This approach was developed to be faster than the previous basket methods, whilst also improving on the error of the measured parameters. Throughout this chapter, the results of this method will be compared to those for the other basket heating methods, to establish whether this approach is an improvement on the existing methods.

However, this approach is not without its flaws. Assumptions applied in the numerical model will have an impact on the model accuracy and the estimated parameters. These assumptions include:

- Heat generation is assumed to be due to a single zero-order reaction, or several simultaneous zero-order reactions assumed to be one overall reaction.
- Reactant consumption is assumed negligible, such that a zero-order reaction can be assumed.
- The thermal conductivity, k, and specific heat capacity, C_p, are assumed constant (i.e. independent of temperature).

These assumptions introduce a degree of artificial bias into the estimation of the model parameters.

6.2. Development of the Parameter Estimation Approach

The Parameter Estimation Approach was developed as an alternative to the existing basket methods, the steady-state method and the cross-point temperature method. The detergent powder formulations characterised using the Parameter Estimation Approach were originally characterised using these existing basket methods. These methods both have their advantages and disadvantages, and it was thought that a model based approach could be developed to improve on these methods using the Parameter Estimation capabilities of gPROMS ModelBuilder. The advantages and disadvantages of the existing methods are detailed below.

Steady-State Method

Advantages:

- This is a well-established approach that has been used to measure self-heating reaction kinetics of powder based systems since its inception by Bowes and Cameron (1971).
- This approach is well detailed in literature and has been used to characterise powders such as milk-powder, coal, and sawdust.
- The kinetics measured using this method are essentially fit to the measured critical ambient temperatures, such that models using these kinetics agree exactly with experimentally measured critical ambient temperatures.

Disadvantages:

- This method is particularly slow. Each experiment takes between 5 (50mm equi-cylindrical basket) and 8 hours (70mm equi-cylindrical basket) to complete, and not every experiment yields a data point. On average, about 5 experiments were required to determine the critical ambient temperature to within 0.5°C.
- The basket size is limited. The low thermal conductivity of the detergent powder means that large baskets of powder would take far too long to run.
- Because of how long these experiments take, and the limitation in basket size, few data points are used in this method. In this case only three points were used.

Cross-Point Temperature Method

Advantages:

- This method is developed from the same energy balance as the steady-state method, making them comparable.
- It is a faster alternative to the steady-state method. Each experiment takes between 1.5 (50mm equi-cylindrical basket) and 3.5 hours (70mm equi-cylindrical basket) to complete. Every experiment yields a data point.
- Although not as much as the steady-state method, there is a considerable amount of literature detailing this method.

Disadvantages:

- It is difficult to verify the results of this method without comparing the predicted critical ambient temperatures with those measured experimentally.
- It was found that this method is very susceptible to thermocouple errors. This can be seen from how the three cross-point cases explored often failed to agree with one another. It can also be seen from the scatter of the points measured. Simulating these experiments showed that the approximation used for the conduction term in determining the cross-point can affect the results. In particular, the thermocouple placement errors largely affect the results.

The Parameter Estimation Approach was developed to improve upon these methods. The following points illustrate the promise that this method has:

- This approach is based on the same energy balance as two existing basket methods, again making these methods and the results comparable.
- The basket setup used in this approach is the same as that used in the cross-point temperature method, meaning that the kinetics can be determined using both approaches for a single set of experiments.
- This approach fits a numerical model to a large portion of the measured temperature profiles. This means that this approach uses thousands of data points, across three thermocouples and a number of experiments. In this case up to 13 experiments were used in the different fittings, although there is no limit to the amount that could be used. In comparison, the steady-state method

used 3 data points, and the cross-point temperature method used between 10 and 15 data points.

- Using the same experimental procedure as the cross-point temperature method means that this approach preserves the time advantage that the cross-point temperature method has over the steady-state method.

These points detail how the proposed parameter estimation approach is potentially advantageous over the existing basket methods. This chapter will detail the experimental procedure, the numerical model used for fitting, the Maximum Likelihood Function used to determine the best fit parameters, the initial temperature profile approximation for the experimental data, and the DSC experiments used to determine the specific heat capacity and activation energy values prior to fitting.

6.3. Detergent Powder Composition

This approach was used the estimate the self-heating parameters of the four detergent powder formulations outlined in Sections 3.2 and 5.1. This chapter focuses on the characterisation of the formulation referred to as Micronized Formulation 1, while Section 7.2 focuses on the application of this approach to three other formulations: non-Micronized Formulation 1, Formulation 2, and Formulation 3. Micronized Formulation 1 is a model composition that is representative of the spray-dried powder present in a commercial laundry detergent product, with a finer, micronized grade of sodium sulphate used to reduce the composition variability that can be seen between particles and between different sizes of particles.

The particle size distribution of these formulations were measured by sieving. This also allowed the specific heat capacity, C_p, and activation energy, E, of individual size ranges to be measured, giving an insight into the variability of the self-heating behaviour with particle size. Experiments were performed on four size ranges for each formulation. The size ranges used were >150µm and <250µm, >250µm and <355µm, >355µm and <425µm, and >425µm and <600µm. The percentage contribution of each of these size ranges to the overall composition can be seen in Table 6-1. This size distribution analysis also allowed the mass median particle diameter, D_{50}, the diameter for which 50% of the

particles are smaller to be measured. This is shown in Table 6-2 along with the bulk-densities of the formulations.

Table 6-1: Percentage contribution of each size range to the overall powder size distribution for each of the four detergent powder formulations.

	Micronized Formulation 1	**Non-Micronized Formulation 1**	**Formulation 2**	**Formulation 3**
150 - 250µm	20%	21%	10%	8%
250 - 355µm	15%	22%	46%	34%
355 - 425µm	7%	10%	13%	12%
425 - 600µm	13%	15%	15%	17%
Total % of Overall Composition	56%	68%	83%	70%

Table 6-2: Mass median particle diameter for each of the four detergent powder formulations.

	Micronized Formulation 1	**Non-Micronized Formulation 1**	**Formulation 2**	**Formulation 3**
Mass Median Particle Diameter (D_{50})	325µm	341µm	329µm	376µm
Bulk Density	683.8 kg m^{-3}	545.2 kg m^{-3}	586.5 kg m^{-3}	610.1 kg m^{-3}

6.4. Oven Heated Basket Experiments

For each detergent formulation 13 experiments were performed. 13 experiments allowed different combinations of these experiments to be used in the fittings, such that the number of experiments required to achieve good results can be determined. Each experiment was performed at a different oven controlled ambient temperature. Experiments for three samples: Micronized Formulation 1, Non-Micronized Formulation 1, and Formulation 3 were run at temperatures from 216°C (489K) to 228°C (501K), while the samples of Formulation 3 were found to not be significantly reactive at these temperatures and instead was run at temperatures from 222°C (495K) to 234°C (507K).

All experiments followed the same procedure as the cross-point temperature method experiments outline in Section 5.3. 60mm equi-cylindrical baskets, were each filled with powder and tapped to a similar mass, with this mass varying by formulation. The baskets were heated in the same Memmert UF75 Forced Convection oven as for the previous experiments. An array of three type K thermocouples (RS Pro 363-0294) were placed within the basket. These thermocouple were glass fibre insulated with a welded exposed junction and supplied with a working range of -60° to 350°C. These thermocouples were inserted to the basket half-height and at radial distances of 0mm, 6mm, and 12mm from the basket centre. An additional thermocouple was placed close to the basket within the oven to give a true reading of the ambient temperature experienced by the basket. The recorded ambient temperature profile was important as this was input in gPROMS ModelBuilder as an experimental control variable. The experiments were run for between 130 and 160 minutes, until such time that significant self-heating had been observed but before thermal runaway had occurred.

6.5. Numerical Model used for Parameter Estimation

The numerical model of an oven heated equi-cylindrical basket of powder as outlined in Section 4.2.1 was used for the fittings. This model consisted of the heat transfer and heat generation equations, where a zero-order reaction model was used. In this model, the temperature evolution in the basket is modelled using the following:

$$\rho C_p \frac{\partial T}{\partial t} = k\nabla^2 T + \rho Q A e^{\frac{-E}{RT}}, \tag{6-1}$$

The drying equations outlined in Section 4.2.2 were not used in this model. This was done because the fitting was only performed to the region after drying had completed of the experimentally measured temperature profiles. This meant that the model could be greatly simplified as the drying parameters did not need to be determined.

6.6. Initial Temperature Profile Approximation

This approach seeks to determine four parameters which are key to predicting self-heating in detergent powders. To determine these values the most appropriate portion

of the experimentally measured temperature profiles must be used. Figure 6-1 shows how a typical experimental temperature profile can be divided into three regions, the initial heating region, the drying region, and the self-heating region.

During the initial region the reaction term in equation (6-1) is of almost negligible influence, and the model reduces to the transient and conductive heat transfer terms. The drying region is self-explanatory, in that the drying of the residual moisture in the particles occurs within this period. The equation describing this behaviour were not included in the model for this investigation as this region is not of interest and the inclusion of these equations would greatly add to the complexity of the model. The self-heating region begins after drying has completed and at the temperatures where the self-heating reaction begins to occur. During this region all four parameters, k, C_p, E, and $\ln QA$, have an influence on the model predicted temperatures and the complexity of including a drying model can be avoided because by this time drying has finished. For this reason this region of the experimental temperature profiles was used for the fittings.

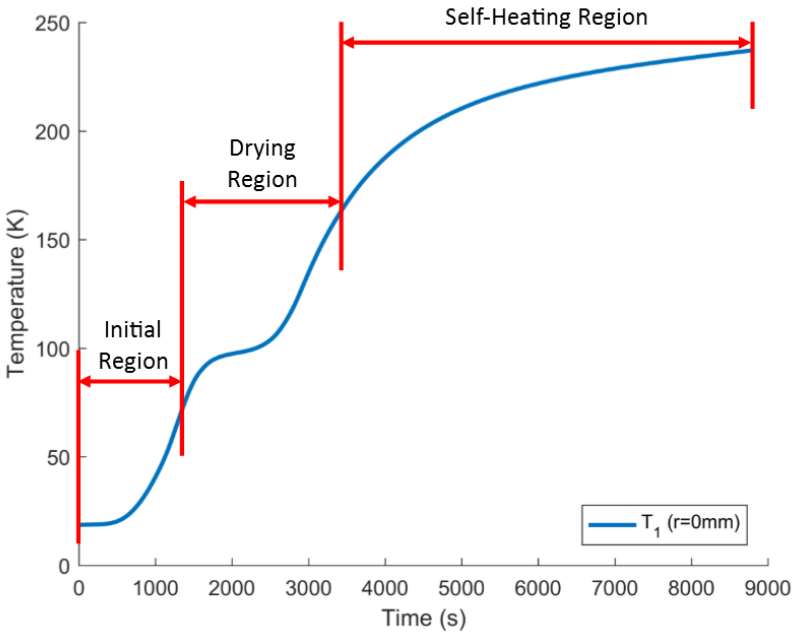

Figure 6-1: Typical experimental temperature profile split in three regions, the initial heating region, the drying region, and the self-heating region.

The model which is to be fit requires initial conditions to run, and because the fitting is to begin in the self-heating region, a steady-state temperature profile cannot be used.

Instead an initial 2D temperature profile in the radial and axial directions is needed. The problem is that this profile is not known, and only the temperatures as measured by the three thermocouples at radial distances of 0mm, 6mm, and 12mm (all measured at an basket half-height, i.e. $z = 0$mm), and the ambient temperature are known. An approximation of the 2D initial temperature profile must be developed from these data.

Before, the profile could be approximated, a start time for each experiment was determined. A similar starting point was desired for each of the experiments. This allowed the initial temperature profiles for each experiment to be compared. All the experiments were compared to find the time for each experiment at which the difference in temperatures across all 13 experiments was minimised.

After determining the starting time for each experiment, the initial temperature profiles for each experiment could be approximated. The first step is to approximate the radial temperature profile at $z = 0$. It was decided that the cubic profile in equation (6-2) was to be used. It was thought that having only three measured temperatures would make fitting difficult, and as such, the assumption that the temperature profile follows this cubic shape was applied. The choice of this profile is validated later.

$$T = p_3 r^3 + p_2 r^2 + p_1 r + p_0. \tag{6-2}$$

To fit this polynomial to the measured temperature data, some mathematical manipulation was required. Instead of fitting the four coefficients, p_0, p_1, p_2, and p_3, this equation could be reduced to one containing parameters which would better describe this system. These parameters include known system input parameters, and 3 parameters that will be determined through fitting. The known parameters are the effective heat transfer coefficient, h, the thermal conductivity, k, the basket radius, R, and the ambient temperature, T_∞. The parameters to be determine through fitting are the temperature at the basket centre, $T_{r=0}$, the temperature at the basket edge, $T_{r=R}$, and the polynomial coefficient p_3, which dictates the shape of the curve.

The polynomial can be reduced by looking at the constraining boundary conditions. The same boundary conditions that apply to the numerical model also apply here:

$$\left.\frac{dT}{dr}\right|_{r=0} = 0, \tag{6-3}$$

$$-k\left.\frac{dT}{dr}\right|_{r=R} = h(T|_{r=R} - T_\infty). \tag{6-4}$$

At $r = 0$ it can be seen that the coefficient $p_0 = T_{r=0}$, the temperature at the basket centre. Taking the first derivative of equation (6-2) with respect to r, and using the boundary condition at $r = 0$, it can be seen that the coefficient p_1 reduces to zero. This reduces the temperature profile to:

$$T = p_3 r^3 + p_2 r^2 + T_{r=0}. \tag{6-5}$$

By taking the first derivative of equation (6-2), applying the boundary condition at $r = R$, and rearranging for p_2 in terms of the radius, R, the conductivity, k, the effective heat transfer coefficient, h, the ambient temperature, T_∞, and the temperature at the basket edge, $T_{r=R}$, the following is found:

$$p_2 = -\frac{1}{2R}\left(3p_3R^2 + \frac{h}{k}(T_{r=R} - T_\infty)\right) \tag{6-6}$$

This is substituted back into equation (6-2) gives the equation that will be fit to the known experimental temperatures:

$$T = p_3 r^3 - \frac{r^2}{2R}\left(3p_3R^2 + \frac{h}{k}(T_{r=R} - T_\infty)\right) + T_{r=0}. \tag{6-7}$$

As mentioned previously, in this equation there are three unknowns that are to be determined through fitting, these being the coefficient p_3, and the two temperature $T_{r=0}$ and $T_{r=R}$. The thermocouple at 0mm could be used as the $T_{r=0}$,but instead this value's errors in placement and readings may mean that the measured value is not the best value for this approximation. This fitting was done using MATLAB and its curve fitting toolbox, whereby the method of least squares is used to determine the best fit values.

Initially, equation (6-7) was fitted to only the three temperature points at 0mm, 6mm, and 12mm. From this, the best fit values of p_3, $T_{r=0}$, and $T_{r=R}$ were determined. Issues then arose with this approach. Using the best fit parameters, the radial temperature profile was calculated. The plot of this profile can be seen as the red line in Figure 6-2. The issue is that the best fit value of the temperature $T_{r=R}$ (yellow point) does not agree with the temperature profile at the basket radius ($r = 0.03$m), as calculated from the

best fit parameters. This issue led to the implementation of an iterative procedure to determine the temperature $T_{r=R}$.

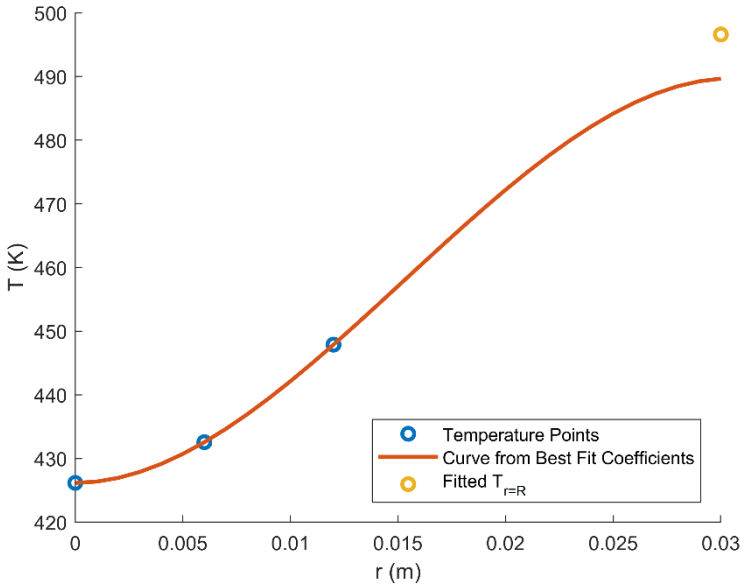

Figure 6-2: Fitting only to the measured temperature points gives rise to the above issue, where the fitted value of $T_{r=R}$ is not in agreement with the temperature profile calculated from the best fit parameters

In this iterative approach, an initial guess for $T_{r=R}$ was specified and this was added to the three measured temperatures at 0mm, 6mm, and 12mm to give four points to which this profile is fit. An iterative procedure was then used to fit for p_3, $T_{r=0}$, and $T_{r=R}$. After each iteration the fitted value of $T_{r=R}$ was compared to the value calculated from equation (6-7) at $r = R$, using the best fit parameters from the fitting. The next guess was set to the mean of these two values and the fitting repeated until the difference between them was less than 0.1°C. The agreement between these two values ensured the matching of the conductive flux at the basket edge to the convective flux at the surface. The resulting profile from this step can be seen in Figure 6-3.

This profile applied to the 2D basket domain in r and z can be seen in Step 1 of Figure 6-4. Because the only measured temperatures are along the basket radius, it was assumed that the profile along the axial direction at $r = 0$ is the same as in the radial direction at $z = 0$. This assumption is validated later. This profile applied to the 2D basket domain in r and z can be seen in Step 2 of Figure 6-4.

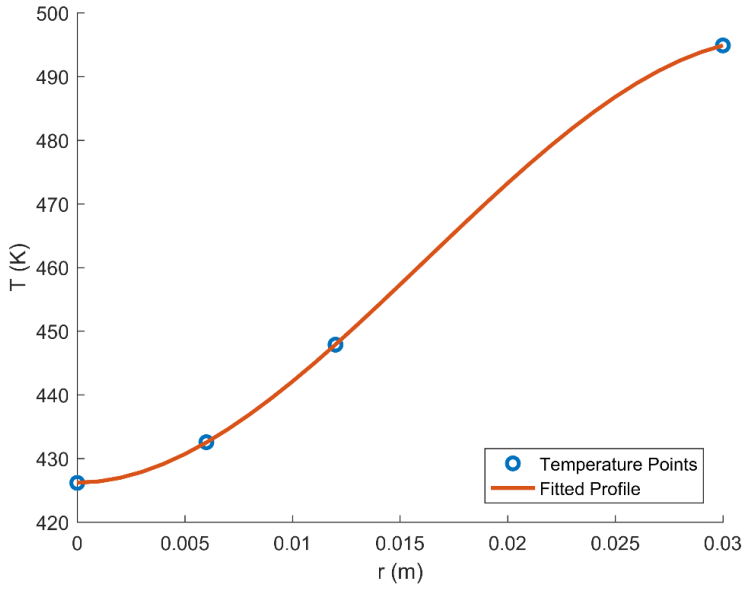

Figure 6-3: Temperature profile fitted to the experimentally measured temperatures along the basket radius (at $z = 0mm$), in accordance with equation (6-5).

The next step is to approximate the edge temperature profile at $z = Z$. Equation (6-7) is still applicable at the edge and is used for this fitting. At the edge, the only known temperature point is the temperature at $(r, z) = (0, Z)$, and this comes from the end temperature of the profile determined in Step 1 at $r = 0$. This means that in the fitting $T_{r=0}$ is known, and only p_3 and $T_{r=R}$ need to be determined. Again the same iterative procedure is used and the results of this step can be seen in Step 3 of Figure 6-4. Although it looks flat, there is in fact a profile to this edge. Because the profile along the edge at $r = 0$ was assumed equal to the profile along the edge at $z = 0$, it was also assumed that the profile along the edge at $r = R$ is equal to that along the edge at $z = Z$. This can also be seen in Step 3 of Figure 6-4.

Step 4 of the procedure is to fit profiles at 29 intermittent axial lengths from $z > 0$ to $z < Z$. Equation (6-7) is again used in this fitting, but for each curve two temperature points are known. These temperatures are those along the already determined profiles at $r = 0$ and $r = R$. This means that $T_{r=0}$ and $T_{r=R}$ in equation (6-5) are both known and only the coefficient p_3 needs to be determined for each of the 29 curves. This also means that the iterative procedure used before is no longer required. The results of this step can be seen Step 4 in Figure 6-4.

Finally, in order to use this profile in gPROMS ModelBuilder a equation needs to be determined that describes this 2D profile in the form $T = f(r, z)$. MATLAB's curve fitting toolbox is again used to fit the following 4th degree polynomial in r and z to a 31x31 grid of points defined by the collection of curves determined in the previous steps:

$$\begin{aligned} T = {} & p_{00} + p_{10}\, r + p_{01}\, z + p_{20}\, r^2 + p_{11}\, r\, z + p_{02}\, z^2 + p_{30}\, r^3 \\ & + p_{21}\, r^2\, z + p_{12}\, r\, z^2 + p_{03}\, z^3 + p_{40}\, r^4 + p_{31}\, r^3\, z \\ & + p_{22}\, r^2\, z^2 + p_{13}\, r\, z^3 + p_{04}\, z^4. \end{aligned} \tag{6-8}$$

The resulting profile can be seen in Figure 6-5.

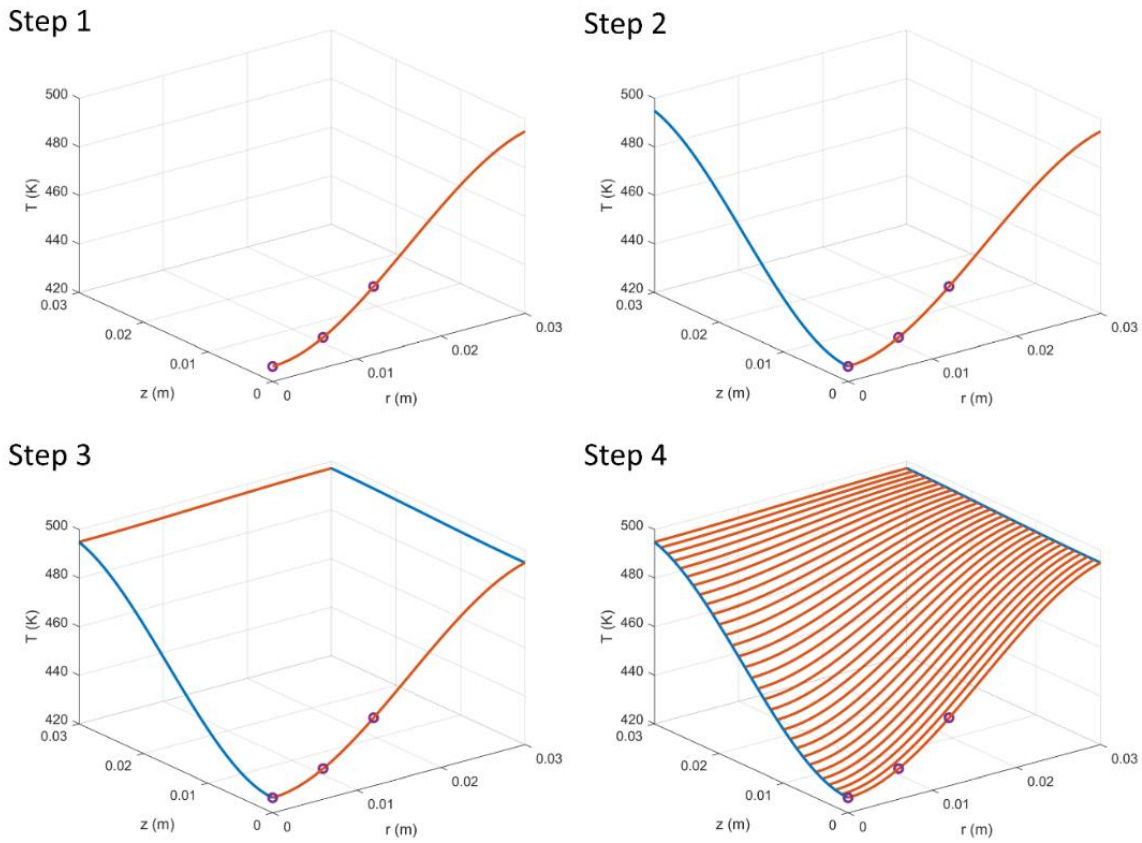

Figure 6-4: Steps involved in approximating the 2D temperature profile from the measured temperature data.

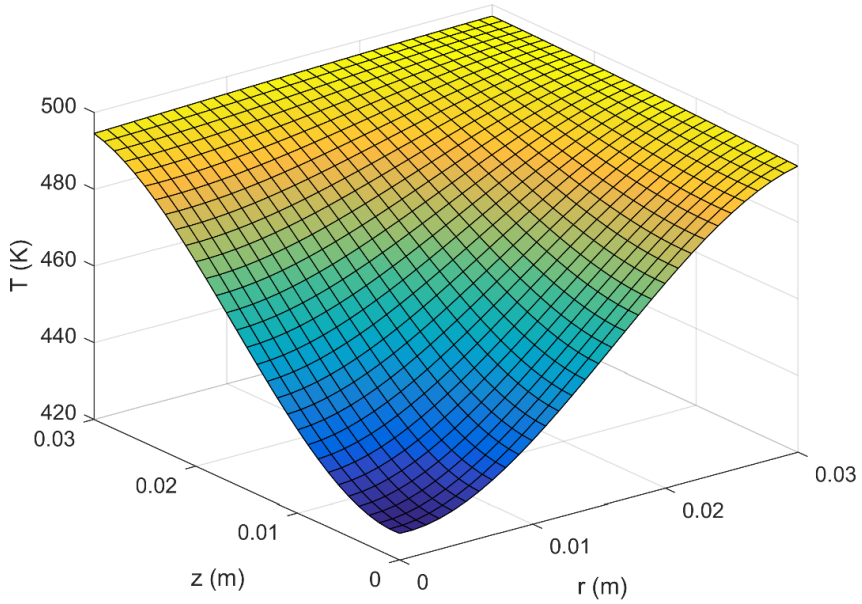

Figure 6-5: 4th degree polynomial fitted to the collection of curves determined in the previous steps shown in Figure 6-4.

This process is repeated for each experiment and these coefficients are then used to define the initial temperature conditions for each experiment. How this profile relates to the basket geometry can be seen in the overlay of the temperature profile onto an image of a basket of powder in Figure 6-6.

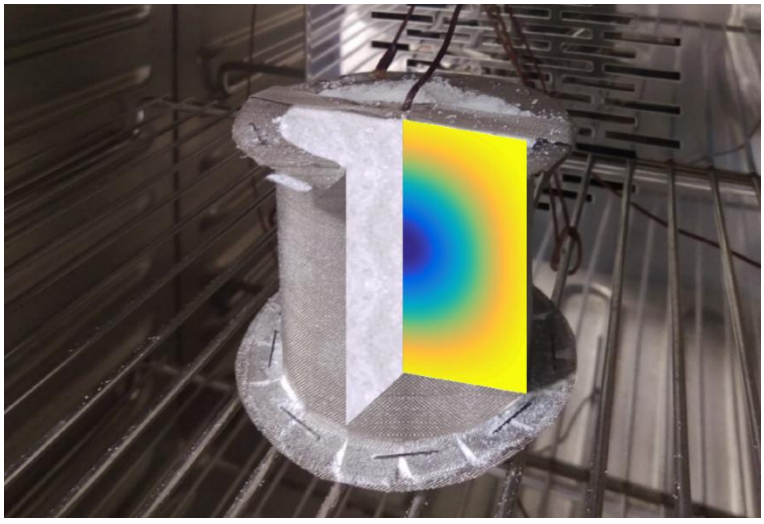

Figure 6-6: Overlay of initial temperature profile onto a photograph of a basket of powder used for conducting these experiments.

6.6.1. Model Verification of the Initial Temperature Profile Approximation Method

This method for approximating the initial temperature profile and the associated assumption were verified using the numerical model. To do this, the approximation method was applied to data from a full, model simulated, 2D temperature profile. This was done to validate the choice of polynomial used to describe the temperature profile in equation (6-2), and the assumption that the radial and axial temperature profiles are equal. The entire, fitted, 2D profile is compared to the original, model simulated, 2D profile from which it came, to determine if this method is a satisfactory approach for approximating the initial temperature profile.

The model was use to simulate a basket heating experiment at an ambient temperature of 224°C (497K). The temperature profile after 3200s was taken from this. This is the data that will be used for this verification. At this time, the temperatures at 0mm, 6mm, and 12mm from the centre were noted, these being the temperatures that would be measured by the three thermocouples in experimental practice. It is to these temperatures that the fitting is performed.

The radial temperature profile is fitted, as outlined in the procedure of the previous section. The profile fitted to these three points agrees well with the model predicted radial temperature profile, as shown in Figure 6-7 (a). The model predicted radial temperature profile at $z = 0$ and the axial profile at $r = 0$ were compared, as shown in Figure 6-7 (b). These profiles are sufficiently similar to validate the approximation used whereby the radial and axial temperature profiles were assumed equal.

The entire, fitted 2D temperature profile approximated from the three simulated thermocouples was compared to the model predicted 2D profile from which these three points were taken. The comparison of these profiles can be seen in Figure 6-8. These profiles are seen to compare very well, with a root mean squared error of 2.75°C. The difference between the minimum and maximum temperatures in this profile is almost 70°C, such that there is an approximate error of 4% across the profile. This suggests that this method for generating an approximated initial temperature profile from the data of three thermocouples and the ambient temperature is satisfactory, and can be applied in the subsequent parameter estimations.

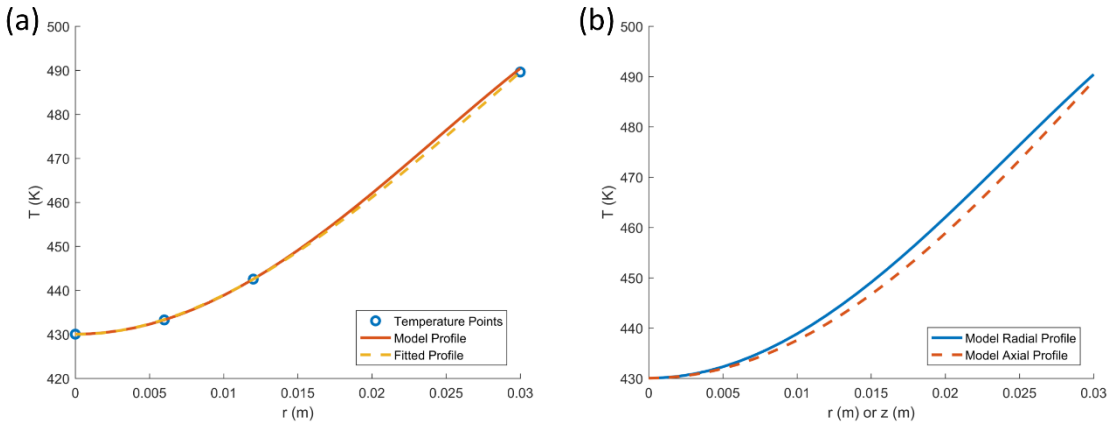

Figure 6-7: Model verification of the Initial temperature profile approximation method using a model simulated basket heating experiment at 224°C (497K). (a) Comparison of model predicted and approximated radial temperature profiles. (b) Validation of the approximation that the radial and axial temperature profiles are assumed equal.

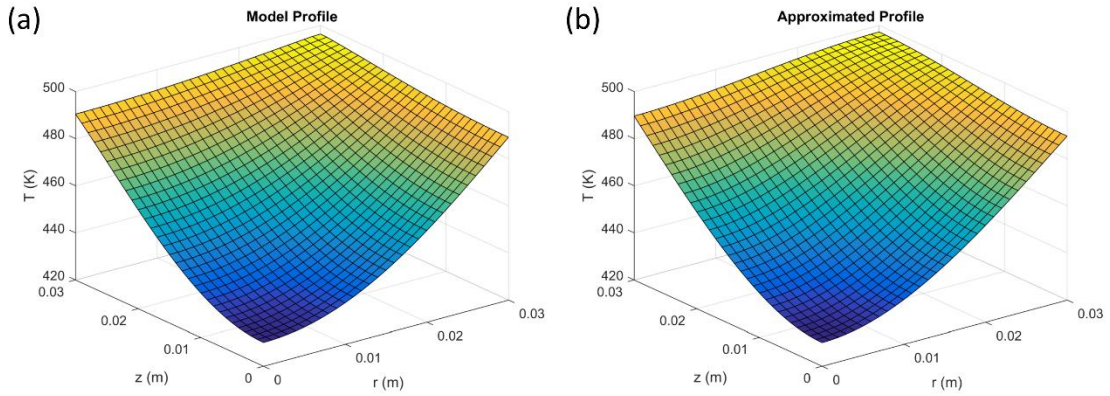

Figure 6-8: (a) The model predicted temperature profile from which the three simulated thermocouples were taken. (b) The fitted temperature profile approximated from the three simulated thermocouples.

6.7. Maximum Likelihood Estimation

Parameter estimation is the process of fitting a number of model parameters to experimental data in order to make the model predictions match the observed data. In this study, four parameters were estimated using this approach: the activation energy, E, the logarithmic term capturing the pre-exponential factor and heat of reaction, $\ln QA$, the thermal conductivity, k, and specific heat capacity, C_p.

Parameter estimation in gPROMS is based on the Maximum Likelihood method, allowing for the simultaneous estimation of both the physical parameters in the model and the

variance of the measuring instruments. The variance is the uncertainty to which the measurements are known and is detailed in Section 6.8 and can be fit as part of this procedure. In this case the variance is the uncertainty in the thermocouple measurements. The method is based on the following objective function:

$$\Phi = \frac{N}{2}\ln(2\pi) + \frac{1}{2}\min_{\theta}\left\{\sum_{i=1}^{NE}\sum_{j=1}^{NV_i}\sum_{k=1}^{NM_{ij}}\left[\ln\left(\sigma_{ijk}^2\right) + \frac{\left(\tilde{z}_{ijk}-z_{ijk}\right)^2}{\sigma_{ijk}^2}\right]\right\}. \quad (6\text{-}9)$$

This objective function can be described by three terms: the constant term, $\frac{N}{2}\ln(2\pi)$, the variance term, $\ln\left(\sigma_{ijk}^2\right)$, and the residual term, $\frac{\left(\tilde{z}_{ijk}-z_{ijk}\right)^2}{\sigma_{ijk}^2}$. This function consists of the following definitions:

- N – Total number of measurements taken during all the experiments.
- θ – Set of model parameters to be estimated. The acceptance values may be subject to given lower and upper bounds, i.e. $\theta^l \leq \theta \leq \theta^u$.
- NE – Number of experiments performed.
- NV_i – Number of variables measured in the *i*th experiment.
- NM_{ij} – Number of measurements of the *j*th variable in the *i*th experiment.
- σ_{ijk}^2 – Variance of the *k*th measurement of the variable *j* in experiment *i*. This is determined by the measured variable's variance model.
- $\tilde{z}_{ijk}$ – *k*th measured value of the variable *j* in experiment *i*.
- z_{ijk} – *k*th (model-) predicted value of the variable *j* in experiment *i*.

In estimating parameters using the maximum likelihood method, gPROMS attempts to determine values for the unknown parameters, θ, that maximises the probability that the model predictions will match the measured values determined experimentally.

6.8. Parameter Estimation Variance Model

The variance, which is the uncertainty to which the measurements are known, was fitted as part of the parameter estimation procedure. All the experiments used the same array of thermocouples and as such one variance value was fitted for each thermocouple. A constant variance model was used (i.e. variance was independent of temperature or

time) and is specified by gPROMS as $\sigma^2 = \omega^2$, where ω is the variance, and σ is the standard deviation.

The variance was fitted because the error associated with the experimental measurements was unknown and is comprised of three factors: the error in thermocouple readings, the error in thermocouple placement, and the variability of the powder between the thermocouples. The thermocouples were sold with a tolerance of ±1.5°C, although when comparing thermocouple readings at the start of the experiment, when the powder was at a steady-state, the difference between all three thermocouples was found to be with 0.25°C. This error alone has been found to be significant in performing the cross-point temperature method, but what is of greater significance is the error in thermocouple placement. Placing the thermocouples accurately is very difficult and there is no way to know how accurate this placement is. Finally the variance associated with sample variability is due largely to the small gap of 6mm between each of the thermocouples. These three factors together contribute to a variance that is difficult to quantify, and as such was estimated as part of this method.

The same thermocouples were used for all the experiments, and in the software this was noted by grouping each of the three thermocouples across all the experiments. In doing so, a single variance value was fit for each thermocouple, using all the experiments used for that particular fitting.

6.9. Determining Specific Heat Capacity from MDSC

From the energy balance in equation (6-1), and from initial fittings using the parameter estimation approach, it could be seen that the thermal conductivity, k, and the specific heat capacity, C_p, are very highly correlated. This means that these two parameters are dependent on one another, such that a change in one value will induce a change in the other. Because of this high degree of correlation, the software had difficulty in fitting both of these values, and as such it was thought measuring a value of the specific heat capacity and fixing this in the parameter estimation would improve the fitting procedure.

The specific heat capacity was measured using Modulated Differential Scanning Calorimetry (Modulated DSC or MDSC), and the method documented by TA

Instruments, the manufactures of the DSC equipment used (Thomas, n.d.). Conventional DSC measures the energy released or absorbed by a sample when it is heated or cooled. Typically the sample is heated either isothermally or at a constant heating ramp rate. Modulated DSC differs from conventional DSC in that a sinusoidal modulation is overlaid on the conventional linear heating or cooling ramp. This gives a profile for which the average sample temperature continuously changes with time but not in a linear fashion. MDSC is preferred over conventional DSC for measuring C_p values because a stable baseline is not required to obtained high accuracy, however, in MDSC the choice of average and modulated heating rates is critical to obtaining good results from this method. Firstly the average heating rate is chosen, and then the temperature modulation period and amplitude is selected accordingly. The key considerations for this approach are:

- The modulation period must be long enough to allow for sufficient heat flow between the sensor and the sample.
- The modulation amplitude must be sufficiently large to provide good sensitivity, but not so large that the resolution is reduced.
- The average heating rate is slow enough to allow for a sufficient number of modulation cycles over the period of interest.

For these detergent powder samples, the temperature range over which MDSC was to be performed was of importance. The temperature range of interest is in excess of 200°C (473K) but at some point this powder will self-heat. The conventional DSC runs performed using the TA Instruments Q2000 DSC in Section 3.4 showed that a range of 200°C (473K) to 230°C (503K) could be used to provide C_p values within the range of interest, but without self-heating occurring and affecting the results.

Before the value of C_p can be measured for this sample, the equipment must first be calibrated using a sample of known specific heat capacity. The sample used was a disk of sapphire. A sapphire disk weighing 25.2mg was sealed in an aluminium pan and placed in the DSC along with a sealed reference pan. At 215°C (488K), the midway temperature in the range to be used for the detergent powder samples, the sapphire disk was heated with at a modulation of ±1°C/min every 120s for 5 minutes. The resulting reversing heat capacity, $Rev\ C_p$, signal is calculated as:

$$Rev\ C_p = \frac{Heat\ Flow\ Amplitude}{Heating\ Rate\ Amplitude} \cdot KC_p. \quad (6\text{-}10)$$

The reversing heat capacity calibration constant, KC_p, is set to zero for the calibration. The reversing heat capacity signal was plotted against time and the heat capacity value at the end of the 5 minute period was determined. Using this, the reversing heat capacity calibration constant, KC_p, can be calculated by the dividing the theoretical value of the heat capacity of sapphire at 215°C by the measured value.

$$KC_p = \frac{Theoretical\ Rev\ C_p}{Measured\ Rev\ C_p} = \frac{1.0315}{1.0950} = 0.942 \quad (6\text{-}11)$$

Having this value for KC_p, the reversing heat capacity can be measured for the detergent powders. Samples of approximately 10mg in mass were placed into aluminium pans and sealed with a lid. Samples of three different size ranges of particles were tested: >150µm and <250µm, >250µm and <355µm, and >355µm and <425µm. These samples were heated from 200°C (473K) to 230°C (503K) using the heating rates recommended by TA Instruments: an average heating rate of 3°C/min, using a modulation period of 120s and a modulation amplitude of ±1°C. The results of this method for Micronized Formulation 1 are discussed below.

6.9.1. Specific Heat Capacity Results for Micronized Formulation 1

Figure 6-9 shows the modulated temperature input of the DSC and the measured modulated heat flow output from the samples of different size ranges. Little difference is seen across the different size ranges of particles. It is difficult to read much else from the heat flow profiles in this form. From this heat flow output, and knowing the reversing heat capacity calibration constant, KC_p, from the sapphire disk calibration, the non-reversing $C_p$value is calculated. This can be seen in Figure 6-10 along with the modulated temperature input of the DSC.

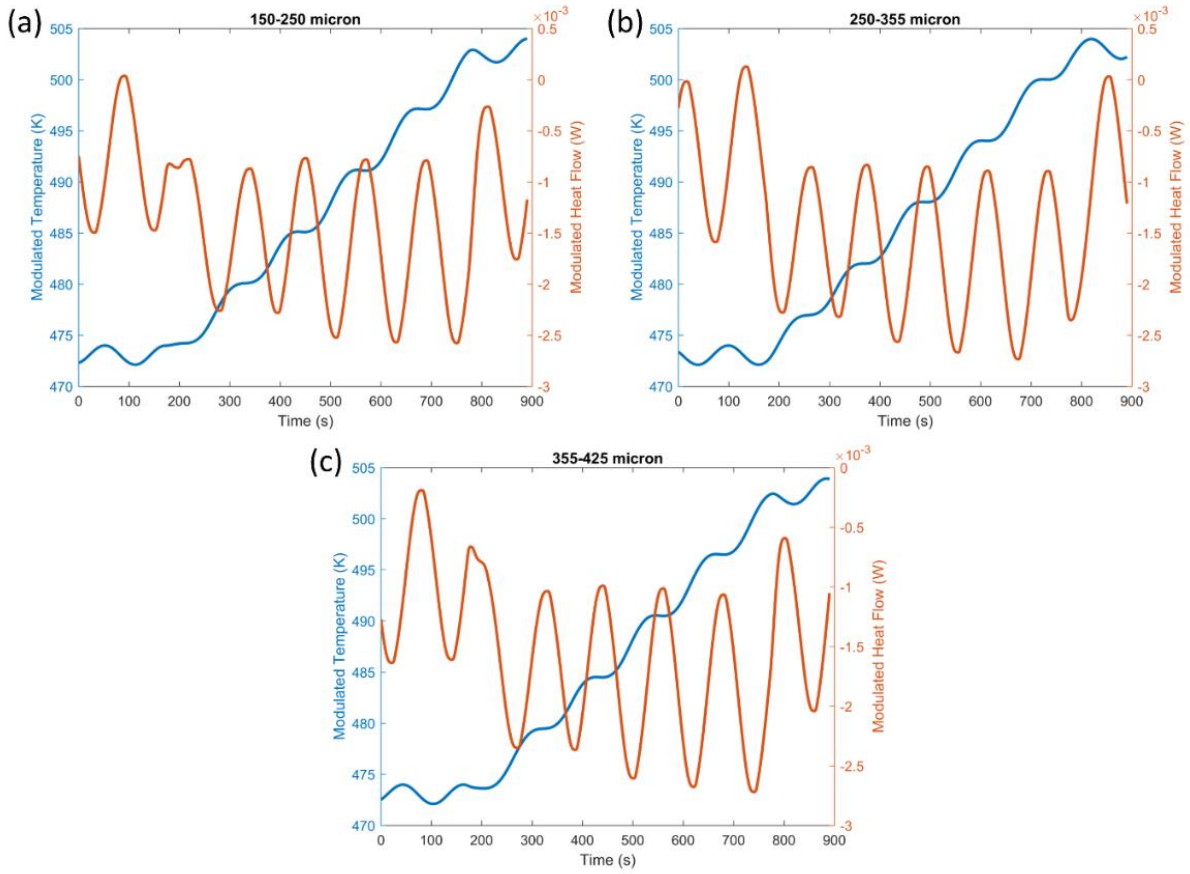

Figure 6-9: Modulated DSC input temperature and sample heat flow as a function of time for particles of size ranges (a) 150-250µm, (b) 250-355µm, and (c) 355-425µm.

The measured non-reversing C_p for the three different size ranges of particles can be seen as a function of temperature in Figure 6-11. It can be seen that C_p is not constant throughout the experiment. This may be due to the modulation period used, which although recommended by the instrument manufacturer, may not be small enough for this case, with only 7 or 8 modulation periods occur within the 30°C range used for these experiments. This would be the first thing to address if these experiments were repeated.

Despite this, each sample is seen to follow a similar profile with a peak at the start of the temperature range and another at the end, although there is no logical order in the plots from a particle size perspective. The weighted average C_p was calculated as the average C_p as a function of temperature, weighted by each size ranges percentage contribution by mass to the overall powder size distribution, shown in Table 6-1.

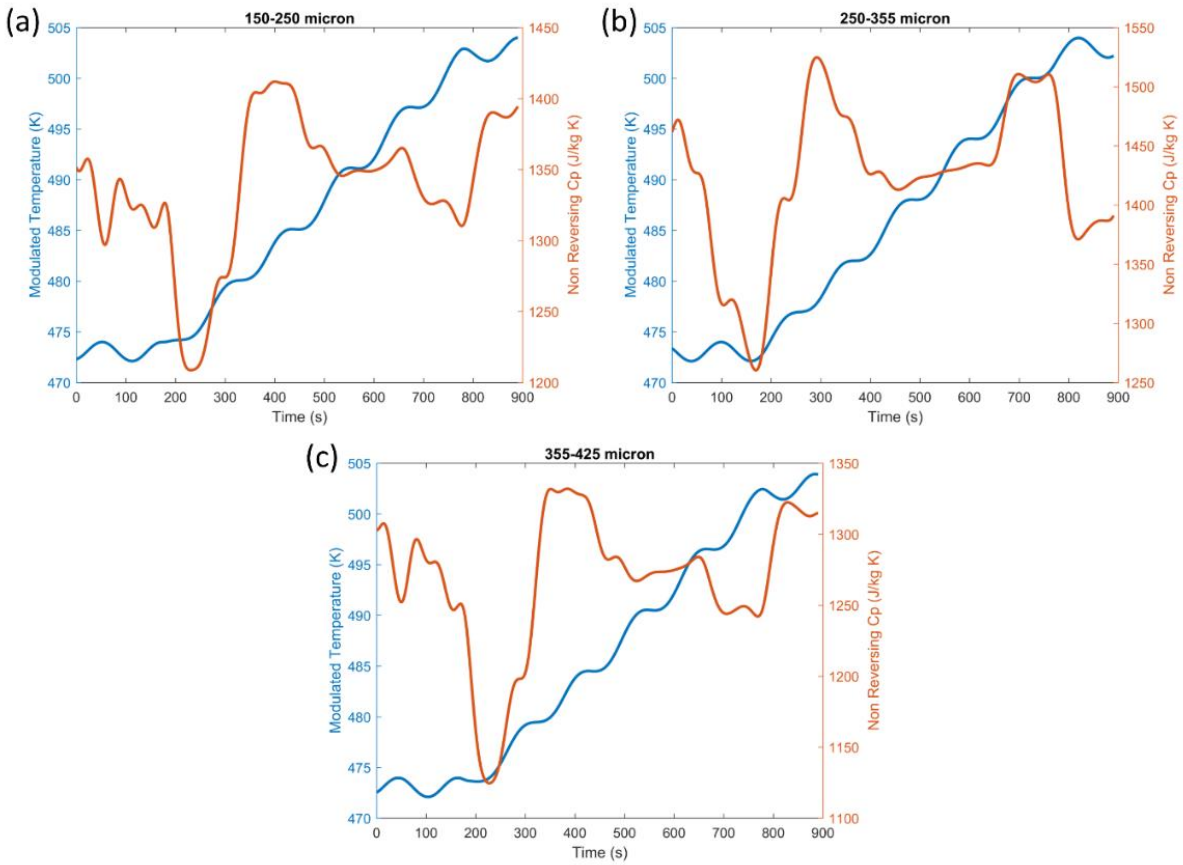

Figure 6-10: Measured non-reversing C_p and modulated DSC input temperature for particles of size ranges (a) 150-250µm, (b) 250-355µm, and (c) 355-425µm.

The most stable region of the profile for all three size ranges is between 485K (212°C) and 496K (223°C), and it was from this region that the value of C_p to be used in the parameter estimation fittings was chosen. Figure 6-12 shows the C_p profiles for this temperature range for the three size ranges and the weighted average C_p. The C_p used in the fitting was calculated as the overall average value of the weighted profile in this temperature range, and has a value of 1367 J kg^{-1} K^{-1}.

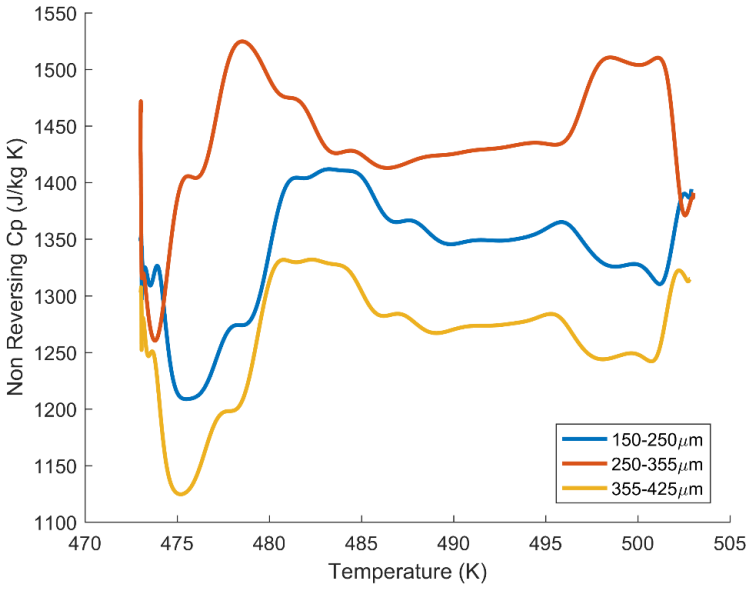

Figure 6-11: Measured non-reversing C_p for samples of three different particle size ranges for the entire duration of the experiment.

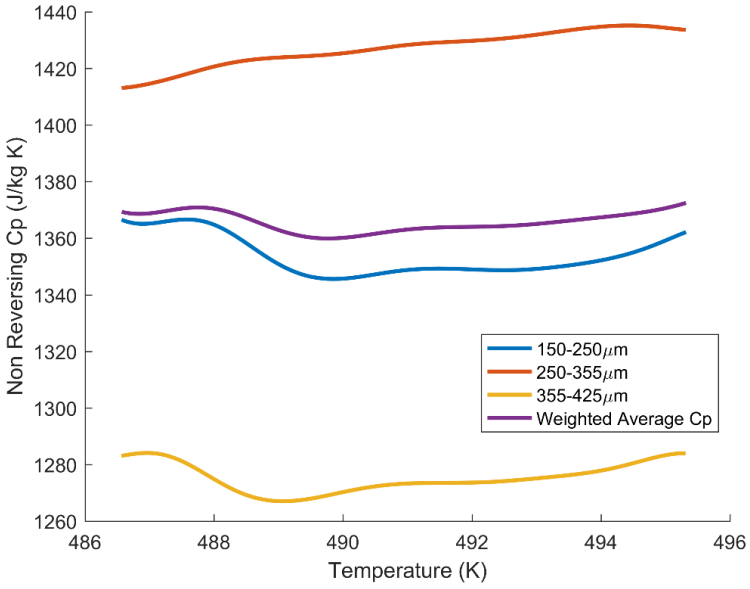

Figure 6-12: Measured non-reversing C_p for samples of three different particle size ranges for the most stable region from which the value used in the fittings was chosen.

6.10. Determining Arrhenius Activation Energy from DSC

It was found from initial fittings using the parameter estimation approach that the pairing of the reaction activation energy, E, and the logarithmic term capturing the pre-exponential factor and heat of reaction, $\ln QA$, are somewhat correlated. In fitting to the basket experiments individually, the software would struggle to estimate these two

parameters simultaneously, with a change in one value being compensated for by a change in the value of the other, with one parameter often getting stuck on the fitting bounds. This problem was not seen to occur when multiple experiments were fitted to simultaneously, because the variation in ambient temperature of the experiments meant different levels of self-heating were exhibited amongst the experiments, making it possibly to fit these kinetics. Nonetheless, the possibility of fixing the activation energy to a measured value was explored in Section 6.11.4.

The activation energy is considerably easier to measure than the logarithmic term. This was done using isoconversional analysis methods and differential scanning calorimetry (DSC). Two isoconversional methods were explored, the Ozawa-Flynn-Wall approach, proposed independently by Ozawa (1965) and Flynn and Wall (1966), and the Friedman method (1964). These two methods both use the same experimental procedure.

These methods have previously been used to characterise a number of materials. Pielichowksi *et al.* (1998) used both of these methods to determine the kinetics of decomposition of potato starch, while Venkatesh *et al.* (2013) used these methods to analysis the decomposition of Nitroimidazoles.

These two methods were independently proposed to provide a model independent estimate of the activation energy without any assumptions regarding the form of the kinetic equation, other than that the system is of Arrhenius type temperature dependence. The Friedman method is often described as a differential isoconversional method, whilst the Ozawa-Flynn-Wall approach is described as an isoconversional integral approach. Both of these approaches are based on the following single-step reaction:

$$\frac{d\alpha}{dt} = f(\alpha)k(T). \tag{6-12}$$

Where α is the degree of conversion, $f(\alpha)$ is the kinetic model, and $k(T)$ is the rate constant which can be substituted for the Arrhenius equation:

$$k(T) = -A\, e^{-\frac{E}{RT}}. \tag{6-13}$$

The Friedman method is the simpler of the two methods to derive mathematically, but requires more mathematical manipulation of the data to determine the results. The Friedman method uses the logarithmic form of equation (2-61) as the basis of its approach:

$$\ln\frac{d\alpha}{dt} = \ln f(\alpha) + \ln A - \frac{E}{RT}. \quad (6\text{-}14)$$

Using the method, the activation energy can be found from the slope of the line ($m = -E/R$) produced by plotting $\ln d\alpha/dt$ against $1/T$ for isoconversional fractions.

The Ozawa-Flynn-Wall method requires some more manipulation, which is outlined in Section 2.4.4.2. Without going into detail, the following equation is reached:

$$\ln\beta = \ln\left(\frac{AE}{R}\right) - \ln G(\alpha) - 5.3305 + 1.052\frac{E}{RT}. \quad (6\text{-}15)$$

It can be seen from this that when $\ln\beta$ is plotted against $1/T$ for isoconversional fractions and a series of measurements at heating rates of $\beta_1 \ldots \beta_j$, a straight line is formed with a slope of $1.052E/R$. The temperature T_{jk} at which the conversion α_k is achieved is taken at the heating rate β_j. The approximation of the exponential integral in this approach has significant errors associated with it. For values of $31 < x < 47$ the errors are smaller than 1%, but for values of $x < 25$ or $x < 100$ these errors are in excess of 3%. An empirical correction factor for this that was suggested by Flynn (Flynn, 1983). Firstly E is estimated using equation (2-69), the mean temperature T_m is determined, and from this the mean value $x_m = E/RT_m$ is determined. This is used to determine the empirical correction factor $F(x)$;

$$F(x) = a_0\left(1 + \frac{a_1 + x}{1 + a_2x + a_3x^2}\right). \quad (6\text{-}16)$$

Where $a_0 = 0.94961$, $a_1 = 7.770439$, $a_2 = 4.56092$, and $a_3 = 0.48843$. The corrected activation energy is calculated by dividing the first estimate of E by the correction factor $F(x_m)$.

The Ozawa-Flynn-Wall method is suited to measuring kinetics of systems where multiple reactions are occurring, such that the activation energy varies with time, although if these reactions are occurring simultaneously and have largely different activation energies, then this method may fail. It is also worth noting that the Ozawa-Flynn-Wall method is less accurate than the Friedman method. If the activation energy, E, is dependent on the conversion, α, or if competitive reactions are occurring then the values obtained using these methods are found to be different. On the other hand, if the activation energy is independent of the conversion, then these two methods should measure the same values (Venkatesh, et al., 2013).

In this investigation, the activation energy, E, was measured for four different particle size ranges of each formulation. Samples of these powders weighing approximately 8mg were placed into Tzero aluminium pans. These pans were placed into the TA instruments Q2000 DSC along with an empty reference pan. This reference pan allows the heat flow in the powder sample to be separated from that of the pan. The DSC was equilibrated at 200°C in air, at which no self-heating is exhibited, and held isothermally for 2 minutes. The temperature is then increased linearly from 200°C (473K) to 500°C (773K). This was done at four different ramped heating rates: 4°C/min, 6°C/min, 8°C/min, and 10°C/min. Data were sampled every 0.2s, measuring the temperature and heat flow in the cell. These two methods were used to measures the activation energy at a range of conversions.

6.10.1. Arrhenius Activation Energy Results for Micronized Formulation 1

Each of the four size ranges of particles were heated at each of the four heating rates, amounting to 16 DSC experiments. The start and end point of the reaction was defined for each experiment. These were chosen as the start and end points of the observed exothermic peak. These can be seen in Figure 6-13, where the four different size ranges of particles have been grouped into separate plots, such that the activation energy can be measured separately for each size range. The exotherms look similar across the four size ranges, again implying that reactivity is independent of particle size in Micronized Formulation 1. These plots were made with respect to temperature and it can be seen how the peak heat flow increases with heating rate. Plotting with respect to time would produce plots with the same peak heat flow but with a variation in the time span of each experiment due to the different heating rates used. The area under the exotherm for each experiment in this plot would be the same.

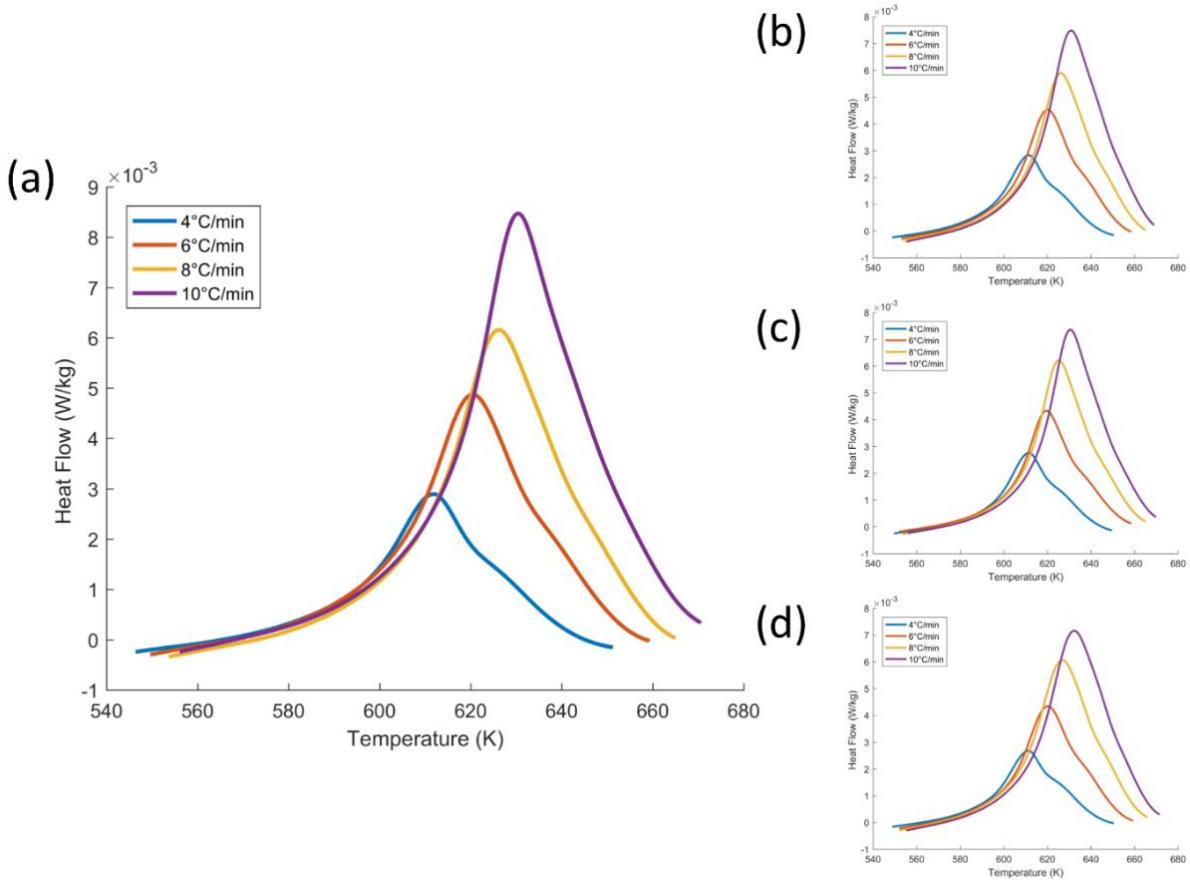

Figure 6-13: Heat flow per unit mass for the four heating rates of 4°C/min, 6°C/min, 8°C/min, and 10°C/min for particles of the size ranges (a) 150-250µm, (b) 250-355µm, (c) 355-425µm, and (d) 425-600µm.

Equation (2-61) on which these two methods are based require the reaction to be expressed as a conversion, α, a value between 0 and 1 indicating the degree to which the reaction has completed, with 0 indicating that the reaction has yet to begin, and 1 indicating that the reaction has completed. To do this, the area under the exotherm of the heat flow against time profiles was found. A sinusoidal baseline was used between the start and end points of each curve and the area between the curve and this baseline determine by numerical integration. The conversion was determined by summing the area of consecutive slices as a fraction of the total area and this can be seen for the four heat rating rates in Figure 6-14 for the four particle size ranges. It can be seen that the lower the heating rate, the lower the temperature at which the conversion occurs. This is because at these lower heating rates, the sample has longer to react at the lower temperatures. Using these conversion curves it is now possible to use both the Friedman

method and the Ozawa-Flynn-Wall method to determine the activation energy of these samples.

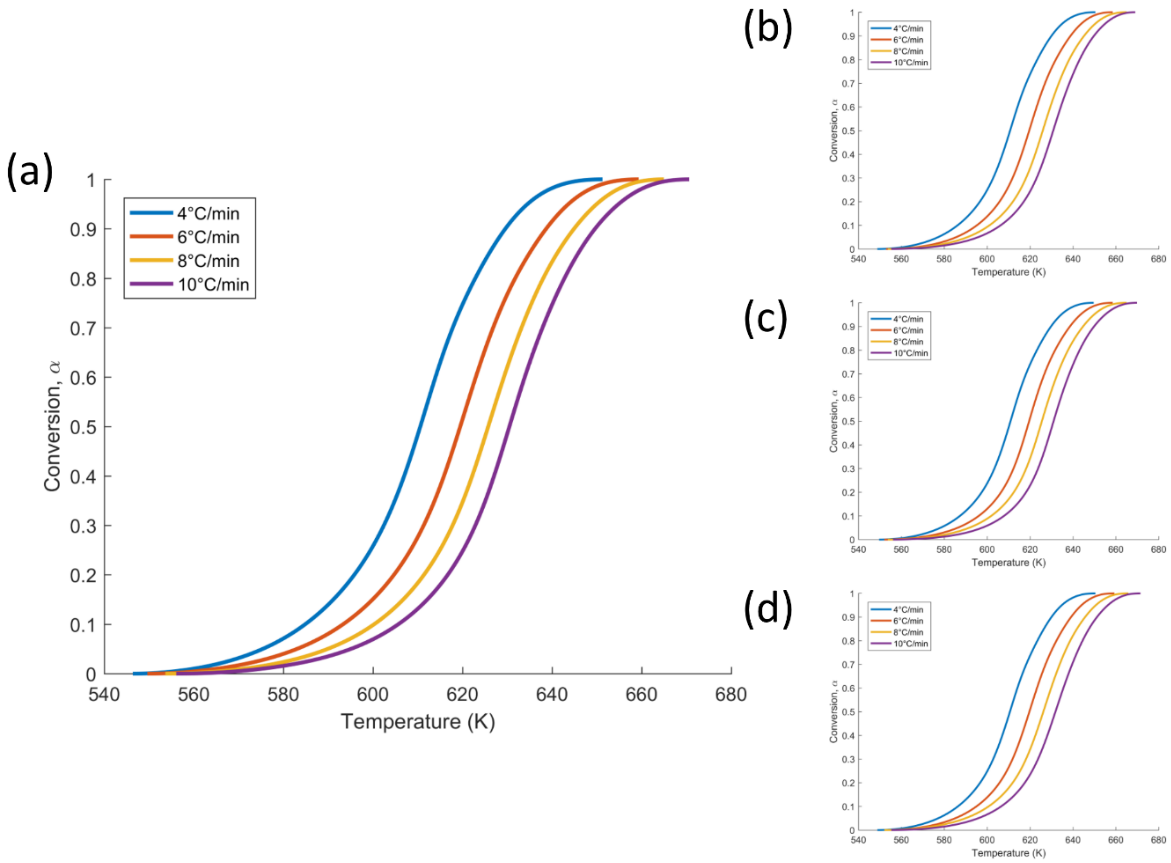

Figure 6-14: Conversion, α, for the four heating rates of 4°C/min, 6°C/min, 8°C/min, and 10°C/min for particles of the size ranges (a) 150-250µm, (b) 250-355µm, (c) 355-425µm, and (d) 425-600µm.

The Friedman method is sometimes referred to as the differential method, and is based on the conversion derivative with time, as outlined in Equation (2-64). The derivative of the conversion curve with respect to time, $d\alpha/dt$, was calculated, and a small degree of smoothing was applied to this curve in order to improve results. The natural logarithm of the derivative, $\ln d\alpha/dt$, was plotted against the reciprocal of the temperature, $1/T$, for each of the four heating rates, as can be seen in Figure 6-15. Linear regression was used to fit lines to these data at isoconversional fractions across the four heating rates. This was done for 17 isoconversional fractions for 0.1 to 0.9 and can be seen as the black lines plotted in Figure 6-15.

The slope of each of the isoconversional fraction lines is equal to $-E/R$, allowing the activation to be easily measured for each of the 17 fitted isoconversional fractions. This was done for each of the four particle size ranges, and is plotted in Figure 6-16 (a).

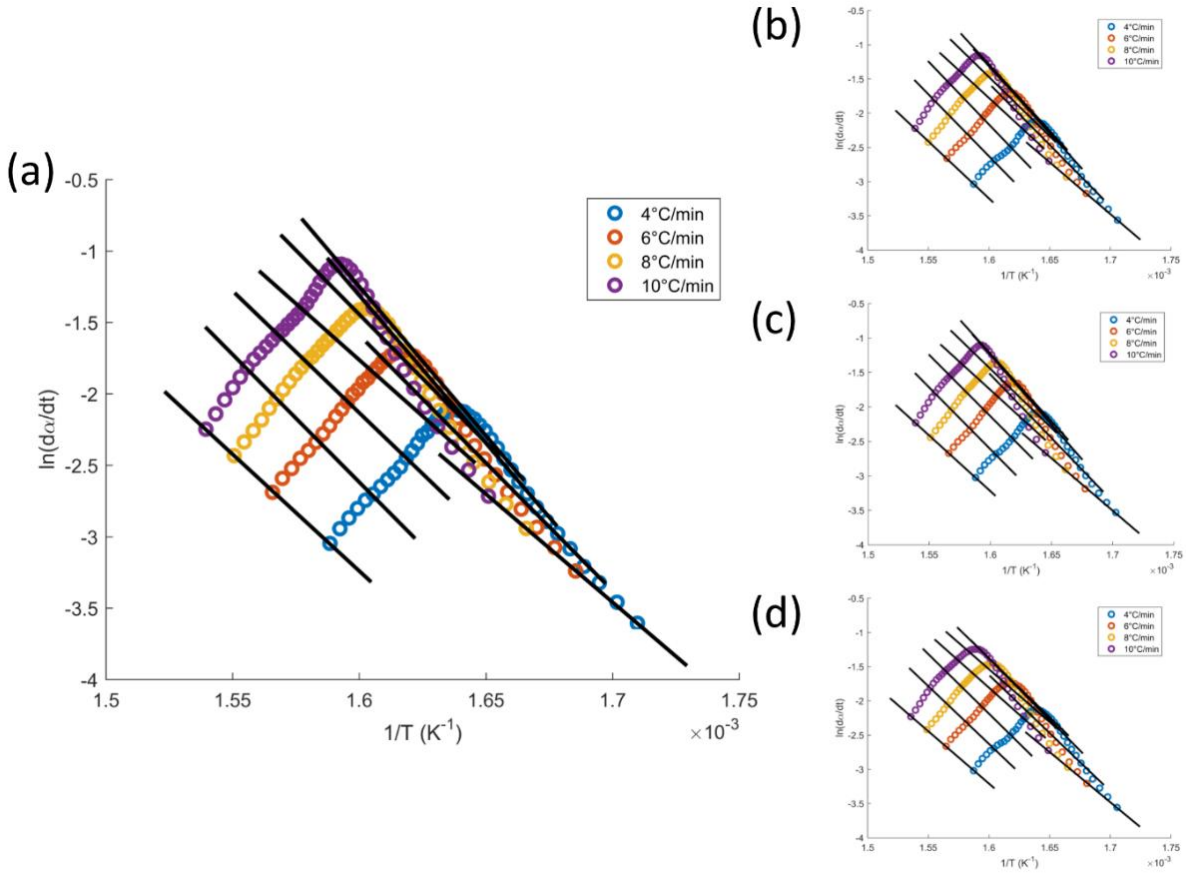

Figure 6-15: Plot of the Friedman method of $\ln d\alpha/dt$ against $1/T$ for isoconversional fractions (black lines), used to measure the activation energy, E, for particles of the size ranges (a) 150-250µm, (b) 250-355µm, (c) 355-425µm, and (d) 425-600µm.

It can be seen that the measured activation energy is very similar for the particle size ranges of 150-250µm, 250-355µm, and 355-425µm, but the measured activation energy for particles of the size range 425-600µm is slightly lower. Four heating rates were used to measure these values, so it is thought repeatability is not the issue. Previous evidence has suggest that reaction variability is not an issue for different particle size ranges of this formulation. However, the difference in measured activation energy is quite small (≈5%), and it is thought this difference may be due to slight differences in composition with size.

It can be seen that the activation energy increases with conversion for all size ranges. This implies that reaction seen to occur may not be a simple single-step reaction, but

instead multiple simultaneous reactions. Investigating this reaction beyond a single step reaction is beyond the scope of this investigation.

The weighted average activation energy as a function of the conversion is shown in Figure 6-16 (b). This was calculated by taking the weighted average of the activation energy at each conversion. This was weighted by the percentage contribution of the particle size ranges to the overall powder mass, as detailed in Table 6-1.

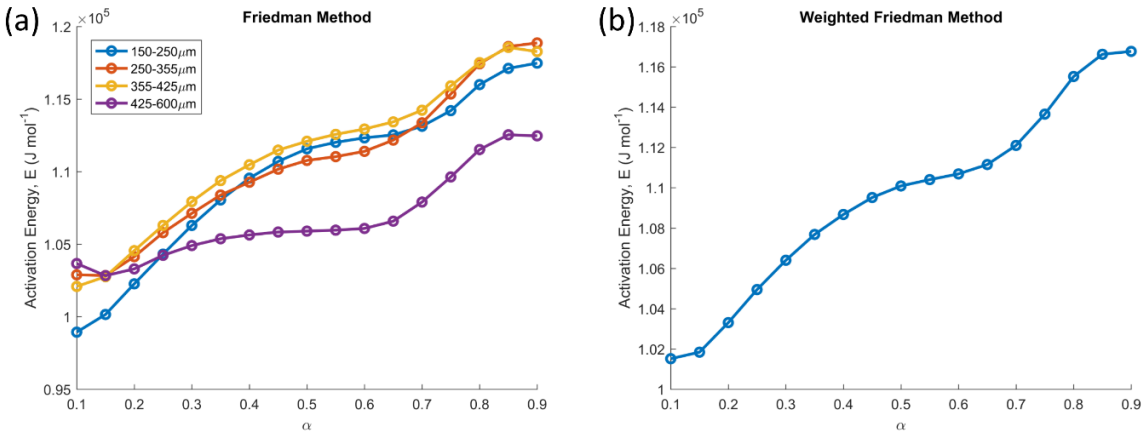

Figure 6-16: Friedman method results showing the activation energy, E, as a function of conversion, α, for (a) the four different particle size ranges tested, and (b) for the weighted average of these four size ranges.

The Ozawa-Flynn-Wall method was also used to determine the activation energy of these powder samples. This methods uses equation (2-69), where the natural logarithm of the heating rate, β, is plotted against the reciprocal of the temperature, $1/T$, for each of the four heating rates, as can be seen in Figure 6-17. Linear regression was used to fit lines to these data at isoconversional fractions across the four heating rates. This was done for 17 isoconversional fractions for 0.1 to 0.9, and this can be seen as the black lines plotted in Figure 6-17.

The slope of each of the isoconversional fraction lines is equal to $-1.052\ E/R$, allowing the activation to be easily measured for each of the 17 fitted isoconversional fractions. This was done for each of the four particle size ranges and the empirical correction factor suggested by Flynn in equation (2-70) was applied to the results. The final values are plotted in Figure 6-18. Again it can be seen that the measured activation energy is very similar for the particle size ranges of 150-250µm, 250-355µm, and 355-425µm, but the measured activation energy for particles of the size range 425-600µm is slightly lower.

It can again be seen that the activation energy increases with conversion for all size ranges as before. The weighted average activation energy was also calculated for this method and this can be seen in Figure 6-18 (b).

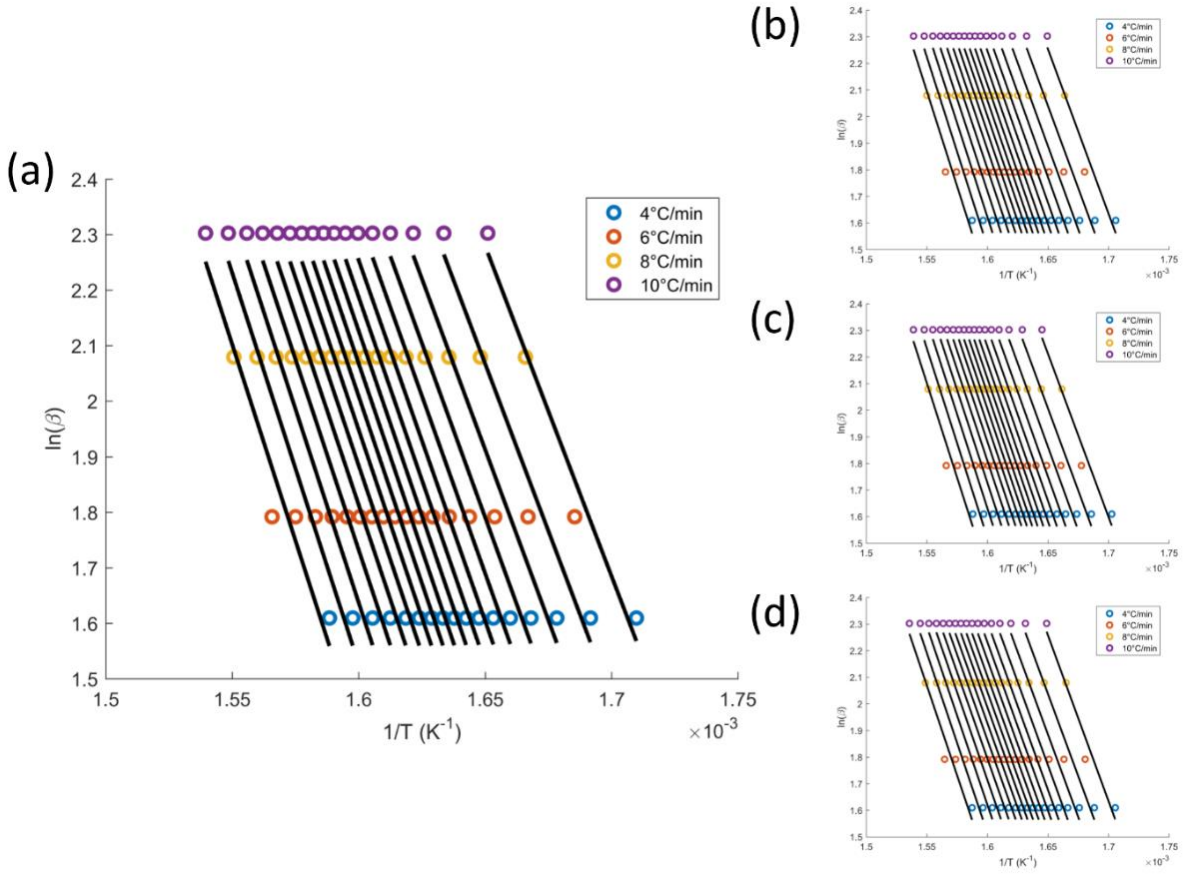

Figure 6-17: Plot of the Ozawa-Flynn-Wall method of $\ln d\alpha/dt$ against $1/T$ for isoconversional fractions, used to measure the activation energy, E, for particles of the size ranges (a) 150-250µm, (b) 250-355µm, (c) 355-425µm, and (d) 425-600µm.

The activation energy as measured using these two methods was compared, and this can be seen in Figure 6-19 for the four particle size ranges. The results of both methods follow similar profiles for all four size ranges, but in each case the Friedman method measured a slightly larger activation energy. This is also consistent with the results of Venkatesh *et al.* (2013) who showed a similar discrepancy for these two methods when measuring the kinetics of decompositions of Nitroimidazoles, and suggested that for systems of competitive or independent reactions these two methods lead to different values of E. This may be what is happening in this system, but studying the possibility of a multi-step reaction is beyond the scope of this investigation.

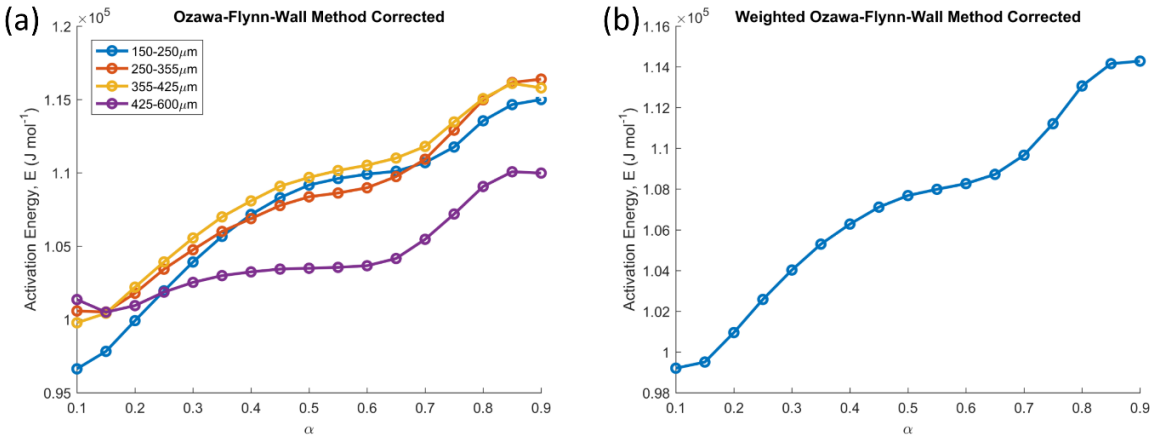

Figure 6-18: Ozawa-Flynn-Wall method results showing the activation energy, E, as a function of conversion, α, for (a) the four different particle size ranges tested, and (b) for the weighted average of these four size ranges.

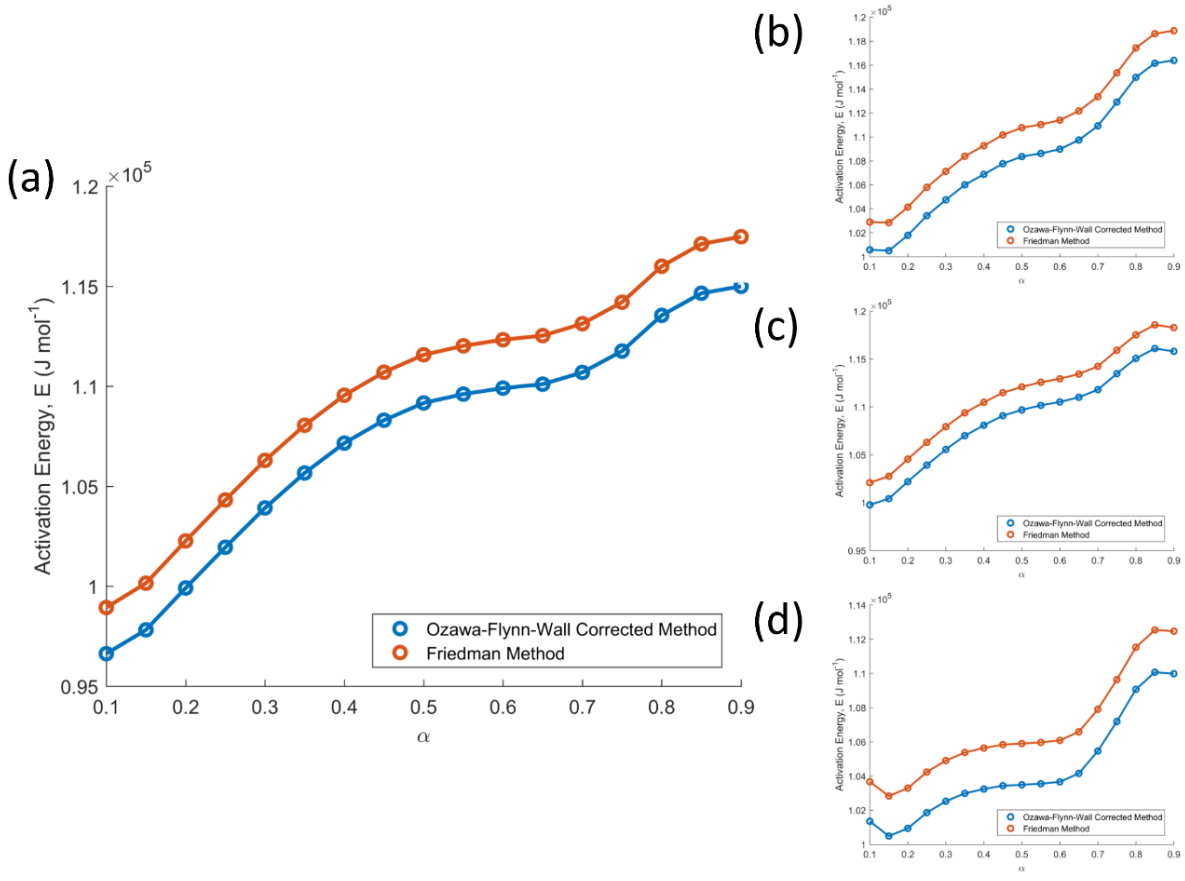

Figure 6-19: Comparison of the activation energy, E, as a function of conversion, α, as measured using the Friedman method and the Ozawa-Flynn-Wall method for particles of the size ranges (a) 150-250µm, (b) 250-355µm, (c) 355-425µm, and (d) 425-600µm.

A value for the activation energy value for use in the Parameter Estimation fittings needs to be chosen. The model used in the Parameter Estimation Approach consists of a zero-order self-heating reaction, and as such the reaction is independent of conversion. A constant value for the activation energy is required. The Friedman method was chosen as the preferred method for two reasons. Firstly it does not require the approximations and correction factors applied during the Ozawa-Flynn-Wall method as it is directly derived from the equation for a single-step reaction. Secondly this method predicted slightly higher values of activation energy which were closer to the value measured using the steady-state method (125.3×10^3 J mol^{-1}), which up until now is the preferred approach. The activation energy at a conversion of 0.5 was chosen for the value to be used in the fittings. This value was 110×10^3 J mol^{-1}.

6.11. Parameter Estimation Approach for Micronized Formulation 1

The Parameter Estimation Approach was performed as outlined previously. The full report of the Parameter Estimation results as produced by gPROMS ModelBuilder for one of the performed fittings can be seen in Appendix G. This report is quite comprehensive and contains a lot of information that it was deemed unnecessary to show here. The more useful of this information has been included in the tables of the subsequent sections.

6.11.1. Choice of Experiments for Parameter Estimation

Basket experiments were run at 13 different oven controlled ambient temperatures from 216°C (489K) to 228°C (501K). For each of these tests an array of three thermocouples was embedded within the powder. These were placed at the basket half-height and at radial distances of 0mm, 6mm, and 12mm from the basket centre. The placement of the thermocouples within the powder is subject to error as the thermocouples were only inserted once the basket was filled with powder and there is no way to verify the position of the thermocouples in the basket. It is assumed that thermocouple placement error is the biggest contributor to the error in these experiments. Experiments with thermocouples out of place may have the potential to

greatly influence the fitted parameters. It is because of this that the objective function in equation (6-9) of the maximum likelihood method was used to find which experiments had the greatest thermocouple placement error.

An initial parameter estimation was performed by fitting to all 13 experiments simultaneously. In doing so, it should be possible to determine which experiments have a high degree of error due to poor thermocouple placement. The three experiments with the highest error can then be omitted from subsequent fittings, where different groupings of 10, 8, 6, and 4 experiments will be used.

The objective function is comprised of a constant term, a variance term, and a residual term as shown in equation (6-9). All 13 experiments were fitted to simultaneously. The report generated by the software, shown in Appendix G, gives a breakdown of the contributions of the different elements of the objective function. If it is assumed that thermocouples in most of the experiments are well placed, it should be visible from the residual term of the objective function as to which experiments have poor placement. The value of the residual term for each experiment can be seen in Table 6-3, with colour indicating the relative severity of the error, ranging from low errors in green, to high errors in red.

The three experiments with the highest residual terms were those at ambient temperatures of 218°C (491K), 222°C (495K), and 226°C (499K). These experiments were omitted from further fittings, such that subsequent fittings were performed for different grouping of the remaining 10 experiments. Fittings were done with different groupings of these experiments to confirm that similar parameters were estimated for each selection, and to explore how many experiments are required to generate adequate results when using this approach to characterise new detergent formulations.

Table 6-3: Contribution of the residual term to the maximum likelihood function for each of the 13 experiments when fitted simultaneously.

Experiment Ambient Temperature	Maximum Likelihood Residual Term
216°C	1567.4
217°C	718.6
218°C	9030.2
219°C	5363.7
220°C	1137.3
221°C	1582.9
222°C	8744.1
223°C	883.3
224°C	1967.5
225°C	4539.3
226°C	65824.2
227°C	3445.8
228°C	4073.3

Five groupings of these experiments were used in the fittings, and are detailed in Table 6-4. The first grouping is the 10 experiments which exclude those deemed to have poor thermocouple placement error through the residual term analysis. The next groupings are two groupings of 8 experiments and a grouping of 6 experiments. These groupings maintained the overall temperature span of the experiments. The final grouping is of 4 experiments, and these were chosen as those not used by the grouping of 6 experiments, such that these two cases are entirely independent of one another. For each grouping, the experiments not used for fitting are used for validation.

Table 6-4: Different selections of experiments for simultaneous fittings.

	10 exps	8 exps (1)	8 exps (2)	6 exps	4 exps
216°C	✓	✓	✓	✓	
217°C	✓	✓	✓		✓
218°C					
219°C	✓	✓		✓	
220°C	✓		✓		✓
221°C	✓	✓	✓	✓	
222°C					
223°C	✓	✓	✓	✓	
224°C	✓		✓		✓
225°C	✓	✓		✓	
226°C					
227°C	✓	✓	✓		✓
228°C	✓	✓	✓	✓	

6.11.2. No Fixed Parameters in the Parameter Estimation

Fittings in this section were performed with none of the four parameters, E, $\ln QA$, k, and C_p, fixed. The best fit parameters from these fittings are shown in Table 6-5. Firstly it can be seen that k is stuck on the lower fitting bound for all fittings. This is discussed in Section 6.11.2.2. However, the fitted parameters values are similar across the different groupings of experiments. The largest difference can be seen between the parameters of the 6 experiments and 4 experiments groupings. These two cases are entirely independent of one another in that they share no experiments in their fittings. These estimated parameters were used in the following equation for δ_{cr} to predict critical ambient temperatures for equi-cylindrical baskets of different sizes:

$$\delta = \frac{E}{RT_\infty^2}\frac{\rho QAL^2}{k}e^{-\frac{E}{RT_\infty}}, \tag{6-17}$$

These predicted critical ambient temperatures are shown in Figure 6-20, and despite the difference in the best fit parameters, the predicted critical ambient temperatures for each set of parameters are very similar, particularly between basket radii of 15mm and

50mm. In this range the predicted critical ambient temperatures are all within 1.5°C of one another. It can also be seen that the critical ambient temperatures as predicted using the parameter estimation approach results are very similar to those measured experimentally.

Table 6-5: Results of the fittings where all parameter were left free. 95% confidence intervals of the fitted parameters are shown in brackets.

	$\boldsymbol{E}$ (J mol^{-1})	$\ln \boldsymbol{QA}$	$\boldsymbol{k}$ (W m^{-1} K^{-1})	$\boldsymbol{C_p}$ (J kg^{-1} K^{-1})
10 exps	138.8 (±1.0) x10^3	34.69 (±0.07)	0.04 (±0.007)**	703.8 (±119)
8 exps (1)	139.1 (±2.0) x10^3	34.75 (±0.12)	0.04 (±0.015)**	698.1 (±261)
8 exps (2)	136.2 (±0.3) x10^3	34.09 (±0.05)	0.04 (±0.002)**	721.7 (±35)
6 exps	141.7 (±12.2) x10^3	35.36 (±0.66)	0.04 (±0.094)**	693.0 (±1592)
4 exps	133.8 (±0.5) x10^3	33.51 (±0.07)	0.04 (±0.003)**	722.4 (±55)
** Stuck on fitting bound				

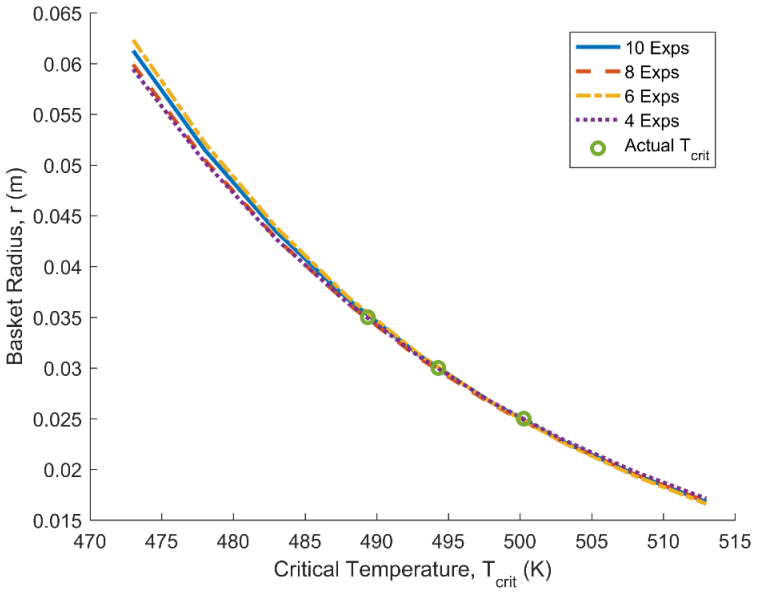

Figure 6-20: Predicted critical ambient temperatures for equi-cylindrical baskets of different radii as calculated using equation (6-17) and the estimated parameters from Table 6-5 for the groupings of 10, 8 (1), 6, and 4 experiments.

It can be seen that the parameters 95% confidence intervals for some groupings are larger, in particular the grouping of 6 experiments. It would be expected that an increase

in the number of experiments used in the fitting would reduce the error associated with the fitting. However, it is evident here that an increase in the number of fitted experiments does not ensure a decrease in the value of the 95% confidence intervals. The variability in these confidence intervals may be due to the difficulty in fitting four parameters simultaneously and the correlation of these parameters to one another.

6.11.2.1. Variance in Thermocouple Measurements

The variance, ω, of the measurements of the three thermocouples was fitted as part of the fitting procedure because it was difficult to define this value prior to fitting, as discussed in Section 6.8. The fitted variance values are shown in Table 6-6, and it can be seen that the variance of the thermocouple measurements across the different fittings are similar, with an acceptable variance of approximately 1°C. Thermocouple 3 (thermocouple at a radial distance of 12mm) has a consistently smaller variance value than the other two thermocouples. Assuming that the error in thermocouple placement and readings are consistent across all three thermocouples, this suggests that errors in placement at the basket centre lead to greater errors in measured temperatures.

Table 6-6: Variance (ω) values as fit by during the Parameter Estimation for each thermocouple and for each grouping of experiments.

	Thermocouple 1 (0mm) ω (°C)	**Thermocouple 2 (6mm) ω (°C)**	**Thermocouple 3 (12mm) ω (°C)**
10 exps	1.117 (±0.025)	1.212 (±0.024)	0.619 (±0.021)
8 exps (1)	0.934 (±0.010)	1.076 (±0.011)	0.572 (±0.006)
8 exps (2)	1.082 (±0.057)	1.188 (±0.051)	0.592 (±0.049)
6 exps	1.144 (±0.357)	1.318 (±0.328)	0.594 (±0.314)
4 exps	0.968 (±0.014)	0.987 (±0.014)	0.607 (±0.010)

The consistent variance across the fittings suggests that the variability in these confidence intervals may be due to the difficulty in fitting four parameters simultaneously, and the correlation of these parameters to one another. The predicted critical ambient temperatures for the grouping of 10 experiments along with this error

is plotted in Figure 6-21. The band of predicted critical ambient temperatures is quite large using these results. Fixing parameters in the fitting may help to reduce this error.

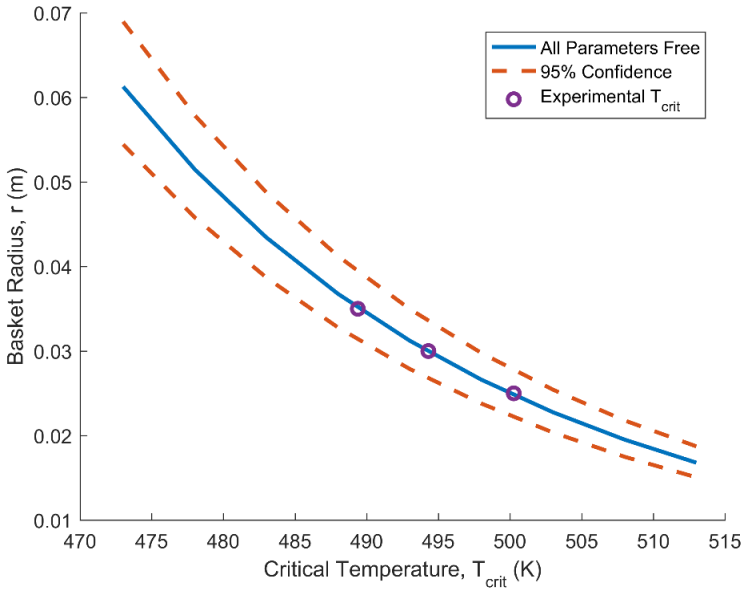

Figure 6-21: Predicted critical ambient temperatures for equi-cylindrical baskets of different radii as calculated using equation (6-17) and the kinetics and standard deviation for the 10 experiments grouping in Table 6-5.

6.11.2.2. Correlation of the Fitted Parameters

It can be seen in Table 6-5 that the value of thermal conductivity is stuck on the lower fitting bound for every grouping of experiments used. Adjusting the fitting bounds was found to have little effect on this, and one parameter of either the thermal conductivity or the specific heat capacity always tends towards one of the fitting bounds. A correlation matrix is generated as part of the report generated by the software. The correlation matrix for the grouping of 10 experiments is shown in Table 6-7. From this it can be seen why there is difficulty in fitting k and C_p. The table shows that the thermal conductivity, k, and the specific heat capacity, C_p, are very highly correlated with a correlation coefficient of 1. This is not surprising because this relationship is evident from the governing energy conservation equation (6-1) of this model. For the initial portion of the fitted temperature profile, the heat generation term has negligible effect, reducing this equation to two terms, the local rate of enthalpy change and the conductive heat transfer in the solid, from which the correlation between k and C_p can be seen. It is because of this correlation that the value of C_p was determined prior to

fitting using Modulated DSC. Interestingly, the activation energy, E, and the logarithmic term, $\ln QA$, have a high correlation coefficient of 0.912, but the same difficulty in fitting these parameters is not seen.

Table 6-7: Correlation matrix of fitted parameters. A value close to 1 indicates a very high correlation between the two parameters.

	$\boldsymbol{E}$	$\boldsymbol{\ln QA}$	$\boldsymbol{k}$	$\boldsymbol{C_p}$
$\boldsymbol{E}$	1	-	-	-
$\boldsymbol{\ln QA}$	0.912	1	-	-
$\boldsymbol{k}$	-0.516	-0.12	1	-
$\boldsymbol{C_p}$	-0.526	-0.132	1	1

6.11.2.3. Validation of Best Fit Parameters

For each of the different groupings, the experiments that were not used as part of the parameter estimation fitting, shown in Table 6-4, were used for validation of the estimated parameters, i.e. for the grouping of 8 (1) experiments, the experiments at ambient temperatures of 220°C (493K) and 224°C (497K) were used. The fit of the model with the parameters from the grouping of 8 (1) experiments to the experimentally measured temperature profiles can be seen in Figure 6-22 and Figure 6-23. Figure 6-22 shows the fit of the model to the individual temperature profiles for each of the three thermocouples for the experiment run at an oven controlled ambient temperature of 220°C (493K). The model is seen to fit well and is within the variance of the thermocouple measurements for the majority of the temperature profile. Figure 6-23 shows to fit to the three thermocouples in one plot for experiments run at 220°C (493K) and 224°C (497K), again showing a reasonable fit.

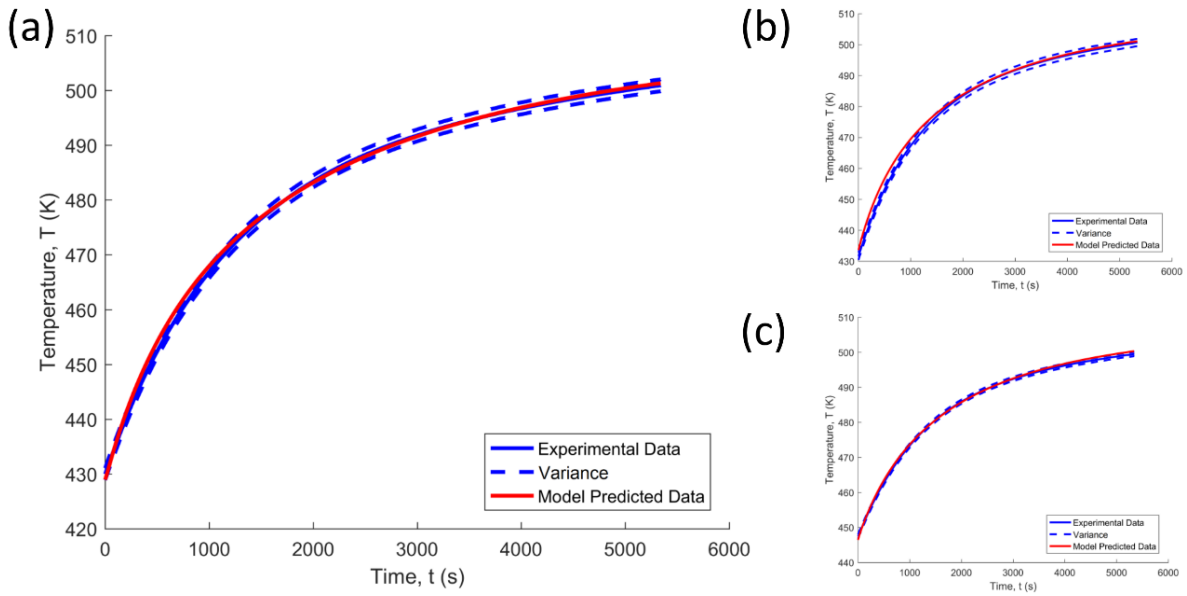

Figure 6-22: Validation of the numerical model using the grouping of 8 (1) experiments best fit parameters against individual experimental temperature profiles at an ambient temperature of 220°C (493K), at radial distances of (a) 0mm, (b) 6mm, and (c) 12mm.

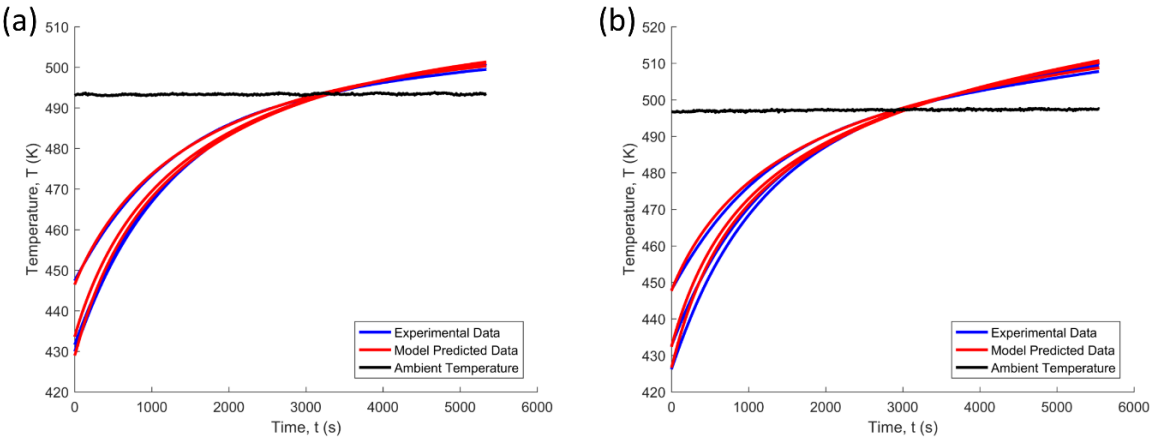

Figure 6-23: Validation of the numerical model using the grouping of 8 (2) experiments best fit parameters against experimentally measured temperature profiles for ambient temperatures of (a) 220°C (493K) and (b) 224°C (497K).

The Root Mean Square Error (RMSE) and R^2 values were calculated for the validation of each of the groupings of experiments. In each case, the RMSE and R^2 values are calculated from the entire temperature profile, for all the experiments used for validation together. This was done for each of the three thermocouples used in the experiments. It can be seen that the grouping with the highest error is the grouping of 4 experiments, but all RMSE values are within 1.2°C, which is small relative to the high

temperatures at which these experiments were run, 216°C (489K) to 228°C (501K). The high R^2 values, all in excess of 0.996, also indicate a good model fit.

Table 6-8: Root Mean Square Root (RMSE) and R^2 values for the fit of the model to the data from the three thermocouples, for each grouping of experiments.

	RMSE (R^2) of T_{0mm}	**RMSE (R^2) of T_{6mm}**	**RMSE (R^2) of T_{12mm}**
8 exps (1)	1.10°C (0.997)	1.06°C (0.997)	0.76°C (0.998)
8 exps (2)	0.83°C (0.998)	0.60°C (0.999)	0.49°C (0.999)
6 exps	0.74°C (0.999)	0.69°C (0.999)	0.49°C (0.999)
4 exps	1.13°C (0.997)	1.19°C (0.996)	0.74°C (0.998)

6.11.3. Specific Heat Capacity, C_p, Fixed in the Parameter Estimation

The value of the specific heat capacity, C_p, was fixed in the parameter estimation. This was fixed to the value of 1367 J kg^{-1} K^{-1}, as determined using MSDC in Section 6.9.1. In doing so, the best fit parameters shown in Table 6-9 were determined.

Firstly it can be seen that by fixing C_p the value of the thermal conductivity, k, is no longer stuck on the fitting bounds. Because C_p is fixed, and because of the correlation between k and C_p, the 95% confidence interval of k has reduced by up to three orders of magnitude in some cases. Overall, the best fit activation energy, E, for all groupings of experiments has consistently reduced by values between 6.0×10^3 and 6.6×10^3 J mol^{-1}. This is due to the correlation between E and k (-0.516), and between E and C_p (-0.526). Because C_p is now fixed to a higher value, which in turn has increased the value of k, the value of E has reduced accordingly. Similarly, the correlation of E and $\ln QA$ (0.912) means that the value of $\ln QA$ has also reduced.

The confidence intervals associated with E and $\ln QA$ have also reduced, and are consistently low across all groupings of experiments, although no correlation between grouping size and error can be seen. This may be because the choice of the experiments in each grouping has a greater impact on the error than the number of experiments.

An overlap of the 95% confidence intervals of E and $\ln QA$ would also be expected between the different groupings of experiments, but was not observed. This is probably

due to the strong correlations between E and $\ln QA$, and how this leads to one value compensating for the other.

Table 6-9: Results of the fittings where the specific heat capacity was fixed. 95% confidence intervals of the fitted parameters are shown in brackets.

	$\boldsymbol{E}$ (J mol^{-1})	$\boldsymbol{\ln QA}$	$\boldsymbol{k}$ (W m^{-1} K^{-1})	$\boldsymbol{C_p}$ (J kg^{-1} K^{-1})
10 exps	132.2 (±0.2) x10^3	33.77 (±0.05)	0.0791 (±5x10^{-5})	1367*
8 exps (1)	132.9 (±0.2) x10^3	33.93 (±0.05)	0.0799 (±5x10^{-5})	1367*
8 exps (2)	130.2 (±0.2) x10^3	33.29 (±0.05)	0.0768 (±5x10^{-5})	1367*
6 exps	135.3 (±0.3) x10^3	34.50 (±0.07)	0.0806 (±6x10^{-5})	1367*
4 exps	127.2 (±0.3) x10^3	32.56 (±0.07)	0.0766 (±7x10^{-5})	1367*
* Fixed in fitting				

The parameter estimates are similar for all groupings of experiments, and any difference in one of the parameters is compensated for by its correlation to other parameters. Figure 6-24 shows how to parameters of the grouping of 10 experiments, 8 (1) experiments, 6 experiments, and 4 experiments compare. In this plot, the critical ambient temperature for equi-cylindrical baskets of different radii is calculated using the parameters from Table 6-9 and equation (6-17). Less than 1°C difference can be seen between the calculated critical ambient temperatures for each set of parameters. These predicted values for all groupings of experiments are also within 0.5°C of the three experimentally measured critical ambient temperatures.

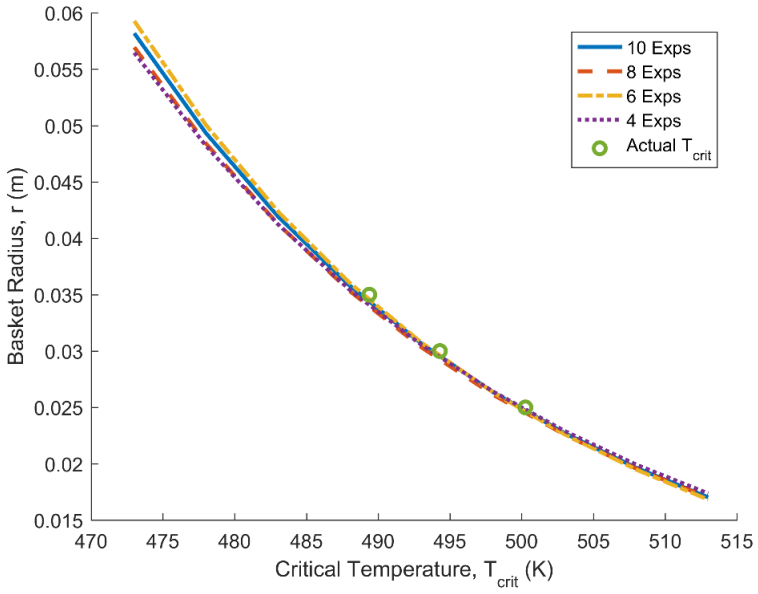

Figure 6-24: Predicted critical ambient temperatures for equi-cylindrical baskets of different radii as calculated using equation (6-17) and the estimated parameters from Table 6-9 for the groupings of 10, 8 (1), 6, and 4 experiments.

6.11.3.1. Variance in Thermocouple Measurements

The fitted variances for the measurements of the three thermocouples are shown in Table 6-10. These variance values have increased slightly relative to those fitted in the previous case where no parameters were fixed in the parameter estimation, shown in Table 6-6. This may be because the fitting is more limited by fixing C_p, even though this improves the results. Nonetheless, the variance values are all within acceptable limits.

Table 6-10: Variance (ω) values as fitted by during the Parameter Estimation for each thermocouple and for each grouping of experiments.

	Thermocouple 1 (0mm) ω (°C)	**Thermocouple 2 (6mm) ω (°C)**	**Thermocouple 3 (12mm) ω (°C)**
10 exps	1.259 (±0.011)	1.338°C (±0.010)	0.769°C (±0.007)
8 exps (1)	1.076 (±0.010)	1.193 (±0.012)	0.729 (±0.008)
8 exps (2)	1.229 (±0.012)	1.317 (±0.012)	0.741 (±0.007)
6 exps	1.290 (±0.014)	1.446 (±0.016)	0.744 (±0.009)
4 exps	1.104 (±0.015)	1.111 (±0.015)	0.756 (±0.011)

Figure 6-25 shows the predicted critical ambient temperatures as calculated using the estimated parameters, and the 95% confidence bounds of the best fit value of the activation energy, E. With these confidence intervals applied, the calculated critical ambient temperatures for any basket radius has a variation of within ±1°C.

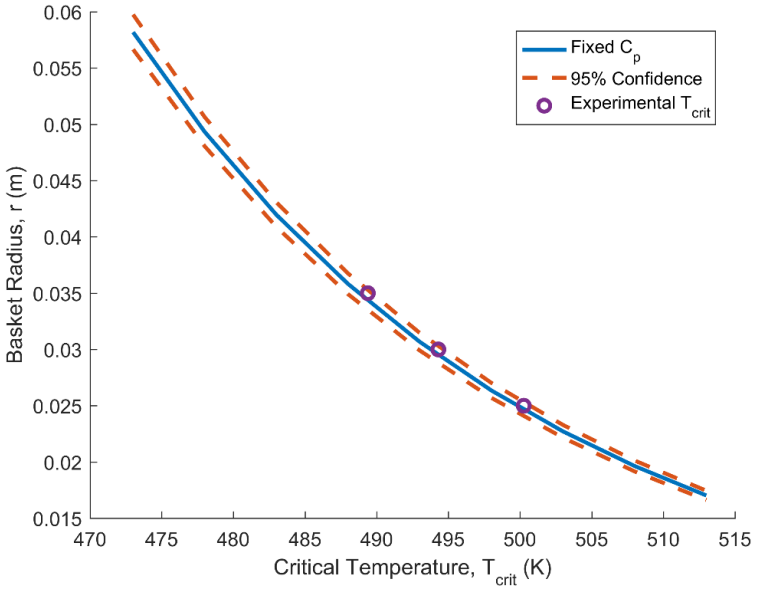

Figure 6-25: Predicted critical ambient temperatures for equi-cylindrical baskets of different radii as calculated using equation (6-17) and the kinetics and standard deviation for the 10 experiments grouping in Table 6-9.

6.11.3.2. Validation of Best Fit Model Parameters

For each of the different groupings, the experiments that were not used as part of the parameter estimation fitting were used for validation of the estimated parameters. The fit of the model with the parameters from the grouping of 8 (1) experiments to the experimentally measured temperature profiles can be seen in Figure 6-26. This figure shows the fit of the model to the individual temperature profiles for each of the three thermocouples for the experiment run at an ambient temperature of 220°C (493K). The model is seen to fit well and is within the variance of the thermocouple measurements for the majority of the temperature profile. Figure 6-27 shows the fit of the model with the parameters from the grouping of 6 experiments to four experiments used as validation for this case: 217°C (490K), 220°C (493K), 224°C (497K), and 227°C (500K). Again the model is seen to agree very well with the experimentally measured data, even

though fewer experiments were used in the fitting of the parameters for this grouping of experiments.

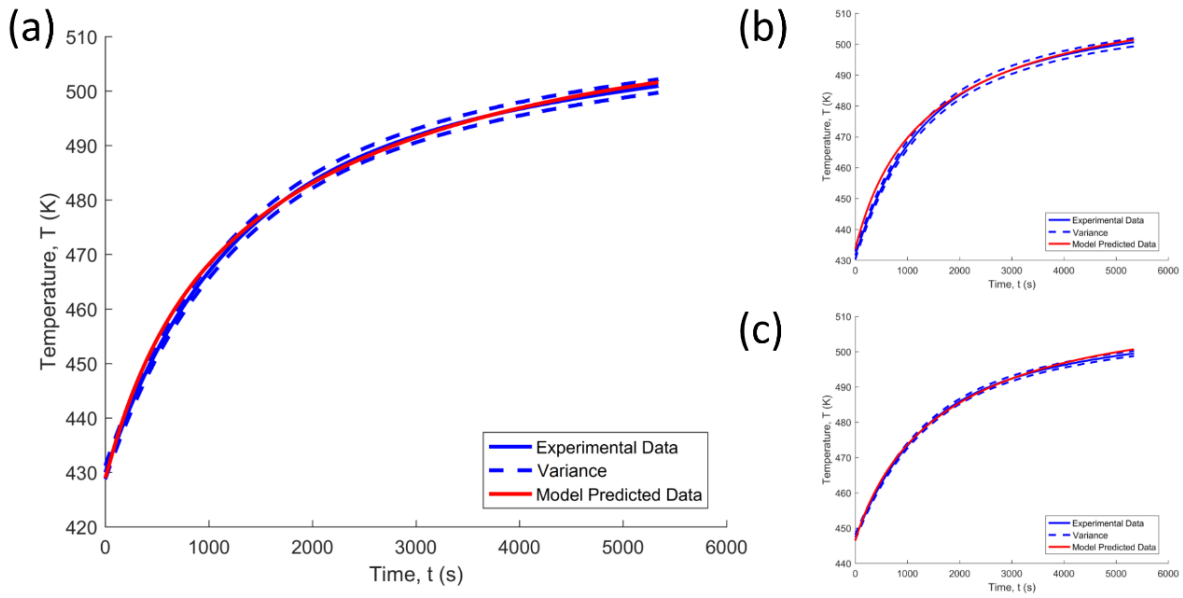

Figure 6-26: Validation of the numerical model using the grouping of 8 (1) experiments best fit parameters against individual experimental temperature profiles at an ambient temperature of 220°C (493K), at radial distances of (a) 0mm, (b) 6mm, and (c) 12mm.

The Root Mean Square Error (RMSE) and R^2 values were calculated for the validation of each of the groupings of experiments, as before. It can be seen that the grouping with the highest error is the grouping of 8 (1) experiments, but all RMSE values are within 1.2°C. The high R^2 values, all in excess of 0.997, also indicate a good model fit.

Table 6-11: Root Mean Square Root (RMSE) and R^2 values for the fit of the model to the data from the three thermocouples, for each grouping of experiments.

	RMSE (R^2) of T_{0mm}	**RMSE (R^2) of T_{6mm}**	**RMSE (R^2) of T_{12mm}**
8 exps (1)	1.15°C (0.996)	1.09°C (0.996)	0.93°C (0.998)
8 exps (2)	0.74°C (0.998)	0.68°C (0.998)	0.57°C (0.998)
6 exps	0.68°C (0.998)	0.64°C (0.998)	0.54°C (0.998)
4 exps	0.82°C (0.998)	0.78°C (0.998)	0.70°C (0.998)

The groupings of 8 (2), 6, and 4 experiments all have reduced RMSE in comparison to those measured in the previous case, where no parameters were fixed in the parameter estimation. The RMSE of these groupings reduced on average by approximately 0.08°C, 0.06°C, and 0.25°C respectively. The RMSE of the grouping of 8 (1) experiments increase on average by approximately 0.08°C.

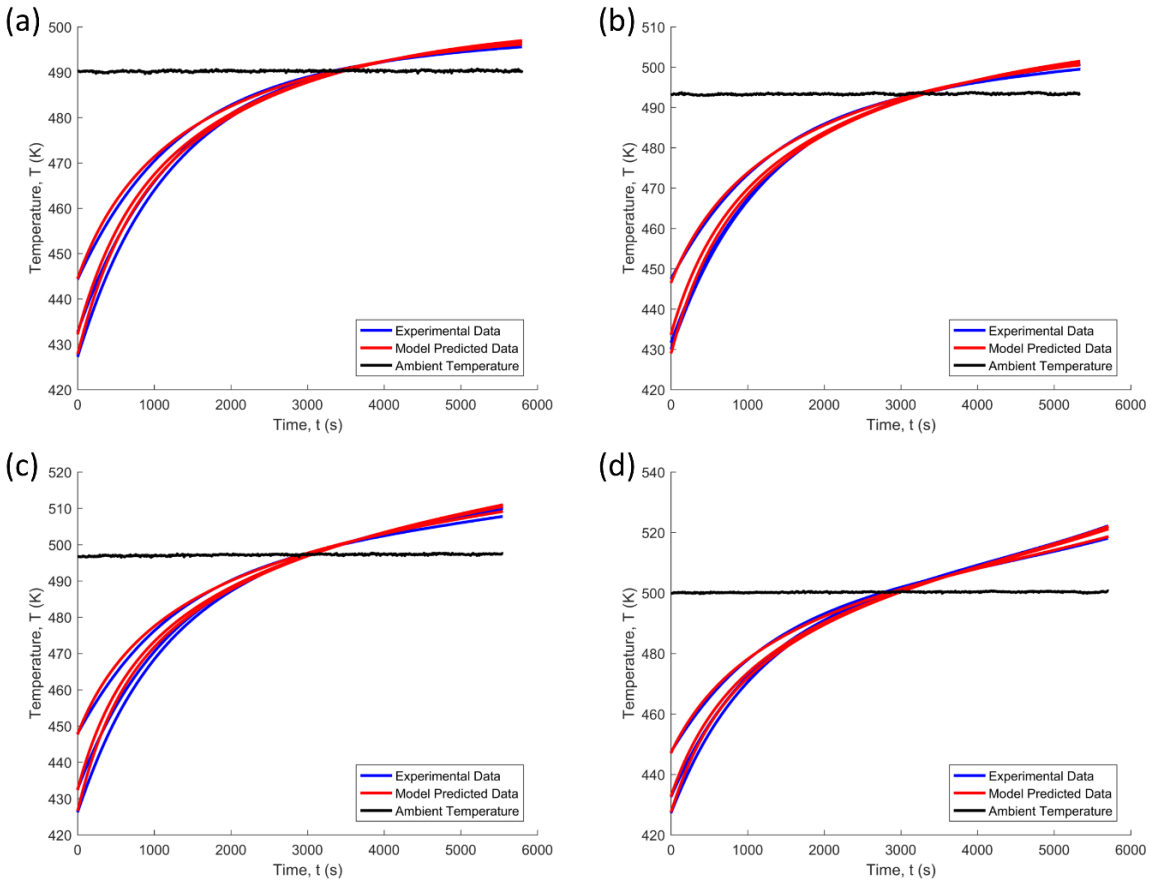

Figure 6-27: Validation of the numerical model using the grouping of 6 experiments best fit parameters against experimentally measured temperature profiles for ambient temperatures of (a) 217°C, (b) 220°C, (c) 224°C, and (d) 227°C.

6.11.4. Specific Heat Capacity, C_p, and Activation Energy, E, Fixed in the Parameter Estimation

It can be seen from the correlation matrix in Table 6-7 that there is significant correlation between E and $\ln QA$, with a correlation coefficient of 0.912. When attempting to fit this model to these experiments individually, it was found that either the activation energy or the logarithmic term would always tend towards one of the fitting bounds. It is thought that this is because of this strong correlation. Fitting to these experiments

simultaneously, as is done in this investigation, is found to alleviate this issue as can be seen in the previous cases. This may be because fitting to a range of experiment, which are run at different ambient temperatures and exhibit different degrees of self-heating, allow the reaction kinetics to be readily fit. This suggest that fixing the activation energy is not required to improve the Parameter Estimation Approach, nonetheless fixing both the specific heat capacity and activation energy in the fitting was discussed.

Fixing both the value of the specific heat capacity, C_p, and the activation energy, E, in the fittings produced the best fit parameters shown in Table 6-12. The activation energy was fixed to the weighted average value determined using the Friedman DSC method of 110x10^3 J mol^{-1}. C_p was again fixed to a value of 1367 J kg^{-1} K^{-1} to the value of the thermal conductivity, k, from being stuck on the lower fitting bound. By fixing the values of C_p and E, the 95% confidence intervals of the thermal conductivity, k, and the logarithmic term, $\ln QA$, have reduced substantially. Some of these intervals have reduced by up to three order of magnitude.

The best fit values of k and $\ln QA$ is consistent across all groupings of the experiments, with average values of 0.0759 W m^{-1} K^{-1} and 28.46 respectively. The values of k are similar to those fitted in the previous case where only C_p was fixed. The fitted value of $\ln QA$ is much lower than that in the previous case, but this is because the fixed value of E, to which this is strongly correlated, is considerably lower than before.

Table 6-12: Results of the fittings where the specific heat capacity was fixed. 95% confidence intervals of the fitted parameters are shown in brackets.

	$\boldsymbol{E}$ (J mol^{-1})	$\boldsymbol{\ln QA}$	$\boldsymbol{k}$ (W m^{-1} K^{-1})	$\boldsymbol{C_p}$ (J kg^{-1} K^{-1})
10 exps	110.x10^3*	28.45 (±6x10^{-4})	0.0764 (±4x10^{-5})	1367*
8 exps (1)	110.x10^3*	28.46 (±6x10^{-4})	0.0742 (±4x10^{-5})	1367*
8 exps (2)	110.x10^3*	28.46 (±6x10^{-4})	0.0770 (±4x10^{-5})	1367*
6 exps	110.x10^3*	28.45 (±8x10^{-4})	0.0776 (±5x10^{-5})	1367*
4 exps	110.x10^3*	28.46 (±8x10^{-4})	0.0745 (±5x10^{-5})	1367*
* Fixed in fitting				

Figure 6-28 shows how to parameters of the grouping of 10 experiments, 8 (1) experiments, 6 experiments, and 4 experiments compare. In this plot, the critical ambient temperature for equi-cylindrical baskets of different radii is calculated using the parameters from Table 6-12 and equation (6-17). Less than 1°C difference can be seen between the calculated critical ambient temperatures for each set of parameters, and this is due to the little freedom allowed to the parameter estimation by fixing two parameters.

These predicted critical ambient temperatures are not in agreement with the three experimentally measured critical ambient temperature. The predicted and experimental values agree at a radius of 35mm, but diverge at radii larger and smaller than this. This strongly suggests that the value of activation energy to which it was fixed in this case was incorrect. The fixed value (110.1×10^3 J mol^{-1}) is about 20×10^3 J mol^{-1} lower than the best fit values of E in the previous case, where only C_p was fixed in the fittings.

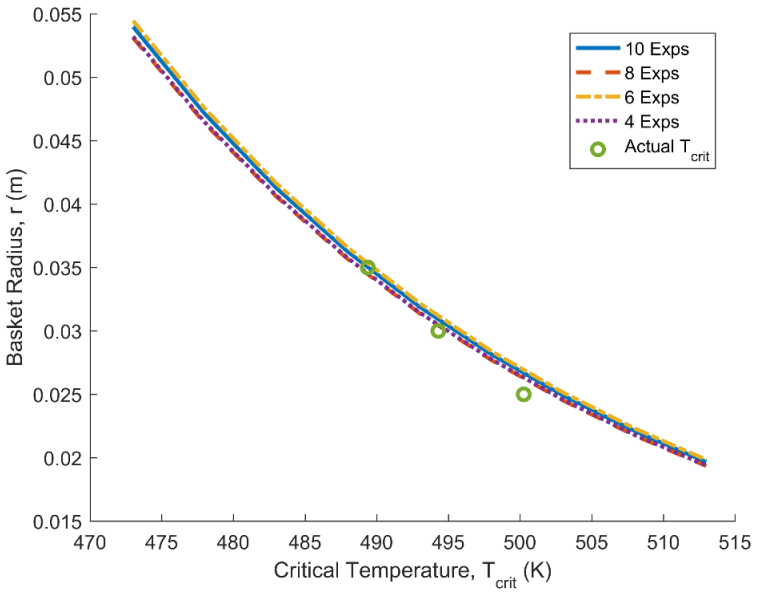

Figure 6-28: Predicted critical ambient temperatures for equi-cylindrical baskets of different radii as calculated using equation (6-17) and the estimated parameters from Table 6-12 for the groupings of 10, 8 (1), 6, and 4 experiments.

The Root Mean Square Error (RMSE) and R^2 values were calculated for the validation of each of the groupings of experiments as before. It can be seen that the grouping with the highest error is the grouping of 4 experiments, as would be expected because the fewest experiments were used for this fitting. All RMSE values are within 1.5°C, which is

higher than the previous two cases. This is because fixing two values in the fitting, especially with such high correlations to the remaining, non-fixed values, greatly reduces the freedom of the parameter estimation. The R^2 values, all in excess of 0.994, are lower than the previous parameter estimation cases.

Table 6-13: Root Mean Square Root (RMSE) and R^2 values for the fit of the model to the data from the three thermocouples, for each grouping of experiments.

	RMSE (R^2) of T_{0mm}	**RMSE (R^2) of T_{6mm}**	**RMSE (R^2) of T_{12mm}**
8 exps (1)	1.40°C (0.995)	1.39°C (0.995)	1.10°C (0.996)
8 exps (2)	0.87°C (0.998)	0.66°C (0.999)	0.65°C (0.998)
6 exps	0.89°C (0.998)	0.86°C (0.998)	0.74°C (0.998)
4 exps	1.40°C (0.995)	1.45°C (0.994)	1.09°C (0.995)

6.11.5. Comparison of the Different Parameter Estimation Approaches

The best fit parameters from the three different parameter estimation cases were compared, these being: 1) no fixed parameters, 2) fixed specific heat capacity, C_p, and 3) fixed C_p and activation energy, E. These were compared by looking at the critical ambient temperatures predicted by the best fit parameters for the grouping of 10 experiments from each approach. The grouping of 10 experiments was chosen because all groupings predicted similar results. This is shown in Figure 6-29.

It can be seen that the results of the approach where only C_p is fixed provides the best match to the experimental data. Fixing both E and C_p leads to the poorest match. This suggests that parameter estimation approach, where C_p is fixed, is capable of accurately measuring the powder reaction kinetics. It also suggest that E as measured using the isoconversional DSC methods is unreliable, or at least inapplicable in this sort of approach.

Fixing C_p improves the agreement with experimentally measured critical ambient temperature only slightly, in comparison to the approach where C_p is not fixed. This shows that the values of the reaction kinetics, E and $\ln QA$, affect the predicted critical ambient temperatures more than the value of k and C_p. However, measuring C_p using

MDSC and fixing it in the fitting is clearly a better approach because of how it allows a value of k to be determined. If C_p is not fixed, then because of the strong correlation between k and C_p, seen from the correlation coefficient of 1 in Table 6-7, the value of k becomes stuck on the lower fitting bound. Comparing Table 6-9 to Table 6-5 also shows that fixing C_p helps to greatly reduce the fitting error of the model parameters.

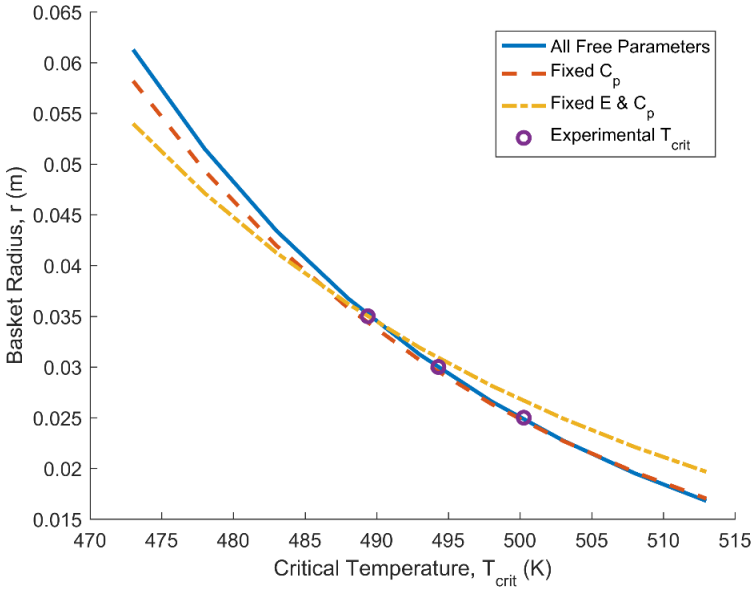

Figure 6-29: Comparison of the three Parameter Estimation Approach cases: no fixed parameters, fixed C_p, and fixed E and C_p.

6.12. Results Comparison with other Characterisation Methods

The Parameter Estimation Approach was developed as an alternative to the existing basket methods, namely the steady-state basket method and the cross-point temperature (CPT) method. These methods were previously used to characterise Micronized Formulation 1 with the measured kinetics summarised in Table 6-14. The parameter estimation approach results are taken from the groupings of 10 experiments.

The steady-state method results are dependent on knowing a value for the thermal conductivity, which was taken as 0.08 W m^{-1} K^{-1}. This method measures the activation energy, E, and the logarithmic term, $\ln QA$, which are also measured by the parameter estimation approach. The results from the Cross-Point Temperature Method are not all directly comparable, in that this method measures E and a logarithmic term $\ln QA/C_p$, which encapsulates the heat of reaction, pre-exponential factor, and specific heat

capacity. Taking the value for C_p of 1367 J kg^{-1} K^{-1} measured using MDSC, the value of $\ln QA$ from the CPT Method is 37.51, which is larger than the parameter estimation approach values, and considerably larger than the steady-state method value, which has the most comparable value of E.

The kinetics as measured using the parameter estimation approach where both E and C_p were fixed are seen to be well below those of the other two parameter estimation approaches, and the steady-state method kinetics. It was already shown in Section 6.11.5 that the kinetics measured by fixing both E and C_p are believed to be wrong. Instead, the parameter estimation approach where only C_p was fixed is believed to be the best approach. The kinetics of this approach are the most similar to those measured using the steady-state method.

Table 6-14: Results from the Parameter Estimation Approach compared with the results from the existing basket methods.

		E (J mol^{-1})	$\ln QA$	$ln\frac{QA}{C_p}$	k (W m^{-1} K^{-1})	C_p (J kg^{-1} K^{-1})
Parameter Estimation Approach	**All Free**	138.8 (±1.0) x10^3	34.69 (±0.07)	-	0.04 (±0.007)**	703.8 (±119)
	Fixed C_p	132.2 (±0.3) x10^3	33.77 (±0.07)	-	0.0791 (±6x10^{-5})	1367*
	Fixed E and C_p	110x10^3*	28.45 (±6x10^{-4})	-	0.0764 (±4x10^{-5})	1367*
Steady-State Method		125.3 (±1.0) x10^3	31.90 (±0.25)	-	-	-
CPT Method		124.3 (±8.8) x10^3	-	30.29 (±2.11)	-	-

** Stuck on fitting bound * Fixed in fitting

The 95% confidence intervals of the parameter estimation approach kinetics, in particular the case where C_p is fixed, are smaller than those of the other methods. The CPT method results in particular have very large confidence intervals. The errors associated with the kinetics from the steady-state method are due to the lack of data

points used in the fitting (3 data points), while the errors associated with the CPT method are due to the sensitivity of the method to thermocouple errors.

These results are easier to compare graphically and the calculated critical ambient temperatures using the parameters from the different methods are shown in Figure 6-30. The parameter estimation approach results shown here are for the grouping of 10 experiments where only C_p is fixed. It can be seen that the results of the parameter estimation approach and the steady-state method agree very well, with less than 0.5°C difference in predicted critical ambient temperatures. This helps to validate the parameter estimation approach as a means of predicting critical ambient temperatures and thermal runaway. The parameters from the CPT method predict very different critical ambient temperatures. For a basket of radius 30mm, the CPT Method under predicts the critical ambient temperature by more than 4°C, with this under prediction increasing with increasing basket radius.

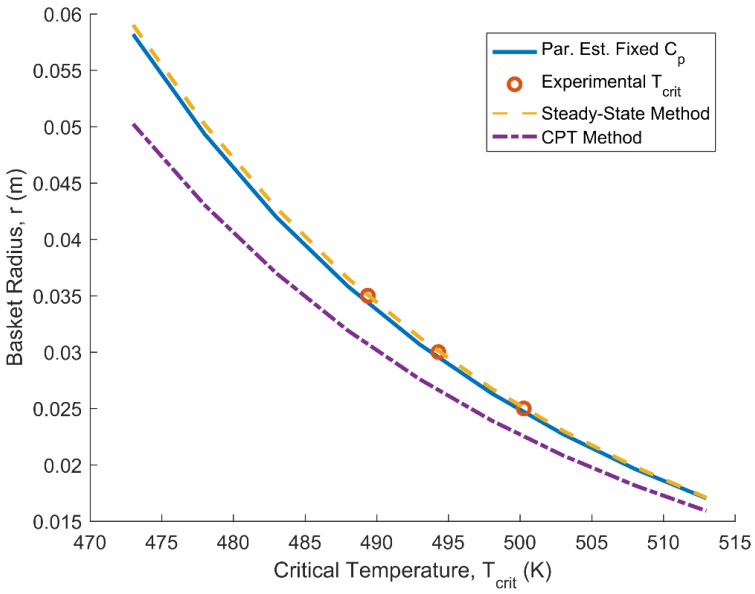

Figure 6-30: Predicted critical ambient temperatures for equi-cylindrical baskets of different radii as calculated using equation (6-17) and kinetics from the steady-state method, cross-point temperature method, and the new parameter estimation approach.

The agreement of the parameter estimation approach and the steady-state method helps to validate this approach as a faster, more accurate means of characterising self-heating powders. This approach requires less than 10 experiments, each taking about 2.5 hours, while the steady-state method requires a number of experiments, typically 4

or 5, each taking between 6 and 8 hours, to determine one data point. The parameter estimation approach uses the same basket setup and measured temperature profiles as the CPT method, yet the results show that this approach is much less susceptible to the errors in thermocouple placements that greatly affect the CPT method results. This improvement may be because this approach fits to large portions of the measured temperature profiles, providing thousands of data points instead of the tens of points used in the CPT method.

6.13. Conclusions in using the Parameter Estimation Approach to Characterise the Detergent Powder Micronized Formulation 1

This investigation aimed to develop a novel methodology, the parameter estimation approach, for characterising the self-heating behaviour of detergent powders. This new approach successfully uses a 2D-axisymmetirc heat transfer model to estimate the best fit powder thermal conductivity, k, specific heat capacity, C_p, and self-heating reaction kinetics, E and $\ln QA$, from experimentally measured temperature profiles within an oven heat basket of detergent powder.

13 experiments were performed, and parameter estimation was performed for groupings of different denominations (10, 8, 6, and 4) of these experiments. Parameter Estimation with for all four parameters, k, C_p, E, and $\ln QA$, free in the fitting produced similar best fit values for all groupings of experiments, but k was consistently stuck on the lower fitting bound. Some variability was also seen in the confidence intervals of the estimated parameters.

Due to the correlated nature of k and C_p, Modulated DSC was used to determine a value of C_p prior to the parameter estimation. Fixing this value in the parameter estimation prevented k from becoming stuck on the fitting bounds, and improved the confidence intervals for the estimated parameters for all groupings of experiments.

The Friedman and Ozawa-Flynn-Wall methods were also used to measure the self-heating reaction activation energy, E, prior to the parameter estimation. Fixing the value of E as well as C_p in the parameter estimation largely reduced the freedom allowed to the fitting, resulting in best fit parameters that did not agree with experimentally

measured critical ambient temperatures as well as the previous approaches. It was decided that the best approach is to only fix the value of C_p in the parameter estimation.

The results of the fittings were validated against basket temperature profiles not used in the fittings. Even for the grouping of experiments with the highest fitting error, all RMSE values were within 1.2°C, which is small relative to the high temperatures at which these experiments were run, 216°C (489K) to 228°C (501K). All validated fittings also had R^2 values in excess of 0.997, indicating a good model fit. The parameters from each grouping of experiments were used to predict critical ambient temperatures for equi-cylindrical baskets of different radii. When using the approach where only C_p was fixed in the fitting, the parameters from all groupings predicted critical ambient temperatures within 0.5°C of the experimentally measured values.

This approach was developed to improve upon the existing basket methods, namely the steady-state method and the cross-point temperature method. This approach has been shown to successfully predict critical ambient temperatures for a range of basket sizes while improving massively on the time required by the steady-state method to measure such values. This approach requires no more than 10 experiments, each taking approximately 2.5 hours to complete, while the Steady-State Approach takes between 6 and 8 hours per experiment, with one data point yielded per 4 or 5 experiments.

This approach uses the same basket setup as used for the cross-point temperature method, but the CPT method fails to agree with experimentally measured critical ambient temperatures, under predicting the critical ambient temperature for a 60mm equi-cylindrical basket by approximately 4°C. This shows that the CPT Method is much more susceptible to errors in thermocouple placement, while the parameter estimation approach is not. This may be because a considerable portion of the temperature profiles from each experiment are used for fitting to, providing thousands of data points, while the CPT method yields only one data point per experiment.

This investigation has shown that the novel parameter estimation approach is a viable, faster, and more accurate alternative to existing basket heating methods. This approach has also been used to characterise three more formulations. This will be discussed in Section 7.2, and will serve to validate this approach further.

7. Parameter Estimation Approach Workflow and Application to Other Detergent Formulations

The previous chapter used the parameter estimation approach to characterise Micronized Formulation 1. Here, a recommended workflow for this method is outlined, and then used to characterise three other detergent powder formulations. These formulations are were discussed in Section 6.3 and are referred to as: 1) Non-Micronized Formulation 1, 2) Formulation 2, and 3) Formulation 3.

7.1. Recommended Workflow for the Parameter Estimation Approach

From this research it is possible to conclude that parameter estimation approach where the value of the specific heat capacity, C_p, is fixed, is a good method for charactersing the self-heating behaviour of detergent powders. Here a recommended workflow for this appraoch is discussed.

Fitting Pre-Requisites:

- Before fitting the convective heat transfer coefficient in the oven needs to be determined. This can be determined using the transient temperature measurement method used by Carson *et al.* (2006) and discussed in Section 4.5.

Specific Heat Capacity, C_p, by MDSC

- Modulated Differential Scanning Calorimetry (MDSC) can be used to measure the powder specific heat capacity, C_p, as was done in Section 6.9. C_p in the parameter estimation is fixed to this value to prevent the thermal conductivity, k, from getting stuck on the fitting bounds due to the high correlation between these two parameters.

Basket Experiments:

- The 60mm diameter equi-cylindrical basket used in this investigation is recommended. This basket size is small enough so the experiments only require approximately 2.5 hours to complete, although a number of different basket sizes could also be used. A 60mm basket is also large enough that an array of three thermocouples can comfortably be inserted into the powder.

- These thermocouples should be spaced at 0mm, 6mm, and 12mm from the basket centre and at basket half-height. Although quite small, this spacing allows for a large enough difference in temperature to be measured for each of the thermocouples, whilst the outermost thermocouple is not too close to the basket edge.
- An array of three thermocouples is required in order to fit the initial temperature profile approximation, as discussed in Section 6.4.
- The 13 experiments used here are not required. The fitting was seen to work for as few as 4 experiments. The recommended approach would be to run 8 experiments at different oven controlled ambient temperatures, such that 6 experiments are used in the parameter estimation, and the remaining 2 can be used for validation.
- Determining the oven controlled ambient temperatures at which to run these experiments requires a degree of trial and error. Running experiments at 200°C, 215°C, and 230°C, and looking at the amount of self-heating exhibited in each experiment would give an indication as to what ambient temperatures to use. Ideally, at the lowest chosen ambient temperature, the baskets would exhibit a core temperature rise of at least of at least 5°C. The other experiments would be run at increasing ambient temperatures in increments of 1°C.

gPROMS Parameter Estimation

- gPROMS was used to determine the best fit parameters using its Parameter Estimation capabilites. C_p is fixed to the value measured using MDSC in the fitting and the best fit k, E, and $\ln QA$ are determined. The statistical analysis of the results provided by gPROMS, in particular the 95% confidence intervals and the standard deviation, will give an indication as to the quality of the fitted results.

Validation of Results

- The results are validated against the two experiments designated beforehand. The fit of the model using the best fit parameters to the experimental data is examined graphically and by means of Root Mean Square Error and R^2 analysis.

- An additional step of this validation would be to experimentally determine the critical ambient temperature of a selected basket size, and compare this with the critical ambient temperature predicted using the best fit parameters.

Predicting Self-Heating and Thermal Runaway in Spray Drying Tower Build-Up

- The parameters determined here can be used to predict self-heating and thermal runaway in powder build-up in spray drying towers. This is discussed in more details in Chapter 8.

This workflow is detailed graphically in Figure 7-1. This workflow could be applied to characterise the self-heating behaviour of different detergent formulations, such that the optimum spray drying operating conditions that prevent self-heating in the wall deposits can be determined.

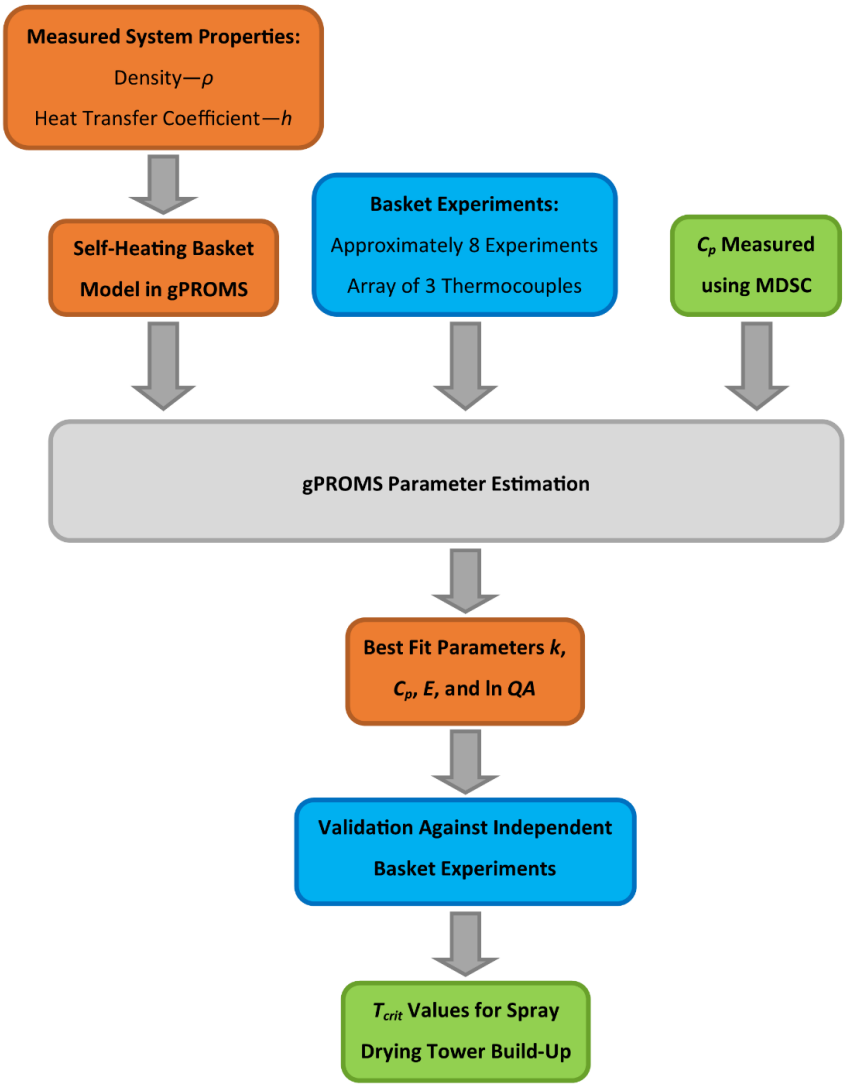

Figure 7-1: Suggested workflow for the Parameter Estimation Approach.

7.2. Application of the Parameter Estimation Approach to Other Detergent Powder Formulations

Three other formulations were characterised using the Parameter Estimation Approach and the results documented here. The same approach was used but these results are not scrutinised to the same degree as for the previous formulation. These results are presented to help justify, and validate, the Parameter Estimation Approach as viable, and effective alternative to the existing characterisation methods. These formulations are were discussed in Section 6.3 and are referred to as: 1) Non-Micronized Formulation 1, 2) Formulation 2, and 3) Formulation 3.

As the name suggests, Non-Micronized Formulation 1 uses a non-micronized grade of sodium sulphate, but in all other ways it is the same as Micronized Formulation 1. The other two formulations, Formulation 2 and Formulation 3, are similar to one another, with Formulation 3 containing 1% Polycarboxylate Polymer, whilst Formulation 2 contains none.

The reaction kinetics of these formulations have already been estimated using the cross-point temperature method in Section 5.5 with mixed results. Reasonable results were achieved using a thermocouple spacing of 12mm, while very poor results, from which no kinetics could be estimated, were achieved using a spacing of 6mm. The same experiments were used to for the cross-point temperature experiments and the parameter estimation approach experiments.

DSC experiments were also discussed in Section 5.5. Non-Micronized Formulation 1 was shown to react similarly for all particle size ranges, whereas Formulation 2 and Formulation 3 did not exhibit this behaviour. The smaller particles in these two formulations produced exotherms with smaller peaks. This showed that there is some variability in reactivity with particle size in these formulations, which could impact on their characterisation.

The objectives of this characterisation are as follows:

- Use the parameter estimation approach, as detailed in the workflow in Section 7.1, to characterise the thermal conductivity, k, specific heat capacity, C_p, and reaction kinetics, E and $\ln QA$, of the three formulations outlined above.
- Compare the measured results with those measured using the steady-state method and the cross-point temperature method.
- Predict critical ambient temperatures using the estimated parameters and validate these against experimentally measured values for a 50mm and 60mm equi-cylindrical basket.
- Show that the parameter estimation approach estimates these parameters with reduced error in comparison to the other basket heating methods.
- Show that this approach can be successfully used to characterise a number of different detergent powder formulations, thus helping to validate this approach.

7.2.1. Parameter Estimation Results for Non-Micronized Formulation 1

7.2.1.1. Specific Heat Capacity as Measured using DSC

The specific heat capacity of Non-Micronized Formulation 1 was measured using the same approach outlined in Section 6.9. This was done for three different size ranges of particles, 150 to 250µm, 250 to 355µm, and 355 to 425µm. From the measured heat flow output the non-reversing $C_p$value was calculated. This can be seen in Figure 7-2 along with the modulated temperature input of the DSC.

It can be seen that C_p is not constant throughout the experiment. This may be due to the modulation period used. The weighted average C_p profile shown was calculated as the average C_p as a function of temperature, weighted by each size ranges percentage contribution by mass to the overall powder size distribution. The most stable region of the profile for all three size ranges is between 488.0K (214.8°C) and 495.5K (222.3°C), and it was from this region that the value of C_p to be used in the parameter estimation fittings was chosen. Figure 7-3 shows the C_p profiles for this temperature range. The C_p used in the fitting was calculated as the overall average value of the weighted profile in this temperature range, and has a value of 1298 J kg^{-1} K^{-1}.

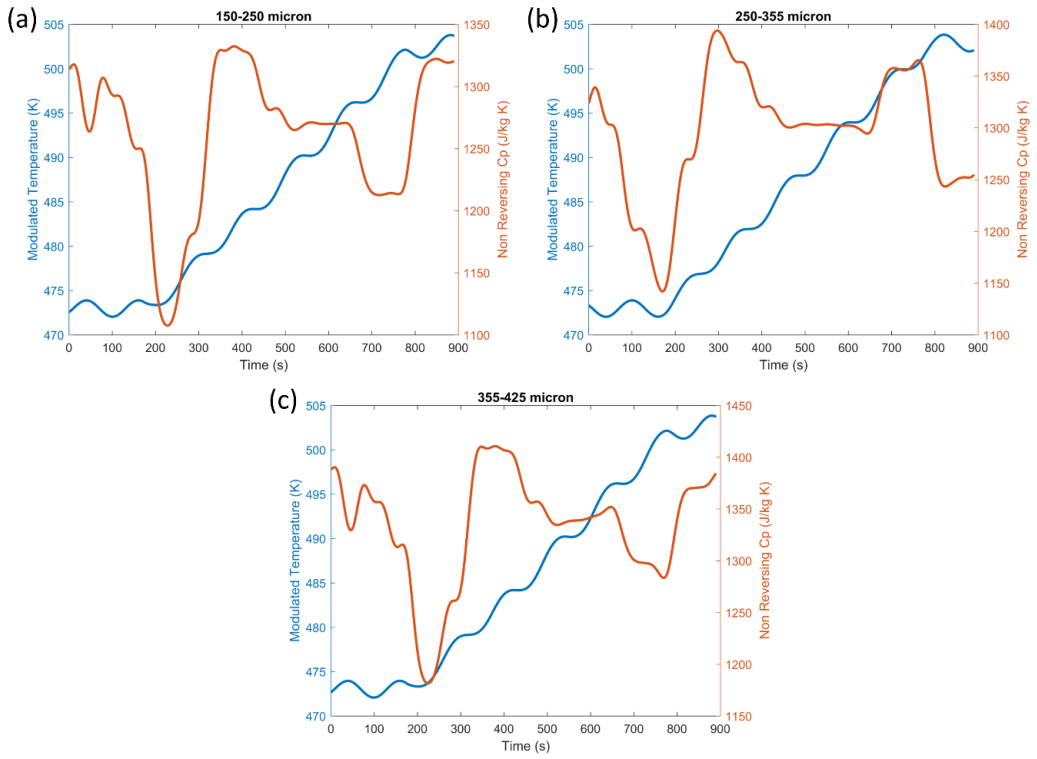

Figure 7-2: Measured non-reversing C_p and modulated DSC input temperature for particles of size ranges (a) 150-250µm, (b) 250-355µm, and (c) 355-425µm.

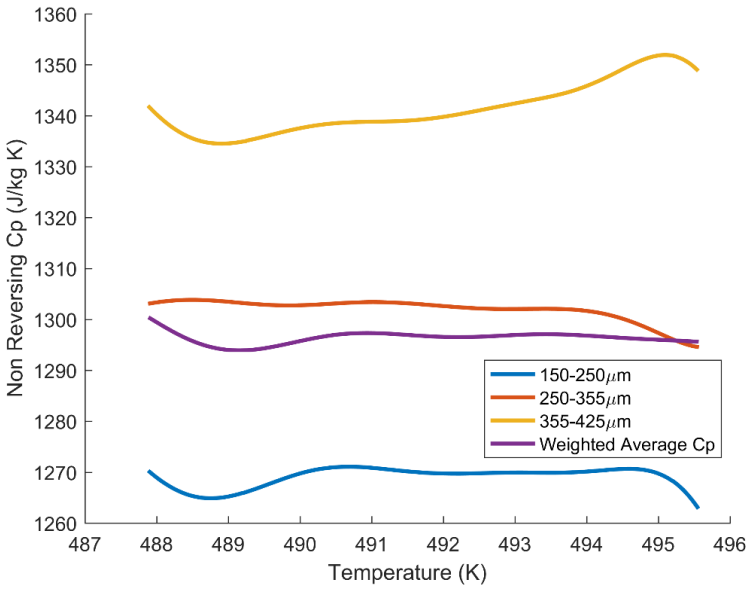

Figure 7-3: Measured non-reversing C_p for samples of three different particle size ranges for the most stable region from which the value used in the fittings was chosen.

7.2.1.2. Choice of Experiments for Parameter Estimation

The Parameter Estimation Approach was performed as outlined previously. Basket experiments were run at 13 different oven controlled ambient temperatures from 216°C (489K) to 228°C (501K). At 216°C (489K) a moderate amount of self-heating is observed, while at 228°C (501K) much more self-heating is observed, culminating in thermal runaway of the basket. An array of three thermocouples was embedded within the powder, and the initial temperature profile approximated using the method in Section 6.6. All 13 experiments were fitted to simultaneously, with none of the four parameters fixed. These experiments were filtered based on the residual term of the maximum likelihood method objective function, as done previously in Section 6.11.1. This residual term should be an indication of poor thermocouple placement. The value of the residual term for each experiment can be seen in Table 7-1, with colour indicating the relative severity. For this formulation, the experiments run at 219°C (492K), 225°C (498K), and 226°C (499K) were omitted, and groupings of 10, 8, 6, and 4 experiments used in the parameter estimations.

Table 7-1: Contribution of the residual term to the maximum likelihood function for each of the 13 experiments when fitted simultaneously.

Experiment Ambient Temperature	Maximum Likelihood Residual Term
216°C	4233.3
217°C	6792.3
218°C	2438.6
219°C	11234.5
220°C	1800.9
221°C	5334.3
222°C	5632.5
223°C	2968.5
224°C	4949.7
225°C	14813.9
226°C	39502.5
227°C	4287.1
228°C	4106.4

7.2.1.3. No Fixed Parameters in the Parameter Estimation

The same issue as with Micronized Formulation 1 arose in fitting to these experiments with all four parameters free in the fitting, whereby the thermal conductivity became stuck on the lower fitting bound. The results of these fittings can be seen in Table 7-2.

Table 7-2: Results of the fittings where no parameters were fixed.

	$\boldsymbol{E}$ (J mol^{-1})	$\ln \boldsymbol{QA}$	$\boldsymbol{k}$ (W m^{-1} K^{-1})	$\boldsymbol{C_p}$ (J kg^{-1} K^{-1})
10 exps	128.0 (±0.1) x10^3	32.28 (±0.04)	0.04 (±0.005)**	874.2 (±105)
8 exps (1)	128.5 (±0.1) x10^3	32.40 (±0.05)	0.04 (±0.008)**	874.9 (±170)
8 exps (2)	129.4 (±0.6) x10^3	32.62 (±0.05)	0.04 (±0.005)**	873.8 (±124)
6 exps	127.1 (±0.5) x10^3	32.06 (±0.06)	0.04 (±0.005)**	875.6 (±111)
4 exps	128.5 (±0.5) x10^3	32.41 (±0.07)	0.04 (±0.004)**	871.6 (±91)
** Stuck on fitting bound				

Again, the correlation matrix in Table 7-3 shows the thermal conductivity, k, and specific heat capacity, C_p, to be entirely correlated. There is a high correlation between the activation energy, E, and the logarithmic term, $\ln QA$, of 0.873, but this does no inhibit the parameter estimation's fitting of these two parameters.

Table 7-3: Correlation matrix of fitted parameters. A value close to 1 indicates a very high correlation between the two parameters.

	$\boldsymbol{E}$	$\ln \boldsymbol{QA}$	$\boldsymbol{k}$	$\boldsymbol{C_p}$
$\boldsymbol{E}$	1	-	-	-
$\ln \boldsymbol{QA}$	0.873	1	-	-
$\boldsymbol{k}$	-0.473	0.0164	1	-
$\boldsymbol{C_p}$	-0.484	0.00465	1	1

7.2.1.4. Specific Heat Capacity, C_p, Fixed in the Parameter Estimation

Because of this correlation, the value of the specific heat capacity was fixed to the value of 1298 J kg^{-1} K^{-1} determined using modulated DSC. The results of this parameter estimation are shown in Table 7-4. It can be seen that by fixing C_p, the value of the thermal conductivity, k, is no longer stuck on the fitting bounds. These results are shown graphically in Figure 7-4 (a) where it can be seen that all groupings of experiments predict similar results. It can also be seen that there is reasonable agreement with the experimentally measured critical ambient temperatures, under predicting these values by approximately 1°C for a 50mm basket and 2.5°C for a 60mm basket.

The confidence intervals of this case, where C_p was fixed, are similar to those where no parameters were fixed. This is different to the results of Micronized Formulation 1, where not fixing C_p produced much larger confidence intervals. For this formulations, there was not the same degree of difficulty in fitting when C_p was not fixed. It can also be seen that there is a slight correlation between grouping size and fitting error for this formulation. Fitting error is seen to decreases slightly with an increase in grouping size.

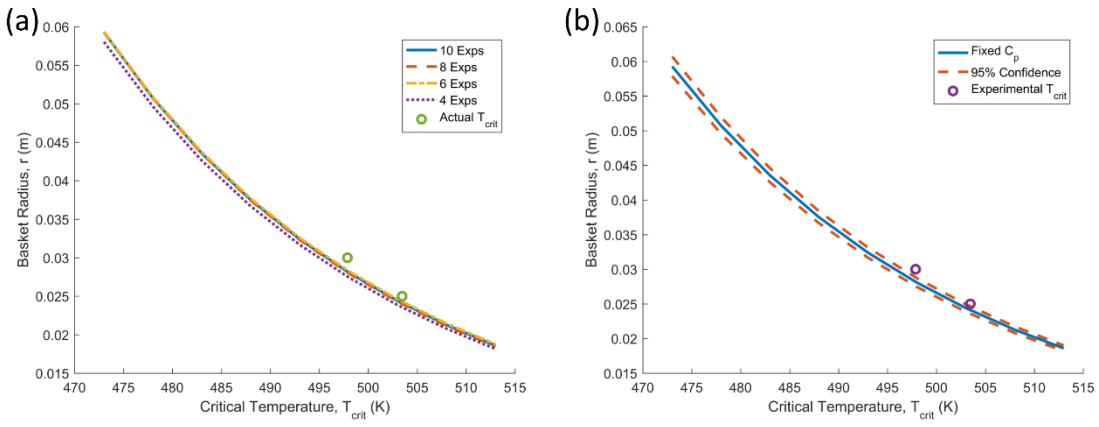

Figure 7-4: (a) Predicted critical ambient temperatures for equi-cylindrical baskets of different radii using the estimated parameters from Table 7-4. (b) Predicted critical ambient temperatures and 95% confidence intervals for the 10 experiments grouping.

For each of the different groupings, the experiments that were not used as part of the parameter estimation fitting were used for validation of the estimated parameters. The Root Mean Square Error (RMSE) and R^2 values were calculated for the validation of each of the groupings of experiments. It can be seen that error is similar across all groupings of experiments, with no single grouping having particularly high errors. All RMSE values

are within 1°C, which is acceptably small. The high R^2 values, all in excess of 0.997, also indicate a good model fit.

Table 7-4: Results of the fittings where the specific heat capacity was fixed.

	E (J mol^{-1})	$\ln QA$	k (W m^{-1} K^{-1})	C_p (J kg^{-1} K^{-1})
10 exps	125.2 (±0.2) x10^3	32.00 (±0.05)	0.0598 (±4x10^{-5})	1298*
8 exps (1)	125.9(±0.2) x10^3	32.15 (±0.05)	0.0598 (±4x10^{-5})	1298*
8 exps (2)	126.7 (±0.2) x10^3	32.34 (±0.05)	0.0598 (±5x10^{-5})	1298*
6 exps	124.4 (±0.3) x10^3	31.80 (±0.06)	0.0598 (±5x10^{-5})	1298*
4 exps	125.5 (±0.3) x10^3	32.06 (±0.07)	0.0599 (±6x10^{-5})	1298*
				* Fixed in fitting

Table 7-5: Root Mean Square Root (RMSE) and R^2 values for the fit of the model to the data from the three thermocouples, for each grouping of experiments.

	RMSE (R^2) of T_{0mm}	RMSE (R^2) of T_{6mm}	RMSE (R^2) of T_{12mm}
8 exps (1)	0.69°C (0.998)	0.93°C (0.997)	0.57°C (0.998)
8 exps (2)	0.56°C (0.999)	0.55°C (0.999)	0.53°C (0.998)
6 exps	0.68°C (0.999)	0.67°C (0.998)	0.60°C (0.998)
4 exps	0.78°C (0.998)	0.91°C (0.997)	0.61°C (0.998)

7.2.1.5. Results Comparison with other Characterisation Methods

The kinetics as measured using the parameter estimation approach, steady-state method, and cross-point temperature method are compared in Table 7-6. The parameter estimation approach results are taken from the groupings of 10 experiments. The steady-state method results are based on only two measured basket critical ambient temperatures, and as such the fitting error could not be calculated. The 95% confidence intervals of the parameter estimation approach are considerably smaller than those of the CPT method. These experiments are compared graphically in terms of predicted critical ambient temperatures in Figure 7-5.

The parameter estimation approach results are similar to the steady-state method results, under predicting the critical ambient temperatures by between 2 and 3°C. The

same experiments were used to calculate the CPT method results and for fitting to in the parameter estimation approach, however, the CPT method results predict very different results. The again shows that the cross-point temperature method is more susceptible to errors in thermocouple placement and readings than the parameter estimation approach.

Table 7-6: Results from the parameter estimation approach compared with the results from the existing basket methods.

		E (J mol^{-1})	$\ln QA$	$ln\frac{QA}{C_p}$	k (W m^{-1} K^{-1})	C_p (J kg^{-1} K^{-1})
Parameter Estimation Approach	**All Free**	128.0 (±0.1) x10^3	32.28 (±0.04)	-	0.04 (±0.005)**	874.2 (±105)
	Fixed C_p	125.2 (±0.2) x10^3	32.00 (±0.05)	-	0.0598 (±4x10^{-5})	1298*
Steady-State Method		134.3x10^3	33.99	-	-	-
CPT Method		111.2 (±11.8) x10^3	-	21.73 (±2.84)	-	-

** Stuck on fitting bound * Fixed in fitting

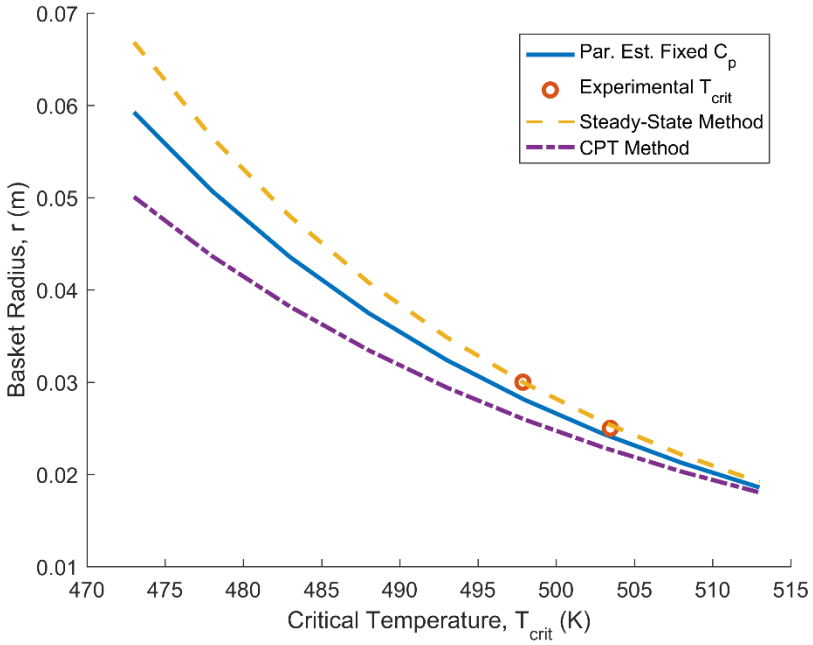

Figure 7-5: Predicted critical ambient temperatures for equi-cylindrical baskets of different radii as calculated using kinetics from the steady-state method, cross-point temperature method, and the parameter estimation approach.

7.2.2. Parameter Estimation Results for Formulation 2

7.2.2.1. Specific Heat Capacity as Measured using DSC

The specific heat capacity of the Formulation 2 was measured using the same approach outlined in Section 6.9. This was done for four different size ranges of particles, 150 to 250µm, 250 to 355µm, 355 to 425µm, and 425µm to 600µm. From the measured heat flow output, the non-reversing $C_p$value was calculated. This can be seen in Figure 7-6 along with the modulated temperature input of the DSC.

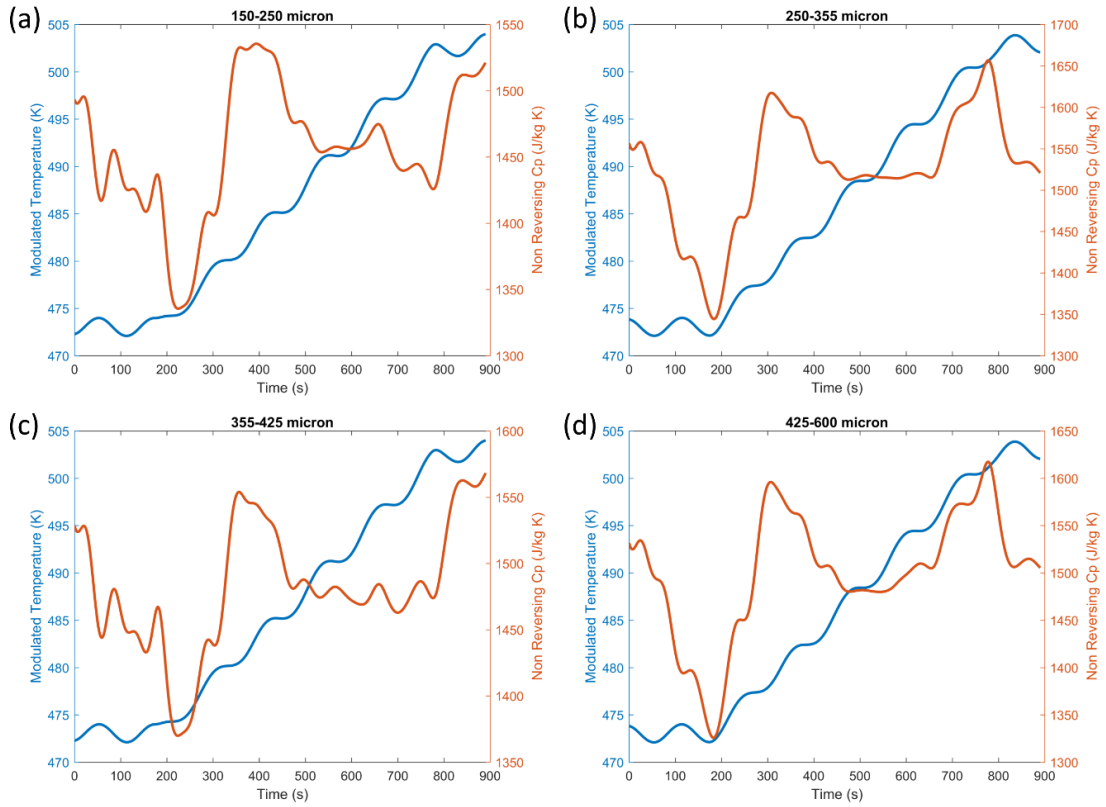

Figure 7-6: Measured non-reversing C_p and modulated DSC input temperature for particles of size ranges (a) 150-250µm, (b) 250-355µm, (c) 355-425µm, and (d) 425-600µm.

Again, it can be seen that C_p is not constant throughout the experiment. The weighted average C_p profile is also shown. The most stable region of the profile for all three size ranges is between 486K and 496K, and it was from this region that the value of C_p was chosen. Figure 7-7 shows the C_p profiles for this temperature range. The C_p used in the

fitting was calculated as the overall average value of the weighted profile in this temperature range, and has a value of 1499 J kg^{-1} K^{-1}.

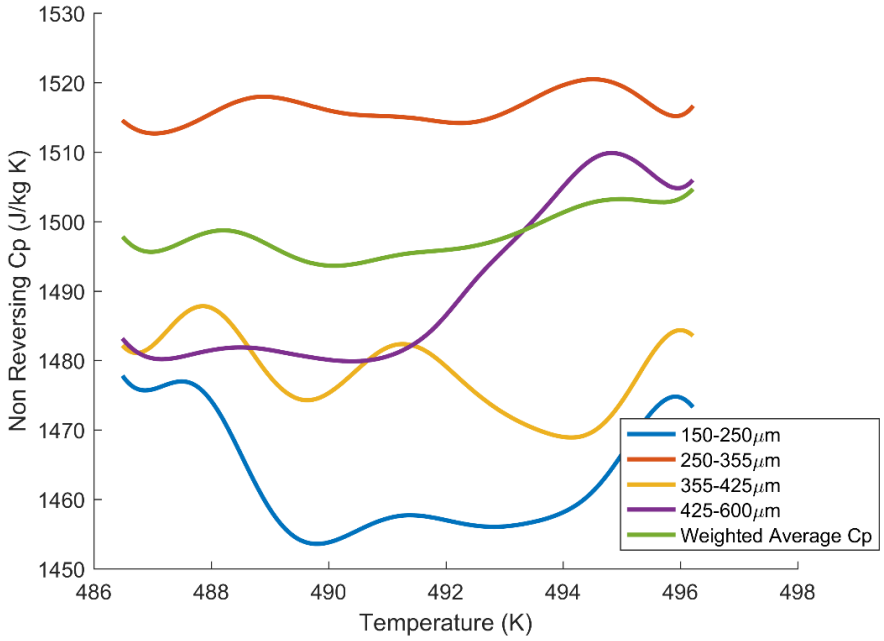

Figure 7-7: Measured non-reversing C_p for samples of four different particle size ranges for the most stable region from which the value used in the fittings was chosen.

7.2.2.2. Choice of Experiments for Parameter Estimation

The Parameter Estimation Approach was performed as outlined previously. Basket experiments were run at 13 different oven controlled ambient temperatures from 222°C (495K) to 234°C (507K). An array of three thermocouples was embedded within the powder. These experiments were filtered based on the residual term of the maximum likelihood method objective function. This residual term should be an indication of poor thermocouple placement. The value of the residual term for each experiment can be seen in Table 7-13. For this formulation, the experiments run at 225°C (498K), 231°C (504K), and 233°C (506K) were omitted, and groupings of 10, 8, 6, and 4 experiments used in the fittings.

Table 7-7: Contribution of the residual term to the maximum likelihood function for each of the 13 experiments when fitted simultaneously.

Experiment Ambient Temperature	Maximum Likelihood Residual Term
222°C	1352.9
223°C	2127.7
224°C	1177.1
225°C	53121.7
226°C	456.2
227°C	1239.3
228°C	1277.8
229°C	4845.4
230°C	2325.2
231°C	15059.7
232°C	1687.8
233°C	17552.5
234°C	2383.6

7.2.2.3. No Fixed Parameters in the Parameter Estimation

The same issue as with the other formulations arose in fitting to these experiments with all four parameters free in the fitting, whereby the thermal conductivity became stuck on the lower fitting bound. The results of these fittings can be seen in Table 7-2.

Table 7-8: Results of the fittings where no parameter were fixed.

	E (J mol^{-1})	$\ln QA$	k (W m^{-1} K^{-1})	C_p (J kg^{-1} K^{-1})
10 exps	129.5 (±0.3) x10^3	32.69 (±0.06)	0.0677 (±0.001)	1386.8 (±22)
8 exps (1)	130.2 (±0.3) x10^3	32.83 (±0.06)	0.0660 (±0.001)	1358.2 (±26)
8 exps (2)	124.7 (±0.3) x10^3	31.64 (±0.05)	0.0749 (±0.001)	1542.4 (±23)
6 exps	130.1 (±0.3) x10^3	32.35 (±0.06)	0.04 (±0.001)**	849.8 (±28)
4 exps	126.7 (±0.5) x10^3	32.57 (±0.11)	0.1252 (±0.002)	2421.1 (±33)
				** Stuck on fitting bound

Again, the correlation matrix in Table 7-15 shows the thermal conductivity, k, and specific heat capacity, C_p, to be entirely correlated. There is also a high correlation between the activation energy, E, and the logarithmic term, $\ln QA$, of 0.97, but this does no inhibit the parameter estimation's fitting of these two parameters.

Table 7-9: Correlation matrix of fitted parameters. A value close to 1 indicates a very high correlation between the two parameters.

	E	$\ln QA$	k	C_p
E	1	-	-	-
$\ln QA$	0.97*	1	-	-
k	-0.503	-0.28	1	-
C_p	-0.52	-0.298	0.999	1

7.2.2.4. Specific Heat Capacity, C_p, Fixed in the Parameter Estimation

Because of this correlation, the value of the specific heat capacity was fixed to the value of 1499 J kg^{-1} K^{-1} determined using modulated DSC. The results of this parameter estimation are shown in Table 7-16. It can be seen that by fixing C_p, the value of the thermal conductivity, k, is no longer stuck on the fitting bounds. These results are shown graphically in Figure 7-12. It can be seen that the parameter estimation approach over predicts the critical ambient temperatures, relative to the experimentally measured values, by approximately 4°C.

Table 7-10: Results of the fittings where the specific heat capacity was fixed.

	E (J mol^{-1})	$\ln QA$	k (W m^{-1} K^{-1})	C_p (J kg^{-1} K^{-1})
10 exps	128.8 (±0.2) x10^3	32.59 (±0.05)	0.0734 (±4x10^{-5})	1499*
8 exps (1)	129.1 (±0.3) x10^3	32.67 (±0.06)	0.0731 (±5x10^{-5})	1499*
8 exps (2)	125.0 (±0.2) x10^3	31.70 (±0.05)	0.0728 (±4x10^{-5})	1499*
6 exps	125.8 (±0.2) x10^3	31.89 (±0.06)	0.0717 (±5x10^{-5})	1499*
4 exps	132.6 (±0.5) x10^3	33.50 (±0.11)	0.0757 (±6x10^{-5})	1499*
* Fixed in fitting				

The confidence intervals of this case, where C_p was fixed, are similar to those where no parameters were fixed. For this formulation there is no clear correlation between grouping size and fitting error.

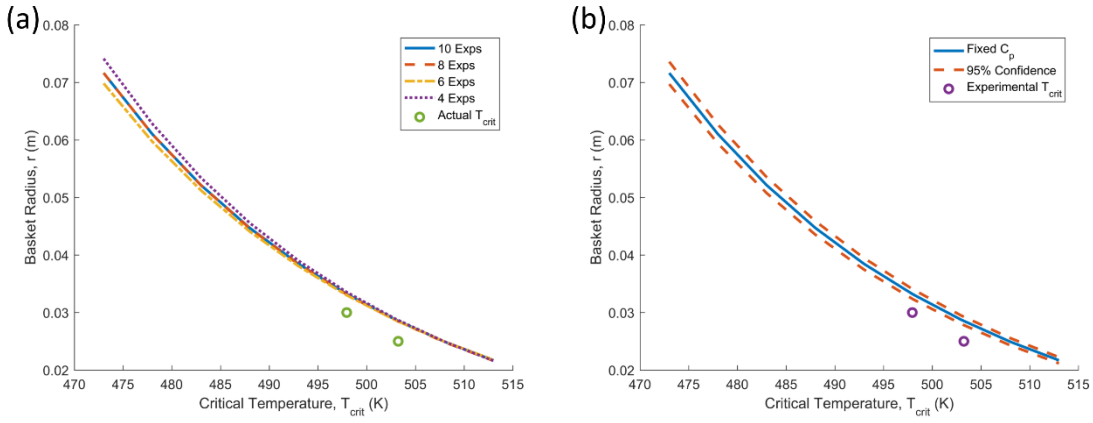

Figure 7-8: (a) Predicted critical ambient temperatures for equi-cylindrical baskets of different radii using the estimated parameters from Table 7-4. (b) Predicted critical ambient temperatures and 95% confidence intervals for the 10 experiments grouping.

For each of the different groupings, the experiments that were not used as part of the parameter estimation fitting were used for validation of the estimated parameters. The Root Mean Square Error (RMSE) and R^2 values were calculated for the validation of each of the groupings of experiments. It can be seen that error is similar across all groupings of experiments, although the grouping of 8 experiments (2) has a slightly higher error, particularly relative to the other grouping of 8 experiments. All RMSE values are within 1.1°C, which is acceptably small. The high R^2 values, all in excess of 0.995, also indicate a good model fit, although not as high as the previous two formulations.

Table 7-11: Root Mean Square Root (RMSE) and R^2 values for the fit of the model to the data from the three thermocouples, for each grouping of experiments.

	RMSE (R^2) of T_{0mm}	**RMSE (R^2) of T_{6mm}**	**RMSE (R^2) of T_{12mm}**
8 exps (1)	0.52°C (0.999)	0.65°C (0.998)	0.39°C (0.999)
8 exps (2)	1.04°C (0.996)	1.01°C (0.995)	0.87°C (0.995)
6 exps	0.93°C (0.997)	0.91°C (0.996)	0.73°C (0.997)
4 exps	0.93°C (0.997)	0.91°C (0.996)	0.58°C (0.998)

7.2.2.5. Results Comparison with Other Characterisation Methods

The kinetics as measured using the parameter estimation approach, steady-state method, and cross-point temperature method are compared in Table 7-18. The parameter estimation approach results are taken from the groupings of 10 experiments. The steady-state method results are based on only two measured basket critical ambient temperatures, and as such the fitting error could not be calculated. The 95% confidence intervals of the parameter estimation approach are considerably smaller than those of the CPT method. These experiments are compared graphically in terms of predicted critical ambient temperatures in Figure 7-13.

Table 7-12: Results from the Parameter Estimation Approach compared with the results from the existing basket methods.

		E (J mol^{-1})	$\ln QA$	$ln\frac{QA}{C_p}$	k (W m^{-1} K^{-1})	C_p (J kg^{-1} K^{-1})
Parameter Estimation Approach	**All Free**	129.5 (±0.3) x10^3	32.69 (±0.06)	-	0.0677 (±0.001)	1386.8 (±22)
	Fixed C_p	128.8 (±0.2) x10^3	32.59 (±0.05)	-	0.0734 (±4x10^{-5})	1499.44*
Steady-State Method		142.3x10^3	35.96	-	-	-
CPT Method		149.2 (±30.7) x10^3	-	30.32 (±7.32)	-	-
* Fixed in fitting						

Interestingly, the CPT and steady-state method for this formulation predict similar critical ambient temperatures, unlike any of the other formulations. However, the very high 95% confidence intervals of the CPT method indicate that this agreement may not be as good as it appears. The parameter estimation approach results are somewhat similar to the steady-state method results, but over predict the critical ambient temperatures at low radii by approximately 5°C.

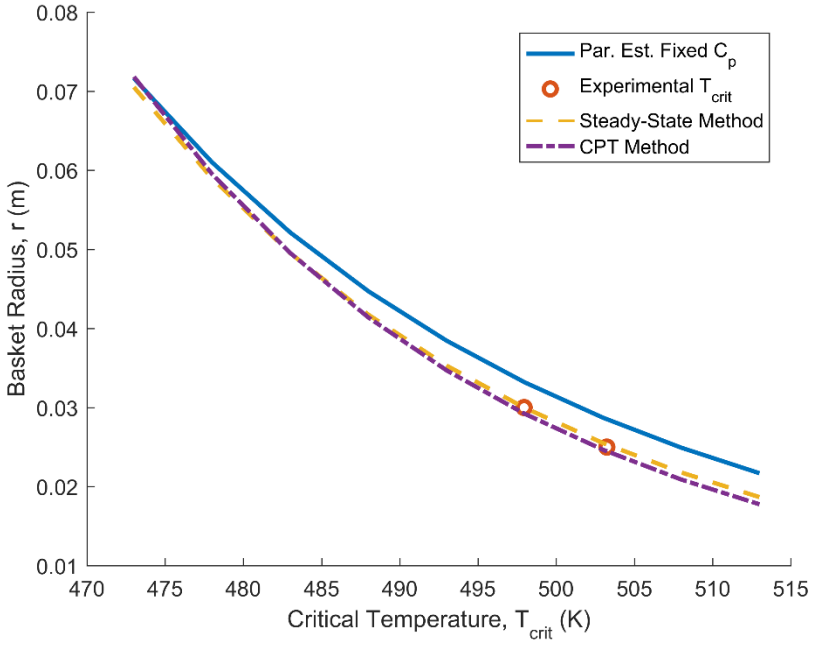

Figure 7-9: Predicted critical ambient temperatures for equi-cylindrical baskets of different radii as calculated using kinetics from the steady-state method, cross-point temperature method, and the parameter estimation approach.

7.2.3. Parameter Estimation Results for Formulation 3

7.2.3.1. Specific Heat Capacity as Measured using DSC

The specific heat capacity of the Formulation 3 was measured using the same approach outlined in Section 6.9. This was done for four different size ranges of particles, 150 to 250µm, 250 to 355µm, 355 to 425µm, and 425µm to 600µm. From the measured heat flow output the non-reversing $C_p$value was calculated. This can be seen in Figure 7-10 along with the modulated temperature input of the DSC.

It can be seen that C_p is not constant throughout the experiment. This may be due to the modulation period used. The weighted average C_p profile shown was calculated as the average C_p as a function of temperature, weighted by each size ranges percentage contribution by mass to the overall powder size distribution. The most stable region of the profile for all three size ranges is between 486K and 496K, and it was from this region that the value of C_p to be used in the parameter estimation fittings was chosen. Figure 7-11 shows the C_p profiles for this temperature range. The C_p used in the fitting was

calculated as the overall average value of the weighted profile in this temperature range, and has a value of 1428 J kg^{-1} K^{-1}.

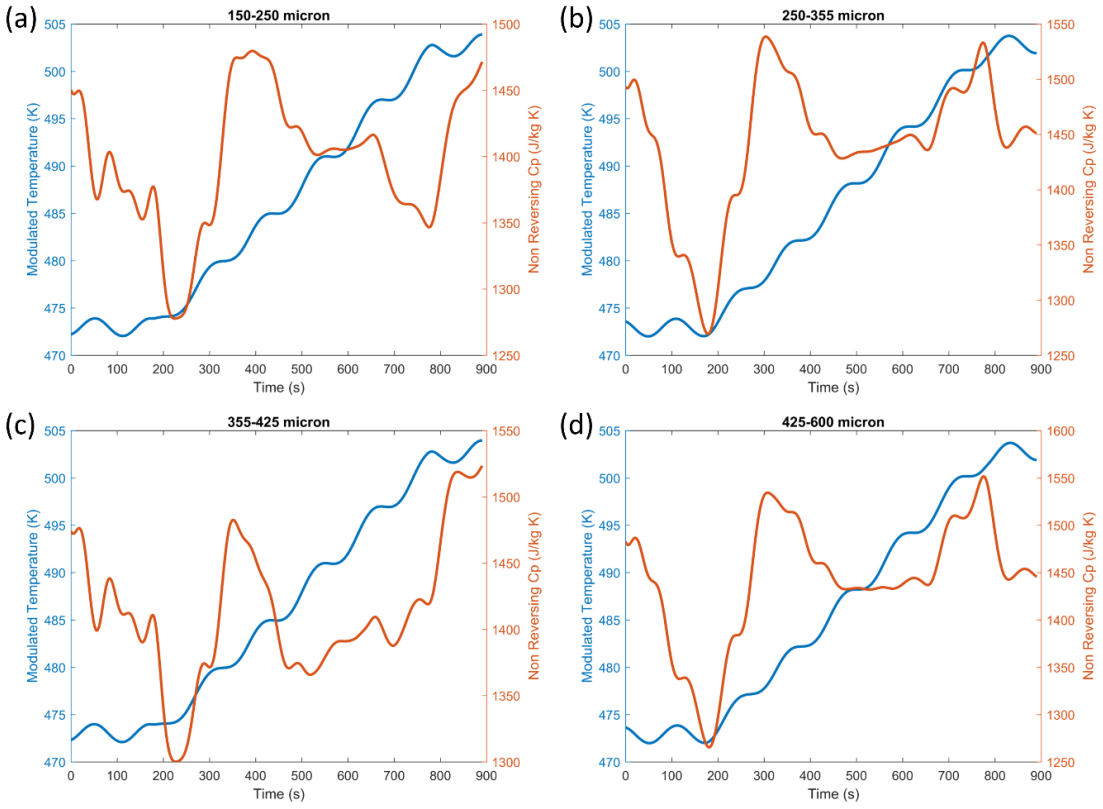

Figure 7-10: Measured non-reversing C_p and modulated DSC input temperature for particles of size ranges (a) 150-250µm, (b) 250-355µm, (c) 355-425µm, and (d) 425-600µm.

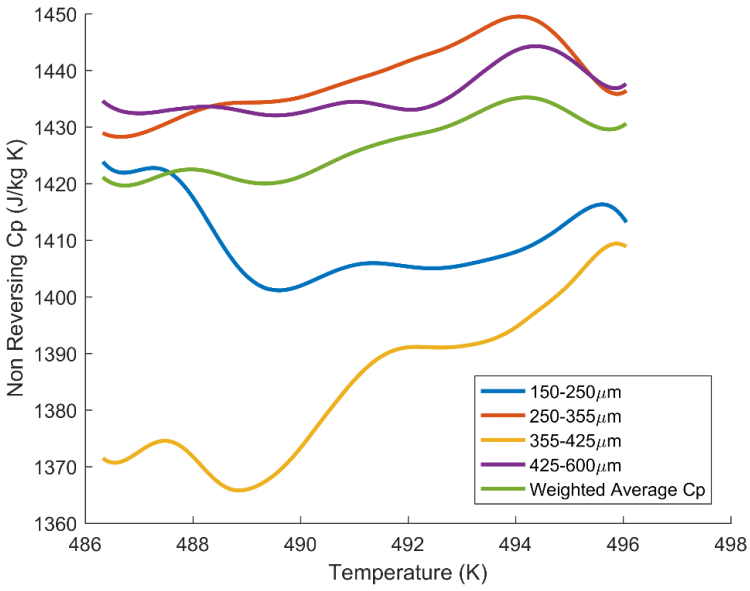

Figure 7-11: Measured non-reversing C_p for samples of four different particle size ranges for the most stable region from which the value used in the fittings was chosen.

7.2.3.2. Choice of Experiments for Parameter Estimation

The parameter estimation approach was performed as outlined previously. Basket experiments were run at 13 different oven controlled ambient temperatures from 216°C (489K) to 228°C (501K). An array of three thermocouples was embedded within the powder. These experiments were filtered based on the residual term of the maximum likelihood method objective function. This residual term should be an indication of poor thermocouple placement. The value of the residual term for each experiment can be seen in Table 7-13. The experiments run at 224°C (497K), 225°C (498K), and 228°C (501K) were omitted, and groupings of 10, 8, 6, and 4 experiments used in the fittings.

Table 7-13: Contribution of the residual term to the maximum likelihood function for each of the 13 experiments when fitted simultaneously.

Experiment Ambient Temperature	Maximum Likelihood Residual Term
216°C	4154.2
217°C	2414.0
218°C	2849.4
219°C	2140.7
220°C	9146.3
221°C	2769.6
222°C	5781.3
223°C	2073.7
224°C	14987.0
225°C	36341.9
226°C	2178.2
227°C	2872.9
228°C	25783.6

7.2.3.3. No Fixed Parameters in the Parameter Estimation

The same issue as with the other formulations arose in fitting to these experiments with no parameters fixed in the fittings, whereby the thermal conductivity became stuck on the lower fitting bound. The results of these fittings can be seen in Table 7-2.

Table 7-14: Results of the fittings where all parameter were left free.

	$\boldsymbol{E}$ (J mol^{-1})	$\boldsymbol{\ln QA}$	$\boldsymbol{k}$ (W m^{-1} K^{-1})	$\boldsymbol{C_p}$ (J kg^{-1} K^{-1})
10 exps	129.6 (±0.1) x10^3	32.65 (±0.03)	0.0412 (±6x10^{-4})	828.3 (±11)
8 exps (1)	131.6 (±0.1) x10^3	33.12 (±0.03)	0.04 (±8x10^{-4})**	805.3 (±12)
8 exps (2)	128.8 (±0.1) x10^3	32.45 (±0.03)	0.0401 (±8x10^{-4})	811.4 (±12)
6 exps	129.4 (±0.2) x10^3	32.59 (±0.04)	0.0402 (±9x10^{-4})	814.4 (±14)
4 exps	132.5 (±0.2) x10^3	33.59 (±0.05)	0.0522 (±8x10^{-4})	1023.4 (±15)
** Stuck on fitting bound				

Again, the correlation matrix in Table 7-15 shows the thermal conductivity, k, and specific heat capacity, C_p, to be entirely correlated. Again there is a high correlation between the activation energy, E, and the logarithmic term, $\ln QA$, of 0.916, but this does no inhibit the parameter estimation's fitting of these two parameters.

Table 7-15: Correlation matrix of fitted parameters. A value close to 1 indicates a very high correlation between the two parameters.

	$\boldsymbol{E}$	$\boldsymbol{\ln QA}$	$\boldsymbol{k}$	$\boldsymbol{C_p}$
$\boldsymbol{E}$	1	-	-	-
$\boldsymbol{\ln QA}$	0.916	1	-	-
$\boldsymbol{k}$	-0.264	0.144	1	-
$\boldsymbol{C_p}$	-0.275	0.133	1	1

7.2.3.4. Specific Heat Capacity, C_p, Fixed in the Parameter Estimation

Because of this correlation, the value of the specific heat capacity was fixed to the value of 1428 J kg^{-1} K^{-1} determined using modulated DSC. The results of this parameter estimation are shown in Table 7-16. It can be seen that by fixing C_p, the value of the thermal conductivity, k, is no longer stuck on the fitting bounds. These results are shown graphically in Figure 7-12 and it can be seen that they agree very well with the experimentally measured critical ambient temperatures, over predicting them by approximately 1°C.

Table 7-16: Results of the fittings where the specific heat capacity was fixed.

	E (J mol^{-1})	$\ln QA$	k (W m^{-1} K^{-1})	C_p (J kg^{-1} K^{-1})
10 exps	127.5 (±0.1) x10^3	32.69 (±0.03)	0.0728 (±2x10^{-5})	1428*
8 exps (1)	129.8 (±0.1) x10^3	33.23 (±0.04)	0.0728 (±3x10^{-5})	1428*
8 exps (2)	127.1 (±0.1) x10^3	32.59 (±0.03)	0.0723 (±2x10^{-5})	1428*
6 exps	127.7 (±0.2) x10^3	32.72 (±0.04)	0.0722 (±3x10^{-5})	1428*
4 exps	131.0 (±0.2) x10^3	33.55 (±0.05)	0.0741 (±3x10^{-5})	1428*
				* Fixed in fitting

The confidence intervals of this case, where C_p was fixed, are similar to those where no parameters were fixed. For this formulation there is no clear correlation between grouping size and fitting error.

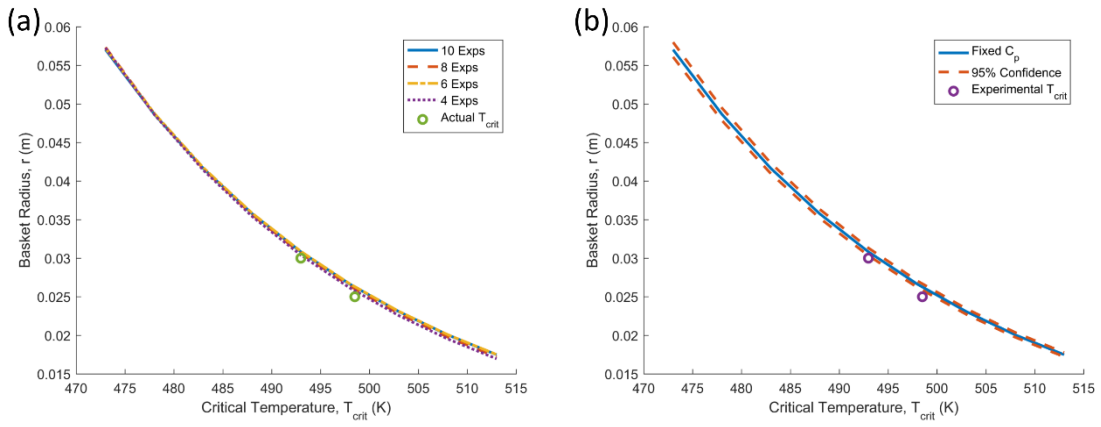

Figure 7-12: (a) Predicted critical ambient temperatures for equi-cylindrical baskets of different radii using the estimated parameters from Table 7-4. (b) Predicted critical ambient temperatures and 95% confidence intervals for the 10 experiments grouping.

For each of the different groupings, the experiments that were not used as part of the parameter estimation fitting were used for validation of the estimated parameters. The Root Mean Square Error (RMSE) and R^2 values were calculated for the validation of each of the groupings of experiments. It can be seen that error is similar across all groupings of experiments, with no single grouping being particularly poor. All RMSE values are within 0.7°C, which is acceptably small. The high R^2 values, all in excess of 0.999, also indicate a good model fit.

Table 7-17: Root Mean Square Root (RMSE) and R^2 values for the fit of the model to the data from the three thermocouples, for each grouping of experiments.

	RMSE (R^2) of T_{0mm}	**RMSE (R^2) of T_{6mm}**	**RMSE (R^2) of T_{12mm}**
8 exps (1)	0.39°C (0.999)	0.31°C (1.000)	0.32°C (0.999)
8 exps (2)	0.53°C (0.999)	0.56°C (0.999)	0.48°C (0.999)
6 exps	0.49°C (0.999)	0.57°C (0.999)	0.38°C (0.999)
4 exps	0.61°C (0.999)	0.49°C (0.999)	0.43°C (0.999)

7.2.3.5. Results Comparison with other Characterisation Methods

The kinetics as measured using the parameter estimation approach, steady-state method, and cross-point temperature method are compared in Table 7-18. The parameter estimation approach results are taken from the groupings of 10 experiments. The steady-state method results are based on only two measured basket critical ambient temperatures, and as such the fitting error could not be calculated. The 95% confidence intervals of the Parameter Estimation Approach are considerably smaller than those of the CPT method. These experiments are compared graphically in terms of predicted critical ambient temperatures in Figure 7-13.

Table 7-18: Results from the Parameter Estimation Approach compared with the results from the existing basket methods.

		E (J mol^{-1})	$\ln QA$	$ln\frac{QA}{C_p}$	k (W m^{-1} K^{-1})	C_p (J kg^{-1} K^{-1})
Parameter Estimation Approach	**All Free**	129.6 (±0.1) x10^3	32.65 (±0.03)	-	0.0412 (±6x10^{-4})	828.3 (±11)
	Fixed C_p	127.5 (±0.1) x10^3	32.69 (±0.03)	-	0.0728 (±2x10^{-5})	1427.87*
Steady-State Method		134.1x10^3	34.30	-	-	-
CPT Method		111.3 (±12.2) x10^3	-	21.69 (±2.94)	-	-
* Fixed in fitting						

The parameter estimation approach results are very similar to the steady-state method results, only slightly over predicting the critical ambient temperatures at very low radii. The same experiments were used to calculate the CPT method results and for fitting to in the parameter estimation approach, however, the CPT method results predict different results. Again, this shows that the cross-point temperature method is more susceptible to errors in thermocouple placement and readings than the parameter estimation approach.

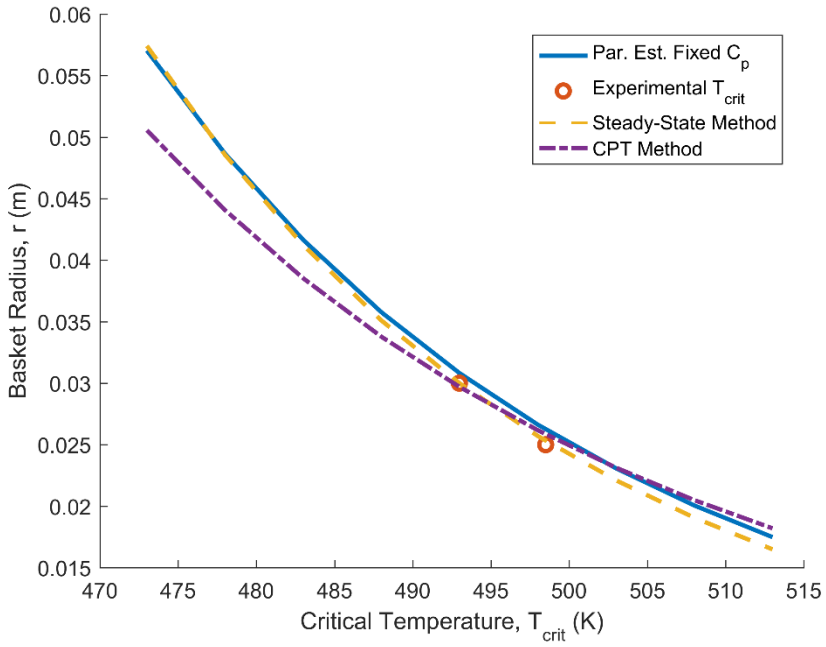

Figure 7-13: Predicted critical ambient temperatures for equi-cylindrical baskets of different radii as calculated using kinetics from the steady-state method, cross-point temperature method, and the parameter estimation approach.

7.3. Conclusions

In this chapter, the parameter estimation approach was used to characterise three more detergent powder formulations. Good results were achieved using this approach. Similar to the characterisation of Micronized Formulation 1 in Section 6.11, there was a very high correlation factor between the specific heat capacity, C_p, and the thermal conductivity, k. With no parameters fixed, k was found to get stuck on the lower fitting bounds. Fixing the value of C_p prevented this from happening. C_p was fixed to a value measuring using Modulated DSC for each formulation. For all formulations, C_p was measured over a range of 200°C (473K) to 230°C (503K), but was not constant across

this entire range. It was though that the modulation size of the heating profile may have been too large. However, a stable sub-region was found for each formulation, and the value taken from this.

For each formulation, all groupings of experiments used in the parameter estimation produced similar results. For Non-Micronized Formulation 1, the predicted critical ambient temperatures were under-predicted by between 2 and 3°C. For Formulation 2, the predicted critical ambient temperatures were similar at high radii, but over-predicted at low radii by approximately 5°C. For Formulation 3, the predicted critical ambient temperatures were over-predicted by approximately 1°C. Overall, the predicted critical ambient temperatures were in reasonable agreement with the experimentally measured values.

These estimated parameters were compared with those measured using the cross-point temperature method, with varying agreement. For all formulations however, the 95% confidence intervals of the estimated parameters using the parameter estimation approach were considerably lower than those of the cross-point temperature method. These methods used the same experiments, and this again shows that the parameter estimation approach is not as susceptible as the cross-point temperature method to errors in thermocouple placement and readings.

By showing that this approach works for a further three formulations, the results of this chapter help to validate the parameter estimation approach as a faster, less error-prone method for characterising the self-heating behaviour of detergent powders.

8. Modelling of Self-Heating in Spray Drying Towers

The primary focus of this research was to explore the means of characterising and predicting self-heating in spray dried detergent formulations. In doing so, the work was focused on oven based basket heating methods for estimating the self-heating reaction kinetics of the detergent powder, and on modelling these basket experiments such that predictions at this scale could be validated.

The original motivation for this research was the desire to develop a methodology for characterising and predicting the self-heating behaviour of detergent formulations. This would allow predictions of self-heating in spray-dryer wall deposits to be made such that the problem of charring, known to occur in these deposits, can be prevented. Future work will see Procter and Gamble apply the knowledge, methods, and models developed here to address this problem in spray drying operations. An approach similar to that outlined here is to be used which will apply the developed model in conjunction with other spray drying models. Having characterised the formulations using the parameter estimation approach, a simple 1D model of heat transfer in an finite slab would allow for a quick assessment as to whether the operating conditions at the time are likely to cause significant self-heating, and possible charring in the wall deposits. A brief example of how this may work is discussed.

8.1. Application of Models to Spray Drying Tower Wall Build-Up

Figure 8-1 shows a graphical representation of a counter current spray drying tower, the kind used to spray dry detergent powders. The regions in yellow are representative of build-up that may occur on the tower wall, although the exact regions may vary. It is thought that the tower could be broken down into regions that are at risk of self-heating. One region particularly at risk is the region close to the air inlets where the temperatures are the highest. For each of these regions four things need to be known to evaluate whether self-heating is a risk under specific operating conditions:

- Detergent powder parameters that influence self-heating, such as the reaction kinetics, density, and thermal conductivity. These can be determined using the parameter estimation approach.

- The build-up thickness. This can either be measured or estimated as a typical or maximum thickness.
- Temperature above the build-up surface.
- Heat transfer coefficient for the heat transfer between the build-up and circulating tower air.

Using CFD models of these counter current spray drying towers that have previously been developed, for a specific tower inlet temperature it would be relatively simple to determine the temperature above the build-up surface in different regions. Using correlations for the Nusselt number ($Nu = hL/k$), where the Nusselt number is correlated as a function of the Reynolds number ($Re = \rho Lu/\mu$, where u is the air velocity and μ is the dynamic viscosity) and Prandtl number ($Pr = \mu C_p/k$), it is also possible to determine the heat transfer coefficient for different regions of the tower.

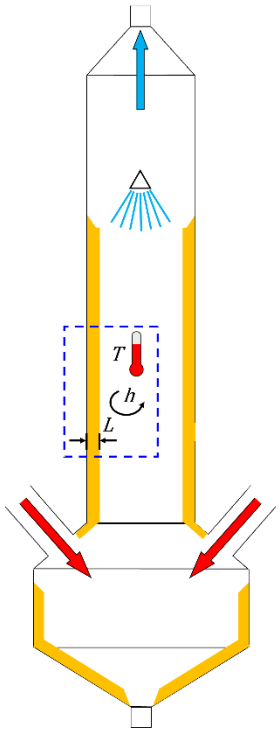

Figure 8-1: Graphical representation of a counter-current spray drying tower with representative build-up shown in yellow. The box represents an example region at risk of self-heating being assessed.

With these parameters known, a simple 1D model of self-heating in an infinite slab can be used to assess the risk of self-heating in each region of the tower. The 1D model consists of the following energy balance, previously used in the models of Chapter 4:

$$\rho C_p \frac{\partial T}{\partial t} = k \frac{\partial^2 T}{\partial x^2} + \rho Q A e^{\frac{-E}{RT}} \quad (8\text{-}1)$$

If it is assumed that the tower walls are perfect insulated, then the following boundary condition applies at the wall:

$$\left.\frac{dT}{dx}\right|_{x=0} = 0, \quad (8\text{-}2)$$

This boundary condition can be replaced with equations denoting conduction through a composite layer wall of the wall and insulation, if it is not reasonable to apply the assumption that the wall is a perfect insulator. At the exposed boundaries Newton's Law of Cooling is applied, whereby heat transfer is dependent on the external effective heat transfer coefficient, h (W m^{-2} K^{-1}), such that:

$$-k \left.\frac{dT}{dx}\right|_{x=L} = h(T|_{x=L} - T_\infty), \quad (8\text{-}3)$$

8.2. Prediction of Self-Heating in Spray Drying Towers

This simple model was applied to show how the temperature above the powder build-up, T_∞, the heat transfer coefficient, h, and the build-up thickness, L, affect the self-heating in these build-ups. For each case the model was run until a steady-state was reached. Figure 8-2 shows how the temperature above the build-up influences the self-heating. At a temperature of 460K (187°C), little self-heating is predicted, with a temperature rise of less than 3°C at the wall. For a temperature of 475K (202°C), significantly more self-heating is predicted, with a temperature rise of more than 15°C at the wall. Thermal runaway was predicted to occur at a temperature of 476K (203°C).

Figure 8-3 shows how the heat transfer coefficient influences the self-heating. Little difference is seen between the predicted temperatures at the wall for each value of h used. The difference primarily comes from the temperature at the build-up surface. For higher heat transfer coefficients the temperature at the build-up surface is closer to the temperature of the air above the surface.

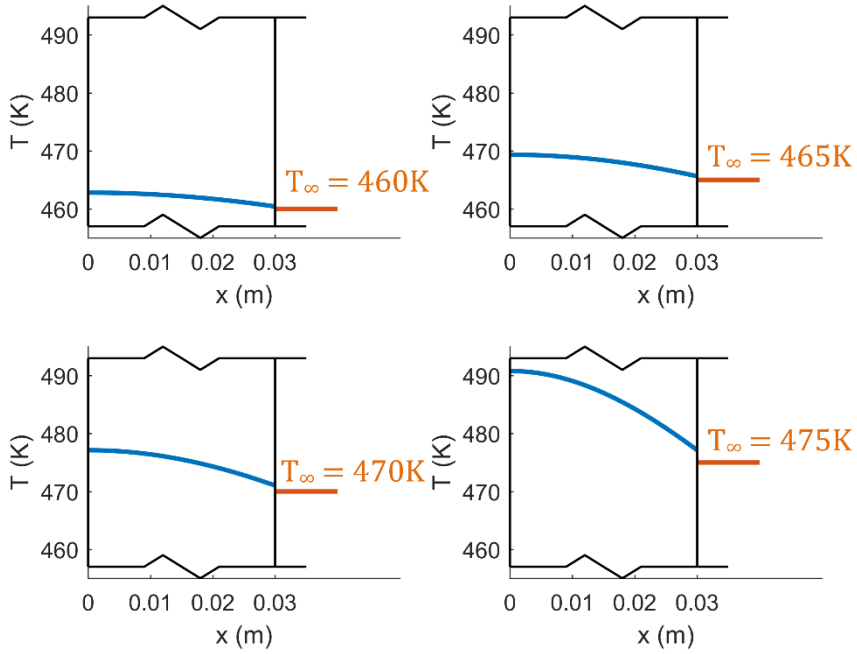

Figure 8-2: Temperature profile across the build-up for ambient temperatures of (a) 460K (187°C), (b) 465K (192°C), (c) 470K (197°C), and (d) 475K (202°C).

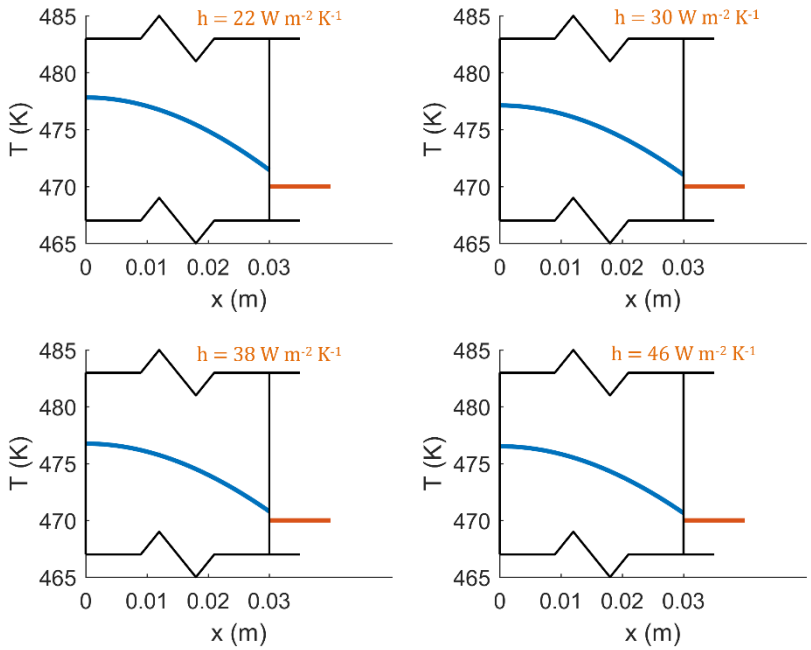

Figure 8-3: Temperature profile across the build-up for heat transfer coefficients of (a) 22 W m^{-2} K^{-1}, (b) 30 W m^{-2} K^{-1}, (c) 38 W m^{-2} K^{-1}, and (d) 46 W m^{-2} K^{-1}.

Figure 8-4 shows how the build-up thickness influences the predicted self-heating at an ambient temperature of 468K (195°C). As expected, a larger build-up thickness leads to more self-heating because the build-up has greater difficulty dissipating the generated

heat. At a thickness of 0.026m a temperature rise of approximately 4°C occurs at the wall, while for a build-up thickness of 0.038m a much larger temperature rise of approximately 15°C occurs. At this ambient temperature, 0.038m is almost the critical thickness of the build-up.

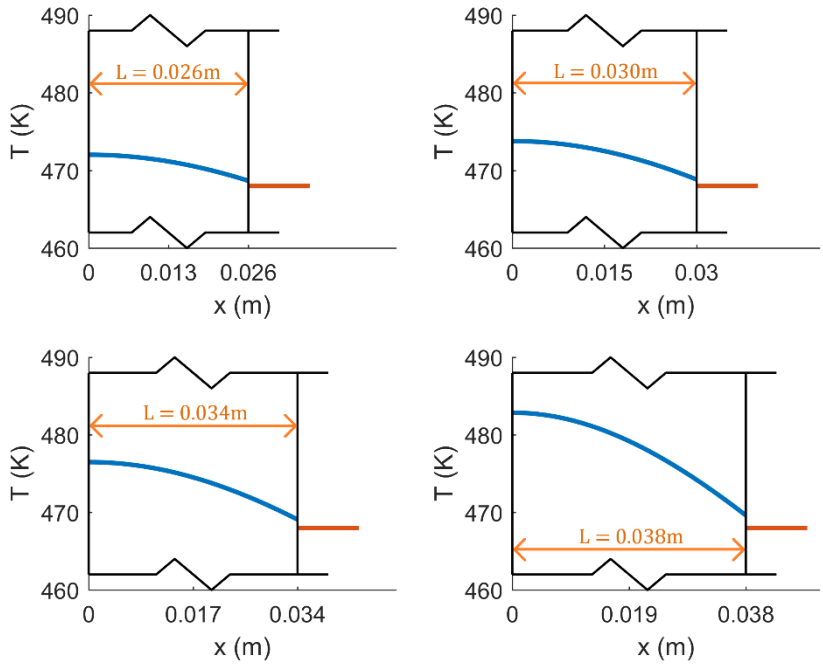

Figure 8-4: Temperature profile across the build-up for thicknesses of (a) 0.026m, (b) 0.030m, (c) 0.034m, and (d) 0.038m.

8.3. Conclusions

This simple model has shown how the knowledge and models developed in this research can be applied to the problem of self-heating in spray drying operations. The parameter estimation approach developed as part of this study can be applied to determine the required parameters of the detergent powder, namely the self-heating reaction kinetics and the thermal conductivity. Existing CFD models can be applied to determine the temperature above the build-up and the heat transfer coefficient. Together these parameters can be used to determine the optimum temperature to prevent significant self-heating for a known build-up thickness. Alternatively this approach can be used to determine the thickness to which the build-up can be allowed to reach at a specified operating temperature before self-heating becomes an issue. In future work the integration of this model with existing spray drying tower models could be explored.

9. Conclusions and Recommended Future Work

9.1. Summary of Research

The aim of this thesis was to explore the problem of self-heating in detergent powders. In doing this, the research was broken down into a number of topics that were explored. Firstly, an evaluation of the self-heating exhibited by a typical detergent powder was performed. Next, a number of experimental methods were used to measure the self-heating reaction kinetics of a typical detergent powder. A numerical model, developed to predict temperature profiles in self-heating powder baskets, was used to evaluate these experimental methods and make predictions of self-heating and thermal runaway. Finally, the numerical model and oven heated basket experiments were combined in a novel parameter estimation approach. This approach was developed, validated, and used as a means of measuring the reaction kinetics and heat transfer properties of four different detergent formulations.

9.2. Self-Heating in Detergents

Initial basket heating experiments were used to evaluate the problem of self-heating in a typical detergent powder. These initial experiments showed the detrimental effects that self-heating can have on detergent formulations. Even if the powder does not lead to complete thermal runaway of the basket, localised thermal runaway at the basket core or at particular points in a layer can be damaging. Even when thermal runaway does not occur, the discolouration or “browning” seen in the sample may be enough to compromise the quality of the finished product.

Initial cross-point temperature method (CPT) experiments showed promise, but also showed there to be a number of issues that needed to be addressed, particularly the issue of thermocouple placement. This issue was addressed in subsequent chapters.

The initial DSC and TGA experiments conducted here showed, at least for Micronized Formulation 1, that variability in reactivity across different size fractions did not exist. The DSC heat flow profile showed the large amount of energy produced by the self-heating reaction and why self-heating can be such an issue. The TGA showed a large

mass loss corresponding to this reaction. These techniques produced repeatable profiles which in later chapters were used to estimate the self-heating reaction kinetics.

Running these experiments under nitrogen, rather than air, showed that these reactions are dependent on oxygen. Without oxygen, the reaction was seen not to occur in the DSC and TGA profiles in the temperature range of interest, confirming that the self-heating reaction in this detergent formulation is an oxidative reaction.

9.3. Experimental Methods for Characterising Self-Heating and Using the Numerical Model to Evaluate these Methods

This aspect of the study sought to determine the best means of estimating the self-heating reaction kinetics of detergent powders. Three methods were used: the steady-state method, the cross-point temperature method, and the DTG curve fitting method.

The first method explored was the steady-state method. This method is based around the critical criterion δ_{cr}. The dimensionless parameter δ is the ratio of the heat generated to the heat dissipated in a self-heating system, and encompasses all the quantities required to describe the problems associated with self-heating, inflammation, and ignition. The critical criterion, δ_{cr}, is a function of the dimensionless exponent, φ ($= E/RT$), and the Biot number, Bi. 1D and 2D dimensionless numerical models were used here to calculate δ_{cr} as a function of φ and Bi. It was shown that using incorrect values for δ_{cr} can impact strongly on the results. The model predictions using these kinetics fitted very well with observed temperature profiles for the majority of the reaction period. The steady-state method however is slow with each test taking between 4 and 8 hours, and a number of tests required to obtain a single data point.

The cross-point temperature method was initially developed as a faster alternative, but it was found that this approach is more susceptible to errors. The estimated kinetics using this approach varied depending on the spacing of the thermocouples used. Using the numerical model to simulate these basket experiments, it could be seen that some variation should exist between the cases for the cross-point approximations used, but the variation should not be to the extent seen here.

Using the model, it was found that using a more accurate finite difference stencil (i.e. 5 point instead of a 3 point stencil) had more of an impact than the inclusion of axial conduction on the cross-point temperature method results. It was shown that a five-point stencil in the radial direction, consisting of three thermocouples, as used here for the case 3 cross-point was sufficient. However, it was shown in the experiments, and in simulating the experiments using the numerical model, that errors in thermocouple readings greatly overshadowed the improvements that accompany this setup.

In the experiments, a relatively large spacing of 12mm was found to give to best results. The kinetics estimated using this spacing predicted thermal runaway for a 60mm equi-cylindrical basket at 223.9°C (497.1K), only 2.6°C greater than the experimentally measured critical ambient temperature of 221.3°C (494.5K). A smaller spacing of 6mm produced more variability and kinetics that significantly over-predicted this temperature at 229.0°C (502.2K). The large discrepancy observed experimentally between the different case kinetics was attributed to a combination of errors in thermocouple placement (±1mm), thermocouple readings (±0.25°C), and the variability caused by the small number of particle diameters that fits in the smaller thermocouple spacing of 6mm.

The numerical model developed as part of this study allowed predictions in temperature profiles and critical ambient temperatures to be made. Having estimated a number of parameters, in particular the drying parameters, and using a zero-order reaction model with the kinetics estimated using the steady-state method, the predictions of this model were found to agree well with the experimentally measured temperature profiles. This agreement was shown for baskets at a range of ambient temperatures.

In this study, n^{th} order kinetics were found using a TGA based method, whereby kinetics were fitted to the normalised mass loss data observed in the sample across the reaction. Applying these kinetics in an n^{th} order model exhibited little self-heating, with critical ambient temperatures over predicted by almost 20°C. The much simpler zero-order model compared considerably better to experimental data. It is also thought that a zero-order model is sufficient when it comes to predicting self-heating in these systems.

9.4. Novel Parameter Estimation Approach

In this investigation a novel methodology, the Parameter Estimation Approach, was developed for characterising the self-heating behaviour of detergent powders. This new approach successfully used a 2D-axisymmetirc heat transfer model to estimate the best fit powder thermal conductivity, k, specific heat capacity, C_p and self-heating reaction kinetics, E and $\ln QA$, from experimentally measured temperature profiles within an oven heated basket of detergent powder. This was done using an equi-cylindrical basket, but with changes to the coordinates system of the model, this could be applied to different basket geometries.

13 experiments were performed, and parameter estimation was performed for groupings of different denominations (10, 8, 6, and 4) of these experiments. Fitting for all four parameters, k, C_p, E, and $\ln QA$ produced similar values for all groupings of experiments, but k was consistently stuck on the lower fitting bound.

The thermal conductivity and the specific heat capacity of the powder are highly correlated through the thermal diffusivity of the powder ($= k/\rho C_p$). Because of this, Modulated DSC was used to determine C_p prior to fitting. Fixing this value in the fitting prevented k from becoming stuck on the parameter estimation fitting bounds, and improved the confidence intervals for the estimated parameters.

The Friedman and Ozawa-Flynn-Wall methods were also used to measure the self-heating reaction activation energy, E, prior to fittings. Fixing the value of E as well as C_p largely reduced the freedom allowed to the fitting, resulting in best fit parameters that did not agree with experimentally measured critical ambient temperatures as well as before. It was decided that the best approach is to only fix the value of C_p in the fittings.

The results of the fittings were validated against basket temperature profiles not used in the fittings. For Micronized Formulation 1, all RMSE values were within 1.2°C, which is small relative to the high temperatures at which these experiments were run, 216°C (489K) to 228°C (501K). All validation fittings also had R^2 values in excess of 0.997, indicating a good model fit. The parameters from each grouping of experiments were used to predict critical ambient temperatures for equi-cylindrical baskets of different radii. When using the approach where only C_p was fixed in the fitting, the parameters

from all groupings predicted very similar critical ambient temperatures and were all in agreement with experimentally measured values.

The Parameter Estimation Approach was also used to characterise three other detergent formulations: Non-Micronized Formulation 1, Formulation 2, and Formulation 3. The same strong correlation between k and C_p was found for each of these formulations, such that k would become stuck on the lower fitting bound when both k and C_p are left free in the fittings. Fixing the value of C_p to values determined using MDSC again vastly improved the fittings. The predicted critical ambient temperatures for a range of basket radii for each formulation, agreed reasonably well with the experimentally measured values. This helped to validate the Parameter Estimation Approach as an alternative to the existing basket heating methods.

This approach was developed to improve upon the existing basket methods, namely the steady-state method and the cross-point temperature method. This approach has been shown to successfully predict critical ambient temperatures for a range of basket sizes while improving massively on the time required by the steady-state method to measure such values. This approach requires no more than 10 experiments, with each taking approximately 2.5 hours to complete.

This approach uses the same basket setup as used for the cross-point temperature method. It was shown that the CPT Method is much more susceptible to errors in thermocouple placement than the Parameter Estimation Approach. It is thought that this is because a considerable portion of the temperature prolife is used for fitting, providing thousands of data points, while the CPT Method yields only one data point per experiment.

This research has proved that the novel parameter estimation approach is a viable, faster, and more accurate alternative to existing basket heating methods. This approach can now be applied to measure the self-heating reaction kinetics of new detergent formulations such that optimum spray dryer operating conditions for limiting the problem of self-heating can be determined.

9.5. Application of Knowledge Gained to Spray Dryer Build-Up

The model and kinetics determined using the methods explored in this study were applied to the problem of predicting self-heating in spray dryer wall deposits. A simple 1D infinite slab model, where one surface is perfectly insulated, and the other subject to Newton's Law of Cooling, was used. This model was used as an example of how this knowledge can be applied to determine the optimum operating conditions of the spray drying tower. The influence of the temperature above the exposed surface, T_∞, the effective heat transfer coefficient, h, and the slab thickness, L, were explored. It is thought that T_∞ and h can be determined from existing CFD models of the spray drying tower, while L can be measured or estimated. These parameters are all found to influence the extent to which the wall build-up self-heats, and this simple analysis shows how the knowledge gained and methods developed here can be used to predict self-heating in spray drying operations.

9.6. Recommended Future Work

There is plenty of scope for future work following this research. With regards the experimental methods explored here, there is scope to improve upon them. The cross-point temperature method in particular, is much faster than the steady-state method, and much simpler than the novel parameter estimation approach to apply, but has been found to be very susceptible to errors. Although improvements were made to thermocouple placement within the powder basket as this investigation progressed, a more accurate placement method is still desired. A means of being able to verify the position of the thermocouples is also desired, and should be explored should the cross-point temperature method be pursued further.

It was concluded that a zero-order reaction model is sufficient for modelling these systems because it is much simpler and fitted well in the regions of interest. However, the n^{th} order reaction model could be explored further. A variation of the DTG fitting method could be applied, whereby a rate constant, fitted at some temperature, is used as a fit parameter instead of the pre-exponential factor. The pre-exponential factor could then be determined from the rate constant afterwards. This approach would be

considerably faster, and would alleviate the issues seen whereby there is difficulty in fitting all three parameters simultaneously.

Using the kinetics determined using the DTG curve fitting approach, this model did not agree very well with the observed behaviour, under predicting the critical ambient temperature by almost 20°C. These kinetics were determined by fitting to the initial portion of the degradation profile because it was assumed that the majority of the observed self-heating was caused by this initial portion of the reaction. However, using the Ozawa-Flynn-Wall and Friedman methods to measure the reaction activation energy, E, the change in E with conversion, α, implied that a multi-step reaction occurs in the sample. Also, the reaction is known to be oxygen dependent, as seen from the lack of an exotherm in the DSC experiments carried out in nitrogen rather than air. Future work could look at incorporating this multi-step reaction and oxygen dependency into the numerical model to provide a better agreement with the observed behaviour.

The novel parameter estimation approach was successfully applied to determine the heat transfer and reaction kinetics of four detergent formulations. The workflow in Chapter 7 showed how this approach could be applied. Future work could see this workflow applied to new formulations. Chapter 8 showed a brief example of how, following this characterisation, the measured parameters could be used in conjunction with a simple 1D model to determine the optimum operating conditions for the spray drying tower for a particular formulation. This was merely a brief example of how this could be applied, and leaves plenty of scope for future work. This approach could be applied to address the problem of self-heating in practice.

The approaches and models developed here could be incorporated with existing models of the spray drying tower, possibly under the gPROMS software platform, to provide a robust solution for the problem of self-heating and charring in spray drying. Having this solution it could be simple for the operators to quickly characterise the detergent formulation using the workflow detailed in Chapter 7, then using the results and this hypothesised model approach they could determine the ideal tower operating conditions or maximum thickness that the wall build-up can be allowed to reach.

10. References

Beever, P. F., 1985. Fire and Explosion Hazards in the Spray Drying of Milk. *Journal of Food Technology,* Volume 20, pp. 637-645.

Beever, P. F. & Crowhurst, D., 1989. Fire and explosion hazards associated with milk spray drying operations. *Journal of the Society of Dairy Technology,* 42(3), pp. 65-70.

Beever, P. F. & Crowhurst, D., 1989. Fire and Explosion Hazards associated with Milk Spray Drying Operations. *Journal of the Society of Dairy Technology,* 42(3), pp. 65-70.

Bird, R. B., Stewart, W. E. & Lightfoot, E. N., 2007. *Transport Phenomena.* 2nd ed. New York: John Wiley and Sons.

Boddington, T., Gray, P. & Harvey, D. I., 1971. Thermal theory of spontaneous ignition: criticality in bodies of arbitrary shape. *Philosophical Transactions of the Royal Society of London,* 270(1207), pp. 467-506.

Bowes, P. C. & Cameron, A., 1971. Self-Heating and Ignition of Chemically Activated Carbon. *Journal of Applied Chemistry and Biotechnology,* Volume 21, pp. 244-250.

Bowes, P. C. & Thomas, P. H., 1966. Ignition and Extinction Phenomena Accompanying Oxygen-Dependent Self-Heating of Porous Bodies. *Combustion and Flame,* 10(3), pp. 221-230.

British Standards Institution, 2007. *BS EN 15188:2007 - Determination of the spontaneous ignition behaviour of dust accumulations,* London: British Standards Institution.

Caballos, D. C. C., Hawboldt, K. & Hellleur, R., 2015. Effect of production conditions on self-heating propensity of terrefied sawmill residues. *Fuel,* Volume 160, pp. 227-237.

Cameron, A. & MacDowall, J. D., 1972. The Self Heating of Commerical Powdered Activated Carbons. *Journal of Applied Chemistry and Biotechnology,* Volume 22, pp. 1007-1018.

Carslaw, H. S. & Jaeger, J. C., 1959. In: *Conduction of Heat in Solids.* Oxford: Oxford University Press, pp. 198-201.

Carson, J. K., Willix, J. & North, M. F., 2006. Measurements of heat transfer coefficients within convective ovens. *Journal of Food Engineering,* Volume 72, pp. 293-301.

Chambré, P. L., 1952. On the Solution of the Poisson-Boltzmann Equation with Application to the Theory of Thermal Explosions. *The Journal of Chemical Physics,* 20(11), pp. 1795-1797.

Chen, X. D., 1994. The Effect of Drying Heat and Moisture Content on the Maximum Temperature Rise During Spontaneous Heating of a Moist Coal Pile. *Coal Preparation,* Volume 14, pp. 223-236.

Chen, X. D., 1997. A New Water Sorption Equilibrium Isotherm Model. *Food Research International,* 30(10), pp. 755-759.

Chen, X. D., 1998. A Temperature Dependence Function of Equilibrium Sorption Isotherms Established by a Reaction Engineering Approach. *Journal of Food Engineering,* Volume 37, pp. 259-269.

Chen, X. D., 1999. On Basket Heating Methods for Obtaining Exothermic Reactivity of Solid Materials: The Extent and Impact of the Departure of the Crossing-Point Temperature from the Oven Temperature. *Trans IChemE,* 77(Part B), pp. 187-192.

Chen, X. D., 2001. Self-Heating Behaviour of Low Moisture Content Particles - Modelling the Basket-Heating of Solid Particles and Some Aspects of the Cross Over Behaviour using Milk Powder as an Example. *ANZIAM Journal,* Volume 43, pp. 165-181.

Chen, X. D., 2008. The Basics of a Reaction Engineering Approach to Modelling Air-Drying of Small Droplets or Thin-Layer Materials. *Drying Technology,* Volume 26, pp. 627-639.

Chen, X. D. & Chong, L. V., 1995. Some Characteristics of Transient Self-Heating inside an Exothermically Reactive Porous Solid Slab. *Trans IChemE,* 73(Part B), pp. 101-107.

Chen, X. D. & Chong, L. V., 1998. Several Important Issues Related to the Cross-Point Temperature (CPT) Method for Measuring Self-Ignition Kinetics of Combustible Solids. *Trans IChemE,* 76(Part B), pp. 90-93.

Chen, X. D., Lake, R. & Jebson, S., 1993. Study of Milk Powder Deposition on a Large Industrial Dryer. *Food and Bioproducts Processing,* 71(C), pp. 180-186.

Chen, X. D. & Xie, G. Z., 1997. Fingerprints of the Drying Behaviour of Particulate or Thin Layer Food Materials Established using a Reaction Engineering Model. *Trans IChemE,* 75(Part C), pp. 213-222.

Chong, L. V. & Chen, X. D., 1999. a Mathematical Model of the Self-Heating of Spray-Dried Food Powders containing Fat, Protein, Sugar and Moisture. *Chemical Engineering Science,* Volume 54, pp. 4165-4178.

Chong, L. V. & Chen, X. D., 1999. A Mathematical Model of the Self-Heating of Spray-Dried Food Powders containing Fat, Protein, Sugar and Moisture. *Chemical Engineering Science,* Volume 54, pp. 4165-4178.

Chong, L. V., Shaw, I. R. & Chen, X. D., 1996. Exothermic Reactivites of Skim and Whole Milk Powders as Measured using a Novel Procedure. *Journal of Food Engineering,* Volume 30, pp. 185-196.

Doyle, C. D., 1962. Estimating Isothermal Life from Thermogravimetric Data. *Journal of Applied Polymer Science,* VI(24), pp. 639-642.

Duane, T. C. & Synnot, E. C., 1992. Ignition Characteristics of Spray-Dried Milk Product Powders in Oven Tests. *Journal of Food Engineering,* Volume 17, pp. 163-176.

Flynn, J. H., 1983. The Isoconversional Method for Determination of Energy of Activation at Constant Heating Rates. *Journal of Thermal Analysis,* Volume 27, pp. 95-102.

Flynn, J. H. & Wall, L. A., 1966. A Quick Direct Method for the Determination of Activation Energy from Thermogravimetric Data. *Journal of Polymer Science Part B: Polymer Letter banner,* Volume 4, pp. 323-328.

Francia, V., Martín, L., Bayly, A. E. & Simmons, M. J. H., 2015. The Role of Wall Deposition and Re-Entrainment in Swirl Spray Dryers. *AIChE Journal,* 61(6), pp. 1804-1821.

Frank-Kamenetskii, D. A., 1969. *Diffusion and Heat Transfer in Chemical Kinetics.* 2nd ed. New York: Plenum Press.

Friedman, H. L., 1964. Kinetics of Thermal Degradation of Char-Forming Plastics from Thermogravimetry. Application to a Phenolic Plastic. *Journal of Polymer Science: Part C,* 6(1), pp. 183-195.

Gray, B. F., Griffiths, J. F. & Hasko, S. M., 1984. Spontaneous Ignition Hazards in Stockpiles of Cellulosic Materials: Criteria for Safe Storage. *Journal of Chemical Technology and Biotechnology,* 34(A), pp. 453-463.

Gray, B. F. & Halliburton, B., 2000. The Thermal Decomposition of Hydrated Calcium Hypochlorite (UN 2880). *Fire Safety Journal,* Volume 35, pp. 223-239.

Hassall, G. J., 2011. *Wall Build-Up in Spray Dryers,* Ph.D. Thesis: University of Birmingham.

Jones, J. C., Chiz, P. S., Koh, R. & Matthew, J., 1996. Continuity of Kinetics between Sub- and Supercritical Regimes in the Oxidation of a High-Volatile Solid Substrate. *Fuel,* 75(15), pp. 1733-1736.

Jones, J. C., Chiz, P. S., Koh, R. & Matthew, J., 1996. Kinetic Parameters of Oxidation of Bituminous Coals from Heat-Release Rate Measurements. *Fuel,* 75(15), pp. 1755-1757.

Jones, J. C. & Raj, S. C., 1989. The propensity to self-heating of solar-dried coal slurry. *Fuel,* Volume 68, pp. 648-650.

Jones, J. C. & Vais, M., 1991. Factors influencing the spontaneous heating of low-rank coals. *Journal of Hazardous Materials,* Volume 26, pp. 203-212.

Jones, J. C. & Wake, G. C., 1990. Measured Activation Energies of Ignition of Solid Materials. *Jouranl of Chemical Technology and Biotechnology,* Volume 48, pp. 209-216.

Krause, U. & Schmidt, M., 2001. The Influence of Initial Conditions on the Propagation of Smouldering Fires in Dust Accumulations. *Journal of Loss Prevention in the Process Industries,* Volume 14, pp. 527-535.

Krause, U., Schmidt, M. & Lohrer, C., 2006. A Numerical Model to Simulate Smouldering Fires in Bulk Materials and Dust Deposits. *Journal of Loss Prevention in the Process Industries,* Volume 19, pp. 218-226.

Liang, H. & Tanaka, T., 1987. The Spontaneous Ignition of Dust Deposits - Ignition Temperature and Induction Time. *KONA Powder and Particle Journal,* Volume 5, pp. 25-32.

Malow, M. & Krause, U., 2004. The Overall Activation Energy of the Exothermic Reactions of Thermally Unstable Materials. *Journal of Loss Prevention in the Process Industries,* Volume 17, pp. 51-58.

Muramatsu, M., Umemura, S. & Okada, T., 1979. A Mathematical Model of Evaporation-Pyrolsis Processes Inside a Naturally Smoldering Cigarette. *Combustion and Flame,* Volume 36, pp. 245-262.

Nelson, M. I. & Chen, X. D., 2007. Survey of Experiemtnal Work on the Self-Heating and Spontaneous Combustion of Coal. *Review in Engineering Geology,* Volume XVIII, pp. 31-83.

Nugroho, Y. S., McIntosh, A. C. & Gibbs, B. M., 1998. Using the Crossing-Point Method to asses the Self-Heating Behaviour of Indonesian Coals. *Symposium (International) on Combustion,* 27(2), pp. 2981-2989.

Opfermann, J. & Kaisersberger, E., 1992. An advantageous variant of the Ozawa-Flynn-Wall analysis. *Thermochimica Acta,* Volume 203, pp. 167-175.

Ozawa, T., 1965. A New Method of Analyzing Thermograivmetric Data. *Bulletin of the Chemical Society in Japan,* 38(11), pp. 1881-1886.

Parks, J. R., 1961. Criticality Criteria for Various Configurations of a Self-Heating Chemical as Functions of Activation Energy and Temperature of Assembly. *The Journal of Chemical Physics,* 34(1), pp. 46-50.

Pielichowski, K., Tomasik, P. & Sikora, M., 1998. Kinetics of gelatinization of potato starch studied by non-isothermal DSC. *Carbohydrate Polymers,* Volume 35, pp. 49-54.

Putranto, A., Chen, X. D. & Webley, P. A., 2011. Modeling of Drying of Food Materials with Thickness of Several Centimeters by the Reaction Engineering Approach (REA). *Drying Technology,* Volume 29, pp. 961-973.

Sato, H., Matsumura, T. & Shibukawa, S., 1987. Apparent Heat Transfer in a Forced Convection Oven and Properties of Baked food. *Journal of Food Science,* 52(1), pp. 185-188.

Semenov, N. N., 1928. *Zh. Russ. Fiz.-Khim. Obshch,* Volume 60, p. 241.

Shepherd, J. S., Fairweather, M., Heggs, P. J. & Hanson, B. C., 2015. Mathematical Modelling of the Pre-Oxidation of a Uranium Carbide Fuel Pellet. *Computers and Chemical Engineering,* Volume 83, pp. 203-213.

Smith, G. D., 1985. Parabolic equations: finite difference methods, convergence, and stability. In: *Numerical Solution of Partial Differential Equations: Finite Difference Methods.* Oxford: Oxford Univeristy Press, pp. 11-38.

Sujanti, W., Zhang, D.-K. & Chen, X. D., 1999. Low-Temperature Oxidation of Coal Studied Using Wire-Mesh Reactors With Both Steady-State and Transient Methods. *Combustion and Flame,* Volume 117, pp. 646-651.

Thomas , P. H., 1960. Some Approximations in the Theory of Self-Heating and Thermal Explosion. *Transactions of the Faraday Society,* Volume 56, pp. 833-839.

Thomas, L. C., n.d. *Modulated DSC Paper #9: Measurement of Accurate Heat Capacity Values (TP 014).* s.l.:TA Instruments.

Thomas, P. H., 1957. On the Thermal Conduction Equation for Self-Heating Materials with Surface Cooling. *Transactions of the Faraday Society,* Volume 54, pp. 60-65.

Thomas, P. H. & Bowes, P. C., 1961. Thermal Ignition in a Slab with One Face at a Constant High Temperature. *Transactions of the Faraday Society,* Volume 467, pp. 2007-2017.

Venkatesh, M., Ravi, P. & Tewari, S. P., 2013. Isoconversional Kinetic Analysis of Decomposition of Nitroimidazoles: Friedman method vs Flynn-Wall-Ozawa Method. *The Journal of Physical Chemistry A,* Volume 117, pp. 10162-10169.

Yang, J., Miranda, R. & Roy, C., 2001. Using the DTG Curve Fitting Method to Determine the Apparent Kinetic Parameters of Thermal Decomposiiton of Polymers.. *Polymer Degradation and Stability,* Volume 73, pp. 455-461.

Appendix A. True Form of the Dimensionless Arrhenius Exponent

Frank-Kamenetskii (1969) outlined two methods for transforming the basic energy balance of the stationary theory of thermal explosion. One of these methods involves approximating the Arrhenius exponent, while the second uses the exact form of the exponent. In using the exact form, the following dimensionless temperature difference must first be defined:

$$\theta = \frac{E}{RT_*^2}\Delta T = \frac{E}{RT_*^2}(T - T_*) \tag{A-1}$$

Where E is the Arrhenius activation energy, R is the universal gas constant, T is the temperature of interest, and T_* is a temperature near to which the reaction takes place. Using the temperature difference, ΔT, the exponent of the Arrhenius term can be expressed as:

$$\frac{E}{RT} = \frac{E}{R(T_* + \Delta T)} \tag{A-2}$$

Expanding this gives:

$$\frac{E}{RT} = \frac{E}{RT_*}\left(\frac{1}{1 + \frac{\Delta T}{T_*}}\right) \tag{A-3}$$

This can also be expressed as:

$$\frac{E}{RT} = \frac{E}{RT_*}\left(1 - \frac{\frac{\Delta T}{T_*}}{1 + \frac{\Delta T}{T_*}}\right) \tag{A-4}$$

The following dimensionless term is defined:

$$\alpha = \frac{E}{RT} \tag{A-5}$$

Using this new term, and by multiplying out the bracketed term of equation (A-4), the following exact form of the exponent is formed:

$$\frac{E}{RT} = \frac{E}{RT_*} - \frac{\theta}{1 + \frac{\theta}{\alpha}} \tag{A-6}$$

Applying this to the Arrhenius term gives the final expression which can be substituted into the governing equation of the stationary theory of thermal explosion:

$$e^{-\frac{E}{RT}} = e^{-\frac{E}{RT_*}} \cdot e^{\frac{\theta}{1+\frac{\theta}{\alpha}}} \tag{A-7}$$

Appendix B. gPROMS Model and Process Scripts

gPROMS ModelBuilder Model Script

```
PARAMETER
    radial_length           AS  REAL    # basket radius, m
    axial_length            AS  REAL    # bakset half height, m
    bulk_density            AS  REAL    # powder bulk density, kg m^-3
    gas_constant            AS  REAL    # universal gas constant, J mol^-1 K^-1
    emissivity              AS  REAL    # powder emissivity
    stefan_boltzmann        AS  REAL    # Stefan-Boltzmann constant, W m^-2 K^-4
    temp_init               AS  REAL    # initial powder temperature, K
    temp_ambient_init       AS  REAL    # initial ambient temperature, K
    temp_ambient_max        AS  REAL    # initial ambient temperature, K
    conductivity            AS  REAL    # thermal conductivity, J kg^-1 K^-1
    specific_heat           AS  REAL    # specific heat capacity, W m^-1 K^-1
    activation_energy       AS  REAL    # activation energy, J mol^-1
    ln_QA                   AS  REAL    # ln(QA)

DISTRIBUTION_DOMAIN
    radial      AS      [ 0 : radial_length ]
    axial       AS      [ 0 : axial_length ]

VARIABLE
    temperature                     AS DISTRIBUTION (radial, axial)
                                    OF  temperature
                        # temperature, K
    heat_transfer_coeff_con         AS heat_transfer_Coeff
                        # convective heat transfer coefficient, W m^-2 K^-1
    heat_transfer_coeff_rad_axial   AS DISTRIBUTION (axial)
                                    OF heat_transfer_Coeff
                        # axial radiative heat transfer coefficient, W m^-2 K^-1
    heat_transfer_coeff_rad_radial  AS  DISTRIBUTION (radial)
                                    OF  heat_transfer_Coeff
                        # radial radiative heat transfer coefficient, W m^-2 K^-1
```

```
    heat_transfer_coeff_eff_axial       AS  DISTRIBUTION (axial)
                                        OF  heat_transfer_Coeff
                        # axial effective heat transfer coefficient, W m^-2 K^-1
    heat_transfer_coeff_eff_radial      AS  DISTRIBUTION (radial)
                                        OF  heat_transfer_Coeff
                        #radial effective heat transfer coefficient, W m^-2 K^-1
    temp_ambient                        AS temperature
                        # ambient temperature, K
    my_time                             AS no_type
                        # time for use in equations


BOUNDARY
# Along 2D Domain Edges
    # radial = 0
    FOR z := 0|+ TO axial_length|- DO
        PARTIAL(temperature(0,z),radial) = 0 ;
    END

    # radial = radial_length
    FOR z := 0|+ TO axial_length|- DO
        -conductivity * PARTIAL(temperature(radial_length,z),radial) =
heat_transfer_coeff_eff_axial(z) * (temperature(radial_length,z) - temp_ambient) ;
    END

    # axial = 0
    FOR r := 0|+ TO radial_length|- DO
        PARTIAL(temperature(r,0),axial) = 0 ;
    END

    # axial = axial_length
    FOR r := 0|+ TO radial_length|- DO
        -conductivity * PARTIAL(temperature(r,axial_length),axial) =
heat_transfer_coeff_eff_radial(r) * (temperature(r,axial_length) - temp_ambient) ;
    END
```

```
# At 2D Domain Corners
   # radial = 0 and axial = 0
      PARTIAL(temperature(0,0),radial) + PARTIAL(temperature(0,0),axial) = 0 ;

   # radial = 0 and axial = axial_length
      PARTIAL(temperature(0,axial_length),radial) + conductivity *
PARTIAL(temperature(0,axial_length),axial) + heat_transfer_coeff_eff_radial(0) *
(temperature(0,axial_length) - temp_ambient) = 0 ;

   # radial = radial_length and axial = 0
      PARTIAL(temperature(radial_length,0),axial) + conductivity *
PARTIAL(temperature(radial_length,0),radial) + heat_transfer_coeff_eff_axial(0) *
(temperature(radial_length,0) - temp_ambient) = 0 ;

   # radial = radial_length and axial = axial_length
      PARTIAL(temperature(radial_length,axial_length),radial) +
PARTIAL(temperature(radial_length,axial_length),axial) = 0 ;

EQUATION
# ------------------ Heat Transfer Coefficeint Equations ----------------------------------
   # convective heat transfer coefficient
   heat_transfer_coeff_con = -1.93153e-4 * (temp_ambient^2) + 0.102499 *
temp_ambient + 13.7055 ;

   # radiative heat transfer coefficeint
   FOR z := 0 TO axial_length DO
      heat_transfer_coeff_rad_axial(z) =
         emissivity * stefan_boltzmann * (temperature(radial_length,z) + temp_ambient)
* (temperature(radial_length,z)^2 + temp_ambient^2) ;
   END #z

   FOR r := 0 TO radial_length DO
      heat_transfer_coeff_rad_radial(r) =
         emissivity * stefan_boltzmann * (temperature(r,axial_length) + temp_ambient)
* (temperature(r,axial_length)^2 + temp_ambient^2) ;
   END #r
```

```
  # effective heat transfer coefficient
  FOR z := 0 TO axial_length DO
    heat_transfer_coeff_eff_axial(z) =
      heat_transfer_coeff_con + heat_transfer_coeff_rad_axial(z) ;
  END #z

  FOR r := 0 TO radial_length DO
    heat_transfer_coeff_eff_radial(r) =
      heat_transfer_coeff_con + heat_transfer_coeff_rad_radial(r) ;
  END #r

# ------------------ Main Model Equations ----------------------------------

## ------ Equations for zero order reaction model ------
  FOR z := 0|+ TO axial_length|- DO
    FOR r := 0|+ TO radial_length|- DO
      bulk_density * specific_heat * $temperature(r,z) =
        conductivity * ( PARTIAL(PARTIAL(temperature(r,z),radial),radial) + (1 /
r)*PARTIAL(temperature(r,z),radial) + PARTIAL(PARTIAL(temperature(r,z),axial),axial) )
        + bulk_density * exp(ln_QA) * EXP(-activation_energy / (gas_constant *
temperature(r,z))) ;
    END #r
  END #z

  # time varying ambient temperature
  IF temp_ambient < temp_ambient_max THEN
    temp_ambient = (0.218152 * my_time) + temp_ambient_init ;
  ELSE
    temp_ambient = temp_ambient_max ;
  END

  # time for use in equations
  $my_time = 1;
```

gPROMS ModelBuilder Process Script

```
UNIT
  Basket_k_Cp_Estimation  AS  Basket_k_Cp_Region_ln_QA_1


SET
  WITHIN Basket_k_Cp_Estimation DO
    # ---------- discretisation method --------
    Radial                  := [ CFDM, 2, 30 ] ;
    Axial                   := [ CFDM, 2, 30 ] ;
    # -----------------------------------------------
    radial_length           := 0.030 ;      # basket radius, m
    axial_length            := 0.030 ;      # basket half height, m
    bulk_density            := 683.76 ;     # powder bulk density, kg m^-3
    gas_constant            := 8.314 ;      # universal gas constant, J mol^-1 K^-1
    emissivity              := 0.5 ;        # powder emissivity
    stefan_boltzmann        := 5.67e-8 ;    # Stefan-Boltzmann const, W m^-2 K^-4
    temp_init               := 293 ;        # initial powder temperature, K
    temp_ambient_init       := 293 ;        # ambient temperature, K
    temp_ambient_max        := 502 ;        # ambient temperature, K
    conductivity            :=  0.08 ;      # thermal conductivity, W m^-1 K^-1
    specific_heat           :=  1367.47 ;   # specific heat capacity, J kg^-1 K^-1
    ln_QA                   :=  32.10654 ;  # ln(QA)
    activation_energy       :=  125260.8 ;  # activation energy, J mol^-1
  END


INITIAL
  WITHIN Basket_k_Cp_Estimation DO
    FOR z := 0|+ TO axial_length|- DO
      FOR r := 0|+ TO radial_length|- DO
        temperature(r,z) = temp_init ;
      END # r
    END # z
    my_time = 1;
  END # within
```

```
SCHEDULE
  SEQUENCE
      CONTINUE FOR 10000
  END
```

Appendix C. Analytical Solution for Temperature Evolution in a Finite Slab

As outline in Section 4.3.1, there exist analytical solutions to the transient temperature profiles for a finite slab. For this solution, at the time $t = 0$ the surfaces of the slab at $x = \pm b$ are suddenly raised to some temperature T_1 and maintained at this temperature from this time onwards. The solution to this case is outlined by Bird *et al.* (2007) and firstly requires a number of dimensionless variables to be defined.

Dimensionless temperature:

$$\Theta = \frac{T_1 - T}{T_1 - T_0} \tag{C-1}$$

Dimensionless coordinate:

$$\eta = \frac{y}{b} \tag{C-2}$$

Dimensionless time:

$$\tau = \frac{\alpha_T t}{b^2} \tag{C-3}$$

α_T is the thermal diffusivity, equal to $k/\rho C_p$, of the body in question. Using these dimensionless variables, the differential equation outlining the heat transfer in this system can be expressed as:

$$\frac{\partial \Theta}{\partial \tau} = \frac{\partial^2 \Theta}{\partial \eta^2} \tag{C-4}$$

Initially the slab is at temperature T_0, such that the initial conditions can be expressed as:

$$\Theta = 1 \qquad at\ \tau = 0 \tag{C-5}$$

At time $t = 0$ the slab faces at $y = \pm b$ are raised to temperature T_1 such that the boundary conditions can be defined as:

$$\Theta = 0 \qquad at\ \eta = \pm 1 \tag{C-6}$$

This problem can be solved by means of separation of variables, where the solution is of the form of the following product:

$$\Theta(\eta,\tau) = f(\eta)\cdot g(\tau) \tag{C-7}$$

Substituting this into equation (C-4), and dividing by $f(\eta)\cdot g(\tau)$ gives:

$$\frac{1}{\mathrm{g}}\frac{dg}{d\tau} = \frac{1}{f}\frac{d^2f}{d\eta^2} \tag{C-8}$$

Where the left hand side is solely a function of τ, and the right hand side is solely a function of η. Both sides are set equal to the constant $-c^2$, although $+c^2$, $+c$, and $-c$ can also be used but produce more complicated solutions. This allows the above equation to be separated in two ordinary differential equations:

$$\frac{dg}{d\tau} = -c^2 g \tag{C-9}$$

$$\frac{d^2f}{d\eta^2} = -c^2 f \tag{C-10}$$

Integrating these equations gives the following:

$$\mathrm{g} = \mathrm{A}\exp(-c^2\tau) \tag{C-11}$$

$$f = B\sin c\eta + \mathrm{C}\cos c\eta \tag{C-12}$$

Where A, B, and C are constant of integration.

The slab in question occupies the space between $y = -b$ and $y = +b$, and because of symmetry about this plane it must be that $\Theta(\eta,\tau) = \Theta(-\eta,\tau)$, and thus $f(\eta) = f(-\eta)$. As such, because $\sin(y) \neq \sin(-y)$, B must be equal to zero. Applying the boundary conditions outlined previously, it can also be shown that:

$$C\cos c = 0 \tag{C-13}$$

C cannot be equal to zero as this leads to an impossible solution, and as such the choice of c has to satisfy this expressions. The infinite choices of c that satisfy this expression, c_n, can be expressed as:

$$c_n = \left(n + \frac{1}{2}\right)\pi \qquad n = 0, \pm1, \pm2, \pm3, \dots, \pm\infty \tag{C-14}$$

Substituting this into the product of equations (C-11) and (C-12) gives the following:

$$\Theta_n = A_n C_n \exp\left[-\left(n+\frac{1}{2}\right)^2 \pi^2 \tau\right] \cos\left(n+\frac{1}{2}\right)\pi\eta \tag{C-15}$$

The subscript n is used to show that the values of A and C are different for each value of n. We now superimpose all solutions of the form of equation (C-15). It can be seen that for any value of n, the exponential and cosine terms have the same value as those for $-(n+1)$, such that the terms with negative indices combine with those with positive indices to give:

$$\Theta_n = \sum_{n=0}^{\infty} D_n \exp\left[-\left(n+\frac{1}{2}\right)^2 \pi^2 \tau\right] \cos\left(n+\frac{1}{2}\right)\pi\eta \tag{C-16}$$

Where $D_n = A_n C_n + A_{-(n+1)} C_{-(n+1)}$.

Using the initial condition outlined before, D_n can now be determined from:

$$1 = \sum_{n=0}^{\infty} D_n \cos\left(n+\frac{1}{2}\right)\pi\eta \tag{C-17}$$

Multiplying both sides by $\cos\left(m+\frac{1}{2}\right)\pi\eta$ and integrating from $\eta = -1$ to $\eta = +1$ gives:

$$\int_{-1}^{+1} \cos\left(m+\frac{1}{2}\right)\pi\eta \; d\eta = \sum_{n=0}^{\infty} D_n \int_{-1}^{+1} \cos\left(m+\frac{1}{2}\right)\pi\eta \cos\left(n+\frac{1}{2}\right)\pi\eta \; d\eta \tag{C-18}$$

After integrating, it can be seen that all integrals on the right hand side are identically zero except for the term where $n = m$, such that:

$$\left.\frac{\sin\left(m+\frac{1}{2}\right)\pi\eta}{\left(m+\frac{1}{2}\right)\pi}\right|_{\eta=-1}^{\eta=+1} = D_m \left.\frac{\frac{1}{2}\left(m+\frac{1}{2}\right)\pi\eta + \frac{1}{4}\sin 2\left(m+\frac{1}{2}\right)\pi\eta}{\left(m+\frac{1}{2}\right)\pi}\right|_{\eta=-1}^{\eta=+1} \tag{C-19}$$

Inserting the limits reduces this to the following expression for D_m:

$$D_m = \frac{2(-1)^m}{\left(m+\frac{1}{2}\right)\pi} \tag{C-20}$$

Substituting this into equation (C-16) gives the following solution for the temperature profile in a finite slab under the outlined conditions:

$$\Theta = 2\sum_{n=0}^{\infty} \frac{(-1)^n}{\left(n+\frac{1}{2}\right)\pi} \exp\left[-\left(n+\frac{1}{2}\right)^2 \pi^2 \tau\right] \cos\left(n+\frac{1}{2}\right)\pi\eta \tag{C-21}$$

Using the original variables, this is expressed as:

$$\frac{T_1 - T}{T_1 - T_0} = 2\sum_{n=0}^{\infty} \frac{(-1)^n}{\left(n+\frac{1}{2}\right)\pi} \exp\left[-\left(n+\frac{1}{2}\right)^2 \pi^2 \frac{\alpha_T t}{b^2}\right] \cos\left(n+\frac{1}{2}\right)\frac{\pi y}{b} \qquad \text{(C-22)}$$

This solution was used to validate the numerical model when applied to finite slab geometries. This was discussed in detail in Section 4.3.1.

Appendix D. Analytical Solution for Temperature Evolution in an Infinite Cylinder

As discussed in Section 4.3.2, there exist analytical solutions for the temperature profile of an infinite cylinder for some special cases. The solution for the geometry is more complex than the finite slab case outlined above and has been explored by Carslaw and Jaeger (1959). Initially the temperature of the cylinder is a function of the radius and given by $T = f(r)$. The surface, at $r = b$ is at a constant temperature, which may be taken as zero. Based on this, the equations for the temperature of the cylinder are:

$$\frac{\partial T}{\partial t} = \alpha\left(\frac{\partial^2 T}{\partial r^2} + \frac{1}{r}\frac{\partial T}{\partial r}\right) \tag{D-1}$$

$$T = 0 \qquad at\ r = b \tag{D-2}$$

$$T = f(r) \qquad at\ t = 0 \tag{D-3}$$

If $T = e^{-\alpha\beta^2 t}u$, where u is solely a function of r, then:

$$\frac{\partial^2 u}{\partial r^2} + \frac{1}{r}\frac{\partial u}{\partial r} + \beta^2 u = 0 \tag{D-4}$$

This is Bessel's equation of order zero. As the solution of the second kind is infinite at $r = 0$, the integral of the temperature equation most suitable for this case is:

$$T = AJ_0(\beta r)e^{-\alpha\beta^2 t} \tag{D-5}$$

Where $J_0(x)$ is the Bessel function of order zero of the first kind. In order to satisfy the boundary conditions outlined above, β must be a root of:

$$J_0(a\beta) = 0 \tag{D-6}$$

This equation is known to have no complex roots, no repeated roots, and an infinite number of real positive roots β_1, β_2, β_3…, with each positive root β having a corresponding root $-\beta$.

$f(r)$ can be expanded into the series:

$$f(r) = A_1 J_0(\beta_1 r) + A_2 J_0(\beta_2 r) + \cdots \tag{D-7}$$

The solution of the problem will be satisfied by:

$$T = \sum_{n=1}^{\infty} A_n J_0(\beta_n r) e^{-\alpha \beta_n^2 t} \tag{D-8}$$

Finding the solution to this equation now involves a large amount of manipulation, outlined in greater detail by Carslaw and Jaeger (Carslaw & Jaeger, 1959). To summarise, by taking equation (D-7), multiplying both sides by $rJ_0(\beta_n r)$, integrating from 0 to a, and using the results of integrals discussed by Carslaw and Jaeger, it can be found that:

$$A_n = \frac{2}{a^2 J_1^2(a\beta_n)} \int_0^a r f(r) J_0(r\beta_n) dr \tag{D-9}$$

Therefore the following can be said:

$$T = \frac{2}{a^2} \sum_{n=1}^{\infty} e^{-\alpha \beta^2 t} \frac{J_0(r\beta_n)}{J_1^2(a\beta_n)} \int_0^a r f(r) J_0(r\beta_n) dr \tag{D-10}$$

Here $J_1(x)$ is the Bessel function of order one of the first kind.

If the initial temperature of the cylinder is constant, $f(r) = T_0$, then the integral in equation (D-10) can be solved to give:

$$T = \frac{2T_0}{a} \sum_{n=1}^{\infty} e^{-\alpha \beta^2 t} \frac{J_0(r\beta_n)}{\beta_n J_1(a\beta_n)} \tag{D-11}$$

If the case is similar to that of the slab discussed previously where the initial temperature is zero and the surface is maintained at some higher temperature T_1 for $t > 0$, then the solution is achieved by subtracting equation (D-11) from T_1:

$$T = T_1 - \frac{2T_0}{a} \sum_{n=1}^{\infty} e^{-\alpha \beta^2 t} \frac{J_0(r\beta_n)}{\beta_n J_1(a\beta_n)} \tag{D-12}$$

The above solution can be expressed using the same dimensionless variables as used in the solution of the infinite slab to allow simpler comparison with numerical results. These are the dimensionless temperature in equation (C-1), the dimensionless coordinate in equation (C-2) with y changed to the radius r, and the dimensionless time in equation (C-3). Additionally a dimensionless Bessel function root is defined as:

$$\gamma_n = a\beta_n \tag{D-13}$$

Substituting these into the solution in equation (D-12) gives the following dimensionless solutions:

$$\Theta = 1 - 2\sum_{n=0}^{\infty} e^{-\gamma_n^2 \tau} \frac{J_0(\gamma_n \eta)}{\gamma_n J_1(\gamma_n)} \tag{D-14}$$

Where $\pm\gamma_n$, $n = 1,2$, …, are the roots of:

$$J_0(\gamma) = 0 \tag{D-15}$$

This solution was used to validate the numerical model when applied to infinite cylinder geometries. This was discussed in detail in Section 4.3.2.

Appendix E. 1-Dimensional Finite Implicit Backwards Model used to solve for δ_{cr}

The 1-dimensional model used to solve for δ_{cr} as a function of α and Biot number for an infinite slab, infinite cylinder, and a sphere. This model is solved using an iterative Finite Implicit Backwards approach.

```
% Define Range of alpha and Biot to solve for
alpha_all=[10 15 20 25 30 35 40 45 50 55 60 65 70 75 80 85 90 95 100];
Bi_all=[1 2 3 4 5 6 7 8 9 10 15 20 25 30 35 40 45 50 55 60 65 70 75 80
85 90 95 100];

alpha_no=0;

% Loop through all Biot values
for Bi=Bi_all(1:end)
    % Loop through all alpha values
    for alpha=alpha_all(1:end)
        clearvars solutions
        alpha_no=alpha_no+1;

        % Define range delta values in which to look
        delta_min=0;
        delta_max=3;
        delta_old=delta_max;

        delta=((delta_max-delta_min)/2)+delta_min;
        delta_diff=1;
        m=1;

        % delta value is found to withtin 1e-6
        while abs(delta_diff)>1e-6

            clearvars theta_all residual

            % Initial dimensionless temperature difference
            theta_0=0;

            % Define dimensionless space and discretization
            z=linspace(0,1,21);
            z=z';
            I=length(z);
            dz=mean(diff(z));

            % Shape factor defienes geometry
            % j=0 is for a slab
            % j=1 is for an infinite cylinder
            % j=2 is for a sphere
            j=0;

            % Defines maximum number of attempts to find solution
            N=1000;

            % Define matrices used in FIB approach
            Matrix_A=zeros(I,I);
            Matrix_C=zeros(I,1);
```

```
            % Initial Temperture Profile
            theta_old(1:I,1)=theta_0;

            % Used to flag if a solution is found
            solution_flag=0;

            for n=1:N;
                % For all central elements
                for i=2:I-1
                    % Define (i,i-1) elements
                    if j==0
                        Matrix_A(i,i-1)=(1/(dz^2));
                    else
                        Matrix_A(i,i-1)=(1/(dz^2))-(j/(2*z(i)*dz));
                    end

                    % Define (i,i) elements
                    Matrix_A(i,i)=(-2/(dz^2));

                    % Define (i,i+1) elements
                    if j==0
                        Matrix_A(i,i+1)=(1/(dz^2));
                    else
                        Matrix_A(i,i+1)=(1/(dz^2))+(j/(2*z(i)*dz));
                    end

                    % Define right hand side term
                    Matrix_C(i,1)=-
((delta)*exp(theta_old(i)/(1+(theta_old(i)/alpha))));
                end

                % Boundary conditions at z=0;
                Matrix_A(1,1)=(-2/(dz^2));
                Matrix_A(1,2)=2/(dz^2);

                % Boundary conditions at z=Z;
                Matrix_A(I,I-1)=(2/(dz^2));
                if j==0
                    Matrix_A(I,I)=(-2/(dz^2))+((-2*Bi)/dz);
                else
                    Matrix_A(I,I)=(-2/(dz^2))+((-2*Bi)/dz)+((-
j*Bi)/z(i));
                end

                % Define right hand side terms for boundary conditions
                Matrix_C(1,1)=-
((delta)*exp(theta_old(i)/(1+(theta_old(i)/alpha))));
                Matrix_C(I,1)=0;
                Matrix_C(I,1)=-
((delta)*exp(theta_old(i)/(1+(theta_old(i)/alpha))));

                % Solve set of equations
                RHS=Matrix_C;
                theta_new=Matrix_A\RHS;
                theta_all(n,:)=theta_new(:);

                % determine residuals between all theta values
                for i=1:I
                    residual(n,:)=abs(theta_all(n,:)-theta_old(:)');
                end

                % Determines if an eligible solution is found
                if all(residual(n,:)<1e-10) && all(theta_new(:)<1e1);
```

```
                    solution_flag=1;
                    break
                end

                % Breaks if residuals are small but no solution found
                if all(residual(n,:)<1e-10);
                    break
                end

                % Stores these results to calculate next residuals
                theta_old(:)=theta_all(n,:);
            end

            % If a solution is found, the value of delta becomes the
new
            % minimum value of delta
            if solution_flag==1
                solutions(m,1)=delta;
                solutions(m,2)=theta_all(n,1);
                delta_min=delta;
                delta=((delta_max-delta)/2)+delta;
                m=m+1;
            end

            % If no solution is found, the value of delta becomes the
new
            % maximum value of delta
            if solution_flag==0
                delta_max=delta;
                delta=((delta-delta_min)/2)+delta_min;
            end

            % The difference in seleected delta values is stored
            delta_diff=delta_old-delta;
            delta_old=delta;

        end

        % When delta is solved for a value of alpha, the solution is
logged
        % to be later tabulated
        alpha_solutions(alpha_no,1)=alpha;
        alpha_solutions(alpha_no,2)=solutions(end,1);
        alpha_solutions(alpha_no,3)=solutions(end,2);
        alpha_solutions(alpha_no,4)=Bi;

    end
end
```

Appendix F. 2-Dimensional Alternating Difference Implicit Model used to solve for δ_{cr}

The 2-dimensional model used to solve for δ_{cr} as a function of α and Biot number for an equi-cylinder. This model is solved using an iterative Alternating Difference Implicit approach.

```
% Define Range of alpha and Biot to solve for
alpha_all=[10 15 20 25 30 35 40 45 50 55 60 65 70 75 80 85 90 95 100];
Bi_all=[1 2 3 4 5 6 7 8 9 10 15 20 25 30 35 40 45 50 55 60 65 70 75 80 85 90 95 100];

alpha_no=0;

% Loop through all Biot values
for Bi=Bi_all(1:end)
    % Loop through all alpha values
    for alpha=alpha_all(1:end)
        clearvars solutions
        alpha_no=alpha_no+1;

        % Define range delta values in which to look
        delta_min=0.1;
        delta_max=5;
        delta_old=delta_max;

        delta=((delta_max-delta_min)/2)+delta_min;
        delta_diff=1;
        m=1;

        % delta value is found to withtin 1e-4
        while abs(delta_diff)>1e-4

            clearvars theta_all residual

            % Initial dimensionless temperature difference
            theta_0=0;

            % Define dimensionless space and discretization
            r=linspace(0,1,21);
            r=r';
            z=linspace(0,1,21);
            z=z';
            I=length(r);
            dr=mean(diff(r));
            J=length(z);
            dz=mean(diff(z));

            % Defines maximum number of attempts to find solution
            N=10000;

            % Define matrices used in FIB approach
            Matrix_A=zeros(I,I);
            Matrix_C=zeros(I,1);

            %Initial Temperture Profile
            theta_old(1:I,1:J)=theta_0;

            % Used to flag if a solution is found
            solution_flag=0;

            for n=1:N;
                %% Solves equations in the radial direction
                for j=1:J
                    for i=1:I

                        % Used to reduce scripting to specify boundary
                        % conditions
                        if i==1;
                            row=1;
                        elseif i>1 && i<I
```

```
                        row=2;
                    elseif i==I
                        row=3;
                    end

                    % Equations for i=0
                    A_I(1,2)=(-2/(dr^2))+(-2/(dz^2));
                    A_I(1,3)=(2/(dr^2));

                    % Equations for central element 0>i<I
                    A_I(2,1)=(1/(dr^2))-(1/(2*r(i)*dr));
                    A_I(2,2)=(-2/(dr^2))+(-2/(dz^2));
                    A_I(2,3)=(1/(dr^2))+(1/(2*r(i)*dr));

                    % Equations for i=I
                    A_I(3,1)=(2/(dr^2));
                    A_I(3,2)=(-2/(dr^2))+(-2/(dz^2))+((-2*Bi)/dr)+(-Bi/r(i));

                    % Picks equaions for matrix A based on row value
                    if i>1
                        Matrix_A(i,i-1)=A_I(row,1);
                    end
                    Matrix_A(i,i)=A_I(row,2);
                    if i<I
                        Matrix_A(i,i+1)=A_I(row,3);
                    end

                    % Defines equations for right hand side depending
                    % on axial position j
                    if j==1;
                        C_I=(-(2/(dz^2))*theta_old(i,j+1))-
((delta)*exp(theta_old(i,j)/(1+(theta_old(i,j)/alpha))));
                    elseif j>1 && j<J
                        C_I=(-(1/(dz^2))*theta_old(i,j-1))+(-
(1/(dz^2))*theta_old(i,j+1))-((delta)*exp(theta_old(i,j)/(1+(theta_old(i,j)/alpha))));
                    elseif j==J
                        C_I=(-(2/(dz^2))*theta_old(i,j-1))-
((delta)*exp(theta_old(i,j)/(1+(theta_old(i,j)/alpha))));
                        Matrix_A(i,i)=Matrix_A(i,i)-((2*Bi)/dz);
                    end
                    Matrix_C(i,1)=C_I;

                end

                % Solve set of equations
                RHS=Matrix_C;
                theta_r=Matrix_A\RHS;
                theta_new(:,j)=theta_r(:);
            end

            %% Solves equations in the axial direction
            for i=1:I-1
                for j=1:J

                    % Used to reduce scripting to specify boundary
                    % conditions
                    if j==1;
                        row=1;
                    elseif j>1 && j<J
                        row=2;
                    elseif j==J
                        row=3;
                    end

                    % Equations for j=0
                    A_J(1,2)=(-2/(dz^2))+(-2/(dr^2));
                    A_J(1,3)=(2/(dz^2));

                    % Equations for central element 0>i<I
                    A_J(2,1)=(1/(dz^2));
                    A_J(2,2)=(-2/(dz^2))+(-2/(dr^2));
                    A_J(2,3)=(1/(dz^2));

                    % Equations for j=J
                    A_J(3,1)=(2/(dz^2));
                    A_J(3,2)=(-2/(dz^2))+(-2/(dr^2))-((2*Bi)/dz);

                    % Picks equaions for matrix A based on row value
                    if j>1
```

```
                            Matrix_A(j,j-1)=A_J(row,1);
                        end
                        Matrix_A(j,j)=A_J(row,2);
                        if j<J
                            Matrix_A(j,j+1)=A_J(row,3);
                        end

                        % Defines equations for right hand side depending
                        % on radial position i
                        if i==1;
                            C_J=(-(2/(dr^2))*theta_new(i+1,j))-
((delta)*exp(theta_new(i,j)/(1+(theta_new(i,j)/alpha))));
                        elseif i>1 && i<I
                            C_J=((-(1/(dr^2))+(1/(2*r(i)*dr)))*theta_new(i-1,j))+((-
(1/(dr^2))-(1/(2*r(i)*dr)))*theta_new(i+1,j))-
((delta)*exp(theta_new(i,j)/(1+(theta_new(i,j)/alpha))));
                        elseif i==I;
                            C_J=(-(2/(dr^2))*theta_new(i-1,j))-
((delta)*exp(theta_new(i,j)/(1+(theta_new(i,j)/alpha))));
                            Matrix_A(j,j)=Matrix_A(j,j)-((2*Bi)/dr)-(Bi/r(i));
                        end
                        Matrix_C(j,1)=C_J;

                    end

                    % Solve set of equations
                    RHS=Matrix_C;
                    theta_z=Matrix_A\RHS;
                    theta_new(i,:)=theta_z(:);
                end

                %% Processing of solution
                % New theat distribution stored
                theta_all(n,:,:)=theta_new(:,:);

                % determine residuals between all theta values
                for i=1:I
                    for j=1:J
                        residual(n,i,j)=abs(theta_new(i,j)-theta_old(i,j));
                    end
                end

                % Determines if an eligible solution is found
                if all(all(residual(n,:,:)<1e-4)) && all(all(theta_new(:,:)<1e2));
                    solution_flag=1;
                    break
                end

                % Breaks if residuals are small but no solution found
                if all(residual(n,:)<1e-4);
                    break
                end

                if all(all(theta_new(:,:)>1e3))
                    break
                end

                % Stores these results to calculate next residuals
                theta_old(:,:)=theta_all(n,:,:);
            end

            % If a solution is found, the value of delta becomes the new
            % minimum value of delta
            if solution_flag==1
                solutions(m,1)=delta;
                solutions(m,2)=theta_all(n,1);
                delta_min=delta;
                delta=((delta_max-delta)/2)+delta;
                m=m+1;
            end

            % If no solution is found, the value of delta becomes the new
            % maximum value of delta
            if solution_flag==0
                delta_max=delta;

                delta=((delta-delta_min)/2)+delta_min;
            end
```

```
            % The difference in seleected delta values is stored
            delta_diff=delta_old-delta;
            delta_old=delta;

        end

        % When delta is solved for a value of alpha, the solution is logged
        % to be later tabulated
        alpha_solutions(alpha_no,1)=alpha;
        alpha_solutions(alpha_no,2)=solutions(end,1);
        alpha_solutions(alpha_no,3)=solutions(end,2);
        alpha_solutions(alpha_no,4)=Bi;

    end
end
```

Appendix G. gPROMS Parameter Estimation Full Report

Below is the full report produced by gPROMS ModelBuilder when performing Parameter Estimation for Pandora 13 Formulation 1 for the grouping of 10 experiments with the value of the specific heat capacity, C_p, fixed in the fitting.

Parameter estimation problem		k_Cp_Estimation_212C_to_224C_60mm_Sim_E_Cp_var_fit_2
Final optimisation status		Optimal
ln(likelihood function)		255026
Activity completed	**on**	13/5/2018
	at	2:00:24

Contents

Objective Function Contribution

Experiment	Measured Variable	Constant Term	Variance Term	Residual Term
Basket_Test_212C_60mm_3485_to_9300_ln_QA	Basket_k_Cp_Estimation → thermocouple_1	5344.55	1341.15	2133.13
	Basket_k_Cp_Estimation → thermocouple_2	5344.55	1692.78	4116.53
	Basket_k_Cp_Estimation → thermocouple_3	5344.55	-1531.03	2224.33
Basket_Test_213C_60mm_3154_to_8950_ln_QA	Basket_k_Cp_Estimation → thermocouple_1	5327.09	1336.76	1880.42
	Basket_k_Cp_Estimation → thermocouple_2	5327.09	1687.25	1022.2
	Basket_k_Cp_Estimation → thermocouple_3	5327.09	-1526.02	2178.04
Basket_Test_215C_60mm_3083_to_8860_ln_QA	Basket_k_Cp_Estimation → thermocouple_1	5309.63	1332.38	5367.59
	Basket_k_Cp_Estimation → thermocouple_2	5309.63	1681.72	3360.84
	Basket_k_Cp_Estimation → thermocouple_3	5309.63	-1521.02	6358.78
Basket_Test_216C_60mm_3401_to_8740_ln_QA	Basket_k_Cp_Estimation → thermocouple_1	4907.13	1231.38	1036.47
	Basket_k_Cp_Estimation → thermocouple_2	4907.13	1554.24	3376.94
	Basket_k_Cp_Estimation → thermocouple_3	4907.13	-1405.72	1517.08
Basket_Test_217C_60mm_3127_to_8840_ln_QA	Basket_k_Cp_Estimation → thermocouple_1	5250.81	1317.63	1522.22
	Basket_k_Cp_Estimation → thermocouple_2	5250.81	1663.09	5073.86
	Basket_k_Cp_Estimation → thermocouple_3	5250.81	-1504.18	1569.68
Basket_Test_219C_60mm_3057_to_8840_ln_QA	Basket_k_Cp_Estimation → thermocouple_1	5315.14	1333.77	1325.89
	Basket_k_Cp_Estimation → thermocouple_2	5315.14	1683.47	1777.49
	Basket_k_Cp_Estimation → thermocouple_3	5315.14	-1522.6	1570.33
Basket_Test_220C_60mm_3254_to_8800_ln_QA	Basket_k_Cp_Estimation → thermocouple_1	5097.35	1279.12	5351.85
	Basket_k_Cp_Estimation → thermocouple_2	5097.35	1614.49	3369.31
	Basket_k_Cp_Estimation → thermocouple_3	5097.35	-1460.21	4048.62
Basket_Test_221C_60mm_3018_to_8790_ln_QA	Basket_k_Cp_Estimation → thermocouple_1	5305.03	1331.23	2949.87
	Basket_k_Cp_Estimation → thermocouple_2	5305.03	1680.27	2465.18
	Basket_k_Cp_Estimation → thermocouple_3	5305.03	-1519.71	4268.98
Basket_Test_223C_60mm_3000_to_8700_ln_QA	Basket_k_Cp_Estimation → thermocouple_1	5238.87	1314.63	2085.42
	Basket_k_Cp_Estimation → thermocouple_2	5238.87	1659.31	1558.82
	Basket_k_Cp_Estimation → thermocouple_3	5238.87	-1500.75	2044.29
Basket_Test_224C_60mm_3198_to_8430_ln_QA	Basket_k_Cp_Estimation → thermocouple_1	4808.81	1206.71	4586.86
	Basket_k_Cp_Estimation → thermocouple_2	4808.81	1523.1	2117.05
	Basket_k_Cp_Estimation → thermocouple_3	4808.81	-1377.56	2459.2
	Total	155713	14595.7	84717.3
			Objective function total	**255026**

TOP

Model Parameters

- Probability of parameter lying between (Final Value - α% Confidence Interval) and (Final Value + α% Confidence Interval) = α%
- The t-value shows the percentage accuracy of the estimated parameters, with respect to the 95% confidence intervals.

Model Parameter	Final Value	Initial Guess	Lower Bound	Upper Bound	Confidence Interval			95% t-value	Standard Deviation
					90%	95%	99%		
Basket_k_Cp_Estimation. activation_energy	1.3222×10^{5}	130000	10000	1×10^{6}	180.8	215.5	283.3	613.5	109.9
Basket_k_Cp_Estimation. conductivity	0.0790539	0.08	0.04	0.4	4.012×10^{-5}	4.781×10^{-5}	6.285×10^{-5}	1654	2.439×10^{-5}
Basket_k_Cp_Estimation. ln_QA	33.7679	32	13.8155	39.1439	0.04331	0.05161	0.06785	654.2	0.02633
Basket_k_Cp_Estimation. specific_heat	1367.47	1367.47	1367.47 *	1367.47 *					
							Reference t-value (95%):	1.64502	

Click here to use above final values in future calculations

* **a parameter that lies at one of its bounds is excluded from the statistical analysis**

TOP

Sensors

- Probability of parameter lying between (Final Value - α% Confidence Interval) and (Final Value + α% Confidence Interval) = α%
- The t-value shows the percentage accuracy of the estimated parameters, with respect to the 95% confidence intervals.

Sensor Group 1					Variance Model: ConstantVariance				
Parameter	Final Value	Initial Guess	Lower Bound	Upper Bound	Confidence Interval			95% t-value	Standard Deviation
					90%	95%	99%		
ω	1.25935	1	0.01	5	0.008961	0.01068	0.01404	117.9	0.005447

Variables Measured by Sensor Group 1	
Variable	Experiments
Basket_k_Cp_Estimation → thermocouple_1	all experiments

TOP

Sensor Group 2					Variance Model: ConstantVariance				
Parameter	Final Value	Initial Guess	Lower Bound	Upper Bound	Confidence Interval			95% t-value	Standard Deviation
					90%	95%	99%		
ω	1.33784	1	0.01	5	0.009504	0.01133	0.01489	118.1	0.005778

Variables Measured by Sensor Group 2	
Variable	Experiments
Basket_k_Cp_Estimation → thermocouple_2	all experiments

TOP

Sensor Group 3					Variance Model: ConstantVariance				
Parameter	Final Value	Initial Guess	Lower Bound	Upper Bound	Confidence Interval			95% t-value	Standard Deviation
					90%	95%	99%		
ω	0.768554	1	0.01	5	0.005816	0.006931	0.009112	110.9	0.003536

Variables Measured by Sensor Group 3	
Variable	Experiments
Basket_k_Cp_Estimation → thermocouple_3	all experiments

TOP

Variance – Covariance Matrix

The variance-covariance matrix contains an approximation of the variances and covariances of the estimated process model and variance model parameters.

Variance-Covariance Matrix

Parameter		No.	1	2	3	4	5	6
Basket_k_Cp_Estimation. activation_energy		1	1.21×10^{4}					
Basket_k_Cp_Estimation.conductivity		2	0.00169	5.95×10^{-10}				
Basket_k_Cp_Estimation.ln_QA		3	2.89	4.02×10^{-7}	0.000693			
Sensor Group 1	ω	4	-0.0939	-2.79×10^{-8}	-2.22×10^{-5}	2.97×10^{-5}		
Sensor Group 2	ω	5	-0.0606	-3.41×10^{-8}	-1.44×10^{-5}	1.27×10^{-6}	3.34×10^{-5}	
Sensor Group 3	ω	6	0.0921	3.66×10^{-8}	2.18×10^{-5}	-1.7×10^{-6}	-1.75×10^{-6}	1.25×10^{-5}

TOP

Correlation Matrix

Correlation Matrix

Parameter		No.	1	2	3	4	5	6
Basket_k_Cp_Estimation. activation_energy		1	1					
Basket_k_Cp_Estimation.conductivity		2	0.63	1				
Basket_k_Cp_Estimation.ln_QA		3	1*	0.626	1			
Sensor Group 1	ω	4	-0.157	-0.21	-0.155	1		
Sensor Group 2	ω	5	-0.0954	-0.242	-0.0944	0.0405	1	
Sensor Group 3	ω	6	0.237	0.425	0.234	-0.0883	-0.0855	1

* high correlation between two parameters

TOP

Lack of Fit Test

Weighted Residual	χ^2-Value (95%)	Comment
169435	170402	Good fit: weighted residual less than χ^2-Value

TOP